

Efficiency and Emission Rates of Flares in a Turbulent Crosswind

by

Damon Burt

A thesis submitted to The Faculty of Graduate Studies and Research

in partial fulfilment of the degree requirements of

Master of Applied Science in Mechanical Engineering

Ottawa-Carleton Institute for

Mechanical and Aerospace Engineering

Department of Mechanical and Aerospace Engineering

Carleton University

Ottawa, Ontario, Canada

June 2022

Copyright © 2022 – Damon Burt

The undersigned recommend to
the Faculty of Graduate Studies and Research
acceptance of the thesis

Efficiency and Emission Rates of Flares in a Turbulent Crosswind

Submitted by **Damon Burt**

in partial fulfilment of the requirements for the degree of

Master of Applied Science in Mechanical Engineering

Dr. Matthew Johnson, Thesis Supervisor

Dr. Ron Miller, Chair, Department of Mechanical and Aerospace Engineering

Carleton University

2022

Abstract

Flaring of gas at upstream oil and gas facilities is a globally significant problem with uncertain emissions. This thesis details a methodology to quantify flare carbon conversion efficiency and emission rates of flares subjected to turbulent crosswind within quantified uncertainties using a closed-loop wind tunnel. Experiments were performed on 1-inch to 4-inch diameter pipe flares burning methane-dominated flare gas mixtures at exit velocities of 0.5–2 m/s in turbulent winds of 2–10 m/s. Flare efficiency was modestly dependent on flare diameter and exit velocity, and highly sensitive to wind speed and flare gas composition. The strong sensitivity to gas composition, even among similar methane-dominated alkane mixtures, is surprising and confounds simple, predictive emissions models. However, the data in this thesis give new insight into emissions of flares subjected to turbulent crosswinds, and developed simple empirical models offer a first-order means to quantifying flare emissions and developing greenhouse gas inventories.

Acknowledgements

I must express my utmost gratitude to my thesis supervisor, Matthew Johnson, for giving me the opportunity to join the lab group and work on a research topic of which you are undoubtedly an expert. You are a model of work ethic and clear explanation of complex problems with real-world purpose. I can't thank you enough for challenging me to do something I wasn't sure I was capable of, but I'll have to make sure I practice using a tape measure.

I would like to thank everyone part of FlareNet for making this work possible. The retrofitting, instrumentation, and troubleshooting of the wind tunnel was a textbook example of group effort and cooperation, while the ungodly hours spent running experiments were commendable. A special thank-you to Brian for the countless hours on Zoom. Your logic and patience were invaluable, and I owe you a great deal to you.

To my EERL colleagues: Cameron, Zack, Ellen, Simon, Scott, Brad, Dave, Alex, Fraser, Milad, and Parvin, it's been a treat working with you all in the lab and field. I'm still looking forward to the two Christmas parties we missed.

Mom, Dad, Katie: I am lucky to have your love and unwavering support, which kept me sane over these last few years.

Table of Contents

Abstract	iii
Acknowledgements	iv
Lists of Tables	viii
List of Figures	x
Nomenclature	xvi
Chapter 1 Introduction	20
1.1 Flaring.....	20
1.2 Types and Uses of Flares.....	21
1.3 Current Understanding of Emissions from Flares	22
1.3.1 Methane Emissions from Flares	22
1.3.2 Black Carbon	23
1.3.3 Nitrogen Oxides.....	23
1.3.4 Volatile Organic Compounds.....	24
1.4 Objectives of the current study	24
1.5 Thesis Layout.....	25
Chapter 2 Previous Research on Flares	26
2.1 Early Research on Flares	26
2.2 Controlled Experiments on Vertical Flares without Crosswind	28
2.3 Wind Tunnel Studies of Flares	28
2.4 Studies of Steam and Air Assisted Flares	30
2.5 Remote Optical Measurements of Flares	32
2.6 Aircraft Measurements.....	34
2.7 Conceptual Analysis of Flares	35
2.8 Influence of Crosswind on Flare Flames	36
Chapter 3 Experimental Setup	39
3.1 Wind Tunnel.....	39
3.2 Interchangeable Flares.....	42
3.3 Flare Gas Control and Metering.....	44
3.4 Windspeed, Temperature, and Pressure Measurement	47
3.5 Gas Sampling and Analysis.....	48
3.6 Turbulence Grid	50
3.7 Data Acquisition System	53
Chapter 4 A Methodology for Quantifying Combustion Efficiencies and Species Emission Rates of Flares Subjected to Crosswind	56
4.1 Abstract.....	56
4.2 Introduction	57

4.3	Theory	59
4.3.1	<i>Derivation of a Species Mass Balance Equation</i>	59
4.3.2	<i>Limit Approach to Determine Species Mass Emission Rates</i>	62
4.3.3	<i>General Fitting Solution to Calculate Species Accumulation Rates in the CV</i>	63
4.4	Carbon Balance Approach to Determine V_{cv}	64
4.4.1	<i>Fuel Stripping Assumption to Close Carbon Balance for V_{cv}</i>	65
4.5	Determining Carbon Conversion Efficiencies.....	66
4.6	Method Validation	67
4.6.1	<i>Sensitivity and Uncertainty Analysis using Simulated Data</i>	67
4.7	Experimental Demonstration of Derived Methodology	69
4.7.1	<i>Cold Flow Tests</i>	69
4.7.2	<i>Combustion Tests</i>	70
4.7.3	<i>Repeatability Tests</i>	73
4.8	Conclusions	74
Chapter 5	Results.....	75
5.1	Efficiency as a Function of Crosswind Speed	75
5.2	Effects of Flare Gas Exit Velocity.....	76
5.3	Effects of Flare Diameter	77
5.4	Influence of Flare Gas Compositions on Inefficiency.....	79
5.4.1	<i>Effects of Varying Hydrocarbon-Dominated Flare Gas Mixtures</i>	79
5.4.2	<i>Effects of Added Inert Diluents to the Flare Gas</i>	81
5.5	Comparison to Previous Correlations	83
5.5.1	<i>Correlation of Exit Velocity: Richardson Number</i>	83
5.5.2	<i>Correlation of Diameter</i>	83
5.5.3	<i>Correlation of Flare Gas Composition</i>	88
Chapter 6	Empirical Modelling	93
6.1	Effects of Flare Gas Composition on Flare Inefficiency.....	93
6.2	Empirical models for inefficiencies of upstream oil and gas flares	100
6.3	Empirical models for methane emission from upstream oil and gas flares	106
Chapter 7	Conclusions and Future Work	112
7.1	Conclusions	112
7.2	Future Work.....	113
References	115	
Appendix A	Supporting Information for Quantifying Combustion Efficiencies and Species Emission Rates of Flares Subjected to Crosswind	122
A.1	Derivation of the Simplified Species Balance Equation	122
A.2	Limit Approach to Determine Species Emission Rates	127
A.2.1	<i>Evaluation of $V_{air,comb,\infty}$</i>	129
A.3	General Fitting Solution to Calculate Species Accumulation Rates	130
A.3.1	<i>Mathematical Form of Concentration Rise in the Tunnel</i>	130
A.3.2	<i>Determining Test Start Time, t_0</i>	133

A.3.3	<i>Measuring Emissions of Batch Sampled Species without Time Resolved Concentrations</i>	137
A.4	Methods to Determine Wind Tunnel Volume	138
A.4.1	<i>Carbon Balance Approach to Determine V_{cv}</i>	138
A.4.2	<i>Tracer-Dilution Approach to Measure V_{cv}</i>	145
A.5	Carbon Conversion Efficiency Assuming Gas-Phase Products of Combustion Only and Assuming Emitted Hydrocarbons Have Same Form as Raw Fuel	147
A.6	Uncertainty Analysis	147
A.6.1	<i>Monte Carlo Simulation of Systematic Uncertainties</i>	147
A.6.2	<i>Sensitivity Analysis</i>	153
A.6.3	<i>Potential Influence of Analyzer Non-Linearity</i>	155
A.7	Experimental Validation of Methodology.....	157
A.7.1	<i>Convergence Tests</i>	157
A.7.2	<i>Cold-flow (Non-Reacting) Validation Experiments</i>	159
A.8	Comparing to Bourguignon et al. (1999)	162
Appendix B	Inefficiency Curves	165
Appendix C	Candidate Empirical Models for Predicting Flare Carbon Conversion Inefficiencies	171
C.1	Candidate inefficiency models for flares burning C1–C4 alkane flare gas mixtures with less than 20% inert fraction	172
C.2	Candidate inefficiency models for flares burning C1–C4 alkane flare gas mixtures with up to 70% inert fraction.....	177
Appendix D	Candidate Empirical Models for Predicting Flare Methane Yields	182
Appendix E	Flare Carbon Conversion Inefficiencies and Methane Yields for Different Fuel Mixtures as a Function of Flare Gas Properties	193
Appendix F	Reference Laminar Flame Speed Calculations	195

Lists of Tables

Table 2.1: Table of measured combustion efficiencies measured using four methods in the 2010 TCEQ study.....	33
Table 3.1: Flare Specifications used in experiments.....	43
Table 3.2: Volume fractions as a % of flare gas mixtures.	44
Table 3.3: Properties of flare gas mixtures. Properties are calculated at 25°C and 1 atmosphere unless otherwise specified.....	45
Table 3.4: Compressed Gas Cylinder Purities	46
Table 3.5: Gas Analyzer Precision and Range.	49
Table 3.6: Table of Analog and Serial Communications Data.	55
Table 4.1: Mole fractions [%] of the light, medium, and heavy 6-component flare gas mixtures (based on analysis of flare gas composition data for Alberta, Canada reported by (Johnson and Coderre 2012)) used in synthetic and experimental data.	70
Table 4.2: Repeatability tests for a 1-inch (26.6-mm) diameter pipe flare burning the M6 flare gas mixture at a nominal exit velocity of 2 m/s (flow rate of 67 SLPM) at a crosswind of 2 m/s. 73	
Table 5.1: Properties of three flare gases representative of the 2.5 th , 50 th , and 97.5 th percentile heating values of flared gases found in the upstream oil and gas industry in Western Canada. Properties are given at 15°C, 101.325 kPa.....	79
Table 6.1: Properties of gas mixtures in Figure 6.1. Properties are calculated at 15°C and 1 atm unless otherwise specified.....	94
Table 6.2: Comparison of candidate empirical models in predicting flare inefficiency of 2–4 inch diameter pipe flares burning C1–C4 alkane flare gas mixtures with <20% inert fraction (N ₂ and CO ₂).	102
Table 6.3: Comparison of candidate empirical models in predicting flare inefficiency of 2–4 inch diameter pipe flares burning C1–C4 alkane flare gas mixtures with up to 70% inert fraction (N ₂ and CO ₂).	105
Table 6.4: Comparison of candidate empirical models in predicting methane yields of 2–4 inch diameter pipe flares burning C1–C4 alkane flare gas mixtures with <20% inert fraction (N ₂ and CO ₂).	108
Table 6.5: Comparison of candidate empirical models in predicting methane yields of 2–4 inch diameter pipe flares burning C1–C4 alkane flare gas mixtures with up to 70% inert fraction (CO ₂ or N ₂)	110
Table A1: Estimated relative order of magnitude of terms on right side of Eq. (4.6) when written for different species calculated for a flare burning CH ₄ at a nominal reference flow rate of 1 m ³ /s at various carbon conversion efficiencies. All terms have units of m ³ /s unless otherwise specified. Values in parentheses indicate percentage of Term 1 on right side of Eq. (4.6).	129
Table A2: Estimated order of magnitude of terms in Eq. B.15 when <i>i</i> = CO ₂ for a flare burning CH ₄ for 10 minutes at various flow rates and carbon conversion efficiencies.	131

Table A3: Volume fractions of hydrocarbons and VOCs in CV at the end of a flare experiment burning different natural gas mixtures (M6 and H6), in 2- and 4-inch diameter flares at exit velocities of 0.5–2 m/s while subjected to crosswinds of 3–4 m/s.	142
Table A4: Summary input parameters and associated uncertainties considered in the Monte Carlo analysis.	148
Table A5: Comparison of upper bound convergence errors from Figure A12 to total bias uncertainties estimate from the Monte Carlo Analysis for tests concluded after 350–700 s. ...	159
Table A6: Cold flow experimental results conducted at the BLWTL simulating a flare burning CH ₄ . Uncertainties in the table were calculated considering an analyzer calibration (span) uncertainty of 2% in the Monte Carlo analysis.	161
Table G1: Experimentally measured Laminar flame speeds of C1–C4 alkanes and relative differences to flame speeds calculated in Cantera using the San Diego mechanism (UCSD 2016). S_L values were calculated at 298.15K and 1 atm [†]	195
Table G2: Reference laminar flame speeds for different flare gas mixtures calculated via Cantera 5.2.1 using the San Diego mechanism (UCSD 2016) at 288.15K and 1 atm.	196

List of Figures

Figure 2.1: Evaluation of flare efficiency when subject to a laminar and turbulent crosswind, (~5% turbulence intensity and integral length scale of 20cm) (Johnson and Kostiuik 2002b)..... 29

Figure 2.2: Universal non-dimensional stability curve from (Kalghatgi 1981b) 38

Figure 3.1: Boundary Layer Wind Tunnel Facility at Western University 39

Figure 3.2: a) Photo of the downstream end of the low-speed test section of the wind tunnel showing the fairings installed along the walls. b) Plan view schematic of the fairings and effective test section width as a function of distance along the test section. 40

Figure 3.3: a) Schematic of mixing barrier locations in high-speed test section and b) Uline drum fans to promote mixing of wind tunnel air. 41

Figure 3.4: CAD model of PLAs developed by Kopp et al. (2010). 42

Figure 3.5: Exploded view of the burner base, mounted with a 4-inch burner nozzle. 43

Figure 3.6: Isometric CAD model of the 4” burner mounted on the vertical and rotational traverse. 44

Figure 3.7: Wind measurements using pitot tube and ultrasonic anemometer (circled) relative to the position of the burner. 47

Figure 3.8: Measured temperatures (using RTDs) in the wind tunnel with a) 1-inch (25.4-mm) diameter flare burning the medium (M6) flare gas mixture at a nominal exit velocity of 2 m/s (flow rate of 66 SLPM) at a crosswinds of 2 m/s and a b) 3-inch (77.9-mm) diameter flare burning the medium (M6) flare gas mixture at a nominal exit velocity of 2 m/s (flow rate of 572 SLPM) at a crosswinds of 2 m/s. Temperature varies by up to ~3 degrees throughout the test. 48

Figure 3.9: Photo of gas analyzers. 49

Figure 3.10: a) CAD drawing of the passive grid designed by (Hossain 2019) and b) the grid installed in the wind tunnel at a position of 10M upwind of the flare..... 51

Figure 3.11: a) Vertical velocity profile of the burner plane, and b) horizontal velocity profiles at the burner plane, measured at a heigh of 1.2m from the floor. 52

Figure 3.12: Spectra measured in the BLWTL experimental test section using Hot Wire Anemometry (data collected by (Hossain 2019). Data is normalized for a burner diameter (d) of 1 inch..... 53

Figure 4.1: Control volume diagram for a closed-loop wind tunnel with a lab-scale flare. 60

Figure 4.2: (a) Absolute anticipated measurement uncertainty in carbon conversion efficiency for flares in a closed-loop wind tunnel, experiencing a conservative air exchange rate of 10 air changes per hour (ACH), as a function of actual carbon conversion efficiency. (b) Relative uncertainties in the methane emission rates under the same range of conditions. H6 and L6 denote the “light” and “heavy” 6-component flare gas mixtures as detailed in Table 4.1..... 68

Figure 4.3: Preliminary tests performed at the Western University Boundary Layer Wind Tunnel Laboratory using methane-based gas flares exposed to various crosswind speeds; (a) schematic of the wind tunnel complex; (b) image of a 3-inch (77.9 mm) diameter flare burning the M6 flare gas mixture in the 3.65 by 3.96 m test section of the tunnel at a crosswind of 2 m/s. 69

Figure 4.4: Concentrations of measured species at the Western University Boundary Layer Wind Tunnel Laboratory with a 2-inch (52.5-mm) diameter flare burning the heavy (H6) flare gas mixture at a nominal exit velocity of 2 m/s (flow rate of 259 SLPM). (a) Measured species concentrations and tunnel temperature for a crosswinds of 2 m/s, and (b) 9 m/s. 71

Figure 4.5: (a) Sample measured carbon conversion efficiency and species emission rate data, and (b) ratio of CH₄ to C₂H₆ in the plume relative to the same ratio in the flare, for a 4-inch (102.26-mm) diameter pipe flare burning the M6 gas mixture at a nominal exit velocity of 0.5 m/s (flow rate of 246 SLPM) while subjected to various crosswind speeds. 72

Figure 5.1: a) Inefficiency, b) species emission rates and c) ratio of CH₄/C₂H₆ in the plume to flare gas for a 4-inch flare burning M6 with an exit velocity of 1 m/s, subject to crosswind speeds of 2 to 9 m/s..... 76

Figure 5.2: Inefficiency curves for a (a) 4-inch and (b) 3-inch diameter flare burning M6 at exit velocities of 0.5 m/s, 1 m/s and 2 m/s..... 77

Figure 5.3: Inefficiency curves for flares with diameters of 1-4 inches burning M6 at an exit velocity of a) 0.5 m/s, b) 1 m/s and c) 2 m/s, at crosswind speeds between 2 and 9 m/s..... 78

Figure 5.4: Inefficiency curves for a 4-inch flare with an exit velocity of a) 0.5 m/s, b) 1 m/s and c) 2 m/s burning 3 fuels: L6, M6 and H6, at crosswind speeds of 2 to 9 m/s..... 80

Figure 5.5: Inefficiency curves for a) 3-inch, b) 2-inch and c) 1 inch flare with an exit velocity of 0.5 m/s burning the L6, M6, or H6 flare gas mixtures 81

Figure 5.6: Inefficiency curves for a 2-inch flare burning M6 with various quantities of CO₂ diluents with an exit velocity of 2 m/s at crosswind speeds between 2 and 9 m/s. 82

Figure 5.7: Inefficiency curves for a 2-inch flare burning Flare Gas M6 at exit velocities between 0.5 and 2m/s, plotted as a function of a) crosswind speeds between 2 and 9m/s and b) the $U_{\infty}/V_j^{1/3}$ parameter from Johnson and Kostiuik (2000). 83

Figure 5.8: 1-4 inch burners burning Flare Gas a) L6, b) M6 and c) H6, plotted against $U_{\infty}(gV_j)^{-1/3}D^{-n}$ developed by Kostiuik et al. (2000) where $n = 1/3$ (Johnson and Kostiuik 2002b). Figures d), e) and f) present histograms of empirical fit errors in predicting inefficiency of individual data points. 85

Figure 5.9: Efficiency of a)-c) 1-4 inch and d)-f) 2-4 inch burners, burning flare gas (L6, M6 and H6), plotted against $U_{\infty}(gV_j)^{-1/3}D^{-n}$ developed by Kostiuik et al. (2000) where n has been optimized to minimize the summed square of residuals. Figures g), h) and i) present histograms of the errors in the empirical fit errors when predicting individual data points. 87

Figure 5.10: Comparing experimental data to the heating value model for natural gas flares developed by Johnson and Kostiuik (2002) and b) histograms of model error in predicting individual data points. 89

Figure 5.11: a) Comparing 1-4 inch experimental data to the Power Factor model from Gogolek et al. (2012) and b) error in predicted inefficiency, and c) comparing 3-4 inch experimental data to the Power Factor model from Gogolek et al. (2012) and d) error in predicted inefficiency using the Power Factor..... 91

Figure 6.1: Inefficiency curves for twelve different flare gas compositions burning on a) a 2-inch flare with an exit velocity of 2 m/s flares and b) a 4-inch flare with an exit velocity of 0.5 m/s... 94

Figure 6.2: Inefficiency curves for flares burning various CH ₄ /C ₂ H ₆ blends from a) 4-inch burners with an exit velocity of 0.5 m/s and b) 2-inch burners with an exit velocity of 2 m/s at crosswind speeds between 2 and 9 m/s.....	95
Figure 6.3: Inefficiency curves for a 2-inch flare burning various 85% CH ₄ with either 15% C ₂ H ₆ or C ₃ H ₈ with an exit velocity of 2 m/s at crosswind speeds between 2 and 9 m/s.....	96
Figure 6.4: Inefficiency as a function of several parameters for 2-inch flares burning flare gases with less than 20% inert dilution at an exit velocity of 2 m/s at a nominal crosswind speed of 4 m/s.....	98
Figure 6.5: Methane yield as a function of several parameters for 2-inch flares burning flare gases with less than 20% inert dilution at an exit velocity of 2 m/s at a nominal crosswind speed of 4 m/s.....	100
Figure 6.6: a) Suggested empirical model for predicting carbon conversion inefficiency of 2–4 inch diameter pipe flares burning C1–C4 alkane-based flare gas mixtures with less than 20% inert fraction (CO ₂ and N ₂) and b) corresponding histograms of the errors in the predicted inefficiency.....	104
Figure 6.7: a) Empirical model for predicting carbon conversion inefficiency of 2–4 inch diameter pipe flares burning C1–C4 alkane flare gas mixtures including data for mixture with higher inert fraction (up to 70% CO ₂ or N ₂) and b) corresponding histograms of the errors in the predicted inefficiency.....	106
Figure 6.8: a) Empirical model for predicting methane yield of 2–4 inch diameter pipe flares burning C1–C4 alkane flare gas mixtures with <20% inert fraction (CO ₂ and N ₂) and b) corresponding histogram of the errors in the predicted methane yield.....	109
Figure 6.9: a) Empirical model for predicting methane yield of 2–4 inch diameter pipe flares burning C1–C4 alkane flare gas mixtures with up to 70% inert fraction (CO ₂ or N ₂) and b) corresponding histogram of the errors in the predicted methane yield.....	111
Figure A1: Example measured CO ₂ volume fraction during a test with labels indicating how test start time t_0 is determined.....	135
Figure A2: Example use of the Fast Fourier Transform (FFT) of measured CO ₂ volume fraction to determine the wind tunnel lap time.....	136
Figure A3: Effective lap time of the wind tunnel as a function of wind speed.....	137
Figure A4: Relative error (expressed as a percentage of the actual value) in calculated wind tunnel volume, V_{cv} , carbon conversion efficiency, or CH ₄ emission rate when calculated using the fuel stripping assumption (Eq. (4.14)) for a synthetic data set generated burning flare gas L6, M6 and H6 that assumed heavy hydrocarbons burn preferentially and only CH ₄ is emitted as a hydrocarbon. The induced error as a function of efficiency is independent of flare gas flow rate.	145
Figure A5: Example uncertainty distributions from the Monte Carlo simulation of a 3-inch (77.9-mm) flare burning the M6 flare gas mixture at a flow rate of 286 SLPM ($V_j= 1\text{m/s}$) while subjected to a crosswind of 2 m/s. (a) Carbon conversion efficiency, (b) methane emissions, (c) carbon dioxide emissions, and (d) carbon monoxide emissions.	150
Figure A6: Comparison of absolute Monte Carlo estimated uncertainties in carbon conversion efficiency using either the a) carbon balance or b) tracer methods to determine V_{cv} for a flare burning the L6 or H6 flare gas mixtures.	151

Figure A7: Monte Carlo estimated uncertainties in emission rates of a) CH ₄ , b) CO ₂ , and c) CO calculated using the carbon balance method.....	152
Figure A8: Monte Carlo Simulation for a) carbon conversion efficiency, b) CH ₄ emissions, c) CO ₂ emissions, and d) CO emissions assuming a 1% linearity error of gas-phase analyzers.....	153
Figure A9: Sensitivity of uncertainty in methane emission rate to individual input variables, while other variables remain fixed. Analysis considers a flare burning 250 SLPM of H6 with 90% carbon conversion efficiency. †CO ₂ /CO/CH ₄ measurement error includes both calibration error and analyzer non-linearity.	154
Figure A10: Sensitivity of uncertainty in methane emission rate to individual input variables with all other variables simultaneously varying. Analysis considers a flare burning 250 SLPM of H6 with 90% carbon conversion efficiency. †CO ₂ /CO/CH ₄ measurement error includes both calibration error and analyzer non-linearity.....	155
Figure A11: (a) Generic parabolas used to simulate non-linearity in gas analyzer response with a maximum deviation of 5%; (b) example non-linear calibration curves generated using the generic parabolas with an example span of 600 ppm.	157
Figure A12: Convergence of (a) carbon conversion efficiency, (b) CH ₄ emission rate, (c) CO ₂ emission rate, and (d) CO emission rate at varying experiment durations for a 4-inch (102.3-mm) diameter flare burning M6 at a flow rate of 246 SLPM.	158
Figure A13: Cold flow experiment results conducted at the BLWTL simulating a flare burning CH ₄ at efficiencies of 80–99% and flow rates of 50–125 SLPM subject to crosswind speeds of 2–9m/s. The error bars represent the total experimental uncertainty, combining bias errors from the Monte Carlo analysis with precision errors from repeated experiments as detailed in Table A6.	160
Figure A14: Reanalysis of selected flare efficiency experimental data from (Johnson and Kostiuik 2000, 2002b) comparing results using the presently derived calculation methodology to the original method of (Bourguignon et al. 1999) which included an error in the tunnel volume-temperature term as noted. Results show the impact of this error was negligible, consistent with the small temperature changes within the CV during their experiments.	164
Figure B1: Inefficiency curves for a-c) L6, d-f) M6 and g-i) H6, plotted as a function of crosswind speed.....	165
Figure B.2 Inefficiency curves of various simple fuel mixtures, plotted as a function of crosswind speed.....	166
Figure B.3 Inefficiency curves for a-c) L6, d-f) M6 and g-i) H6, plotted as a function of Eq. 5.2.	167
Figure B.4 Inefficiency curves of various simple fuel plotted as a function of Eq. 5.2.	168
Figure B.5 Inefficiency curves for a-c) L6, d-f) M6 and g-i) H6, plotted as a function of Eq.5.3, where $n = 1/3$	169
Figure B.6 Inefficiency curves for various simple fuel plotted as a function of Eq.5.3, where $n = 1/3$	169
Figure B.7 Inefficiency curves for a-M6 diluted with inert species as a function of a) wind speed, b) 5.2 and c) Eq.5.3, where $n = 1/3$	170
Figure C1: a) Empirical model using $AF_{mass,stoic}$ as a correlating parameter to predict carbon conversion inefficiency of 2–4 inch diameter pipe flares burning C1–C4 alkane-based flare gas	

mixtures with less than 20% inert fraction (CO ₂ and N ₂) and b) corresponding histograms of the errors in the predicted inefficiency.	172
Figure C2: c) Empirical model using S_L as a correlating parameter to predict carbon conversion inefficiency of 2–4 inch diameter pipe flares burning C1–C4 alkane-based flare gas mixtures with less than 20% inert fraction (CO ₂ and N ₂) and d) corresponding histograms of the errors in the predicted inefficiency.	173
Figure C3: e) Empirical model using LHV_{mass} as a correlating parameter to predict carbon conversion inefficiency of 2–4 inch diameter pipe flares burning C1–C4 alkane-based flare gas mixtures with less than 20% inert fraction (CO ₂ and N ₂) and f) corresponding histograms of the errors in the predicted inefficiency.	174
Figure C4: g) Empirical model using LHV_{vol} as a correlating parameter to predict carbon conversion inefficiency of 2–4 inch diameter pipe flares burning C1–C4 alkane-based flare gas mixtures with less than 20% inert fraction (CO ₂ and N ₂) and h) corresponding histograms of the errors in the predicted inefficiency.	175
Figure C5: i) Empirical model using mean carbon number ($C_{\#}$) as a correlating parameter to predict carbon conversion inefficiency of 2–4 inch diameter pipe flares burning C1–C4 alkane-based flare gas mixtures with less than 20% inert fraction (CO ₂ and N ₂) and j) corresponding histograms of the errors in the predicted inefficiency.	176
Figure C6: a) Empirical model using $AF_{mass,stoic}$ as a correlating parameter to predict carbon conversion inefficiency of 2–4 inch diameter pipe flares burning C1–C4 alkane-based flare gas mixtures with up to 70% inert fraction (CO ₂ and N ₂) and b) corresponding histograms of the errors in the predicted inefficiency.	177
Figure C7: c) Empirical model using S_L as a correlating parameter to predict carbon conversion inefficiency of 2–4 inch diameter pipe flares burning C1–C4 alkane-based flare gas mixtures with up to 70% inert fraction (CO ₂ and N ₂) and d) corresponding histograms of the errors in the predicted inefficiency.	178
Figure C8: e) Empirical model using LHV_{mass} as a correlating parameter to predict carbon conversion inefficiency of 2–4 inch diameter pipe flares burning C1–C4 alkane-based flare gas mixtures with up to 70% inert fraction (CO ₂ and N ₂) and f) corresponding histograms of the errors in the predicted inefficiency.	179
Figure C9: g) Empirical model using LHV_{vol} as a correlating parameter to predict carbon conversion inefficiency of 2–4 inch diameter pipe flares burning C1–C4 alkane-based flare gas mixtures with up to 70% inert fraction (CO ₂ and N ₂) and h) corresponding histograms of the errors in the predicted inefficiency.	180
Figure C10: i) Empirical model using mean carbon number ($C_{\#}$) as a correlating parameter to predict carbon conversion inefficiency of 2–4 inch diameter pipe flares burning C1–C4 alkane-based flare gas mixtures with up to 70% inert fraction (CO ₂ and N ₂) and j) corresponding histograms of the errors in the predicted inefficiency.	181
Figure D1: a) Empirical model using $AF_{mass,stoic}$ as a correlating parameter to predict carbon conversion inefficiency of 2–4 inch diameter pipe flares burning C1–C4 alkane-based flare gas mixtures with less than 20% inert fraction (CO ₂ and N ₂) and b) corresponding histograms of the errors in the predicted inefficiency.	183
Figure D2: c) Empirical model using S_L as a correlating parameter to predict carbon conversion inefficiency of 2–4 inch diameter pipe flares burning C1–C4 alkane-based flare gas mixtures with	

less than 20% inert fraction (CO ₂ and N ₂) and d) corresponding histograms of the errors in the predicted inefficiency.	184
Figure D3: e) Empirical model using LHV_{mass} as a correlating parameter to predict carbon conversion inefficiency of 2–4 inch diameter pipe flares burning C1–C4 alkane-based flare gas mixtures with less than 20% inert fraction (CO ₂ and N ₂) and f) corresponding histograms of the errors in the predicted inefficiency.	185
Figure D4: g) Empirical model using LHV_{vol} as a correlating parameter to predict carbon conversion inefficiency of 2–4 inch diameter pipe flares burning C1–C4 alkane-based flare gas mixtures with less than 20% inert fraction (CO ₂ and N ₂) and h) corresponding histograms of the errors in the predicted inefficiency.	186
Figure D5: i) Empirical model using mean carbon number ($C_{\#}$) as a correlating parameter to predict carbon conversion inefficiency of 2–4 inch diameter pipe flares burning C1–C4 alkane-based flare gas mixtures with less than 20% inert fraction (CO ₂ and N ₂) and j) corresponding histograms of the errors in the predicted inefficiency.	187
Figure D6: a) Empirical model using $AF_{mass,stoic}$ as a correlating parameter to predict methane yields of 2–4 inch diameter pipe flares burning C1–C4 alkane-based flare gas mixtures with up to 70% inert fraction (CO ₂ and N ₂) and b) corresponding histograms of the errors in the predicted methane yield.	188
Figure D7: c) Empirical model using S_L as a correlating parameter to predict methane yields of 2–4 inch diameter pipe flares burning C1–C4 alkane-based flare gas mixtures with up to 70% inert fraction (CO ₂ and N ₂) and d) corresponding histograms of the errors in the predicted methane yield.	189
Figure D8: e) Empirical model using LHV_{mass} as a correlating parameter to predict methane yields of 2–4 inch diameter pipe flares burning C1–C4 alkane-based flare gas mixtures with up to 70% inert fraction (CO ₂ and N ₂) and f) corresponding histograms of the errors in the predicted methane yield.	190
Figure D9: g) Empirical model using LHV_{vol} as a correlating parameter to predict methane yields of 2–4 inch diameter pipe flares burning C1–C4 alkane-based flare gas mixtures with up to 70% inert fraction (CO ₂ and N ₂) and h) corresponding histograms of the errors in the predicted methane yield.	191
Figure D10: i) Empirical model using mean carbon number ($C_{\#}$) as a correlating parameter to predict methane yields of 2–4 inch diameter pipe flares burning C1–C4 alkane-based flare gas mixtures with up to 70% inert fraction (CO ₂ and N ₂) and j) corresponding histograms of the errors in the predicted methane yield.	192
Figure E1: Carbon conversion inefficiency of 2-inch diameter flares burning a range of flare gas mixtures flare at an exit velocity of 2 m/s at a nominal crosswind speed of 4 m/s plotted as a function of several different potential correlating parameters.	193
Figure E2: Methane yields of 2-inch diameter flares burning a range of flare gas mixtures flare at an exit velocity of 2 m/s at a nominal crosswind speed of 4 m/s plotted as a function of several different potential correlating parameters.	194
Figure F1: Reference laminar flame speeds for different flare gas mixtures calculated via Cantera 5.2.1 using the San Diego mechanism (UCSD 2016) at 288.15K and 1 atm.	196

Nomenclature

Symbol	Description	Units	First Use Page
AF	air to fuel ratio	[-]	79
D	burner diameter	m	84
$C_{\#}$	carbon number	[-]	97
b	width of grid obstructions	m	50
$C(s)$	solid-phase carbon	[-]	65
d_e	effective burner diameter	m	37
η	carbon conversion efficiency	[-]	59
g	gravitational constant	m/s ²	84
γ	coefficient to account for number of moles of combustion products introduced into the tunnel relative to the number of moles of fuel	[-]	163
Hz	Hertz	s ⁻¹	48
I_u	turbulence intensity	[-]	50
L_x	integral length scale	m	50
\dot{m}	mass flow rates	kg/s	59
M	grid spacing of obstructions	m	50
M	molar mass of species	kg/kmol	59
MW	molecular weight	kg/kmol	79
σ	standard deviation	[-]	50
T	temperature	K	59
t	time	s	64
t_{lap}	time required for parcel of gas to travel around the wind tunnel	s	134
T_{ad}	adiabatic flame temperature	K	97
θ_e	fuel mass fraction at burner exit	[-]	37
θ_s	fuel mass fraction in stoichiometric mixture	[-]	37
P	pressure	kPa	59
R	momentum flux ratio	[-]	36
R^2	coefficient of Determination	[-]	102
R_H	Reynolds stability number	[-]	37
R_u	universal ideal gas constant	J/molK	62
R_{uu}	autocorrelation function	[-]	50
ρ	rho	kg/m ³	36
S_L	laminar flame speed	m/s	37
u_i	velocity component in direction i	m/s	50
U_{∞}	wind speed	m/s	36
\dot{V}	volume flow rates	m ³ /s	61

Symbol	Description	Units	First Use Page
$V_{air,comb}$	stoichiometric volume of combustion air	m^3/s	61
V_{cv}	volume of control volume	m^3	61
ν	kinematic viscosity	m^2/s	37
V_j	flare gas exit velocity	m/s	36
X	mole fraction	[-]	59
x	average number of carbon atoms in hydrocarbons	[-]	61
$X_{HC,cv}$	mole fraction of hydrocarbons contained in the CV air	[-]	61
ν			
Y_{CH_4}	methane yield	$\frac{g_{CH_4}}{kg_{HC,fg}}$	98

Acronym	Description	First Use Page
AFTIR	Active Fourier Transform Infrared	33
ALAR	Airborne Laboratory for Atmospheric Research	34
BC	Black Carbon	23
BLWTL	Boundary Layer Wind Tunnel Laboratory	39
CAD	Computer Aided Design	44
CFD	Computational Fluid Dynamics	35
CGA	Compressed Gas Association	46
CV	control volume	59
CZG NHV	Combustion zone net heating value	30
DIAL	Differential absorption light detection	32
DRE	Destruction Removal Efficiency	34
EOG	Earth Observation Group	20
EPA	Environmental Protection Agency	22
FFID	Fast flame ionization detection	103
FFT	Fast Fourier Transform	52
FID	Flame Ionization detector	163
FTIR	Fourier transform infrared	32
GC	Gas chromatograph	45
GC-MS	Gas chromatography-mass spectrometry	141
<i>HC</i>	hydrocarbons	61
HHV	Higher Heating Value	45
IFTS	Imaging Fourier transform spectrometer	33
IPCC	International Panel on Climate Change	23
LES	Large Eddy Simulation	35
LGR	Los Gatos Research	55
LHV	Lower Heating Value	45
MFC	Mass Flow controller	33

Acronym	Description	First Use Page
MFR	Mass Flow Ratio	31
NI	National Instruments	53
NPS	National Pipe Standard	43
NSERC	National Science and Engineering Research Council	39
ODE	Ordinary differential equation	63
OGI	Optical Gas Imaging	23
PFTIR	Passive Fourier Transform Infrared	33
PF	Power Factor	89
PIRS	Passive imaging radiometric spectrometer	33
PLA	Pressure loading actuators	41
RANS	Reynolds averaged Navier Stokes	35
RMSE	Root mean square error	104
RTD	Resistance temperature detector	47
SSE	Sum squared error	104
TCEQ	Texas Commission on Environmental Quality	30
THC	Total hydrocarbons	26
UAV	Unmanned aerial vehicles	34
UMHC	Unmeasured hydrocarbons	65
VIIRS	Visible Infrared Imaging Radiometer Suite (VIIRS)	21
VOC	Volatile Organic Compounds	20

Chemical Formula	Description	First Use Page
C(s)	Solid phase Carbon (soot)	65
	Hydrocarbons heavier than	
C2+	methane	66
C ₂ H ₆	Ethane	44
C ₃ H ₈	Propane	44
C ₄ H ₁₀	Butane	44
CH ₄	Methane	23
CO	Carbon Monoxide	26
CO ₂	Carbon Dioxide	20
C _x H _y	General Hydrocarbon	61
H ₂ O	Water	27
H ₂ S	Hydrogen Sulfide	27
N ₂	Nitrogen	44
NO _x	Nitrogen Oxides	23
O ₂	Oxygen	26

Subscript	Subscript Denotation	First Use
0	time 0	67
<i>cv</i>	control volume	59
<i>ex</i>	exfiltration	60
<i>f</i>	flare gas	60
<i>i</i>	species i	60
<i>in</i>	infiltration	60
<i>inert</i>	inert species	60
∞	ambient conditions	60
<i>j</i>	flare gas exit velocity	76
<i>p</i>	plume	60
<i>prod, comb</i>	produced from combustion	60
<i>r</i>	reburning of species in the CV	60
<i>stoic</i>	stoichiometric conditions	99
<i>mass</i>	mass of property	97
<i>vol</i>	volume of property	99
<i>tr</i>	tracer gas	146

Chapter 1 Introduction

1.1 Flaring

Flaring at oil and gas facilities is the process of burning unwanted or surplus gas in an open-atmosphere, non-premixed turbulent flame, typically from the top of a simple vertical pipe. Satellite data suggest that global flaring volume increased to 161 billion m³ in 2019, approximately 90% of which was attributed to upstream oil and gas production sites (EOG 2021). Flaring is preferred over direct venting of gas to atmosphere to reduce net greenhouse gas emissions, since methane (the dominant component of natural gas and generally the largest component of flare gas at upstream production sites) has a global warming potential 82.5/29.8 times greater than carbon dioxide on a 20/100 year time horizon (Forster et al. 2021). However, emissions from flares are also generally undesirable.

In addition to producing CO₂, incomplete combustion, i.e. “inefficient” flaring, can result in the emission of unburned fuel (Gvakharia et al. 2017; Johnson et al. 2001), volatile organic compounds (Knighton et al. 2012), nitrogen oxides (Torres et al. 2012c; McDaniel 1983), and carbonaceous soot or black carbon (Conrad and Johnson 2017; Weyant et al. 2016; Johnson et al. 2013; Fortner et al. 2012; McEwen and Johnson 2012). The composition of unburned fuel emissions can vary, but typical flared gases are mostly methane-dominated alkane hydrocarbons with small amounts of alkenes, aromatics, and hydrogen sulphide, and diluents such as helium, nitrogen and carbon dioxide (Tyner and Johnson 2020; Conrad and Johnson 2017; Johnson and Coderre 2012). Methane is an important climate forcer as noted above, and nitrogen oxides and VOCs can also have important secondary climate impacts in the atmosphere (IPCC 2021). Black carbon is a strong climate forcer, both through direct absorption in the atmosphere and through changes in surface albedo when deposited on snow and ice (Bond et al. 2013). Black carbon emissions from flaring at the northern latitudes of Russia are thought to be an especially important contributor to Arctic temperature rise and accelerating ice melt due to the earth’s decreasing surface albedo (Sand et al. 2016).

Flare emissions also have potential human health impacts. Emissions such as black carbon have been associated with cardiovascular mortality and cardiopulmonary hospital admissions (Luben et al. 2017; Li et al. 2016; Janssen et al. 2011), while elevated VOC concentrations have been found

to adversely affect human health (Mølhave et al. 1997). Recent studies have also found correlations between proximity to flaring and elevated health risks. A study of 23,487 women in the Eagle Ford Shale in Southern Texas found up to 50% higher odds of preterm birth, as well as shorter gestation periods for residents within 5 km of flaring sites (Cushing et al. 2020). In the Bakken, Eagle Ford Shale, and Permian Basin, an estimated 535,000 people live within 5 km of flaring activities. Native Americans on the Fort Berthold Indian Reservation in the Bakken and people of colour in the Permian and Eagle Ford Shale were found to be disproportionately impacted by flaring activities (Cushing et al. 2021). Similar studies using VIIRS measurements between March 2012 and December 2016 and 2010 US Census data revealed flare events impacted majority Hispanic populations within 5 km twice as much as populations with <20% Hispanic populations (Johnston et al. 2020). More generally, an estimated 17.6 million US residents live within 1 mile of an active oil or gas well (Czolowski et al. 2017).

Unfortunately, there remains significant uncertainty on the magnitudes of flare emissions and the factors that influence them. Since flares operate in the open atmosphere, they are subject to variable environmental conditions that can impact the flame and emissions. Data for flares subjected to turbulent crosswinds are especially lacking in the literature. Moreover, proven models to predict emissions of flares with different fuel compositions, crosswind velocities, exit velocities, and diameters do not exist. This severely restricts the ability to create accurate pollutant emission inventories and regulations. This thesis is intended to partially fill this gap by completing what is believed to be the first-ever comprehensive set of experiments to quantify emissions from flares subjected to a turbulent crosswind.

1.2 Types and Uses of Flares

Flares may be broadly classified as unassisted or assisted. Assisted flares typically inject steam or air at or near the burner tip to suppress visible smoke emissions and promote the mixing of air with the flame. Steam and air assisted flares are typically found at refineries and chemical plants where process steam, air, and/or power are available and associated infrastructure can justify the capital costs of an engineered flare tip (Sorrels and Coburn 2019). However, approximately 90% of global gas flaring is attributed to upstream oil and gas production sites (EOG 2021). These sites rarely employ engineered flare systems and often do not have on-site electricity. Thus, steam- and air-assisted flares can be inferred to contribute limited quantities to global flare emissions. The present analysis considers simple flares typically found in the upstream oil and gas industry,

which generally consist of an open-atmosphere flame established at the end of a simple, vertical pipe.

There are several reasons why flaring may occur. Emergency flaring is the intermittent flaring of flammable gases, often in large, short duration releases for safety or maintenance reasons (McEwen and Johnson 2012). Process flaring may be necessary during well testing to determine well reservoir size, which may occur on the orders of days or weeks until well pressures and flow rates are stabilized (McEwen and Johnson 2012). Production flaring to destroy unwanted produced gas may persist over the lifetime of an oil producing well (Ohio EPA 2012), even when no gas is initially present in a reservoir. Solution gases which may be dissolved in formation liquids under high reservoir pressure may come out of solution when the produced oil is brought to the atmospheric pressure at the surface (Johnson and Coderre 2012). Due to the higher market value of oil and lack of infrastructure to gather and process associated gas in certain regions, oil-producing well sites may use continuously operating production flares to dispose of the associated gas (Ohio EPA 2012).

1.3 Current Understanding of Emissions from Flares

1.3.1 Methane Emissions from Flares

Methane accounts for a significant portion of flared gases in the upstream oil and gas industry (Johnson and Coderre 2012), and flaring is shown to be a potentially important source of methane emissions (Zavala-Araiza et al. 2021; Gvakharia et al. 2017; Johnson et al. 2001). Controlled experiments on scaled-down flares in a low-turbulence wind tunnel have shown that unburned flare gas may be directly ejected from the flame at higher wind speeds (Johnson and Kostjuk 2002a; Johnson et al. 2001). Combining point sampling using a fast flame ionization detector with laser imaging, Johnson et al. (2001) proposed a mechanism in which at low-momentum flux ratios (i.e., low flare exit velocity relative to crosswind speed), a standing vortex on the leeward side of the flare stack stretches the vortices from the shear layer between flame and air and pulls them toward the underside of the flame. These vortices can then be intermittently ejected below the main tail of the flame, allowing them to escape combustion.

Malfunctioning or unlit flares have also been implicated as a significant source of methane emissions under field conditions. A recent study by Irakulis-Loitxate et al. (2021) using satellite-based spectroscopy suggested that 21% of emitted methane was the result of active flaring

processes with emission rates between 1640 and 2640 kg/h, attributed to either inefficient or malfunctioning flares. A separate survey of the Permian Basin between September and November 2019 using airplane-based imaging spectrometers with detection limits between 10–20 kg CH₄/h identified 1100 methane sources. The survey determined that unlit or inefficient flares accounted for 7.4% of detected plumes, and 12% of total measured methane emissions in the region (Cusworth et al. 2021). Three helicopter-based surveys were conducted in the Permian Basin between February and June 2020 using optical gas imaging (OGI) cameras found that 11% of flares had combustion issues, while 6.5% were the result of inefficient or malfunctioning flares, and estimated a basin-wide flare efficiency of 93% (Lyon et al. 2021).

1.3.2 Black Carbon

Black carbon (BC), or soot, has been studied in both theoretical and laboratory measurements (Mehr 2020; McEwen and Johnson 2012; Ellzey et al. 1990; Becker and Liang 1982), and field measurements (Conrad and Johnson 2017; Gvakharia et al. 2017; Weyant et al. 2016; Johnson et al. 2011, 2013). BC emission rates from individual flares can vary by scale several orders of magnitude (Conrad and Johnson 2017; Weyant et al. 2016) and likely vary strongly with operating conditions and flare gas composition. In addition, differences in estimated magnitudes of emissions rates among studies may be at least partially related to under sampling in techniques relying on extractive samples from the plume (Seymour and Johnson 2021). However, it seems likely that BC emissions account for less than 0.5% of the total carbon mass in the fuel for propane-fueled flares (Torres et al. 2012b; Ellzey et al. 1990; Pohl et al. 1986) and < 0.1% for flares burning methane-dominated fuel mixtures (McEwen and Johnson 2012). Given the present experiments focus on methane-dominated flare gas mixtures typical of upstream oil and gas production sites flares, the present analysis is limited to gas-phase emissions and BC emissions are not considered further in this thesis.

1.3.3 Nitrogen Oxides

Oxides of nitrogen such as nitric oxide and nitrogen dioxide (NO_x) may also be produced as part of the combustion process. Since these species are precursors for tropospheric ozone, emissions of NO_x from flaring are a global concern (IPCC 2021). Torres et al. (2012b) reported NO_x emissions were reported for a limited number of tests on steam- and air-assisted flares burning propane and natural gas mixtures. They found yields ranging from 0.009- 0.033lb NO_x/MMBTU for steam-assisted flares and 0.037-0.083lb NO_x/MMBTU for air- assisted flares. Using an air-blower, Talebi

et al. (2014) considered the impact of a crosswind on NO_x emissions diffusion flames burning methane, propane and butane using an unspecified-diameter, lab scale burner. Results show a slight decrease in NO_x emissions with increased crosswind, such that NO_x emissions for a vertical flame may be considered to represent a maximum. For the present thesis, equipment to measure NO_x emissions in the wind tunnel was not available during the experiments and NO_x emissions from flares in crossflow is left for future studies.

1.3.4 Volatile Organic Compounds

Volatile organic compounds (VOCs) may be emitted by flares, either as raw fuel that escapes combustion, or through complex reformation processes that occur prior to complete combustion. The EPA specifies an emission factor of 0.66 lb/MMBTU (U.S. EPA 2018), which is based on various flares at refinery and chemical manufacturing processing facilities. Knighton et al. (2012) reported direct measurement of VOCs as a function of flare efficiency for steam- and air-assist flares burning primarily propene or propane, and natural gas diluted with nitrogen. VOC products were found to be dependent on fuel composition rather than flare type. Propane flares produced ~80% ethene and propene-based products, while propene products contained more oxygenated materials such as formaldehyde and acetaldehyde (accounting for approximately 20–25% of VOC products). While methods to quantify VOC emissions have been developed and are provided in more detail in Chapter 4, measured volume fractions of VOCs were generally near detection limits in the present experiment and are not considered in detail in the present work.

1.4 Objectives of the current study

Despite the magnitudes of flaring and their associated emission of atmospheric pollutants, there remains limited understanding of the mechanisms that result in flare emissions. This data and knowledge gap is especially true for flares subjected to a turbulent crosswind. Through controlled experiments using a large-scale wind tunnel, this thesis investigates the impacts of turbulent crosswinds on unassisted pipe flares representative of those found in the upstream oil and gas industry. A detailed methodology, using an unsteady mass-balance approach, was first developed to quantify flare performance, including efficiency and emission rates. Experiments were then performed to evaluate flare efficiency as a function of wind speed, flare properties such as burner diameter and exit velocity, and fuel properties of various gas mixtures. These experiments considered flares burning methane-dominated gas mixtures representative of the upstream oil and gas industry in Western Canada while subjected to turbulent crosswinds representative of

typical atmospheric conditions. Flare diameters ranged from 1 to 4 inches, which overlaps with the 3–12 inch diameter range commonly seen in the field (Conrad and Johnson 2017; McEwen and Johnson 2012). Results confirm conclusions of previous studies that crosswind speed, flare gas exit velocity and burner diameter have an impact on flare inefficiency, while providing new insight into the emissions patterns at scales relevant to field conditions. Flare inefficiency is shown to be surprisingly sensitive to flare gas composition. Although a detailed understanding of the specific mechanisms driving emissions remains elusive, empirical models to predict flare efficiency and methane yield are developed, which may offer significant improvements over existing rules of thumb used to create national greenhouse gas inventories.

1.5 Thesis Layout

Chapter 2 of this thesis reviews previous research of flare emissions, including field measurements and controlled experiments at various scales. Chapter 3 details the closed-loop wind tunnel facility and experimental setup used to perform flare experiments. Chapter 4 introduces a detailed methodology in which an unsteady mass balance approach is used to relate measured accumulations in a closed-loop wind tunnel to emission rates and flare efficiency. The methodology is assessed with a detailed uncertainty analysis. Chapter 5 presents the results of flare experiments and compares current experimental data to previously developed empirical models. Chapter 6 describes extended analysis of the experimental data in an attempt to develop an empirical relationship to predict flare inefficiency and methane yield over a range of operating conditions and scales. Chapter 7 concludes the thesis with a summary of key outcomes in relation to the specified objectives and suggested ways the work may be extended.

Chapter 2 Previous Research on Flares

2.1 Early Research on Flares

The PhD thesis of Siegel (1980) was one of the earliest studies to explicitly consider flare emissions. A 0.7 m diameter steam-assisted test flare was constructed and single point samples were collected from a moveable crane to measure CO, O₂, NO_x, and ionizable organic compounds (THC). Experiments at quiescent conditions (defined as <1 m/s winds) concluded that combustion efficiencies exceeded 99%. Attempts were made to assess the impacts of crosswind using a blower applied to the flames but it was not possible to determine an overall efficiency due to the variability in the flame position and the challenges in measuring gas velocity along a principle flow direction. Instead, local conversion efficiencies (at the sample point only) were assessed, which were also found to be greater than 99%.

McDaniel (1983) used single point sampling to measure O₂, CO₂, CO, NO_x, and THC above 101.5 mm outer diameter, vertical, steam- and air-assisted flares in quiescent conditions. Combustion efficiency was found to decline under excessive steam, as well as high exit velocities of flare gas. Although the lowest measured efficiency was 55%, McDaniel (1983) concluded that “when flares are operated under conditions which are representative of industrial practices, the combustion efficiencies in the plume are greater than 98%”. It is noted that all tests occurred in wind speeds less than 5 miles per hour (~2.2 m/s). Although flame position was observed to meander due to slight variations in ambient wind conditions, no corresponding variation was seen in the calculated combustion efficiency.

In what has become one of the most widely quoted studies on flaring, Pohl et al. (1986) measured efficiencies from 3-, 6- and 12-inch diameter flares burning propane with nitrogen dilution at the Flare Test Facility at the Energy and Environment Research Group Corporation. The facility was constructed with a screened enclosure that shielded the flare from the influence of wind. Extractive samples were collected from a single-point sample probe positioned directly above the flare. Although reported uncertainties on the measured combustion inefficiency were as high as 50%, these were deemed slight since in practice the flare inefficiency was typically on the order of 1%, such that uncertainty range on inefficiency would be 0.5-1.5%. Pohl et al. (1986) concluded that the combustion efficiencies of flares operated within the stability limit of the flame were

greater than 98% and that the combustion efficiency was independent of the three burner diameters used in experiments. Additionally, they concluded that soot from smoky flares accounted for less than 0.5% of the unburned hydrocarbon emissions. This study is often credited as the basis for the common industry assertion that efficiencies of industrial flares are >98%.

Stroscher (1996) performed experiments on small diffusion flames burning natural gas from 2- and 6-mm diameter tubes using a combination of single point and multiprobe sampling methods. In quiescent conditions, measured combustion efficiencies of these flames exceeded 97.3%. However, when 23% condensate vapour was mixed the natural gas feeding the burner, efficiencies were reduced to 87.2-89.6%.

Stroscher (1996) also attempted field measurements on flares at two oilfield battery sites in Alberta, one producing “sweet” gas and one producing “sour” gas containing H₂S. Using single-point extractive sampling from a probe held near the flame by a hydraulic lift, Stroscher (1996) reported combustion efficiencies as low as 62% for a 12 cm diameter pipe flare at the sweet battery site when condensate was directed to the flare. Mean wind speeds at the site were up to 3.5 m/s during the measurements. At the sour battery site, a combustion efficiency of 84% was measured for a 7.6 cm diameter flare burning solution gas containing 23% H₂S. Further tests suggested there was a correlation between the height of liquid in the flare knockout drum and flare efficiency, which varied from 71.0–63.9% (as reported) as the liquid level increased from 9–69 cm.

However, no uncertainty analysis is included with these data and there is cause for doubt on the accuracy of the results. In addition to potential uncertainty from an apparent lack of background correction in the employed methodology (see Corbin and Johnson, 2014), it is unclear whether the local efficiency measured at the probe location is necessarily representative of the overall flare (similar to the challenges noted by Siegel (1980) in his attempt to measure flare efficiency under the influence of crosswind). McEwen and Johnson (2012), citing other authors, suggested that efficiency measurements using single point sampling of an inhomogeneous flare plume may be challenged to accurately represent overall combustion efficiency of vertical, pilot scale flares (Pohl et al. 1986) and laboratory scale flares in a crosswind (Howell 2004; Poudenx 2000). Recent experiments and analysis by Seymour and Johnson (2021) have shown that H₂O and BC volume fractions can independently vary within in a turbulent plume, such that single point sampling

methods relying on fixed ratios of species to complete a mass balance can be prone to error if sampling periods are short and/or sample numbers are small.

2.2 Controlled Experiments on Vertical Flares without Crosswind

McEwen and Johnson (2012) studied black carbon (BC, i.e., soot) emissions from vertical, 12.7- to 76.2-mm diameter flares burning methane-based fuels representative of the upstream oil and gas industry in Western Canada. Experiments were performed in a lab setting and the flares were surrounded by a screen to shield the flame from room air currents. A simple empirical relationship was presented to estimate soot yield as a function of the flare heating value over a range of conditions. However, carbon conversion efficiencies and methane emission rates were not reported.

Corbin and Johnson (2014) published a detailed methodology to quantify carbon conversion efficiency and species emission rates in flare experiments in which the entire combustion plume is captured and mixed prior to extractive sampling. The method has since been used in several papers measuring the performance of steam- and air-assist flares (Bello et al. 2021; Zamani et al. 2021; Ahsan et al. 2019a) as further discussed below. The associated thesis by Corbin (2014) reported carbon conversion efficiencies greater than 97.84% for vertical, turbulent diffusion flares up to 3 inches in diameter burning a variety of flare gas mixtures. Similarly, gas-phase combustion efficiencies (i.e., omitting soot) of methane-based flare gases exceeded 99.5% for all but one test (which was measured as 98.7%, and believed to be an experimental outlier), while hydrocarbon emissions were <0.008 kg carbon/kg flare for all tests. The thesis concluded that gas-phase combustion efficiencies were “universally high for turbulent non-premixed diffusion flames operating with high heating values and in the absence of crosswinds”.

2.3 Wind Tunnel Studies of Flares

The majority of understanding of mechanisms causing emissions have been derived from lab-scale flares in wind tunnels under controlled conditions. Bourguignon et al. (1999) developed a methodology to quantify efficiencies of flares burning in a closed loop wind tunnel based on measuring the accumulation of species concentrations using an unsteady mass-balance approach. This approach was used to measure carbon conversion efficiencies of flares up to 2 inches in diameter, burning natural gas and propane in crosswinds up to 17 m/s (Johnson and Kostjuk 2000). Experiments showed that crosswind strongly affects the combustion efficiency of the flare,

although this sensitivity is partially reduced at higher flare gas exit velocities and larger flare diameters. Inefficiencies were shown to be the result of fuel stripping (Johnson et al. 2001). Based on these findings, an empirical model was developed to correlate experimental results over a range of the above-mentioned parameters (Johnson and Kostiuk 2002b). However, the majority of experiments, and all experiments considered in their model, were for low-turbulence crosswinds.

Johnson and Kostiuk (2002) did perform one set of experiments comparing flare efficiency for a 24.7mm (1-inch) flare burning natural gas at an exit velocity of 3 m/s, subjected to a low-turbulence and moderate-turbulence (~5% turbulence intensity and integral length scale of 20cm) crosswind. While a measurable difference between datasets was noted (Figure 2.1), they suggested that the effects of atmospheric turbulence were small relative to the inherent data scatter of other parameters such as wind speed, exit velocity, energy and mass density, and stack diameter.

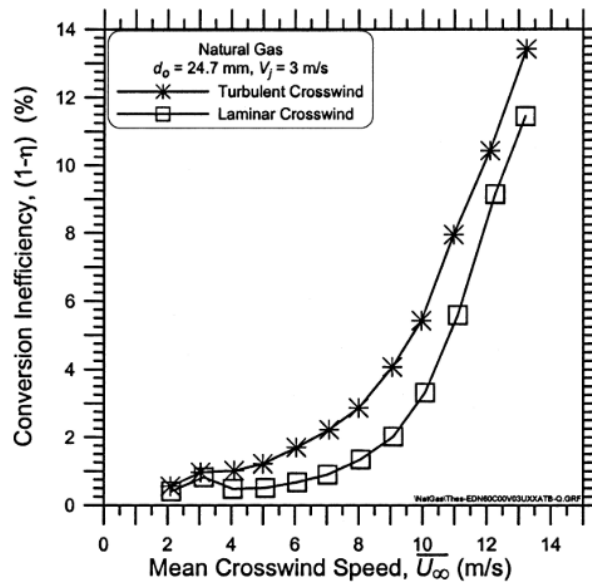


Figure 2.1: Evaluation of flare efficiency when subject to a laminar and turbulent crosswind, (~5% turbulence intensity and integral length scale of 20cm) (Johnson and Kostiuk 2002b)

To the author’s knowledge, only two other studies have considered effects of crossflow on flares using wind tunnel experiments. Ellzey et al. (1990) considered soot yields from small-scale (1.04 to 2.16 mm diameter) propane diffusion flames under cross-flow and co-flow conditions. Soot yields were found to decrease with both increased exit velocity and increased crosswind speed, while jet diameter had minimal effect. Reductions in soot yield were attributed to “smaller-scale

motion which would thoroughly mix the fuel and air”, where flame structures of various scales would “help to homogenize the mixture and produce lower soot yield”.

Talebi et al. (2014) applied a crosswind to an unspecified-diameter, pilot scale diffusion flame that also had some capability for steam and air injection. Unfortunately, the experimental apparatus is not well documented, but experiments considered methane and methane/propane/butane blends. Although combustion efficiency data are not directly reported, CO emissions were found to increase and NO_x emissions decrease as wind was applied to the burner.

2.4 Studies of Steam and Air Assisted Flares

Steam and air-assist flares, used in the oil and gas industry to achieve smokeless combustion (EPA 2000), have been considered in both laboratory and full-scale settings. McDaniel (1983) was the first to show that over-steaming can reduce flare efficiency. A 2010 flare study conducted by the Texas Commission on Environmental Quality (TCEQ) (Allen and Torres 2011) considered this issue in much greater detail. Using a 20” diameter “snorkel” sampling probe suspended from a crane, samples from the plumes of steam- and air-assist flares burning propane, propylene, and natural gas diluted with N₂ were collected in semi-controlled experiments (i.e., the flame was not shrouded from the atmosphere). The goal of these experiments was to determine relationships between flare design and operating conditions with flare emissions and combustion efficiency. Tests were performed using a 24-inch diameter air-assisted flare and a 36-inch diameter steam-assisted flare, each with three natural gas pilots, in the open atmosphere where uncontrolled crosswinds were as high as 7.1 m/s (16 mph).

Results of the TCEQ study reported by Torres et al. (2012b) presented emissions of steam-assisted flares in terms of the combustion zone net heating value (CZG NHV), which is the ratio of the sum of the lower heating value of the flare gas and the combustion heating value of the flare pilot to the total volume of flare and assist gases. Steam-assisted flares were found to have a propylene destruction removal efficiency (DRE) greater than 95% when CZG NHV was greater than 250 BTU/scf. Below this CZG NHV, propylene DRE dropped dramatically, and was measured as low as ~20% at a CZG NHV of ~100 BTU/scf. While CZG NHV was not calculated for air-assisted flares, propylene DRE was reported as a function of stoichiometric ratio, which was defined as the ratio of air assist provided to stoichiometric air required. As the stoichiometric ratio was

increased, a linear decrease in propylene DRE was observed, and was measured as low as ~65% at high air-assist flow rates (stoichiometric ratio >40).

In another publication based on the TCEQ study, Torres et al. (2012a) determined the location of steam addition has important implications for combustion efficiency. For a 350 BTU/scf flare gas with a steam-to-flare gas ratio of 1, combustion efficiency varied from 30-80% depending on the amount of centre steam. They also noted flare gas composition had a much smaller affect on DRE than heating value or air/steam assist flow rates for combustion efficiencies greater than 90%. Furthermore, they estimated the impact of crosswind on combustion efficiency of steam-assisted flares by comparing tests with identical operating conditions but differing wind speed. Combustion efficiency varied by less than 2.5% over crosswind speeds between 0-7.1m/s. However, momentum flux ratios for these tests ranged between 0.304-7.94, meaning the flames were mostly jet dominated and the impact of crosswind could be expected to be small.

The effect of steam- and air addition on 1-inch laboratory flares has been investigated by Ahsan et al. (2019b) and Zamani et al. (2021). Ahsan et al. (2019b) determined a steam-fuel mass flow ratio (MFR) of ≤ 1.8 was required to achieve combustion efficiencies >97%, and an air-fuel (MFR) of ≤ 5 to achieve combustion efficiencies >95%. Zamani et al. (2021) determined carbon conversion efficiency for unassisted flares “was essentially 100%” and remained near 100% for both steam and air assisted flares up to some critical flow rate of assisting fluid. Past this point, the flame would become unstable and blow out. In general, this critical flow rate was found to occur at much lower assist flows rates of steam than air. Addition of both assist gases at an MFR of 1.5 was determined to reduce BC emissions by an order of magnitude. However, they concluded that evaluating combustion efficiency in terms of the MFR “did not provide a general and consistent correlation for any subset” of cases considered in their study. They further suggested a thermal mechanism in which less radiation heat loss (from lower soot levels) resulted in increased NO_x emissions as air-assist rates were increased, and decreased NO_x emissions as steam-assist rates were increased.

The results of Zamani et al. (2021) differ slightly from those of Torres et al. (2012a). While Torres et al. (2012a) observed a linear decrease in combustion efficiency with the addition of air, Zamani et al. (2021) observed little change followed by a rapid decrease. Torres et al. (2012a) determined that an air-fuel MFR of <24 achieved combustion efficiencies greater than 96.5%, while Ahsan et al. (2019b) determined an air-fuel MFR of ≤ 5 was required. Ahsan et al. (2019b) performed

experiments using a 2.54 cm burner diameter, while Torres et al. (2012a) performed experiments using a 67 cm diameter burner, and Ahsan et al. (2019b) attributed the discrepancy in results between the studies to these differing burner diameters.

2.5 Remote Optical Measurements of Flares

Several researches have attempted remote optical measurements of flare efficiency using a range of methods that remain an active topic of research. Kuipers et al. (1996) used passive Fourier transform infrared (FTIR) and differential absorption light detection (DIAL) techniques to measure efficiencies of natural gas flares under field conditions. They found good agreement between the two methods, reporting efficiencies between 99.6 – 99.9% while noting small increases in CH₄ emissions from the flares at higher crosswind speeds.

Boden et al. (1996) used a DIAL technique to measure CH₄ emissions from steam-assisted refinery gas flares with diameters between 3 and 12 inches. While the author notes significant scatter in their data, “combustion efficiencies were found to be greater than 98% under normal operating conditions”. They attributed the measurement scatter to C₁-C₆ concentrations that approached equipment detection limits, and fluctuations in flare gas and wind conditions.

Blackwood (2000) used an open path FTIR technique to measure carbon monoxide (CO) destruction efficiency of two flares at an unspecified plant, burning predominantly CO-based fuels with trace concentrations of hydrocarbons and sulfur gases. They concluded through the measurement of CO and CO₂, as well as CF₄ and SF₆ tracer gases, that CO destruction efficiency was approximately 95%. However, they note occasional efficiencies below 95%, and as low as 49%. They noted difficulty in using the appropriate spectral backgrounds to determine plume contributions of measured CO and CO₂, while uncertainty in tracer stability may have resulted in overestimated efficiencies. A similar study by Yang and Chang (2006) using an open-path FTIR method was used to obtain concentration profiles and destruction removal efficiency of an unspecified waste gas flare. Their results suggested the flare had an ethylene destruction efficiency of 20.8%-58.1%, and n-butane 57.2%-74.7%, although it was noted that flare fuel flow rate and wind speed varied over these tests.

The wide-ranging estimates of flare efficiencies obtained using optical methods may be partially attributable to uncertainties in the measurement techniques. A component of the 2010 TCEQ study (Allen and Torres 2011) compared measurements of flare combustion efficiency using

passive and active FTIR and passive imaging radiometric spectrometer (PIRS) with results using extractive sampling methods. Results were grouped based on combustion efficiencies determined using the extractive sampling method and compared as summarized in Table 2.1. None of the optical techniques showed consistent correspondence with the extractive sampling results. For combustion efficiencies greater than 95% based on extractive sampling, PIRS measured 0-98%, AFTIR measured 89.3-100% and PFTIR measured 93.9-99.9%. Additional data for efficiencies below 80% were plotted but a comparison was not presented, likely because the various techniques produced significant scatter in combustion efficiencies such that quantitative analysis would provide no information of value. Wormhoudt et al. (2012) confirmed that for combustion efficiency determined using either extractive sampling or PFTIR (the most promising of the three optical methods based on the results shown in Table 2.1), 58 of 141 tests in the TCEQ study disagreed by more than the combined nominal error bars.

Table 2.1: Table of measured combustion efficiencies measured using four methods in the 2010 TCEQ study.

	Method			
	Extractive	PIRS	AFTIR	PFTIR
Combustion Efficiency [%]	80-85	33-98	58-81.6	78.4-94.7
	85-90	80-90	71.2-87.3	82.2-93.9
	90-95	80-98	87.8-97.4	86.5-97.8
	95-99	0-98	89.3-100	93.9-99.9

More recently, Miguel et al. (2021) have conducted lab tests investigating the viability of hyperspectral imaging to measure flare efficiency using a Telops Hyper-Cam MW imaging Fourier transform spectrometer (IFTS). In a heated vent experiment, which released known amounts of heated CH₄ and CO₂ to simulate simplified conditions in a flare plume, flow rates measured by the IFTS closely matched known MFC flow rates, but CH₄ and CO₂ emission rates were overpredicted by 17% and 10% respectively. This discrepancy was attributed to anomalies in the spectral data, which they concluded highlights the challenge of hyperspectral imaging. A separate experiment sought to measure combustion efficiency and species emission rates from a small, 11.3mm diameter lab-scale steam- and air-assist flare burning 5 SLPM of CH₄. Although the IFTS technique measured combustion efficiency to within 3% of the accepted GC/MFC-measured efficiency, the

estimated methane emissions were wrong by a factor of -0.75 to 8.27 (measured values of 0.075, 0.139 0.146 and 0.019 g/s vs. reference GC/MFC value of 0.030, 0.015, 2.590 and 0.062 g/s). They suggested that hyperspectral imaging using IFTS is viable in quantifying combustion efficiency, while noting the need for further experiments to address measurement discrepancies.

2.6 Aircraft Measurements

Several recent studies have also attempted to measure flare efficiencies using aircraft measurements. Caulton et al. (2014) performed aircraft sampling of 10 flares in North Dakota and 1 flare in Pennsylvania. Purdue's Airborne Laboratory for Atmospheric Research (ALAR) was used to fly transects through the flare and background CH₄ and CO₂ were subtracted to produce ΔCH_4 and ΔCO_2 time series. A regression of ΔCH_4 and ΔCO_2 was performed, where the slope was taken as the efficiency of the flare. Flare efficiencies by this definition ranged from >99.6->99.8% efficient at the 25th quartile for crosswinds up to 15m/s, and results showed only a weak relationship between crosswind speed and efficiency. Gvakharia et al. (2017) also performed aircraft measurements in the Bakken Region. From a sample size of 37 flares, they reported a median CH₄ destruction removal efficiency (DRE) of approximately 97%, tailing to lower values. Similar to Caulton et al. (2014), they found a weak correlation between emissions and crosswind speed.

Zavala-Araiza et al. (2021) presented airborne-based, mass-balance measurements of CH₄ and CO₂ from Mexico's onshore and offshore natural gas operations using the method developed by Conley et al. (2017), where circles are flown around target plumes at multiple altitudes and Gauss's theorem is applied to estimate flux contributions from the circled plume. They determined that flaring at onshore sites had an efficiency of 94%. They also noted that approximately 70% of CH₄ emissions in the offshore study were related to flaring, which was corroborated using visible infrared imaging radiometer suite (VIIRS) measurements from the Suomi National Polar-Orbiting Partnership satellite.

Measurements of flares have also been attempted using unmanned aerial vehicles (UAVs) and ships. Krause and Leirvik (2018) performed UAV-based measurements of BC from flares by transecting a well test flare plume in the North Sea using a handheld TSI DustTrak DRX Aerosol Monitor (Model 8534) attached to a UAV. BC emission factors were determined to be 0.42-0.84 kg BC/tonne of combined oil and gas being flared at a total flow rate of 81,620 m³/d. Zang

et al. (2020) performed ship-based surveys of oil and natural gas platforms in the Bohai sea in a similar fashion to aircraft-based measurements. Using a Picarro cavity ringdown analyzer to measure CH₄ and CO₂ concentrations in the vicinity of flare operations, they estimated a mean flaring efficiency for oil-associated gas of 98.5 +/- 0.5%, and a methane emission rate of 0.026 +/- 0.017 Tg/yr.

Similar to laboratory-scale experiments, plume inhomogeneity may result in variable measurements using aircraft-based methods. Gvakharia et al. (2017) noted that multiple aircraft passes on the same flare plume produced inconsistent results “suggesting fluctuation in efficiency”. Caulton et al. (2014) observed large variability in CH₄ emissions due to small plume sizes and possible plume heterogeneity, and Weyant et al. (2016) suggested variability in BC emissions sampled from the same flare across multiple days may be due to varying gas flow rates and compositions.

2.7 Conceptual Analysis of Flares

The combustion efficiency of flares has also been considered using computational fluid dynamics (CFD) modelling using Reynolds-averaged Navier Stokes equations. Aboje et al. (2017) used K-epsilon and shear-stress transport models, while Lawal et al. (2013) used K-epsilon turbulence models, to predict various properties of flares in a crosswind, which were compared to experimental data. K-epsilon turbulence models have been used by Castiñeira and Edgar (2006) to study simple, steam- and air- assisted jet flames based on experiments performed by Barlow and Carter (2000) and Frank and Barlow (1998). In general, they found that steam- and air-assisted flares result in efficient flaring (> 97%) prior to over-steaming or airing. However, given the likely role of coherent fluid structures in the aerodynamic drivers of flare inefficiencies (Johnson and Kostiuik 2002a; Johnson et al. 2001), RANS models may not be sufficient to capture the relevant physics of the flame.

More recently, Jatale et al. (2016) used Large Eddy Simulation (LES) to predict combustion efficiencies for flares in a crosswind with good agreement to experimental data from Gogolek and Hayden (2004), apart from CH₄ concentrations in the plume of flares subject to low crosswinds. However, these simulations were not able to consider detailed chemistry and instead modelled the combustion in terms of a simple progress variable. More generally, the uncontrolled nature of the turbulent combustion, the complex fuel and combustion chemistry, and the wide

range of scales and flow regimes of operating flares exceeds the capabilities of most or all current computational methods. Moreover, there is significant uncertainty in available chemical models. As an example, Saffaripour et al. (2013) showed that high-fidelity simulations including detailed chemical modelling were challenged to predict soot concentrations of idealized, laminar flames with simplified fuels within an order of magnitude. While computational capabilities are expected to improve, the level of difficulty in predicting combustion performance computationally is only expected to be exacerbated when introducing complicating factors such as crosswind. Therefore, only experimental methods have been considered in the evaluation of flares in a crosswind.

2.8 Influence of Crosswind on Flare Flames

Of the cited studies above, only Johnson and Kostiuik (2000, 2002) considered the effects of crosswind as an explicitly controlled parameter. However, crosswind effects on flame shape and stability have been researched more broadly, where a flare may be considered as a canonical example of a reacting jet in crossflow. Although research has generally focussed on a general description and modelling of flame properties rather than flare efficiency and emission rates, many of the characteristics discussed have implications for flare performance and will be further considered in Chapter 5.

Gollahalli et al. (1975) demonstrated that the momentum flux ratio, R , of jet to crosswind influences the characteristics of turbulent diffusion flames, where:

$$R = \frac{\rho_j V_j^2}{\rho_\infty U_\infty^2} \quad 2.1$$

and ρ_j is the density of the jet gas, ρ_∞ is the ambient density of air, V_j is the jet exit velocity from the burner, and U_∞ is the crosswind speed. At small values of R (i.e., a low jet momentum), the flame stabilizes in the wake of the stack, and fuel from the stack is drawn into the wake. As R is increased, the flame length increases as well. Above a certain value of R , the flame becomes detached from the tube and stabilizes above the stack. Flame length, liftoff distance, and flame stability are also considered as functions of crosswind and jet velocities.

The low momentum jet flames described by Gollahalli et al. (1975) were further characterized by Huang and Wang (1999) using Mie scattering flow visualization and laser Doppler velocimetry to characterise five flow modes at different ranges of momentum flux ratio. At low momentum flux ratios, downwash occurs as the flame deflects to the low-pressure, leeward side of the burner,

which they determined was closely related to flame stability, while an increase in jet-to-wind momentum flux ratio would lead to flame blow-off.

Kalghatgi (1981a) developed a non-dimensional formula to describe the blowout stability limit of gaseous jet diffusion flames in still air as a function of laminar premixed flame speed (S_L), burner diameter (d_e), and kinematic viscosity (ν) and density (ρ) of the fuel:

$$\overline{U}_e = 0.017R_H(1 - 3.5 \times 10^{-6}R_H) \quad 2.2$$

where $R_H = \frac{HS_L}{v_e}$, and $H = \left[4 \frac{\overline{\theta}_e}{\theta_s} \left(\frac{\rho_e}{\rho_\infty} \right)^{\frac{1}{2}} + 5.8 \right] d_e$. The model correlates data across multiple burner diameters and gas compositions. A subsequent paper (Kalghatgi 1981b) extended this analysis to describe blowout stability of diffusion flames in a crosswind. For a given fuel and burner diameter, Kalghatgi (1981b) suggested there is a crosswind speed above which a stable flame is not possible. Below this maximum crosswind speed, two stability limits exist. At low jet velocity, increased crosswind causes the flame to be blown off, except in cases where the burner diameter is large and jet velocity is small, such that the flame becomes wake stabilized. A similar phenomenon was described by Gollahalli et al. (1975). An upper limit of stability was also determined, where blow-out closely resembles, yet is often slightly higher than that of a flame in still air. All data points were collapsed onto a single curve (Figure 2.2) plotted on nondimensionalized axes using operating conditions such as exit velocity and burner diameter, atmospheric parameters such as wind speed, and gas properties such as laminar flame speed, kinematic viscosity, and density.

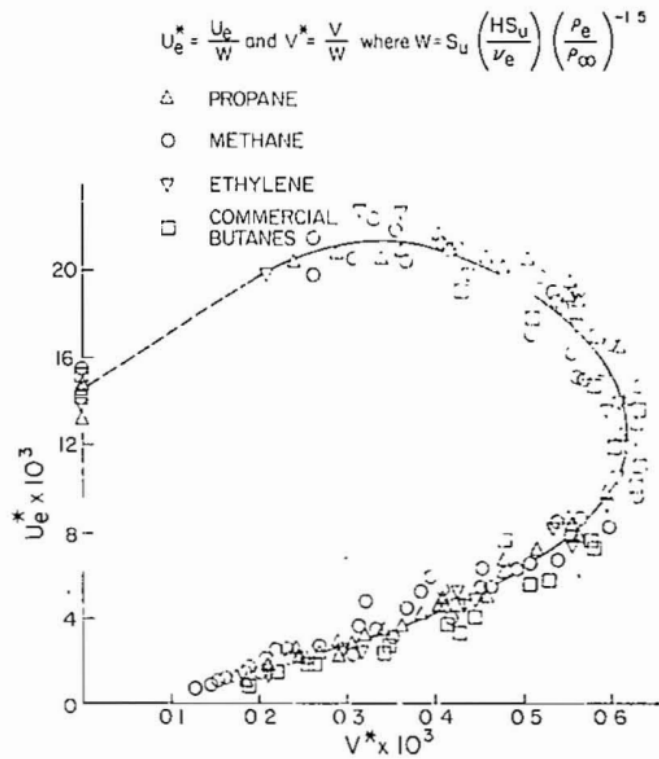


Figure 2.2: Universal non-dimensional stability curve from (Kalghatgi 1981b)

The preceding review has shown that data on carbon conversion efficiencies of flares in crosswind remains sparse and a thorough understanding of the mechanisms driving efficiencies is lacking. Moreover, the only comprehensive experiments to consider crosswind effects have been performed in scaled down ≤ 2 inch flares with simple fuels in low-turbulence crosswinds. Similarly, available field measurement data are often inconsistent and generally lack any form of detailed uncertainty analysis. In short, a comprehensive, parametric evaluation of flare performance over a range of operating conditions representative of real-world scenarios remains elusive. The experiments presented in the following chapters are intended to help fill this key knowledge gap.

Chapter 3 Experimental Setup

3.1 Wind Tunnel

Experiments were performed in the Boundary Layer Wind Tunnel II Laboratory (BLWTL), located at Western University in London, ON, Canada. The BLWTL (Figure 3.1) is an industrial-sized, closed loop wind tunnel facility originally constructed in 1984 to investigate the aerodynamics of buildings and bridges. As part of the NSERC FlareNet strategic network, the facility was retrofitted to permit controlled flare experiments.



Figure 3.1: Boundary Layer Wind Tunnel Facility at Western University

The closed loop wind tunnel is approximately 2000m^3 in volume, with both high speed and low speed test sections. The present experiments used the larger, low-speed test section, which is nominally 5m wide by 4m high by 52 m long with a maximum wind speed of 10 m/s. To overcome the added drag of the turbulence grid (see Section 3.6) and added obstructions to enhance mixing within the tunnel, a pair of false wall fairings were constructed along the walls of the low speed test section as shown in Figure 3.2. The fairings were fabricated from plywood supported by 2x4 framing, and reduced the effective width of the test section from 5m to 3.65m. This decreased the effective cross-section area of the test section by 27%, producing a corresponding increase in the achievable wind speed.

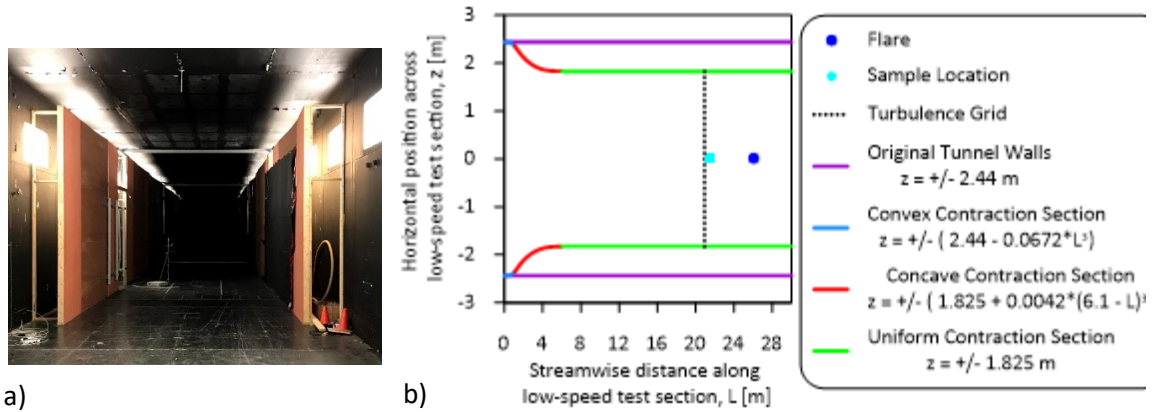


Figure 3.2: a) Photo of the downstream end of the low-speed test section of the wind tunnel showing the fairings installed along the walls. b) Plan view schematic of the fairings and effective test section width as a function of distance along the test section.

The wind tunnel fan sits at the downstream end of the high-speed test section, upstream of the low-speed test section, and is powered by a 289 hp motor. Perforated screens at the entrance to the low-speed test section control and reduce turbulence from the fan and establish uniform flow. A pair of large exterior doors (~5.025m wide by 3.95m) on the downstream end of the low-speed test section and the upstream end of the high-speed test section can be opened to effectively convert the tunnel from a closed loop facility to an open circuit facility. Between experiments, these doors could be opened to rapidly purge the tunnel with fresh, outdoor air.

To promote mixing of the wind tunnel air, three barriers fabricated from plywood and 2x4 framing are mounted vertically in the high speed-test section. Mixing barriers are approximately 0.5 m wide, extend from the floor to ceiling and are fastened to the wind tunnel using wood screws, spaced equally at distances of ~10-30 m upstream of the wind tunnel fan as illustrated in Figure 3.3. In addition, four Uline 48" drum fans (Model H-6989) with flow rates of 19,500 cfm have been placed along the centreline of the low-speed test-section of the wind tunnel at a distance of approximately 15-20 m downwind of the flare, facing in alternate directions to prevent inducing swirl.

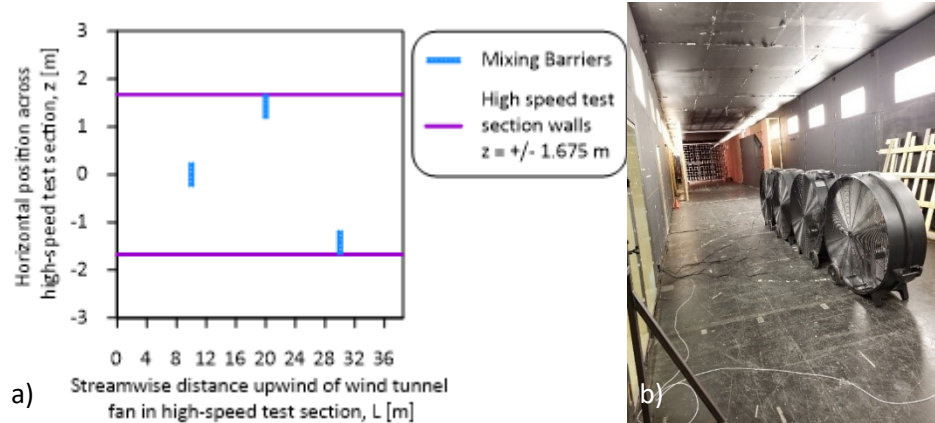


Figure 3.3: a) Schematic of mixing barrier locations in high-speed test section and b) Uline drum fans to promote mixing of wind tunnel air.

This unique facility also features a wave tank / pool area beneath the floor of the low-speed test section, which is accessible through movable floor panels. The tank was previously used to study the interaction of wind and waves with offshore structures and ships. However, the wave tank has been decommissioned, and for the present setup, was used to house the base of the flare which extends upwards through the wind tunnel floor. Initial test experiments suggested that the wave tank could create a space for wind tunnel gases to accumulate. In addition to being a possible safety hazard, this could affect the assumption of a uniform ambient concentration outside the wind tunnel as considered in the methodology presented in Chapter 4. To avoid this possibility, the wave tank beneath the test section floor was slightly pressurized using a pair of pressure loading actuator (PLA) blowers. Shown in Figure 3.4, these PLAs were originally developed by Kopp et al. (2010) to apply pressures of up to 23kPa as part of experiments to improve wind damage resistance of light frame structures during severe wind storms. For the present experiments, the PLAs were run at approximately 75% capacity to apply continuous positive pressure to the wave tank.

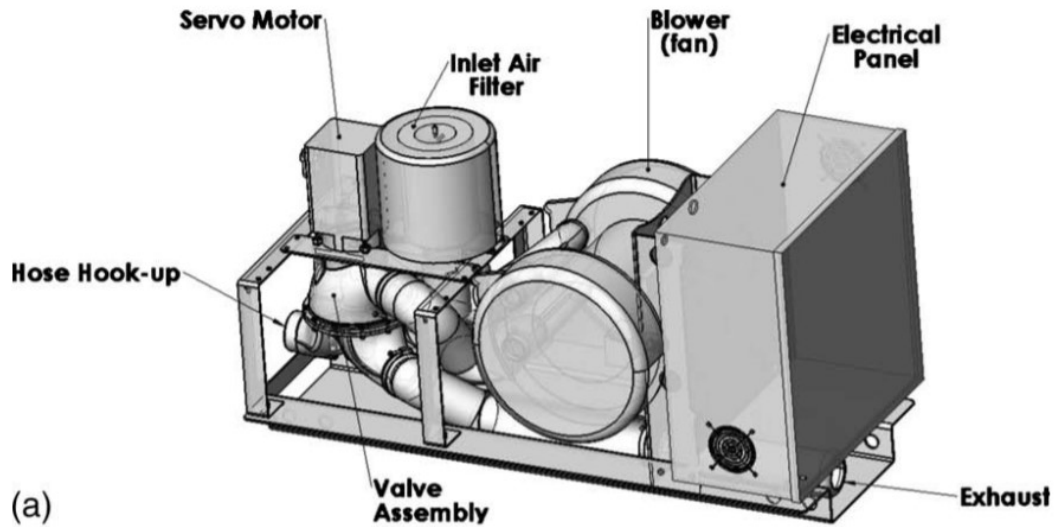


Figure 3.4: CAD model of PLAs developed by Kopp et al. (2010).

3.2 Interchangeable Flares

The flare stack is positioned on the centerline of the test section floor, 26 m downstream of the perforated screen at the entrance to the low-speed side, and 5.08 m downstream of the turbulence grid (Section 3.6). The flare consists of a permanent aluminum burner base and interchangeable contraction nozzles and flare stacks, with the stack tip kept at a minimum of 1.4m above the wind tunnel floor to minimize boundary effects. The burner base (Figure 3.5) consists of a diffuser disk and expanded aluminum foam to breakup and evenly distribute the incoming flow of fuel, followed by a relaminarizing section that includes three mesh screens of increasing fineness (U.S. Mesh size 26x26, 32x32 and 42x42), separated by spacers. This system ensures uniform flow at the entrance of the interchangeable converging nozzle.

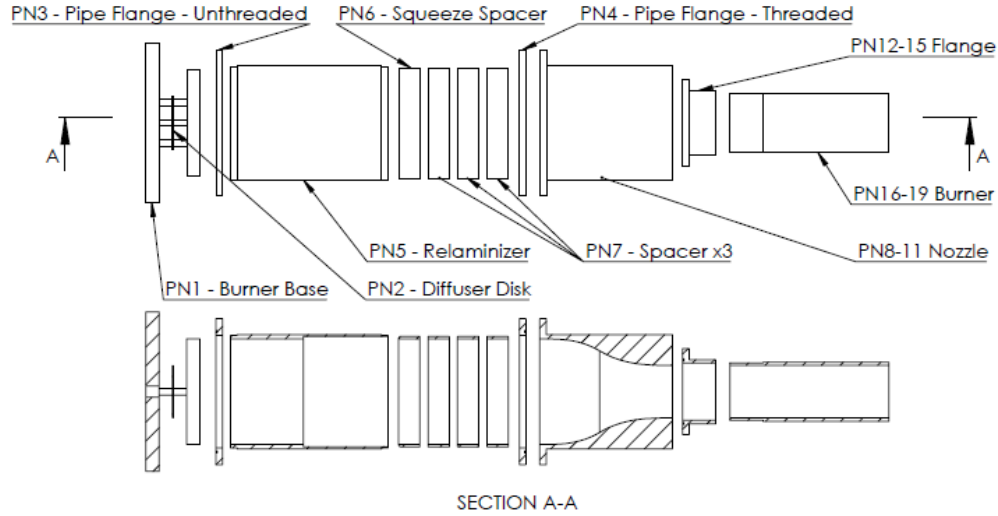


Figure 3.5: Exploded view of the burner base, mounted with a 4-inch burner nozzle.

The interchangeable nozzles and flare stacks were constructed of NPS Schedule 40 stainless steel. As detailed in Table 3.1, four flare stacks with nominal diameters of 1, 2, 3, and 4 inches were used in the experiments. The contraction nozzles for each flare stack have parabolic contours to ensure attached flow through the contraction and uniform flow at the exit. Each flare stack is flange mounted to its corresponding nozzle. Importantly, these burner diameters partially overlap the 3-12 inch diameters of full scale flares commonly found at upstream oil and gas production sites in Canada and internationally (Conrad and Johnson 2017; McEwen and Johnson 2012).

Table 3.1: Flare Specifications used in experiments

Nominal Flare Diameter	Inner Diameter [m]	Outer Diameter [m]	Stack Length [m]
1 in	0.02665	0.03340	2.133
2 in	0.05250	0.06033	2.133
3 in	0.07793	0.08890	2.133
4 in	0.1022	0.1143	2.133

The base section of the flare was mounted on a vertical and rotational traverse system (see Figure 3.6) that allowed both vertical positioning of the flare and continuous, slow rotary motion of the flare stack using Tritex II Linear and Rotary Actuators. Only the flare stack protruded into the tunnel test section and the exit plane of the flare stack was positioned approximately 1.5m above the test section floor. The rotary actuator continuously rotated the flare stack back and forth from -180° to 180° along its axis at ~ 3.3 rev/min. This rotation ensured uniform heating of the flare stack, which was necessary to avoid bending of the flare stack from uneven thermal

expansion that could occur when the flame was stabilized on the leeward side of the stack given that the wind direction in the tunnel is fixed.

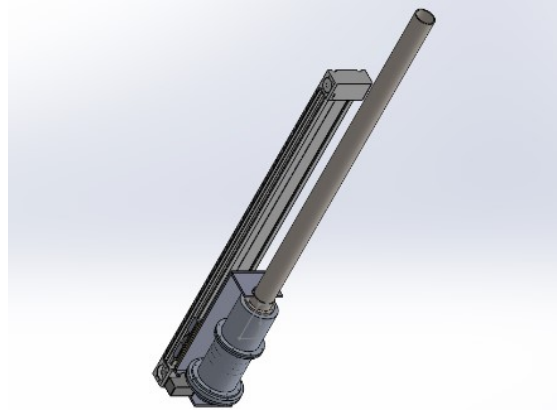


Figure 3.6: Isometric CAD model of the 4" burner mounted on the vertical and rotational traverse.

3.3 Flare Gas Control and Metering

The present experiments used controlled flare gas mixtures of varying amounts of CH₄, C₂H₆, C₃H₈, C₄H₁₀, CO₂, and N₂. These mixtures, summarized in Table 3.2 and Table 3.3, were chosen to be representative of flare gases in the upstream oil and gas industry in Western Canada based on the analysis of Johnson and Coderre (2011).

Table 3.2: Volume fractions as a % of flare gas mixtures.

Flare Gas	Volume Fractions [%]					
	CH ₄	C ₂ H ₆	C ₃ H ₈	C ₄ H ₁₀	N ₂	CO ₂
Methane	100	0	0	0	0	0
AB_L6	93.31	0.32	0.09	0.27	1.38	4.64
AB_M6	86.03	6.81	2.35	1.99	1.61	1.21
AB_H6	75.16	11.44	6.02	4.48	1.69	1.21
AB-M6_w20%N ₂	69.67	5.51	1.90	1.61	20.00	1.30
AB-M6_w20%CO ₂	69.67	5.51	1.90	1.61	1.30	20.00
AB-M6_w40%CO ₂	52.25	4.14	1.43	1.21	0.98	40.00
AB-M6_w60%CO ₂	34.83	2.76	0.95	0.81	0.65	60.00
AB-M6_w70%CO ₂	26.13	2.07	0.71	0.60	0.49	70.00
92.5CH ₄ -7.5C ₂ H ₆	92.5	7.5	0	0	0	0
85CH ₄ -15C ₂ H ₆	85	15	0	0	0	0
85CH ₄ -15C ₃ H ₈	85	0	15	0	0	0
50CH ₄ -50C ₂ H ₆	50	50	0	0	0	0
50CH ₄ -50N ₂	50	0	0	0	50	0
NATURAL GAS	92.68	6.24	0.21	0.04	0.40	0.43
NATURAL GAS_w20%N ₂	74.15	4.99	0.16	0.04	20.32	0.34

Table 3.3: Properties of flare gas mixtures. Properties are calculated at 25°C and 1 atmosphere unless otherwise specified.

Flare Gas	Property											
	MW [kg/kmol]	Density [kg/m ³] (15°C 1atm)	HHV [MJ/kg]	LHV [MJ/kg]	kinematic viscosity ×10 ⁵ [m ² /s]	Stoichiometric air to fuel ratio (molar) [-]	Stoichiometric mixture fraction [-]	Specific heat capacity [kJ/kgK]	Flame Speed [m/s] (15°C and 1 atm)	Mean Carbon Number [-]	Adiabatic Flame Temperature [K]	Dyn. Visc. Mix ×10 ⁵ [Pa-s]
Methane	16.04	0.678	55.51	50.03	1.69	9.52	0.0550	2.23	0.359	1.000	2224.3	1.11
AB_L6	17.69	0.748	47.81	43.10	1.59	9.04	0.0633	2.04	0.308	0.953	2214.0	1.15
AB_M6	19.03	0.805	51.60	46.70	1.40	10.50	0.0589	2.05	0.334	1.147	2229.1	1.09
AB_H6	21.76	0.920	51.03	46.35	1.18	11.88	0.0595	1.97	0.348	1.340	2236.6	1.05
AB-M6_w20%N ₂	20.79	0.879	38.25	34.62	1.45	8.50	0.0778	1.79	0.314	0.929	2208.1	1.18
AB-M6_w20%CO ₂	23.78	1.006	33.44	30.26	1.24	8.50	0.0880	1.63	0.290	0.929	2188.8	1.21
AB-M6_w40%CO ₂	28.84	1.220	20.68	18.72	1.11	6.38	0.1350	1.33	0.229	0.696	2122.7	1.31
AB-M6_w60%CO ₂	33.89	1.433	11.73	10.62	9.98	4.25	0.2158	1.12	0.145	0.464	2002.9	1.38
AB-M6_w70%CO ₂	36.42	1.540	8.19	7.41	0.950	3.19	0.2828	1.04	0.094	0.348	1895.7	1.41
92.5CH ₄ -7.5C ₂ H ₆	17.09	0.723	55.04	49.70	1.58	10.06	0.0554	2.17	0.363	1.075	2229.1	1.08
85CH ₄ -15C ₂ H ₆	18.15	0.767	54.62	49.40	1.40	10.59	0.0558	2.11	0.367	1.150	2227.7	1.04
85CH ₄ -15C ₃ H ₈	20.25	0.856	53.82	48.82	1.23	11.66	0.0565	2.05	0.396	1.300	2232.1	1.02
50CH ₄ -50C ₂ H ₆	23.06	0.975	53.16	48.38	1.09	13.09	0.0573	1.92	0.385	1.500	2236.6	1.50
50CH ₄ -50N ₂	22.03	0.932	20.22	18.22	1.61	4.76	0.1377	1.47	0.271	0.500	2122.6	1.39
NATURAL GAS	17.16	0.726	54.11	48.85	1.58	9.93	0.0563	2.15	0.347	1.060	2228.2	1.06
NATURAL GAS_w20%N ₂	19.33	0.818	38.43	34.69	1.58	7.94	0.0775	1.83	0.324	0.848	2203.6	1.24

During the initial phases of this work and for lower flow rate experiments, flare gases were directly supplied from compressed gas cylinders, with purities presented in Table 3.4. A compressed natural gas system (CNG Canada Falcon Series MCH 14) was subsequently commissioned to enable higher flow rate experiments. This system allowed compression and storage of natural gas into two banks of high-pressure (3000 psi) cylinders that could be subsequently used to supply experiments. Because the composition of the supplied natural gas can vary, an ABB NGC8206 gas chromatograph (GC) was used to measure the composition of each batch of stored gas and a Coriolis flow mass flow meter (Endress-Hauser Promass M100) was used to recalibrate the mass

flow controller used to control and meter the flow of natural gas during experiments. Natural gas could then be supplied as the main feedstock for the flare and mixed with supplemental controlled flows of any or all species in Table 3.4 to consistently produce the standard experimental mixtures of Table 3.2.

The individual gas species were supplied from compressed cylinders using pressure regulators and appropriate CGA fittings. Praxair gas pressure regulators were used for C₃H₈ (2002 series) and N₂ (2012 series) cylinders. CH₄, C₂H₆ and CO₂ were each regulated by Blackstone heated pressure regulators (Model SAN 209-45). C₄H₁₀ cylinders were plumbed without regulators due to the low cylinder pressure (16.3psig). A heated water bath (Thermo Scientific SAHARA PPO S5P Heated Bath Circulator) set to 50°C supplied heated water to the Blackstone regulators. These heated regulators were necessary to overcome Joule-Thomson cooling from the rapid expansion of gas from cylinder pressure to delivery pressure, which otherwise could cause the regulators to freeze.

From the regulators, gases flowed through stainless-steel tubing to calibrated Bronkhorst thermal mass flow controllers (MFCs). Multipoint calibrations were performed for each MFC and gas using Mesa Labs DryCal piston prover gas flow measurement systems. A Mesa Labs Metrology Series (model 800) was used for flow rates between 0.5-50 SLPM with a specified accuracy of 0.15%, and a Mesa Labs Defender Series (model 1020) for flow rates between 50-500 SLPM with a specified accuracy of 0.25%). The specific regression statistics for each calibration were used in the uncertainty analysis, but generally the calibrated MFCs were expected to be accurate within 0.5% of the measured flow rate, and 0.1% of the rated full scale flow rate. Each MFC was controlled by serial communications through the main flare computer. Gases exiting the MFCs were piped to a mixing manifold, mixed with the main flow of natural gas as appropriate, and flowed to the burner base through an approximately 50 ft long, 1-1/2" corrugated stainless steel gas line underneath the floor the tunnel test section.

Table 3.4: Compressed Gas Cylinder Purities

Species	Purity (%)
Methane (CH ₄)	99
Ethane (C ₂ H ₆)	99
Propane (C ₃ H ₈)	99
Butane (C ₄ H ₁₀)	99
Carbon Dioxide (CO ₂)	99.9
Nitrogen (N ₂)	99.998

3.4 Windspeed, Temperature, and Pressure Measurement

A pitot-static tube, mounted adjacent to the flare stack (Figure 3.7), is used to measure wind speeds in the wind tunnel. The pitot-static tube is connected to an Ashcroft differential pressure transducer with a range of 0.25" WC (62.21 Pa) and a rated accuracy of 0.25%. In addition to a pitot-static tube, a 3D ultrasonic anemometer, a Trisonica Mini by Anemoment, is installed in the wind tunnel to provide a secondary measurement of wind speed. The anemometer is capable of measuring wind speeds up to 50m/s with a resolution of 0.1m/s. Accuracies for wind speeds measured in the wind tunnel are rated as ± 0.1 m/s. The anemometer is mounted at the same location as the pitot tube. However, the pitot-static tube is the instrument used to measure wind speeds during flare experiments. The Trisonica Mini ultrasonic anemometer is also used to measure absolute pressure in the wind tunnel. It is rated for pressures from 50-115 kPa, at a resolution of 0.1kPa and an accuracy of ± 1 kPa. Finally, a Vaisala PTB110 barometer is mounted on the outside wall of the wind tunnel and is used to measure barometric pressure in the laboratory. The barometer has a range of 50-110kPa, an accuracy of ± 0.03 kPa at 20°C, and provides an output voltage of 0-2.5V.

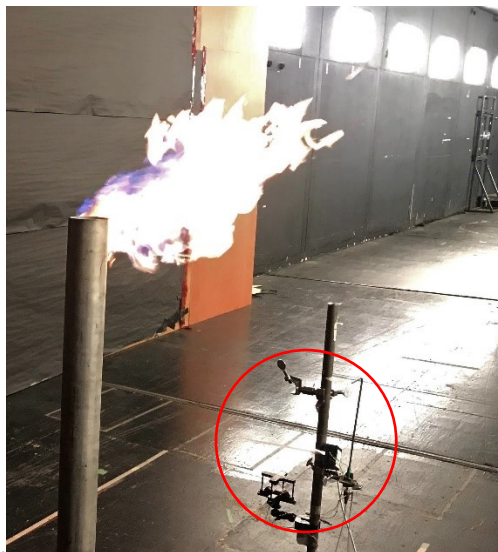


Figure 3.7: Wind measurements using pitot tube and ultrasonic anemometer (circled) relative to the position of the burner.

A set of seven, 4-wire Wika TR40 industrial resistance temperature detectors (RTDs) are spaced approximately equally throughout the wind tunnel to continuously measure temperatures. On the low speed test section, two RTDs are placed approximately 10 and 20m upwind of the flare, while two RTDs are placed approximately 10 and 15m downwind of the flare. Three additional

RTDs are placed along the high speed test section of the wind tunnel, approximately 10, 25 and 50 m upwind of the wind tunnel fan. An eighth RTD is used to measure ambient laboratory temperature and is located at a height of approximately 2 m, on the exterior wall of the low speed test section. The RTDs are attached to 4-pin terminators and provide 0-400 Ω output signals read by an RTD card (see Table 3.6), and have an operating range of -50 to 250°C , with an estimated maximum uncertainty of $\pm 0.68^{\circ}\text{C}$ over the range of observed temperatures ($<50^{\circ}\text{C}$) in the wind tunnel. As shown in Figure 3.8, although temperatures could rise during tests from a combination of heating from the flare, wind tunnel fan and temperature gradients between the wind tunnel and laboratory, temperatures at different points did not vary beyond approximately 3 degrees throughout the test. Furthermore, an average of wind tunnel temperature was used in calculations in Chapter 4.

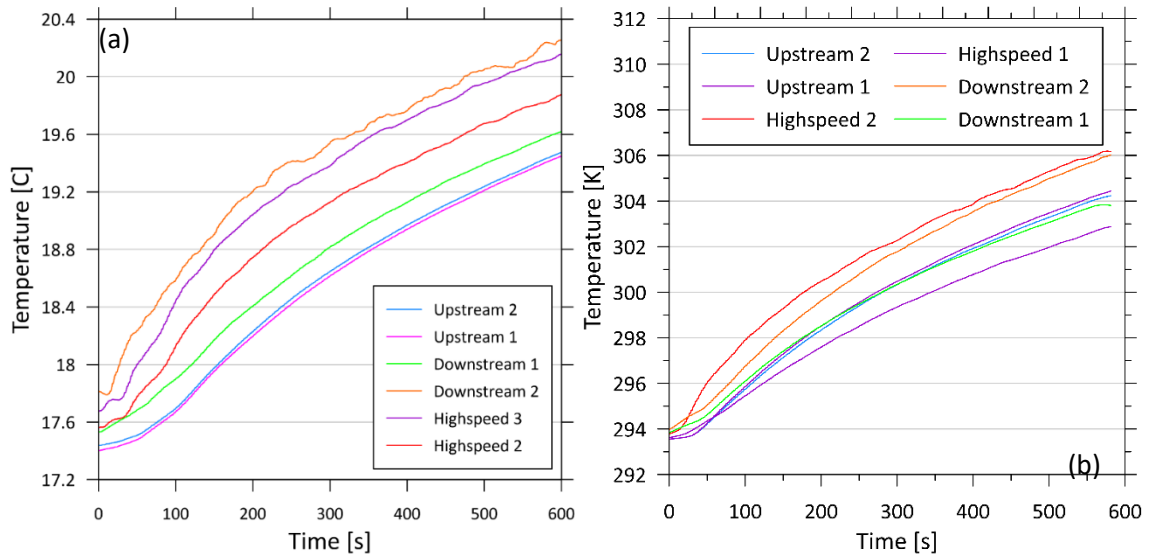


Figure 3.8: Measured temperatures (using RTDs) in the wind tunnel with a) 1-inch (25.4-mm) diameter flare burning the medium (M6) flare gas mixture at a nominal exit velocity of 2 m/s (flow rate of 66 SLPM) at a crosswinds of 2 m/s and a b) 3-inch (77.9-mm) diameter flare burning the medium (M6) flare gas mixture at a nominal exit velocity of 2 m/s (flow rate of 572 SLPM) at a crosswinds of 2 m/s. Temperature varies by up to ~ 3 degrees throughout the test.

3.5 Gas Sampling and Analysis

The real time (~ 1 Hz) concentrations of carbon-containing gas-phase products of combustion in the tunnel are measured using a suite of spectroscopic gas analyzers (Figure 3.9). As summarized in Table 3.5, CO_2 is measured using a Los Gatos Research cavity enhanced laser absorption analyzer Multi-gas Carbon Emissions Analyzer (Model 909-0042) with a precision of 200 ppb over a range of 0.1-3000 ppm. A Los Gatos Research $\text{N}_2\text{O}/\text{CO}$ -23r (Model 916-0015) is used to measure

CO with a precision of 0.1 ppb. An Aeris Technologies Mid-Infrared Laser Absorption Spectroscopy analyzer (Ultra Series) is used to measure CH₄ and C₂H₆ with a precision of 1 ppb. As is detailed in Chapter 4, analyzers are assumed to have linearity and calibration errors of up to 2%. Samples are drawn from a single, 10 m ¼" Teflon sample line that is centered within the tunnel cross section, approximately 5 m upstream of the flare. The sample line is connected to a sampling manifold that directs gas to individual analyzers. The sample for the Los Gatos Research analyzers passed through a pair of external filters (United Filtration Systems 12-57-50K), while Aeris Analyzers contain internal filters (United Filtration Systems DIF-MN40-SP-1/8").



Figure 3.9: Photo of gas analyzers.

Table 3.5: Gas Analyzer Precision and Range.

Species	Analyzer	Precision [ppb]	Measurement Range [ppm]
CH ₄	Ultra Series (CH ₄ /C ₂ H ₆)	1.00	0-100
	Multi-gas Carbon Emissions Analyzer	0.300	0-100
CO ₂	Multi-gas Carbon Emissions Analyzer	200	0-30000
CO	N ₂ O/CO-23r	0.100	0-10
	Ultra Series (N ₂ O/CO)	0.500	0-500
	GGA-24EP	70.0	0.1-10000
C ₂ H ₆	Ultra Series (CH ₄ /C ₂ H ₆)	0.500	0-10
N ₂ O	Ultra Series (N ₂ O/CO)	0.500	0-500
	N ₂ O/CO-23r	0.100	0-10

3.6 Turbulence Grid

A passive turbulence grid (Figure 3.10), fabricated of horizontally and vertically oriented wooden bars, was used to generate turbulence in the crossflow over the flare. Grids of this type create approximately homogeneous and isotropic flow with decay in the downstream direction slow enough such that the turbulent kinetic energy equation, $\frac{\partial}{\partial t} \langle \frac{1}{2} u_i u_i \rangle - \epsilon$, can be approximated as $U \frac{\partial}{\partial x_1} \langle u_i u_i \rangle = -\epsilon$, by use of the Taylor hypothesis (Mydlarski 2017). The key parameters for characterizing the turbulent flow created by the grid are the turbulence intensity and integral length scale. Turbulence intensity (I_u) is the standard deviation of velocity fluctuations divided by the mean velocity as:

$$I_u = \frac{\sqrt{u'^2}}{\bar{u}} \quad 3.1$$

The integral length scale (L_x) represents the size of the largest vortices in the flow that contain significant amounts of energy, and can be estimated from the autocorrelation function $R_{uu}(\tau)$ as:

$$L_x = \bar{u} \int_0^{\infty} \frac{R_{uu}(\tau)}{\sigma_u^2} d\tau \quad 3.2$$

Grid generated turbulence is a function of the spacing, M , of the obstructions (in this case bars of width b), as well as the flow approaching the grid with a uniform velocity. The flow immediately downstream of the grid is inhomogeneous and has wake-jet like structures that transition to transversely homogeneous turbulence with uniform mean velocity. When the distance downstream x is sufficiently far, the flow is effectively homogeneous and isotropic. The parameters M , b and x may be varied such that a desired turbulent flow behind the grid can be developed.

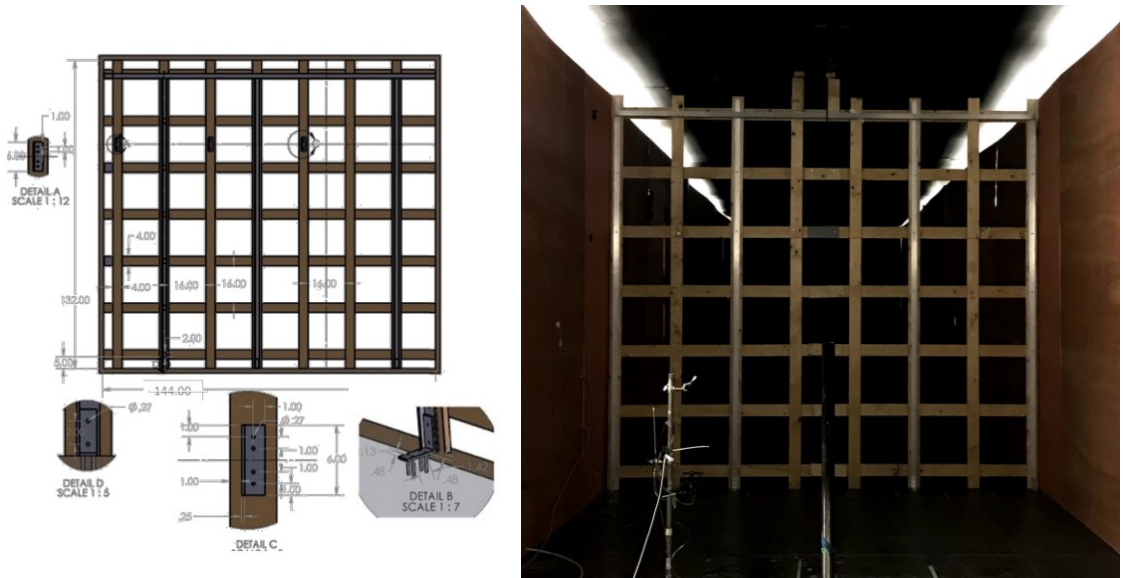


Figure 3.10: a) CAD drawing of the passive grid designed by (Hossain 2019) and b) the grid installed in the wind tunnel at a position of 10M upwind of the flare.

For the present experiments, a passive grid with bar width $b=0.1016\text{m}$ (4in) and a bar spacing of $M=0.508\text{m}$ (20 inches) was placed in the experimental test section $x=5.08\text{m}$ (equal to 10 bar spacings or $10M$) upstream of the flare stack. Hossain (2019) evaluated the grid-generated turbulence at three positions upwind of the flare, described in terms of the distance of the bar spacing: $10M$ ($x=5.08\text{ m}$), $19M$ ($x=9.65\text{ m}$), and $40M$ ($x=20.3\text{ m}$). Vertical velocity profiles (see Figure 3.11a) show that the crosswind reaches 95% of the mean crosswind velocity at a height of 60 cm from the ground. Therefore, the burner tip is kept at approximately 1.5 m from the wind tunnel floor to avoid boundary layer effects on wake-stabilized flames. Vertical velocity profiles (see Figure 3.11b) collected by (Hossain 2019) at a height of 1.2 m show that velocities vary from 95-105% of the mean crosswind velocity at distances within 1 m of the centre plane (stack location) of the tunnel.

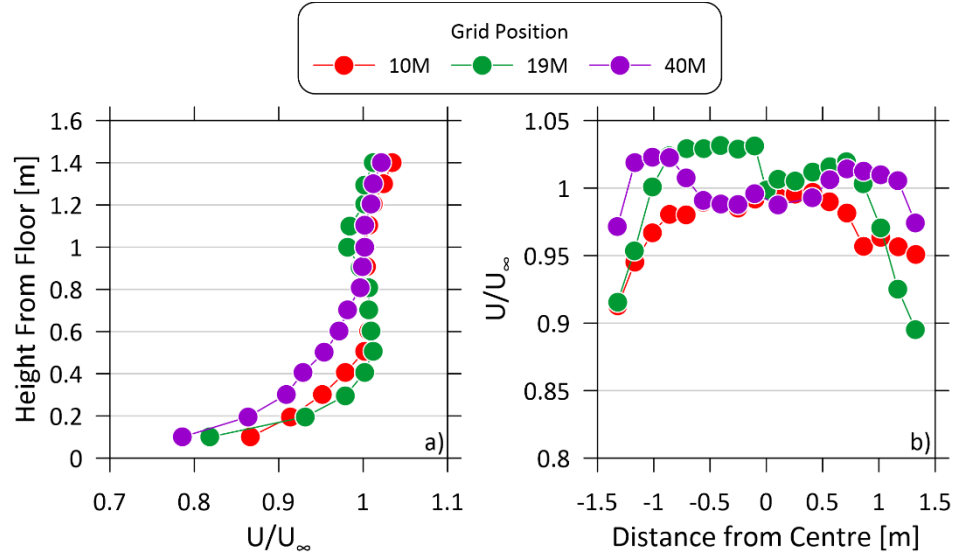


Figure 3.11: a) Vertical velocity profile of the burner plane, and b) horizontal velocity profiles at the burner plane, measured at a height of 1.2m from the floor.

The energy spectra at the flare stack were evaluated using hot-wire anemometry for the three grid positions and are shown in Figure 3.12. Velocity time series for the three grid positions were evaluated and converted to frequency using a Fast Fourier Transform (FFT), and the energy spectrum of the turbulent flow was evaluated. Each scenario was compared to a full-scale energy spectrum representative of real-world turbulence (ESDU 1993), and represented by a form of the von Karman spectral equation:

$$\frac{f S_{uu}}{\sigma_u^2} = \frac{4f_u}{(1 + 70.8f_u^2)^{\frac{5}{6}}} \quad 3.3$$

The significance of this is that the grid positioned at 10M upstream of the flare produced turbulent kinetic energy at scales approaching the shear layer scale (see Figure 3.5), which has been hypothesized to be the cause of fuel stripping (Johnson and Kostiuik 2002a; Johnson et al. 2001). This grid position was used in all experiments presented in this thesis. The results presented in this thesis consider this grid position alone, as it acts as an input boundary condition to produce the most representative turbulence to field-scale scenarios.

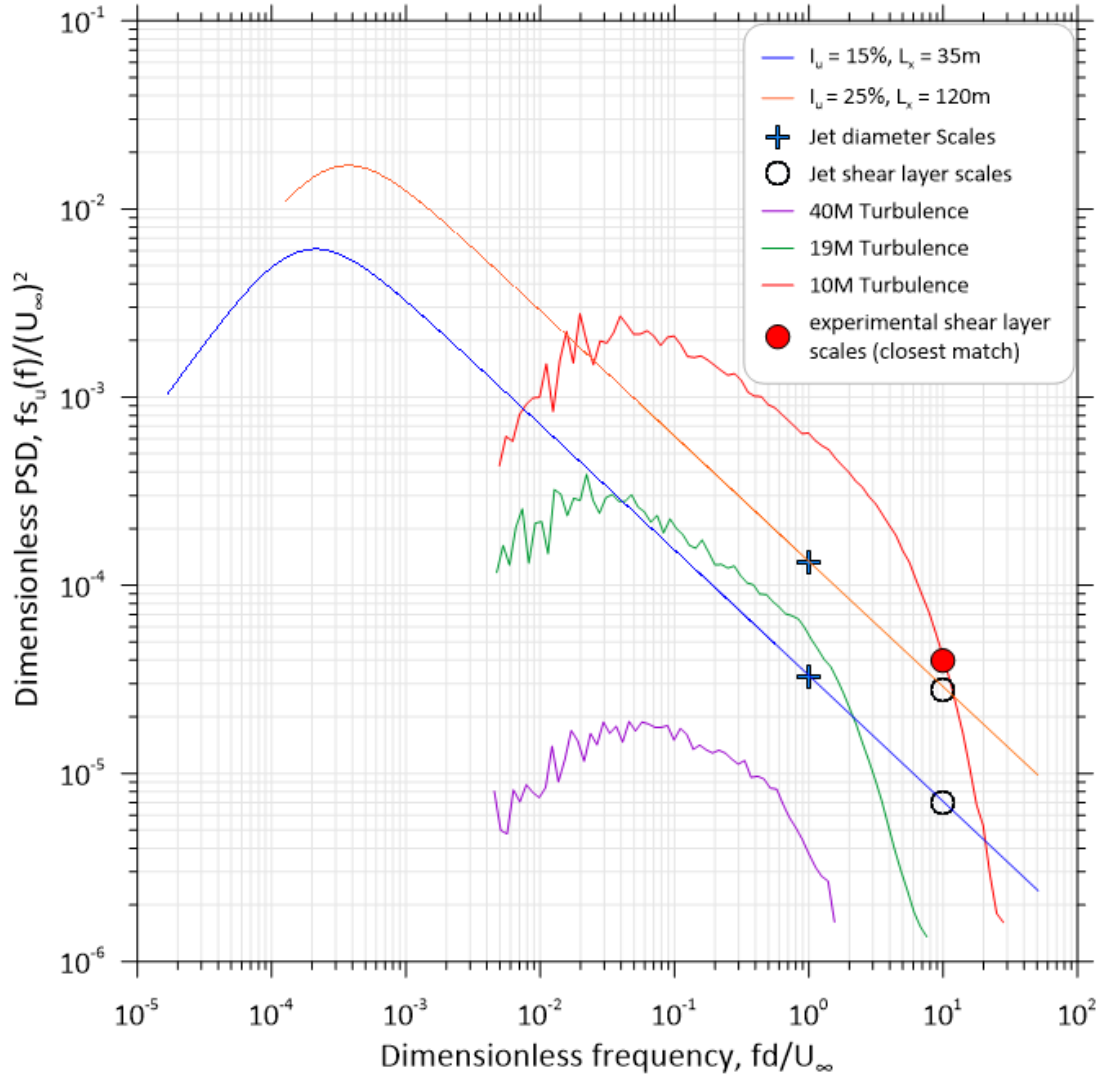


Figure 3.12: Spectra measured in the BLWTL experimental test section using Hot Wire Anemometry (data collected by (Hossain 2019)). Data is normalized for a burner diameter (d) of 1 inch.

3.7 Data Acquisition System

Customized software written in LabVIEW is used to control the wind tunnel and fuel supply system and acquire data from all instruments. As detailed in Table 3.6, resistance, voltage and current signals are acquired via a National Instruments (NI) cDAQ9189 data acquisition card, read at a frequency of 10Hz, and averaged and logged at 1 Hz using NI 9216, 9476 and 9207 modules. The 4-wire RTDs are read using 0-400 Ω read ins on an NI 9216 module. Wind tunnel speed measured using the pitot and an Ashcroft pressure transducer (0-5 V signal), Los Gatos analyzers (0-5 V signals), Vaisala PTB110 barometer pressure sensor (0-2.5 V), gas cylinder pressures from Ashcroft

pressure transducers (4-20mA), natural gas tank pressure (4-20mA) and the associated glycol heating system (4-20mA) are acquired using the NI 9207 module. The cDAQ9189 is also used to control the wind tunnel fan, exterior wind tunnel doors, and pneumatic shut-off valves on the gas manifold system using NI 9263 and 9221 output cards via the cDAQ9189. The MFCs, the Trisonica Mini anemometer, rotational traverse and Coriolis flow mass flow meter are read at 1 Hz as digital signals via serial communications to the flare computer. The Aeris analyzers are also read by the flare computer using USB-RS232 serial communications, however sample rate from the instruments deviates slightly from 1 Hz. Therefore, time stamps are logged and linearly interpolated in post-processing to align with other times. For the experiments conducted as part of this thesis, the above-mentioned parameters are logged by LabVIEW and subsequently exported to a text file for processing using Matlab. Future improvements include the data acquisition and subsequent processing to occur concurrently in LabVIEW.

Table 3.6: Table of Analog and Serial Communications Data.

Analog					
National Instruments Data Acquisition Card	Input/Output	Input/Output Range	Parameter	Parameter Range	Parameter Accuracy
9216	Input	0-400 Ω	RTDs	-50° to 150°C	0.68°C
9207	Input	4-20mA	Natural gas tank pressure	0-5000 psi	
		4-20mA	Natural gas glycol heating system	0-100°C	0.87% Relative, 0.05% Absolute
		4-20mA	Gas cylinder pressures	0-3000kPa	0.5% Relative 1% Absolute
		0-5V	Pitot-static tube	0-62.21 Pa	0.25%
		0-5V	LGR analyzers	Table 3.5	Table 3.5
		0-2.5	Barometric pressure	50-110 kPa	0.03 kPa
9263	Output	0-10V	Wind tunnel fan	0-12m/s	-
9476	Output	Relay switch	Pressure actuated valves/gas manifold system	Closed-Open	-
		Relays/Limit Switches	Exterior wind tunnel doors	Closed-Open	-
Serial					
Input/Output		Parameter	Communications	Range	Accuracy
Input		Aeris analyzers*	USB-RS232	Table 3.5	Table 3.5
Input		Coriolis mass flow meter	Modbus RS485	0-20 kg/h	0.50%
Input/Output		MFCs	RS232	Varied (0-1500 SLPM)	0.5% Relative 0.1% Absolute
Input		Trisonica Mini ultrasonic anemometer	USB-RS232	0.1-50 m/s, 50-115 kPa	0.1 m/s, 1 kPa
Output		Rotational traverse	RS232	180°C-180°C	-

Chapter 4 A Methodology for Quantifying Combustion

Efficiencies and Species Emission Rates of

Flares Subjected to Crosswind

This chapter has published as a peer reviewed article in the Journal of the Energy Institute and should be cited as:

D.C. Burt, D.J. Corbin, J.R. Armitage, B.M. Crosland, A.M. Jefferson, G.A. Kopp, L.W. Kostiuk, M.R. Johnson (2022), A Methodology for Quantifying Combustion Efficiencies and Species Emission Rates of Flares Subjected to Crosswind, Journal of the Energy Institute, 104:124–132. (doi: [10.1016/j.joei.2022.07.005](https://doi.org/10.1016/j.joei.2022.07.005))

This paper was co-authored by the thesis author, Damon Burt and his M.A.Sc. supervisor Prof. Matthew Johnson, with contributions from Darcy Corbin, Joshua Armitage, Brian Crosland, Melina Jefferson, Gregory Kopp and Larry Kostiuk. Mr. Burt produced the synthetic data and calculated the associated uncertainties via Monte Carlo Uncertainty Analysis. Retrofitting of the closed-loop wind tunnel and subsequent instrumentation to perform controlled combustion experiments was led by Darcy Corbin and Matthew Johnson. Experimental validation measurements, as well as writing and editing of the manuscript were performed jointly.

4.1 Abstract

Despite strong indications that flares subjected to crosswinds can undergo fuel stripping mechanisms that reduce efficiency and lead to emission of unburned fuel, most published flare experiments have not considered the impact of a crosswind. Knowledge of flare performance in turbulent crosswinds representative of atmospheric wind is especially lacking. Accurate experiments to fill this gap can only be achieved in an environment where the wind conditions can be controlled. This work presents a methodology to determine the carbon conversion efficiency and species emission rates of a flare burning in a closed-loop wind tunnel. The developed methodology is based on solving an unsteady mass balance to relate measured accumulation rates in a closed-loop wind tunnel to emission rates, while extending the applicability and correcting errors of an earlier method. The developed methodology considers complicating factors such as infiltration and exfiltration of gases into and out of the wind tunnel, potential for reburning of products within the wind tunnel, and presence of inert species in the fuel stream. The methodology is assessed with a comprehensive Monte Carlo uncertainty and sensitivity analysis. Results suggest that carbon conversion efficiency can be measured with a

systematic bias uncertainty of $\lesssim \pm 0.5\%$, ranging from 0.04% for a 99% efficient flare and 0.55% for a 70% efficient flare at 95% confidence and methane emission rates can be measured within $\pm 3.25\%$ at 95% confidence. Demonstration experiments in a large closed-loop wind tunnel show that precision (repeatability) uncertainties will be larger but that overall (combined bias and precision) uncertainties of $< 10\%$ are readily achievable.

4.2 Introduction

In the energy and petrochemical industries, flaring is the ubiquitous process of burning unwanted flammable gases in a turbulent, non-premixed flame. Satellite data suggest that global flaring volume increased to 161 billion m^3 in 2019, approximately 90% of which was attributed to upstream oil and gas production sites (EOG 2021). Incomplete combustion, i.e. “inefficient” flaring, can result in the emission of unburned fuel (Gvakharia et al. 2017; Johnson et al. 2001), volatile organic compounds (Knighton et al. 2012), and carbonaceous soot or black carbon (Conrad and Johnson 2017; Weyant et al. 2016; Fortner et al. 2012; McEwen and Johnson 2012; Johnson et al. 2011). Given that most flare gas is rich in methane (Johnson and Coderre 2012), a short-lived climate pollutant with a global warming potential many times that of CO_2 (Forster et al. 2021), inefficient flaring can be an important source of greenhouse gas emissions. In addition, black carbon emissions from flaring at northern latitudes in Russia are thought to be an especially important contributor to Arctic temperature rise (Sand et al. 2016). Quantitative understanding of flare performance over the broad range of operating conditions encountered in the field is crucial from an environmental and regulatory perspective.

Although many different approaches for measuring flare emissions have been attempted, including remote optical techniques (Zeng et al. 2016; Wormhoudt et al. 2012; Spellicy et al. 2006; Yang and Chang 2006), aircraft sampling techniques (Gvakharia et al. 2017; Caulton et al. 2014), extractive probe sampling from full-sized flare plumes (Herndon et al. 2012; Torres et al. 2012b; Strosher 2000; Pohl et al. 1986; McDaniel 1983), sampling of laboratory and pilot scale flares via a large sampling hood (Corbin and Johnson 2014; McEwen and Johnson 2012), and closed-loop wind tunnel measurements (Johnson and Kostiuik 2000; Bourguignon et al. 1999), results have not always been consistent and models to predict emissions under a range of operating conditions (especially the influence of crosswind) remain elusive. For example, in airborne measurements of flares in North Dakota, Caulton et al. (Caulton et al. 2014) measured destruction efficiencies generally $> 98.8\%$ (lower quartile) whereas Gvakharia et al. (Gvakharia et al. 2017) reported a

median destruction efficiency of 97%, with a log-normally distributed tail toward much lower values. Using extractive sampling techniques, McDaniel (McDaniel 1983) and Pohl et al. (Pohl et al. 1986) found combustion efficiencies of normally operating flares >98%, whereas Strosher (Strosher 1996) reported efficiencies as low as 62% for sampled flares at upstream production sites. Comparing results from extractive sampling to optical measurements using a Passive Fourier Transform Infrared (PFTIR) technique, Wormhoudt et al. (2012) found disagreement beyond the combined nominal error bars of the methods in 41% of tests.

These discrepancies may partially be attributed to the wide variety of flare configurations and operating conditions. However, the uncertainties in results and variances among methods are also a direct reflection of the difficulty of the problem, where the time-varying and spatially inhomogeneous nature of the unconfined turbulent combustion plume complicates accurate measurements (Seymour and Johnson 2021; Wormhoudt et al. 2012). These challenges are exacerbated in high crosswind conditions, where wind tunnel experiments (Johnson et al. 2001; Poudenx 2000) and flow visualization (Johnson and Kostiuik 2002a) suggest that methane can be emitted on the underside of the wind-deflected flame, separate from the main plume of hot products. While the cited studies and measurements/methods provide insight into the potential range of flare performance, systematic experiments and analysis to quantify and understand the impact of operating conditions on flare emissions (e.g. crosswind speed, ambient turbulence level, flare gas composition, exit velocity, and diameter) remain as a goal to be achieved.

Controlled, large-scale experiments with complete capture of the flare plume offer a means to eliminate many of the challenges of representative plume sampling, and could enable the required breadth of repeatable and accurate experiments to develop comprehensive models to predict flare emissions. Corbin and Johnson (Corbin and Johnson 2014) reviewed existing calculation approaches and proposed a robust methodology for quantifying emissions within precisely quantified uncertainties based on a steady-state carbon mass balance. However, this approach is not readily extended to experiments within closed-loop wind tunnels as would be necessary to systematically investigate effects of crosswind on flare emissions, which requires an unsteady mass balance to account for species accumulation within the wind-tunnel over time. Bourguignon et al. (Bourguignon et al. 1999) developed such a methodology based on measured accumulation rates via an unsteady mass balance, which was used to measure combustion efficiencies of 0.5 to 2-inch diameter propane and natural gas flares subjected to low-turbulence

crossflow in a closed-loop wind tunnel (Johnson and Kostiuik 2000, 2002b). However, as will be shown below, the work of Bourguignon et al. includes a critical error in the mathematical development, which has been corrected in the presently derived methodology. Fortunately, as shown in the Supplementary Information (SI) this error is greatest when the rate of change of temperature is large and had a negligible impact on earlier published results using this method for which temperature change was generally small. The method of Bourguignon et al. (Bourguignon et al. 1999) was also not readily extensible to quantifying emission rates of species that cannot be measured continuously in the wind tunnel (e.g. extractive sampling VOC species for analysis via gas chromatograph). The present methodology removes this limitation.

The objectives of this paper are to develop and experimentally validate a robust methodology for quantifying carbon conversion efficiency (η) and species emission rates from flares in a closed-loop wind tunnel. The developed methodology is based on solving the unsteady carbon mass balance which relates the accumulation rates of measured gas-phase species in a control volume to combustion inefficiency ($1 - \eta$) and species emission rates, while considering complicating factors such as infiltration and exfiltration of gases, potential for reburning of products, and the presence of inert species in the fuel stream. The derived approach is sufficiently generalized to be readily extended to any unsteady accumulation problem involving reacting flows within a fixed control volume and can quantify combustion efficiency and species emission rates using both continuously and batch-sampled measured data. The methodology is successfully used in a demonstration experiment to measure emissions from a flare subjected to different magnitudes of turbulent crosswind while burning a methane-rich gas mixture typical of flares at upstream oil and gas production sites. Most importantly, the derived approach enables a comprehensive uncertainty analysis that is essential to interpreting measurements and comparing results.

4.3 Theory

4.3.1 Derivation of a Species Mass Balance Equation

This section provides a summary of the unsteady mass balance approach to determine carbon conversion efficiency and species emission rates within a fixed-volume control volume (CV). Full derivation details can be found in the Supporting Information. As shown in Figure 4.1, the CV is defined to include the internal volume of a closed-loop wind tunnel while excluding the flame. The figure introduces various mass flow rates (\dot{m}), mole fractions (X), molecular masses (M), temperatures (T), and pressures (P) for conditions in the CV (denoted by the subscript cv),

conditions of flare gas (denoted by the subscript f), conditions of the hot gases in the flare plume (denoted by the subscript p), and ambient conditions (denoted by the subscript ∞). The term $\dot{m}_{i,prod,comb}$ is the mass emission rate of species i produced from combustion (including any amount of species i emitted as un-combusted hydrocarbon material that originated from the flare gas) and entering the CV; $\dot{m}_{i,inert}$ is the mass emission rate of species i originating as an inert species in the flare gas (e.g. non-reacting CO_2 in the flare gas) and entering the CV; $\dot{m}_{i,in}$ is the mass infiltration rate of species i transported as a component of the ambient air leaking into the CV; $\dot{m}_{i,ex}$ is the mass exfiltration rate of species i from the CV; and $\dot{m}_{i,r}$ is the rate of creation or destruction of mass of species i due to reburning of species that exit the CV and subsequently enter the flame as a component of the combustion air. Species within the CV are assumed to be well-mixed, and this assumption is further considered in SI Section A.3.

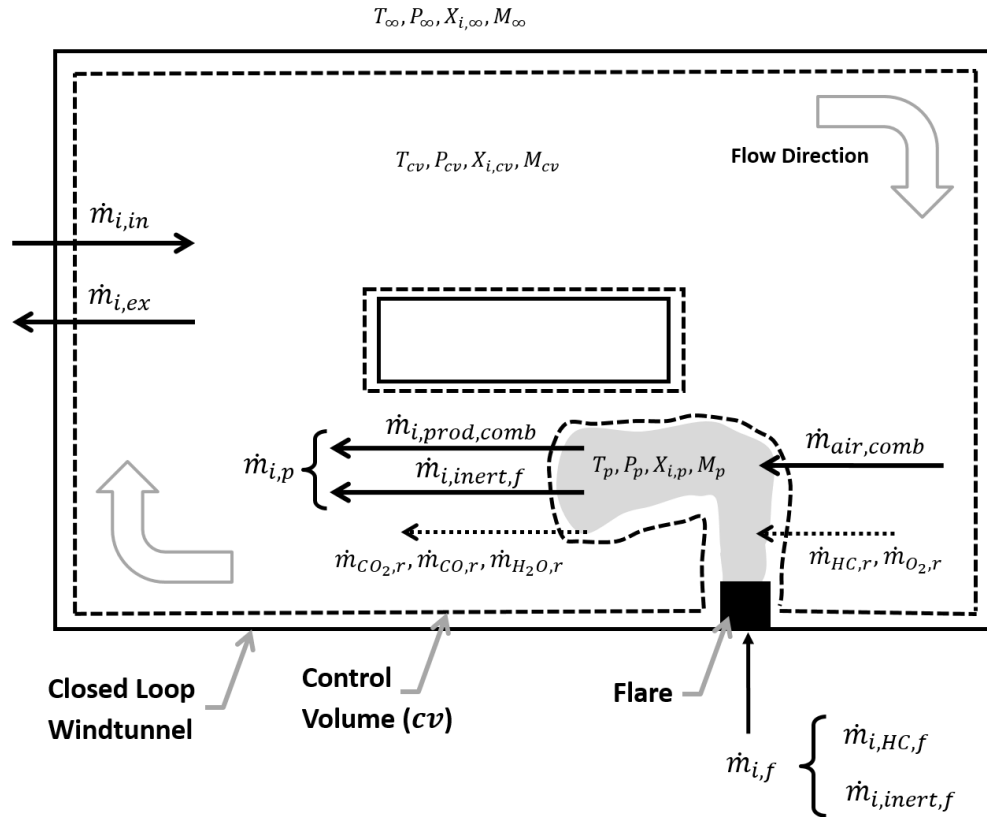


Figure 4.1: Control volume diagram for a closed-loop wind tunnel with a lab-scale flare.

The unsteady species mass balance is then written as:

$$\frac{dm_{i,cv}}{dt} = \dot{m}_{i,p} + \dot{m}_{i,in} - \dot{m}_{i,ex} \pm \dot{m}_{i,r} \quad (4.1)$$

where for simplicity, the mass of species i emitted in the plume of the flare, $\dot{m}_{i,p} = \dot{m}_{i,prod,comb} + \dot{m}_{i,inert}$, may be defined as the sum of the mass emission rate of species i produced through combustion and any mass flow rate of species i originating as an inert component of the flare gas that passes through the flame and is released into the CV via the combustion plume. Using the ideal gas law to express mass flows in terms of volume flow rates, \dot{V} , at ambient temperature and pressure, Eq. (4.1) can be expressed as:

$$V_{cv} \frac{d}{dt} \left(\frac{X_{i,cv}}{T_{cv}} \right) = \frac{X_{i,p} \dot{V}_{p,\infty}}{T_{\infty}} + \frac{X_{i,\infty} \dot{V}_{in}}{T_{\infty}} - \frac{X_{i,cv} \dot{V}_{ex}}{T_{cv}} - \left\{ \frac{X_{i,cv} \dot{V}_{air,comb,\infty}}{T_{\infty}} \right\}_{i=HC} + \left\{ \frac{x X_{HC,cv} \dot{V}_{air,comb,\infty}}{T_{\infty}} \right\}_{i=CO_2} \quad (4.2)$$

where V_{cv} represents the volume of the CV, $\dot{V}_{air,comb,\infty}$ represents the volume flow rate of air consumed during combustion of the flare gas, and x represents the average number of carbon atoms in the hydrocarbons (denoted by the subscript HC having the form C_xH_y) within the CV. The fourth term on the right-hand side represents hydrocarbons in the ambient air that could potentially be reburned as part of the combustion air that is drawn from the CV, while the fifth term represents the production of CO_2 resulting from the reburning of hydrocarbons in the ambient air. For simplicity, the fourth and fifth terms (i.e. reburning terms) on the right side of Eq. (4.2) are written assuming that combustion is complete; this proves valid since the terms themselves are shown to be negligible in almost all cases (See SI, Section A.2, Table A1).

Up to this point, the development is similar to that of Bourguignon et al. (Bourguignon et al. 1999), but from here the analysis diverges. Bourguignon et al. substituted an expression for the exfiltration term (third term on the right side of Eq. (4.2)) based on an overall mass balance of the CV to account for the potential temperature difference between gases entering and leaving the tunnel. However, this substitution failed to properly account for the change in mass within the CV as the temperature changes. The implication of this oversight is further discussed in Section A.8 of the SI. Instead, an overall mass balance for the CV can be written:

$$\frac{dm_{cv}}{dt} = \dot{m}_p + \dot{m}_{in} - \dot{m}_{ex} - \dot{m}_{air,comb} = \dot{m}_f + \dot{m}_{in} - \dot{m}_{ex} \quad (4.3)$$

where \dot{m}_p is the total mass flow rate of emitted products of combustion, $\dot{m}_{air,comb}$ is the total mass flow rate of air required for combustion, and \dot{m}_f is the mass flow rate of flare gas.

Substituting in the ideal gas law, expanding the differential term using the quotient rule, and simplifying (See SI, Eq. B.9-B.10), this overall mass balance can be rewritten as:

$$-\frac{P_{\infty}V_{cv}M_{cv}}{R_uT_{cv}^2}\frac{dT_{cv}}{dt} = \frac{P_{\infty}}{R_u}\left(\frac{M_f\dot{V}_{f,\infty}}{T_{\infty}} + \frac{M_{\infty}\dot{V}_{in}}{T_{\infty}} - \frac{M_{cv}\dot{V}_{ex}}{T_{cv}}\right) \quad (4.4)$$

This expression can then be rearranged to solve for the exfiltration rate, \dot{V}_{ex} , and substituted into the species mass balance expression in Eq. (4.2). Again, expanding the differential term using the quotient rule, and simplifying (See SI, Eq B.11-B.13), a final expression representing the net accumulation rate of any species i in the CV, $\frac{dX_{i,cv}}{dt}$, can be derived:

$$V_{cv}\frac{dX_{i,cv}}{dt} = \frac{X_{i,p}\dot{V}_{p,\infty}T_{cv}}{T_{\infty}} + \frac{X_{i,\infty}\dot{V}_{in}T_{cv}}{T_{\infty}} - X_{i,cv}\frac{M_f\dot{V}_{f,\infty}T_{cv}}{M_{cv}T_{\infty}} - X_{i,cv}\frac{M_{\infty}\dot{V}_{in}T_{cv}}{M_{cv}T_{\infty}} - \left\{\frac{X_{i,cv}\dot{V}_{air,comb,\infty}T_{cv}}{T_{\infty}}\right\}_{i=HC} + \left\{\frac{xX_{HC,cv}\dot{V}_{air,comb,\infty}T_{cv}}{T_{\infty}}\right\}_{i=CO_2} \quad (4.5)$$

This expression is notably different from the analogous expressions in Bourguignon et al. (Bourguignon et al. 1999), where the latter include an erroneous $1/T_{cv}$ within the left side differential.

4.3.2 Limit Approach to Determine Species Mass Emission Rates

For a steady burning flare, Eq. (4.5) is valid for all times during an experiment. However, to accurately determine the accumulation rates of species emitted by combustion, it is useful to consider limiting conditions near the start of an experiment ($t \rightarrow t_0$) when all properties in the wind tunnel approach ambient conditions, such that $X_{i,cv} \rightarrow X_{i,\infty}$, $T_{cv} \rightarrow T_{\infty}$, $M_{cv} \rightarrow M_{\infty}$, $X_{HC,cv} \rightarrow X_{HC,\infty}$. In this limit, Eq. (4.5) reduces to:

$$V_{cv}\frac{dX_{i,cv}}{dt}\Big|_{t \rightarrow t_0} = X_{i,p}\dot{V}_{p,\infty} - X_{i,\infty}\frac{M_f}{M_{\infty}}\dot{V}_{f,\infty} - \{X_{i,\infty}\dot{V}_{air,comb,\infty}\}_{i=HC} + \{xX_{HC,\infty}\dot{V}_{air,comb,\infty}\}_{i=CO_2} \quad (4.6)$$

The expected order of magnitude of the remaining four terms appearing on the right side of Eq. (4.6) can be estimated considering a flare burning CH₄ at various assumed carbon conversion efficiencies (see SI, Section A.2, Table A1). The calculations assume combustion with air (79% N₂, 21% O₂) containing typical background volume fractions of CO₂ at 400 ppm, CH₄ at 2 ppm, and CO at 1 ppm. For cases with assumed efficiencies less than 100%, the unconverted fuel carbon is assumed to be split equally between emissions of CO and CH₄. From this order of magnitude analysis, the reburning term for CO₂ (4th term on the right side) is negligible in all test scenarios

considered, with a magnitude less than 0.002% of the first term on the right side. This simplifies Eq. (4.6) to:

$$X_{i,p}\dot{V}_{p,\infty} = V_{cv}\left.\frac{dX_{i,cv}}{dt}\right|_{t\rightarrow t_0} + X_{i,\infty}\frac{M_f}{M_\infty}\dot{V}_{f,\infty} + \{X_{i,\infty}\dot{V}_{air,comb,\infty}\}_{i=HC} \quad (4.7)$$

Eq. (4.7) outlines the means for calculating the volumetric emission rate of any species i in the CV, defined as $X_{i,p}\dot{V}_{p,\infty}$, based on a measurement of the initial accumulation rate of that species $\left.\frac{dX_{i,cv}}{dt}\right|_{t\rightarrow t_0}$ (further discussed in Section 4.3.3) and other measurable or calculable parameters defined at ambient conditions. An emission rate on a mass basis can then be calculated using:

$$\dot{m}_{i,p} = \rho_{i,\infty}^o X_{i,p}\dot{V}_{p,\infty} = \rho_{i,\infty}^o \left(V_{cv}\left.\frac{dX_{i,cv}}{dt}\right|_{t\rightarrow t_0} + X_{i,\infty}\frac{M_f}{M_\infty}\dot{V}_{f,\infty} + \{X_{i,\infty}\dot{V}_{air,comb,\infty}\}_{i=HC} \right) \quad (4.8)$$

where $\rho_{i,\infty}^o$ is the mass density of the pure species i at the same ambient conditions as $\dot{V}_{p,\infty}$. In principle all variables in Eq. (4.8) are known or measurable, but V_{cv} and $\dot{V}_{air,comb,\infty}$ can be difficult to directly measure with precision. V_{cv} is most accurately quantified using a carbon balance as further discussed in Section 0. At high flare efficiencies, $\dot{V}_{air,comb,\infty}$ approaches the easily calculable stoichiometric value. However, as flare efficiencies decrease and products of incomplete combustion increase, $\dot{V}_{air,comb,\infty}$ cannot be calculated without additional information. Conveniently, as detailed in the SI, Section A.2.1, the importance of the $\dot{V}_{air,comb,\infty}$ term rapidly diminishes as the efficiency decreases, and calculations over a broad range of potential conditions are sufficient to accurately constrain this term.

4.3.3 General Fitting Solution to Calculate Species Accumulation Rates in the CV

Similar to the approach used by (Bourguignon et al. 1999) and (Johnson 2001), the initial accumulation rate of the target species, $\left.\frac{dX_{i,cv}}{dt}\right|_{t\rightarrow t_0}$, can be accurately determined by measuring the concentrations in time and fitting the observed trend to calculate the slope at the start of an experiment. The solution to the species mass balance, Eq. (4.5), defines the expected shape of the accumulation rate function, which can be rearranged as an ordinary differential equation (ODE) with CV temperature as a time-varying coefficient, Eq. (4.9). As shown in SI, Section A.2, Table A1, the reburning term for CO₂ is negligible in all scenarios and has been omitted:

$$\frac{dX_{i,cv}}{dt} = T_{cv}(t) \left(\frac{(X_{i,p}\dot{V}_{p,\infty} + X_{i,\infty}\dot{V}_{in})}{V_{cv}T_{\infty}} - X_{i,cv}(t) \frac{\left(\frac{M_f}{M_{cv}}\dot{V}_{f,\infty} + \frac{M_{\infty}}{M_{cv}}\dot{V}_{in}\right)}{V_{cv}T_{\infty}} - \left\{ X_{i,cv}(t) \frac{\dot{V}_{air,comb,\infty}}{V_{cv}T_{\infty}} \right\}_{i=HC} \right) \quad (4.9)$$

Eq. (4.9) can be solved via integration (see SI Eq. B.16-B.21 for full derivation) and expressed as:

$$X_{i,cv}(t) = \frac{A_i - C_i e^{-B_i \int_{t_0}^t T_{cv}(t) dt}}{B_i} \quad (4.10)$$

where $A_i = \frac{X_{i,p}\dot{V}_{p,\infty} + X_{i,\infty}\dot{V}_{in}}{V_{cv}T_{\infty}},$

$$B_i = \frac{\left(\frac{M_f}{M_{cv}}\dot{V}_{f,\infty} + \frac{M_{\infty}}{M_{cv}}\dot{V}_{in} + \{\dot{V}_{air,comb,\infty}\}_{i=HC}\right)}{V_{cv}T_{\infty}}, \text{ and}$$

$$C_i = A_i - B_i X_{i,\infty}$$

The time-varying temperature coefficient, $T_{cv}(t)$, can be easily measured such that its integral can be explicitly evaluated from the start of a test, t_0 , to any time t . It is then possible to fit a curve to the measured species concentrations using the Levenberg-Marquardt or similar algorithm to solve for the coefficients A_i , B_i , and C_i . The slope of the concentration at the start of the test, i.e., the accumulation rate of the species of interest, can then be calculated by differentiating Eq. (4.10) and evaluating at t_0 using the curve fit parameters:

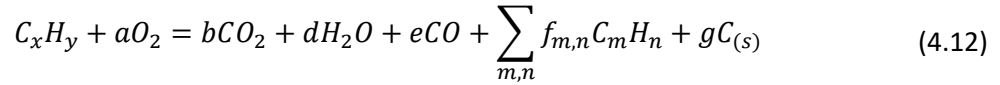
$$\left. \frac{dX_{i,cv}}{dt} \right|_{t \rightarrow t_0} = T_{cv}(t_0)(C_i) \quad (4.11)$$

A related method to measure emission rates of batch-sampled species is presented in Section S3.3 of the SI.

4.4 Carbon Balance Approach to Determine V_{cv}

The effective volume of the CV (i.e. participating volume of the wind tunnel) is challenging to measure with accuracy. Two experimental measurement approaches were considered: injection and measurement of a separate inert tracer species during a flare experiment, or use of a carbon mass balance on the combustion process. As detailed in the SI, Section A.6, the carbon balance approach proved to be more accurate and was used in the demonstration and validation experiments.

Incomplete combustion of a general hydrocarbon fuel (C_xH_y) may be summarized as:



where $a, b, d, e, f_{m,n}$, and g are stoichiometric coefficients, and potential products of incomplete combustion of gas flares may include carbon monoxide (CO), and unburned/reformed hydrocarbons, $\sum_{m,n} C_mH_n$ (which may have a different form than the raw fuel C_xH_y and may include both measured and unmeasured hydrocarbons during an experiment), and solid-phase soot ($C_{(s)}$). Available data on soot emission rates of gas flares suggest that soot emissions are likely to account for less than 0.5% of the carbon mass in the fuel for propane-fueled flares (Torres et al. 2012b; Ellzey et al. 1990; Pohl et al. 1986) and < 0.1% for flares burning methane-dominated fuel mixtures (McEwen and Johnson 2012). Therefore, carbon produced by combustion in the form of soot can be omitted from the products when calculating V_{cv} . A carbon balance for (4.12) can then be expressed in terms of volume flow rates as:

$$\sum_i (\#_{C,i} \dot{V}_{f,\infty} X_{i,f}) = \sum_i (\#_{C,i} \dot{V}_{p,\infty} X_{i,p}) \quad (4.13)$$

where $\#_{C,i}$ is the number of carbon atoms in substance i .

4.4.1 Fuel Stripping Assumption to Close Carbon Balance for V_{cv}

To implement the methodology derived in this paper, measurements of time-resolved species concentration within the CV are essential. Although a range of modern gas analysis equipment may be suitable, the present analysis used optically based extractive sampling equipment comprising a Los Gatos Research cavity enhanced laser absorption analyzer (Model GGA-24EP) to measure CO_2 and Aeris Technologies Mid-Infrared Laser Absorption Spectroscopy analyzers (Ultra Series) to measure CH_4 , C_2H_6 , and CO. However, because not all potential products of combustion in (4.12) may be directly or easily measurable, additional assumptions about unmeasured products must be employed. Previous studies suggest that unburned hydrocarbons in the plume are primarily caused by fuel stripping (Johnson et al. 2001; Johnson and Kostiuik 2000). This means that the emitted hydrocarbons tend to have the same form as the raw flare gas such that the hydrocarbon concentrations in the plume may be inferred based on measured CH_4 concentrations in the plume:

$$\left\{ X_{i,p} = \frac{X_{i,HC,f}}{X_{CH_4,f}} X_{CH_4,p} \right\}_{i=UMHC} \quad (4.14)$$

where $UMHC$ denotes an unmeasured hydrocarbon species.

The carbon balance in Eq. (4.13) can thus be expressed for all carbon-containing substances listed in the combustion reaction by expanding the right hand side of Eq. (4.13) for each measured species, while using Eq. (4.14) for any unmeasured hydrocarbons. The volume of the CV, V_{cv} (See SI Section A.4.1) can then be calculated as:

$$V_{cv} = \left[\begin{aligned} & \sum_i (\#_{C,i} \dot{V}_{f,\infty} X_{i,f}) - \sum_{i \neq HC} \#_{C,i} X_{i,\infty} \frac{M_f}{M_\infty} \dot{V}_{f,\infty} \\ & - \sum_{i=HC} \#_{C,i} X_{i,\infty} \frac{M_f}{M_\infty} \dot{V}_{f,\infty} - \sum_{i=UMHC} \#_{C,i} \frac{X_{i,f}}{X_{CH_4,f}} X_{CH_4,\infty} \frac{M_f}{M_\infty} \dot{V}_{f,\infty} \\ & - \sum_{i=HC} \#_{C,i} X_{i,\infty} \dot{V}_{air,comb,\infty} - \sum_{i=UMHC} \#_{C,i} \frac{X_{i,f}}{X_{CH_4,f}} X_{CH_4,\infty} \dot{V}_{air,comb,\infty} \end{aligned} \right] \quad (4.15)$$

$$/ \left[\begin{aligned} & \sum_{i \neq HC} \#_{C,i} \frac{dX_{i,cv}}{dt} \Big|_{t \rightarrow t_0} + \sum_{i=HC} \#_{C,i} \frac{dX_{i,cv}}{dt} \Big|_{t \rightarrow t_0} \\ & + \sum_{i=UMHC} \#_{C,i} \frac{X_{i,f}}{X_{CH_4,f}} \frac{dX_{CH_4,cv}}{dt} \Big|_{t \rightarrow t_0} \end{aligned} \right]$$

Note that Eq. (4.15) is generalized such that, depending on what hydrocarbon species are measurable in any implementation of this approach, emitted hydrocarbon species are either included in the summation $\sum_{i=HC}$ or $\sum_{i=UMHC}$. In the present demonstration experiments where time-resolved measurements of C_2H_6 were possible, the use of the fuel stripping assumption to close the carbon balance method can be directly checked by comparing measured methane-ethane ratios in the plume and comparing to their ratios in the raw flare gas. Section 4.7 demonstrates that the fuel stripping assumption is most valid at higher crosswind speeds (where emissions are highest and carbon conversion efficiency is lowest). By contrast at low wind speeds (when emissions are low and carbon conversion efficiencies are high), the small amount of emitted hydrocarbons are dominated by methane, implying that heavier species (C_2+) tend to burn first. These contrasting scenarios were considered in the Monte Carlo uncertainty and sensitivity analysis presented in Section 4.6, which demonstrates that the methodology is robust and final uncertainties in measured emission rates are insensitive to the assumption used when calculating V_{cv} .

4.5 Determining Carbon Conversion Efficiencies

Combustion efficiency of a flare may be defined in several ways but is most usefully defined as the carbon conversion efficiency (η), which evaluates the percentage of carbon mass in the

hydrocarbon fuel stream that is fully reacted and converted to carbon dioxide. On a molar basis, this may be expressed as:

$$\eta[\%] = \frac{\text{moles of carbon in produced } CO_2}{\text{moles of carbon in hydrocarbon fuel stream}} \times 100 \quad (4.16)$$

Allowing for the potential of having carbon dioxide in the flare gas and substituting Eq. (4.7) where $i = CO_2$, the carbon conversion efficiency can be expressed in terms of known or measurable quantities as:

$$\eta = \frac{V_{cv} \left. \frac{dX_{CO_2,cv}}{dt} \right|_{t \rightarrow t_0} + X_{CO_2,\infty} \frac{M_f}{M_\infty} \dot{V}_{f,\infty} - \dot{V}_{f,\infty} X_{CO_2,f}}{\sum_{i=HC} (\#_{C,i} \dot{V}_{f,\infty} X_{i,f})} \quad (4.17)$$

where V_{cv} can be obtained from Eq. (4.15), $\left. \frac{dX_{CO_2,cv}}{dt} \right|_{t \rightarrow t_0}$ can be obtained using Eq. (4.11), and all remaining terms are known for a given flare gas input.

4.6 Method Validation

4.6.1 Sensitivity and Uncertainty Analysis using Simulated Data

The experimental approach was first examined by performing a detailed calculation and uncertainty analysis on a synthetic data set. These simulated data considered a wind tunnel volume of 2 000 m³ (approximating that of the Western University Boundary Layer Wind Tunnel Laboratory used in the validation experiments) at a conservatively large infiltration/exfiltration rate of the CV of 10 air changes per hour. The analysis considered a range of flare gas flow rates (25–1000 SLPM) and carbon conversion efficiencies (70–99%) for two different multicomponent flare gas mixtures representative of upstream oil and gas sector flares (L6 and H6, see Table 4.1 for compositions). As detailed in SI Section A.6, these simulated data were intentionally distorted with precision, bias, and linearity errors to test the robustness of the method under a conservatively large range of expected measurement and instrumentation errors.

Carbon conversion efficiency and species emission rates were then calculated by applying the presented method to the distorted synthetic data. A Monte Carlo uncertainty analysis was used to derive overall measurement uncertainties. For each test condition, 10 000 draws from representative parameter distributions (See SI Section A.6) were used to calculate 95% confidence intervals for measured carbon conversion efficiencies and species emission rates. Because carbon conversion efficiency is commonly quoted as a percentage, to reduce unit confusion, uncertainties on carbon conversion efficiency are presented in “absolute” terms, i.e., the

expected difference between the measured value and true value. However, for species emission rates uncertainties are quoted on a relative basis, defined as the ratio of the uncertainty to the measured value in percent, which permits direct comparison among species and conditions.

Figure 4.2a shows that the anticipated absolute uncertainties in the carbon conversion efficiency are less than $\leq 0.5\%$ in all considered scenarios. More importantly, the certainty of the measurement increases as the efficiency increases. Thus a 99% efficient flare should be quantifiable at 95% confidence within a range of 98.96–99.04%, and a 70% efficient flare within 69.45-70.55%. Figure 4.2b shows that relative uncertainties in pollutant species emission rates (in this case, CH_4) can also be accurately measured, within $\pm 2.5\text{--}3.5\%$ in all cases. The emission rate uncertainties are primarily limited by the concentrations of species in the CV to be measured and the linearity of the gas analyzers (see SI Section A.6). Thus, uncertainties increase as the flare efficiency increases, since less unburned methane is produced at higher flare efficiencies. The consistently high level of precision over the range of synthetic test cases suggests the methodology will be useful in quantifying flare emissions over a diverse range of operating conditions. Notably the predicted uncertainties in efficiency and emission rates are not notably affected by flare gas composition or flow rate within the anticipated range of test conditions.

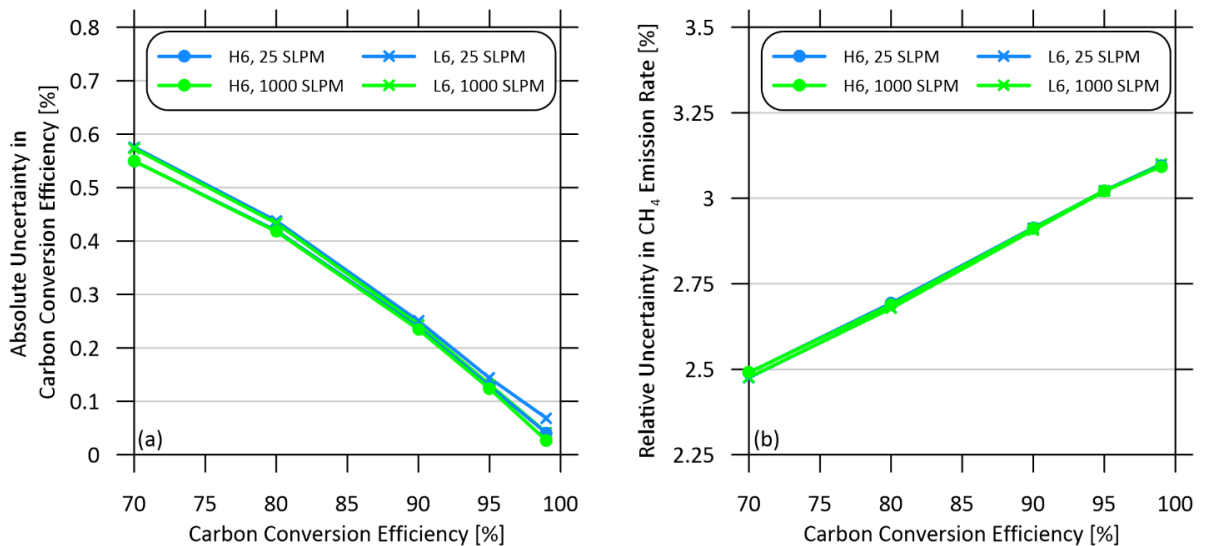


Figure 4.2: (a) Absolute anticipated measurement uncertainty in carbon conversion efficiency for flares in a closed-loop wind tunnel, experiencing a conservative air exchange rate of 10 air changes per hour (ACH), as a function of actual carbon conversion efficiency. (b) Relative uncertainties in the methane emission rates under the same range of conditions. H6 and L6 denote the “light” and “heavy” 6-component flare gas mixtures as detailed in Table 4.1

4.7 Experimental Demonstration of Derived Methodology

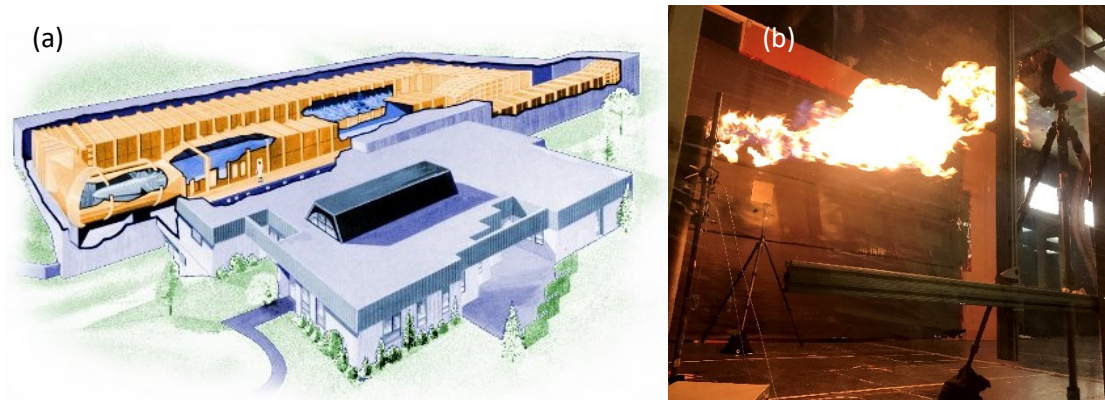


Figure 4.3: Preliminary tests performed at the Western University Boundary Layer Wind Tunnel Laboratory using methane-based gas flares exposed to various crosswind speeds; (a) schematic of the wind tunnel complex; (b) image of a 3-inch (77.9 mm) diameter flare burning the M6 flare gas mixture in the 3.65 by 3.96 m test section of the tunnel at a crosswind of 2 m/s.

Validation experiments were conducted at the Western University Boundary Layer Wind Tunnel Laboratory (Figure 4.3a), which is a large closed-loop wind tunnel ($\sim 2000 \text{ m}^3$ internal volume) with a 3.65-m wide by 3.96-m tall (16 by 13-foot) cross-section test section that has been retrofitted to permit combustion experiments with flares up to four inches in diameter. This partially overlaps with the 3–12 inch diameters of full scale flares commonly found at upstream oil and gas production sites in Canada and internationally (Conrad and Johnson 2017; McEwen and Johnson 2012). Prior to each experiment, the wind tunnel is purged with fresh outdoor air that enters and exits via two large ($\sim 5.025 \text{ m}$ by 3.95 m) exterior doors on the downstream end of the tunnel test section. Extractive samples are drawn from a single sample probe, centered within the tunnel cross-section and located 5.08 m upstream of the flare. This location allows products of combustion to mix as they traverse around the tunnel prior to being sampled. The implications of the probe location for signal interpretation are discussed further in A.3.1. A set of six resistance temperature detectors (RTD) placed around the tunnel are used to continuously measure the temperature within the CV.

4.7.1 Cold Flow Tests

As further detailed in SI Section A.7.2, test experiments were first performed to evaluate the ability to accurately measure species accumulation rates within the wind tunnel. These tests involved releasing known amounts of CH_4 , CO , and CO_2 through the burner without combustion. The flow rates were chosen to represent expected concentrations in the flare plume at different

carbon conversion efficiencies. These initial tests demonstrated the ability to calculate carbon conversion inefficiency to within 0.13% at an inefficiency of 1% (relative uncertainty of 14%), and 1.1% at an inefficiency of 20% (relative uncertainty of 5.5%), while methane emission rates could be calculated to within <5.7–16.5% relative uncertainty (Figure A13 of the SI).

4.7.2 Combustion Tests

The methodology was then evaluated in combustion experiments in which the carbon conversion efficiencies and methane emission rates of 1–4 inch diameter flares burning multicomponent fuel mixtures were measured under varying crosswind conditions and the measurement bias and precision (repeatability) uncertainties were scrutinized. At the time of writing the wind tunnel flare facility is equipped to burn controllable mixtures of gaseous hydrocarbons from CH₄ to C₄H₁₀, plus CO₂ and N₂, while performing real time measurements of combustion products in the tunnel including CH₄, C₂H₆, CO₂, and CO at parts per billion levels. Table 4.1 shows the compositions of three flare gas mixtures, representative of the range of gas compositions at upstream oil and gas industry sites in Western Canada (Johnson and Coderre 2012), that were used in both synthetic and experimental data in this paper.

Table 4.1: Mole fractions [%] of the light, medium, and heavy 6-component flare gas mixtures (based on analysis of flare gas composition data for Alberta, Canada reported by (Johnson and Coderre 2012)) used in synthetic and experimental data.

Species	Flare Gas Mixture		
	L6	M6	H6
CH ₄	93.31	86.03	75.16
C ₂ H ₆	0.32	6.81	11.44
C ₃ H ₈	0.09	2.35	6.02
C ₄ H ₁₀	0.27	1.99	4.48
CO ₂	1.38	1.61	1.69
N ₂	4.64	1.21	1.21

Example measured concentrations inside the tunnel for a 3-inch flare burning the M6 mixture at different crosswind speeds are plotted in Figure 4.4. At lower wind speeds (Figure 4.4a), the measured concentrations near the beginning of the test show a stair-step behavior (most apparent in the CO₂ data) that is associated with the longitudinal mixing of species in the tunnel after the flare is first ignited. This behavior quickly diminishes as the test proceeds and gives way to an orderly accumulation trend. By contrast, at higher wind speeds (Figure 4.4b), mixing within the wind tunnel is enhanced and the stair-step behavior gives way to a smoothly increasing trend.

However, the enhanced infiltration/exfiltration at higher wind speeds means the accumulation trend is notably non-linear. Nevertheless, the overlaid fit curves (black) show that the measured trends are well-described by fits according to Eq. (4.10) in all cases. Using these fits, the initial accumulation rates, $\left. \frac{dX_{i,cv}}{dt} \right|_{t \rightarrow 0}$, can be retrieved using Eq. (4.11) and used to calculate the carbon conversion efficiency and species emission rates. Systematic tests (see SI Section A.7.1) were performed to determine optimal durations for experiments; the measured accumulation rates converge after approximately 5 minutes and further increases in measurement time have negligible effect on the calculated accumulation rates, emission rates, or carbon conversion efficiency. At the conclusion of an experiment, the gases are shut off and the wind tunnel is purged for the next test.

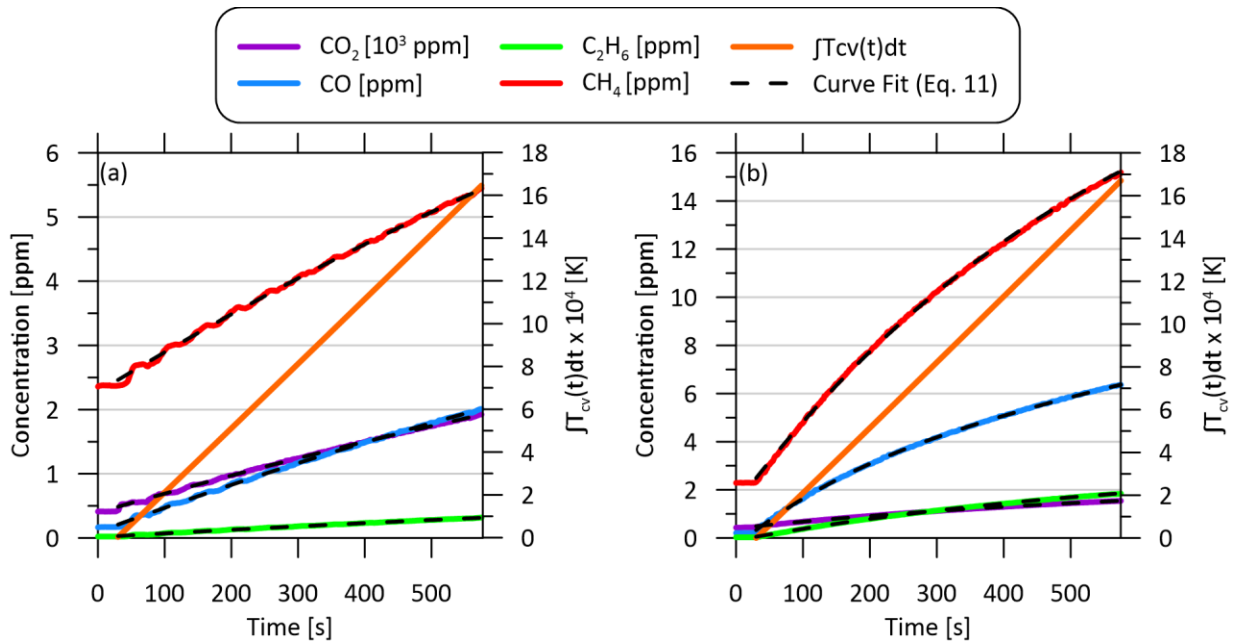


Figure 4.4: Concentrations of measured species at the Western University Boundary Layer Wind Tunnel Laboratory with a 2-inch (52.5-mm) diameter flare burning the heavy (H6) flare gas mixture at a nominal exit velocity of 2 m/s (flow rate of 259 SLPM). (a) Measured species concentrations and tunnel temperature for a crosswinds of 2 m/s, and (b) 9 m/s.

Figure 4.5 plots the measured carbon conversion inefficiency (i.e., $1 - \eta$), carbon species emission rates, and methane-ethane ratios for 4-inch diameter flare burning the M6 fuel mixture at a flare gas exit velocity of 0.5 m/s under a range of crosswind speeds. The plotted Monte Carlo computed measurement bias uncertainties on carbon conversion inefficiency illustrate the robustness of the methodology based on analysis of accumulation of species concentrations in the wind tunnel over time. For this flare, inefficiencies fall below 1% at low wind speeds, but increase dramatically with

increased crosswind. The stacked bars in Figure 4.5a illustrate how the relative proportions of emitted incomplete combustion species vary as wind speed is increased, and are ultimately dominated by emissions of unburned fuel rather than CO.

To further investigate the validity of the fuel stripping mechanism introduced in Eq. (4.14), Figure 4.5b compares the measured ratios of CH_4 to C_2H_6 to their ratio in the flare gas for the same experimental data. The ratio approaches unity as crosswind speed is increased, confirming that emissions are dominated by stripping of unburned fuel. However, at lower wind speeds, where carbon conversion efficiency is highest and emissions are lowest (Figure 4.5a), the methane-ethane ratio increases, suggesting the small amount of emitted hydrocarbons are dominated by methane. This was confirmed with comprehensive VOC analysis of samples taken from the tunnel (See SI, Section A.4.1.1), implying that the heavier hydrocarbons are preferentially consumed and emissions of hydrocarbon species larger than methane are negligible under these conditions. Considering these two cases (unburned hydrocarbons are a result of fuel stripping or dominated by methane) as limiting scenarios, the Monte Carlo analysis presented in Section 4.6.1 demonstrates that the calculated carbon conversion efficiency and the emission rates of measured species are insensitive to the assumption used to close the carbon balance for V_{cv} (Section 4.4.1). Essentially, the fuel-stripping assumption is most accurate when it matters most, i.e., at higher wind speeds with larger emissions of incomplete combustion products.

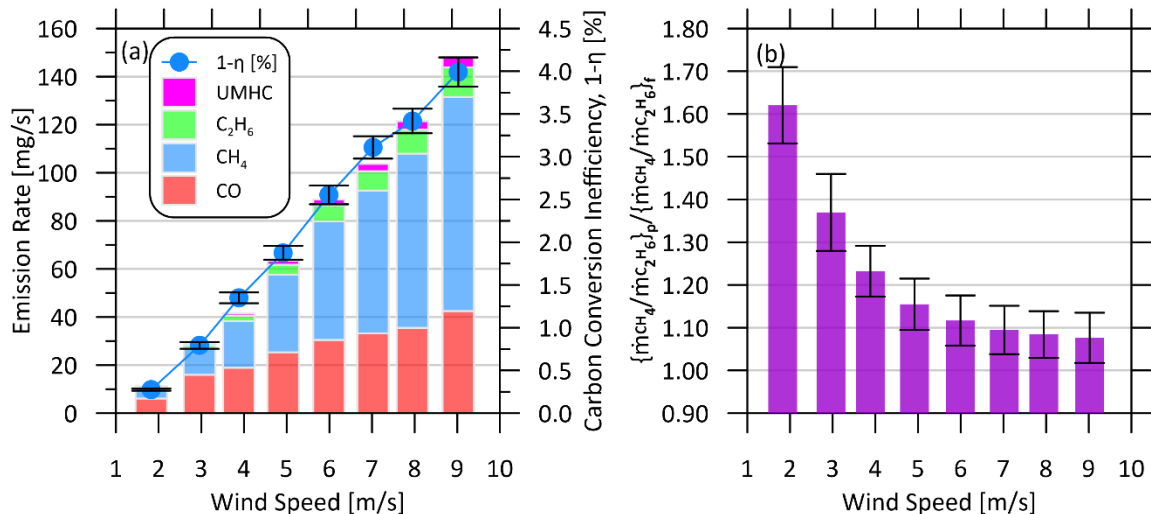


Figure 4.5: (a) Sample measured carbon conversion efficiency and species emission rate data, and (b) ratio of CH_4 to C_2H_6 in the plume relative to the same ratio in the flare, for a 4-inch (102.26-mm) diameter pipe flare burning the M6 gas mixture at a nominal exit velocity of 0.5 m/s (flow rate of 246 SLPM) while subjected to various crosswind speeds.

4.7.3 Repeatability Tests

Repeated experiments were performed under a fixed set of conditions to evaluate the combined bias and precision uncertainties of the implemented experiment and methodology. These experiments were conducted with the smallest (1-inch diameter) flare at highly efficient conditions, resulting in small emissions and larger relative uncertainties, to estimate the upper bound of anticipated uncertainties in the current experimental setup. As summarized in Table 4.2, for a 1-inch flare burning a typical medium flare gas mixture (M6) with a nominal 2 m/s exit velocity in a crosswind speed of 2 m/s, the carbon conversion inefficiency are calculable within a total relative uncertainty of 0.06% (combining bias and precision uncertainties in quadrature), and methane emission rates are calculable within <9% relative uncertainty. This demonstrates the robustness of the methodology in accurately quantifying flare performance parameters. The bias errors represent 95% coverage of the results of the Monte Carlo error propagation analysis, while the precision errors represent the 95% confidence interval of the repeated test results. The total uncertainty is obtained by combining these in quadrature.

Table 4.2: Repeatability tests for a 1-inch (26.6-mm) diameter pipe flare burning the M6 flare gas mixture at a nominal exit velocity of 2 m/s (flow rate of 67 SLPM) at a crosswind of 2 m/s.

Test Number	Carbon Conversion Efficiency, η [%]	Yield CH ₄ [mg/s]	Yield CO ₂ [mg/s]	Yield CO [mg/s]	Yield C ₂ H ₆ [mg/s]
1	99.37	3.20	2521.49	2.95	0.34
2	99.19	4.22	2517.79	3.55	0.28
3	99.32	3.49	2521.11	3.11	0.42
4	99.40	3.10	2522.87	2.74	0.32
5	99.45	2.78	2524.21	2.66	0.26
6	99.48	2.63	2525.11	2.52	0.23
Average	99.37	3.24	2522.10	2.92	0.31
Average Bias Error (95% coverage)	0.11	0.57	2.61	0.37	0.07
Precision Error (95% coverage)	0.03	0.245	1.118	0.160	0.029
Total Uncertainty (95% Confidence Interval)	0.05	0.15	3.93	0.24	0.04
Relative Total Uncertainty (95% Confidence Interval, %)	0.06%	8.86%	0.16%	8.08%	13.82%

4.8 Conclusions

A methodology for accurately and repeatably determining the carbon conversion efficiency and species emission rates of a flare burning in a closed-loop wind tunnel has been derived and demonstrated. Building on the work of Bourguignon et al. (Bourguignon et al. 1999) solving an unsteady mass balance to relate measured accumulation rates in a closed-loop wind tunnel to emission rates, the present work corrects a key error in this earlier derivation while extending this approach to include calculation of species emission rates and detailed uncertainty analysis. The revised approach can be applied to both continuously measured and batch-sampled species and is generalized to allow use with a range of hydrocarbon sampling equipment. The methodology was tested using Monte Carlo simulations on noise-distorted synthetic data and subsequently demonstrated in full-scale experiments in the Western University closed-loop Boundary Layer Wind Tunnel Laboratory. Comparison of measured ratios of CH₄ to C₂H₆ in the plume and in the flare gas suggest that emissions tend to be dominated by stripping of unburned fuel, allowing for a simplifying assumption in cases where not all emitted hydrocarbons are measured. Overall, the derived methodology is capable of measuring flare carbon conversion efficiency within $\lesssim 1\%$ absolute uncertainty, that decreases as flare efficiency increases. Methane emission rates are shown to be quantifiable within $\lesssim 10\%$ uncertainty, which is dominated by the uncertainty of the employed gas analyzers. The successful development and validation of a robust methodology to quantify flare emissions is a critical step in enabling quantitative experiments to support better control and regulation of flare emissions globally.

Chapter 5 Results

This chapter presents carbon conversion efficiency data for 1 to 4-inch diameter pipe flares subjected to crossflowing, turbulent wind. Experiments were conducted at the BLWTL following the methodology presented in Chapter 4. Data are generally plotted in terms of the carbon conversion inefficiency ($1-\eta$ [%]), where:

$$\eta = \frac{\text{moles of carbon in produced } CO_2}{\text{moles of carbon in hydrocarbon fuel stream}} \quad 5.1$$

The major parameters of interest to be investigated were crosswind speed, flare diameter, flare gas exit velocity, and flare gas composition, where the latter considered various fractions of C₁-C₄ hydrocarbons, CO₂, and N₂. These mixtures (summarized in Table 3.2) were chosen to be representative of the high-methane content natural-gas mixtures commonly flared in the upstream oil and gas industry. Results are first presented in a manner that attempts to isolate the effects of each major parameter on the measured flare inefficiency.

5.1 Efficiency as a Function of Crosswind Speed

Figure 5.1a shows measured inefficiencies for a 4-inch diameter flare burning flare gas M6 at an exit velocity of 1 m/s while subjected to turbulent crosswinds of 2–9 m/s. This may be considered a nominal reference case for a full-scale pipe flare at an upstream oil or gas production site. The results demonstrate a monotonic relationship with higher inefficiencies (i.e., higher emissions of non-CO₂ species and decreased carbon conversion efficiency) at higher crosswind speeds. Notably, for this case, the inefficiencies exceed 2% at crosswind speeds ≥ 6 m/s, which corresponds to flare efficiencies falling below the nominal 98% threshold commonly assumed in pollutant inventories.

Figure 5.1b plots the distribution of carbon mass from inefficient burning (i.e., mass of carbon in products other than CO₂) among CH₄, C₂H₆, CO, and UMHC (unmeasured hydrocarbons). The small contribution from UMHC was calculated via the fuel stripping assumption detailed in Chapter 4, Section 2.4.1. At crosswind speeds less than ~ 4 m/s, inefficiency is predominantly a result of emissions of CH₄ and CO with approximately 60% of the carbon mass from inefficient combustion emitted as CH₄. However, as crosswind speeds increase, emission rates of measured hydrocarbons (CH₄ and C₂H₆) continuously increase, whereas CO emissions rise more slowly. This

is illustrated in Figure 5.1c, where the ratio of emitted carbon mass in CH₄ vs. CO has a minimum of one at 3 m/s and rises sharply to two as crosswind increases.

Also shown on Figure 5.1c is the as the measured ratio of CH₄/C₂H₆ in the products normalized by the same ratio in the raw fuel, i.e., $\{\dot{m}_{CH_4}/\dot{m}_{C_2H_6}\}_p/\{\dot{m}_{CH_4}/\dot{m}_{C_2H_6}\}_f$. As crosswind speeds increase, this normalized ratio approaches unity, implying that inefficiencies at higher wind speeds are driven by stripping of unburned fuel consistent with the results of Johnson et al. (2001). Although incomplete combustion emissions are still dominated by methane at lower wind speeds, the increased fraction of CO and decreased fraction of C₂H₆ (relative to that in the raw fuel), suggest that other mechanisms in addition to fuel stripping may be occurring. Nevertheless, Figure 5.1 suggests that when inefficiencies are high and incomplete combustion emissions are comparatively large, stripping of unburned fuel is the dominant cause.

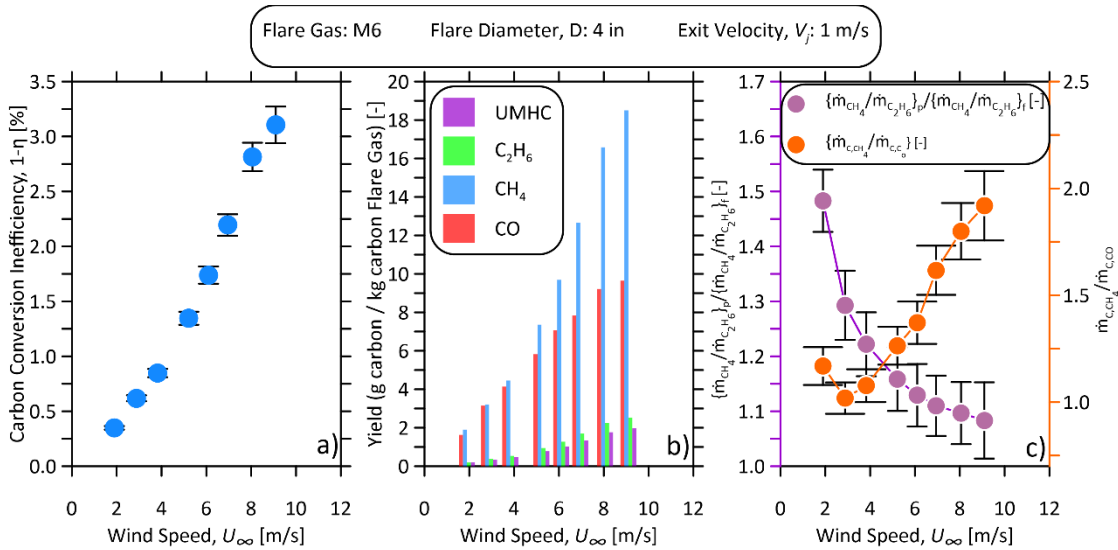


Figure 5.1: a) Inefficiency, b) species emission rates and c) ratio of CH₄/C₂H₆ in the plume to flare gas for a 4-inch flare burning M6 with an exit velocity of 1 m/s, subject to crosswind speeds of 2 to 9 m/s

5.2 Effects of Flare Gas Exit Velocity

The isolated effects of flare gas exit velocity, V_j , on flare inefficiency are plotted in Figure 5.2 for (a) 4-inch and (b) 3-inch diameter flares burning the M6 mixture at exit velocities of 0.5, 1, and 2 m/s. Simple, empirical power-law regressions of inefficiency data are shown to help visualize the trends of flare inefficiency versus exit velocity. Although there is little difference among the cases for wind speeds below ~4 m/s (where inefficiencies are all below ~2%), increased flare gas exit velocity leads to a slower increase in inefficiency as crosswind increases. The effect of exit

velocity is also non-linear. Specifically, inefficiencies are larger for 0.5 m/s exit velocities than for 1 m/s exit velocities but similar between 1 and 2 m/s velocities for each diameter. Moreover, for both the 3" and 4" diameter cases, the curves with wind speed become more non-linear as exit velocity is reduced. At a crosswind of 5 m/s, the empirical fits suggest that inefficiency increases by 13.5% (from 1.4% to 1.6%) for the 4" flare, and by 20% (from 1.6 to 2.0%) for the 3" flare as the exit velocity is reduced from 2 m/s to 0.5 m/s. At a crosswind of 9 m/s, the effects of exit velocity are stronger, with inefficiency increasing by 44% (from 2.5% to 4.5%) for the 4" flare, and by 35% (from 3.1% to 4.8%) for the 3" flare as the exit velocity is reduced from 2 m/s to 0.5 m/s.

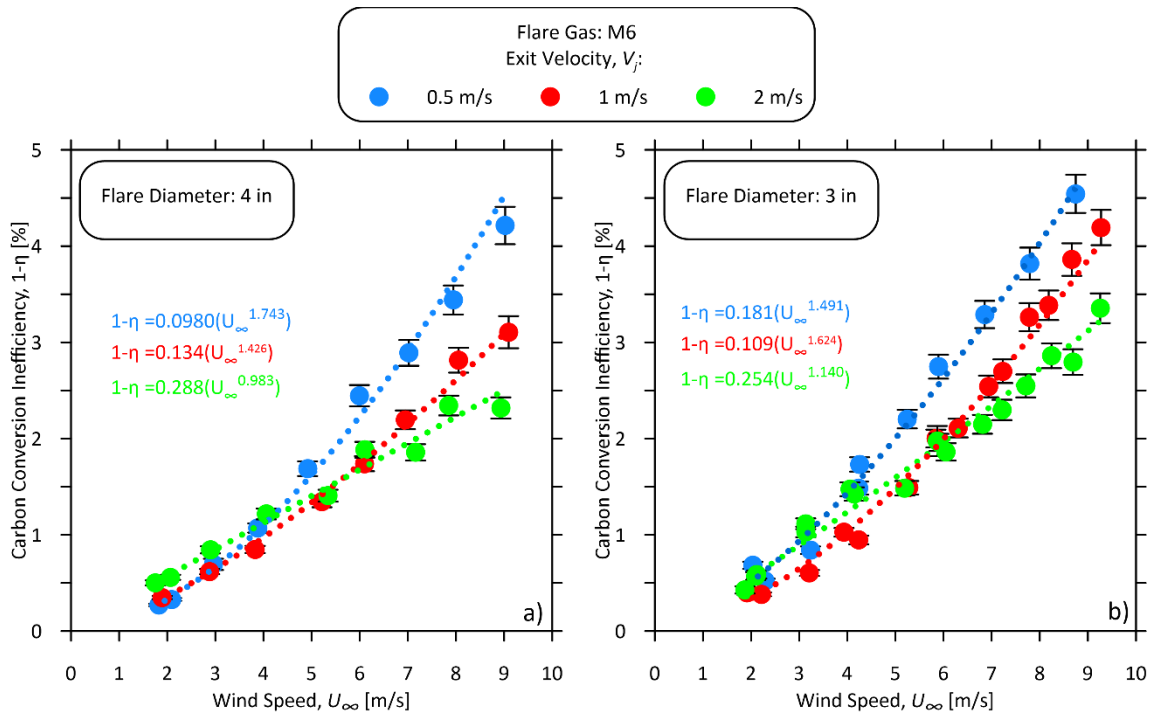


Figure 5.2: Inefficiency curves for a (a) 4-inch and (b) 3-inch diameter flare burning M6 at exit velocities of 0.5 m/s, 1 m/s and 2 m/s.

5.3 Effects of Flare Diameter

As introduced previously, burner diameters of 1 to 4" were used in these experiments, which partially overlaps the ~3–12 inch diameters of full scale flares commonly found at upstream oil and gas production sites in Canada and internationally (e.g., Johnson and Coderre 2012). Figure 5.3 plots inefficiencies of 1–4-inch flares burning flare gas M6 at exit velocities between 0.5 and 2 m/s.

The influence of flare diameter on flare inefficiency appears to be closely coupled with the effects of flare gas exit velocity. While there is little difference between the 3” and 4” diameter flares in all cases of Figure 5.3, inefficiencies increase as flare diameter is reduced to 1”. This effect is also much stronger as the flare gas exit velocity is reduced. For the smallest 1-inch diameter flare, the increase in inefficiency with increased crosswind is also notably non-linear. However, across all exit velocities, the trend of inefficiency vs. crosswind approaches a linear relationship as the flare diameter is increased to 4 inches.

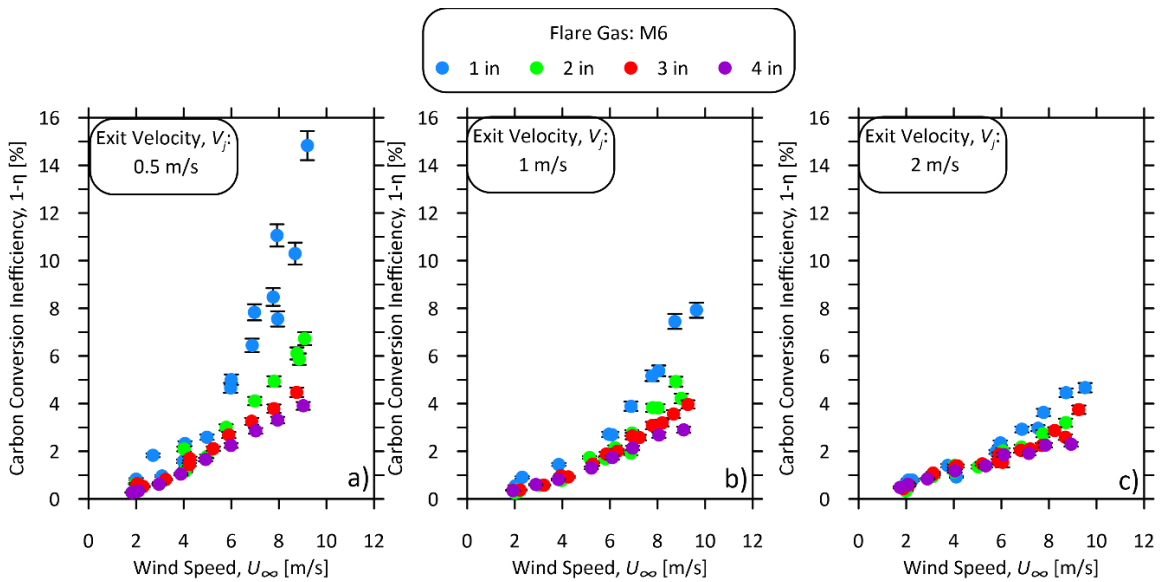


Figure 5.3: Inefficiency curves for flares with diameters of 1-4 inches burning M6 at an exit velocity of a) 0.5 m/s, b) 1 m/s and c) 2 m/s, at crosswind speeds between 2 and 9 m/s.

For the 1-inch diameter flare with $V_j = 0.5$ m/s (Figure 5.3a), the inefficiency increases from 0.5% to 14.8% (a relative increase in incomplete combustion emissions of 28%) as the crosswind is increased from 2 to 9 m/s. With the 4-inch diameter flare at the same $V_j = 0.5$ m/s, the change in inefficiency is much less dramatic, increasing from 0.26% to 4.2% (a 14.5% relative increase in emissions). However, at an exit velocity of $V_j = 2$ m/s (Figure 5.3c), the influence of flare diameter is much less apparent and the trends for the 2–4 inch flares mostly overlap. In summary, the results thus far suggest that both flare gas exit velocity and flare diameter are important parameters in determining the flare inefficiency, but their effects are likely interrelated as will be further explored in Chapter 6.

5.4 Influence of Flare Gas Compositions on Inefficiency

5.4.1 Effects of Varying Hydrocarbon-Dominated Flare Gas Mixtures

Results presented in Sections 5.1–5.3 considered flares with a fixed gas composition (M6). Although the majority of flare gases in the upstream oil and gas industry are expected to be methane-dominated based on the analysis of Johnson and Coderre (2012) for Western Canada and Conrad and Johnson (2019) for selected regions internationally, compositions at individual flare sites can vary significantly. Table 5.1 presents the species mole fractions and mixture properties for three flare gas compositions used extensively in this thesis. These light (L6), medium (M6), and heavy (H6) six component mixtures (C1–C4 alkanes plus CO₂ and N₂) were chosen to represent the 2.5th, 50th, and 97.5th percentile mixtures (based on heating value) of flared gases found in western Canada (Tyner and Johnson 2020; Johnson and Coderre 2012).

Table 5.1: Properties of three flare gases representative of the 2.5th, 50th, and 97.5th percentile heating values of flared gases found in the upstream oil and gas industry in Western Canada. Properties are given at 15°C, 101.325 kPa

Mixture Designation	L6	M6	H6
CH ₄ [%]	93.31	86.03	75.16
C ₂ H ₆ [%]	0.32	6.81	11.44
C ₃ H ₈ [%]	0.09	2.35	6.02
C ₄ H ₁₀ [%]	0.27	1.99	4.48
N ₂ [%]	1.38	1.61	1.69
CO ₂ [%]	4.64	1.21	1.21
MW [kg/kmol]	17.69	19.03	21.76
Density [kg/m ³]	0.7480	0.8047	0.9203
Stoichiometric Air to Fuel (AF) ratio [molar]	9.04	10.50	11.88
Lower heating value, LHV [MJ/m ³]	32.24	37.58	42.66
Higher heating value, HHV [MJ/m ³]	35.76	41.53	46.96

Figure 5.4 compares the carbon conversion inefficiencies for a 4-inch flare burning the L6, M6, or H6 mixtures at exit velocities of 0.5–2 m/s. There is a clear trend in which the lighter fuels have larger inefficiencies and appear to be more sensitive to crosswind. The differences are somewhat surprising given the similarities of the fuel compositions (methane content within 75-93%, lower heating value within 32.24-42.66 MJ/m³) and suggest flare gas composition is a critically sensitive parameter in determining flare emissions. For example, at an exit velocity of 0.5 m/s and crosswind speed of 9 m/s, the flare inefficiency of 5.45% when burning L6 represents a 65% relative increase in incomplete combustion emissions over the same flare burning H6 which results in an inefficiency of 3.3%. Over the range of tested wind speeds and flare gas exit

velocities, inefficiencies with the lighter L6 mixture are up to 60-90% higher than with the H6 mixture, implying that incomplete combustion emissions may approximately double with relatively small differences in fuel composition.

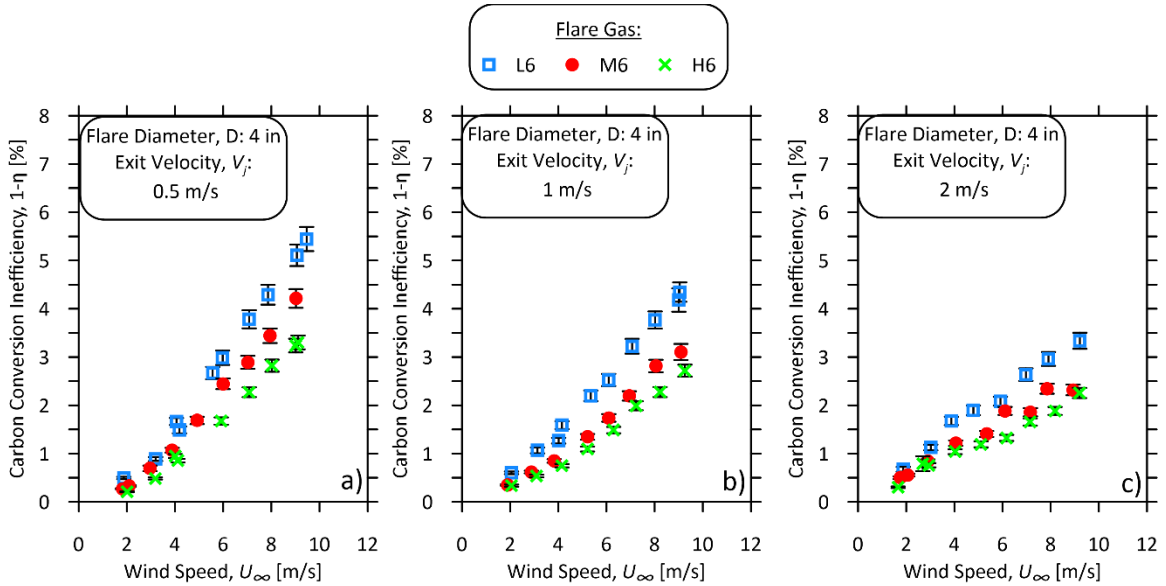


Figure 5.4: Inefficiency curves for a 4-inch flare with an exit velocity of a) 0.5 m/s, b) 1 m/s and c) 2 m/s burning 3 fuels: L6, M6 and H6, at crosswind speeds of 2 to 9 m/s.

To investigate the influence of fuel composition on smaller diameter flares, Figure 5.5 plots inefficiency curves for the L6, M6, and H6 mixtures for 1-, 2- and 3-inch diameter flares (Figure 5.5a–c), each at an exit velocity of 0.5 m/s. The trend of higher inefficiency with lighter fuels is consistent across all flare diameters. However, the smallest flare is again the most sensitive, and shows the most non-linear trends with increasing crosswind. It is possible that the 1-inch diameter flare approaches a scaling limit of the experiment, which will be further considered in Chapter 6.

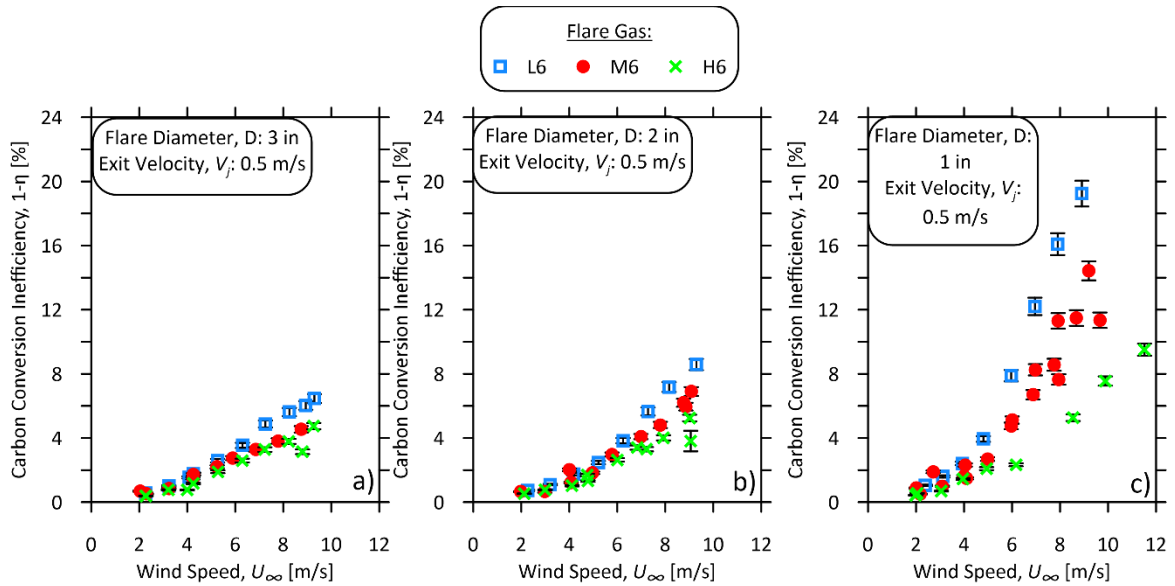


Figure 5.5: Inefficiency curves for a) 3-inch, b) 2-inch and c) 1 inch flare with an exit velocity of 0.5 m/s burning the L6, M6, or H6 flare gas mixtures

5.4.2 Effects of Added Inert Diluents to the Flare Gas

In certain situations in the upstream oil and gas sector, e.g., flares associated with gas treatment processes, flare gas may contain a large fraction of inert species, most commonly CO_2 . Previous work by Johnson and Kostiuik (2002) using natural gas and propane-based fuels diluted with CO_2 and N_2 has demonstrated that flare efficiency can be strongly and adversely affected by increased inert content in the fuel. To consider the implications of high inert content and to further elucidate the impacts of varying flare gas composition, experiments were completed using a 2-inch diameter flare burning M6 blended with up to 70% CO_2 at an exit velocity of 2 m/s.

Figure 5.6a shows that increasing CO_2 dilution in the fuel induces a strong non-linear increase in flare inefficiency. As the CO_2 fraction is increased, the impacts of increased crosswinds are exacerbated, resulting in a non-linear trend. Flares burning M6 with 70% CO_2 at crosswinds greater than 5 m/s were not stable, and the flame would consistently blow out prior to successful completion of an experiment. Even at low crosswind speeds, increased CO_2 content notably increased the inefficiency of the flame. For CO_2 fractions of 40, 60, and 70%, extrapolation of the curves to zero crosswind suggests minimum flare inefficiencies of 2.9%, 8.2%, and 17.4%, which corresponds to efficiencies well-below the nominal 98% standard.

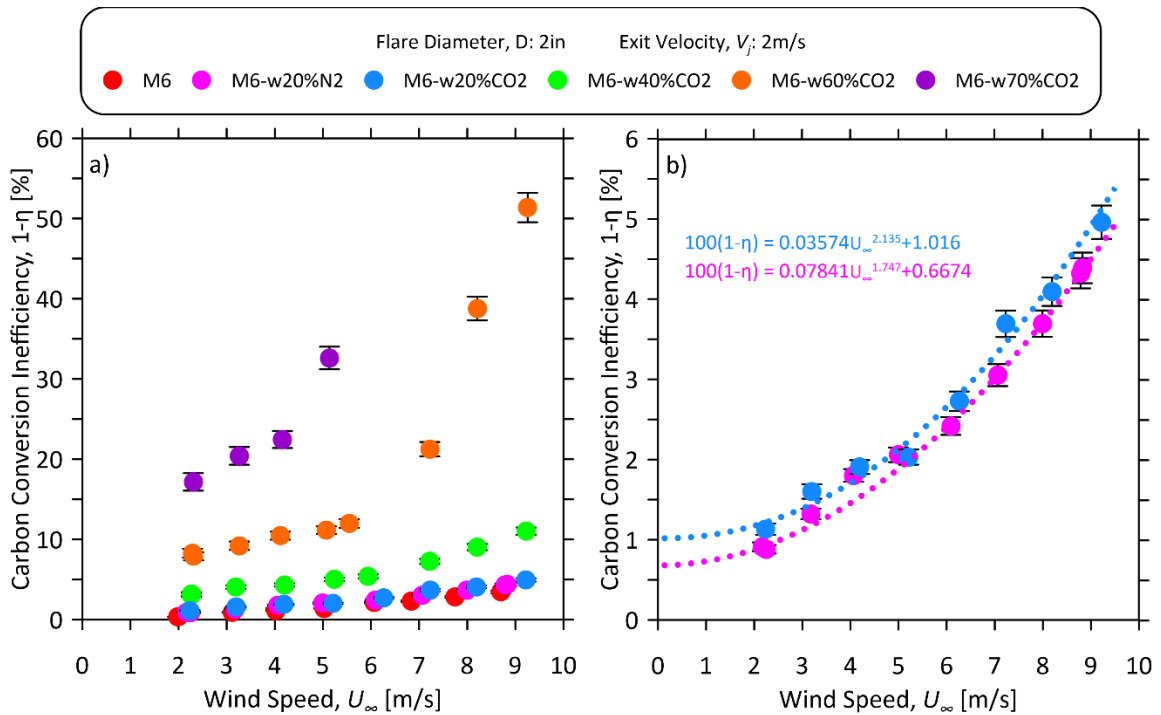


Figure 5.6: Inefficiency curves for a 2-inch flare burning M6 with various quantities of CO₂ diluents with an exit velocity of 2 m/s at crosswind speeds between 2 and 9 m/s.

Figure 5.6b compares inefficiency curves for the same 2-inch flare burning M6 diluted with either 20% CO₂ or N₂ at an exit velocity of 2 m/s. Swapping CO₂ for N₂ decreases the flare gas molecular weight and hence the density by 12.6% without changing the heating value. Similarly, the specific heat capacity of the stoichiometric products of combustion would be 9.8% higher when swapping CO₂ for N₂, implying a slightly lower adiabatic flame temperature of 2188.8 K vs 2208.3 K. Comparing empirical fits of the inefficiency curves, inefficiencies of M6 diluted with CO₂ are 26% more inefficient than when diluted with N₂ as a crosswind of 2 m/s and 14% more inefficient at a crosswind of 9 m/s. Previous experiments by Johnson and Kostiuik (2002) showed similar differences between CO₂- and N₂-diluted fuel mixtures, with greater differences at higher inert fractions. Ideally, the present experiments comparing the effects of CO₂ vs. N₂ (or other inert) diluents could be repeated at inert fractions greater than at 20%. However, this was not possible give the limits of the current fuel handling system in supplying N₂ (which unlike CO₂ is not stored as a liquid within the compressed gas cylinders). However, it is clear that fuel diluent has strong impact on inefficiencies and their future study will be crucial to develop a low heating-value model for flare inefficiency.

5.5 Comparison to Previous Correlations

5.5.1 Correlation of Exit Velocity: Richardson Number

Previous work by Johnson and Kostiuik (2000) on flares in low-turbulence crosswinds similarly found that inefficiencies of natural gas and propane flames strongly depended on both crosswind speed and flare gas exit velocity. They proposed a simplified velocity ratio originally based on the Richardson number as a parameter to correlate these effects such that:

$$\eta \propto \frac{U_{\infty}}{V_j^{1/3}} \quad 5.2$$

Figure 5.7 plots the present inefficiency data for a 2-inch flare burning M6 at exit velocities between 0.5 and 2m/s versus wind speed and versus the $U_{\infty}/V_j^{1/3}$ scaling parameter from Johnson and Kostiuik (2000). Figure 5.7b as well as similar plots for other fuels shown in Appendix B suggest the $U_{\infty}/V_j^{1/3}$ parameter remains valid for the turbulent crosswinds considered in the present work.

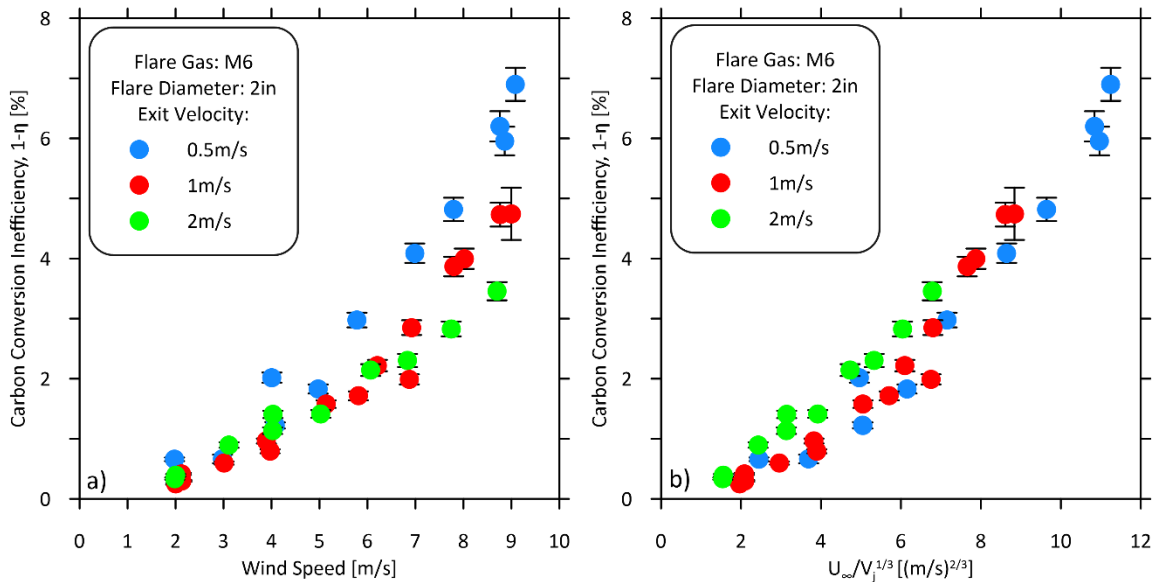


Figure 5.7: Inefficiency curves for a 2-inch flare burning Flare Gas M6 at exit velocities between 0.5 and 2m/s, plotted as a function of a) crosswind speeds between 2 and 9m/s and b) the $U_{\infty}/V_j^{1/3}$ parameter from Johnson and Kostiuik (2000).

5.5.2 Correlation of Diameter

There have been mixed conclusions regarding the importance of flare diameter in the literature, including on the limits of scaling to smaller laboratory-sized burners. Pohl and Soelberg (1985)

compared flame stability for different sized burners (1/16-inch nozzle and 3-inch nozzles). They concluded that flare burners less than 1.5 inches were not similar to flames from larger nozzles. Pohl et al. (1986) determined that flare efficiency was unaffected by flare diameter for diameters greater than 3 inches. Notably however, neither of these works considered the effects of crosswind.

Kostiuk et al. (2000) reported experiments on 10.8-33.3 mm (0.5-1/5") diameter propane-fueled flares in low-turbulence crossflow and proposed an empirical scaling relationship with the following form:

$$1 - \eta \propto \frac{U_{\infty}}{(gV_j)^{1/3}D^n} \quad 5.3$$

where g is the gravitational constant. They found their data for propane-fueled flares were well correlated with $n=1/3$, which conveniently results in a non-dimensional parameter.

However, following further experiments with both natural gas and propane mixtures, Johnson and Kostiuk (2002) noted that while natural gas was "reasonably well correlated with this non-dimensional parameter", employing Eq. 5.3 with coefficient $n=1/2$ provided a slightly improved empirical correlation. Nevertheless, they ultimately suggested $n=1/3$ for use because it resulted in a dimensionless correlation. Figure 5.8a-c plots inefficiencies of 1–4" diameter flares burning the L6, M6, and H6 mixtures against the non-dimensional parameter introduced in Eq. 5.3 with $n=1/3$. Empirical power-law regressions were fitted to experimental data using non-linear least squares analysis. The corresponding panels Figure 5.8 d-f show histograms of the empirical model errors when predicting the individual experimental data points. The percentage error (E%) in predicted carbon conversion inefficiency is calculated as:

$$E = \frac{(1 - \eta)_{theoretical} - (1 - \eta)_{actual}}{(1 - \eta)_{actual}} \times 100\% \quad 5.4$$

The results of Figure 5.8 suggest that Eq. 5.3 with coefficient $n=1/3$ provides approximate scaling of inefficiencies over the full range of 1–4" diameter flares, with 95% confidence intervals of –33% and 69% (L6), –38% and 98% (M6) and –50% and 82% (H6). However, the 1-inch diameter burners are slightly uncorrelated with the larger burner diameters, which is particularly noticeable for the L6 and H6 fuels. The model errors are notably reduced when including data for 2–4"

diameter flares alone, netting correlations within -31% and 66% (L6), -44% and 88% (M6) and -49% and 53% (H6).

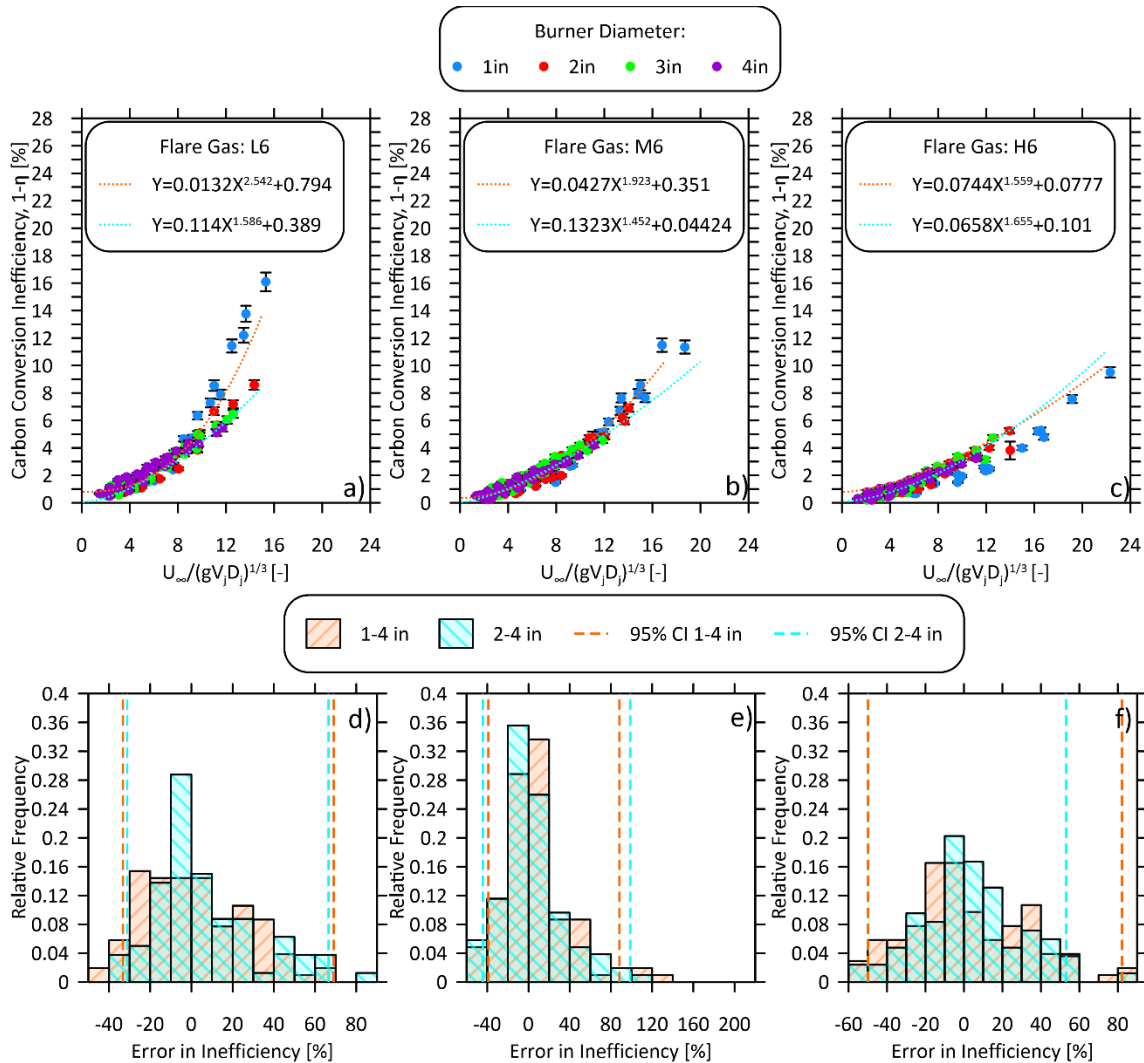


Figure 5.8: 1-4 inch burners burning Flare Gas a) L6, b) M6 and c) H6, plotted against $\frac{U_\infty}{(gV_j)^{1/3}D_j^n}$ developed by Kostiuk et al. (2000) where $n = 1/3$ (Johnson and Kostiuk 2002b). Figures d), e) and f) present histograms of empirical fit errors in predicting inefficiency of individual data points.

Recognizing the empirical nature of the exponent n in Eq. 5.3 from Johnson and Kostiuk (2002), Figure 5.9 presents empirical fits where the value of n was optimized to minimize the summed square of residuals for each data set (i.e., L6, M6 and H6 including 1–4” or 2–4” flare diameters). When considering 1–4” burner diameters, coefficients of 1/3.33, 1/2.95 and 1/11.9 were determined to minimize squared sum of errors. Considering only 2–4” flare diameters, the prediction errors were much lower and the optimized coefficients were 1/3.03 (L6), 1/2.96 (M6)

and 1/5.2 (H6). This suggests that the scaling relationship with diameter is somehow coupled with fuel chemistry. The majority of fitted coefficients deviate from the previously determined coefficient $n = 3$, which non-dimensionalizes Eq. 5.3. Given the significant variance in coefficient relative to small changes in methane-based flare gas compositions, which is exacerbated by 1-inch diameter burners, this suggests additional chemical mechanisms play an important role in flare efficiency that are not properly comprehensible using Eq. 5.3 alone.

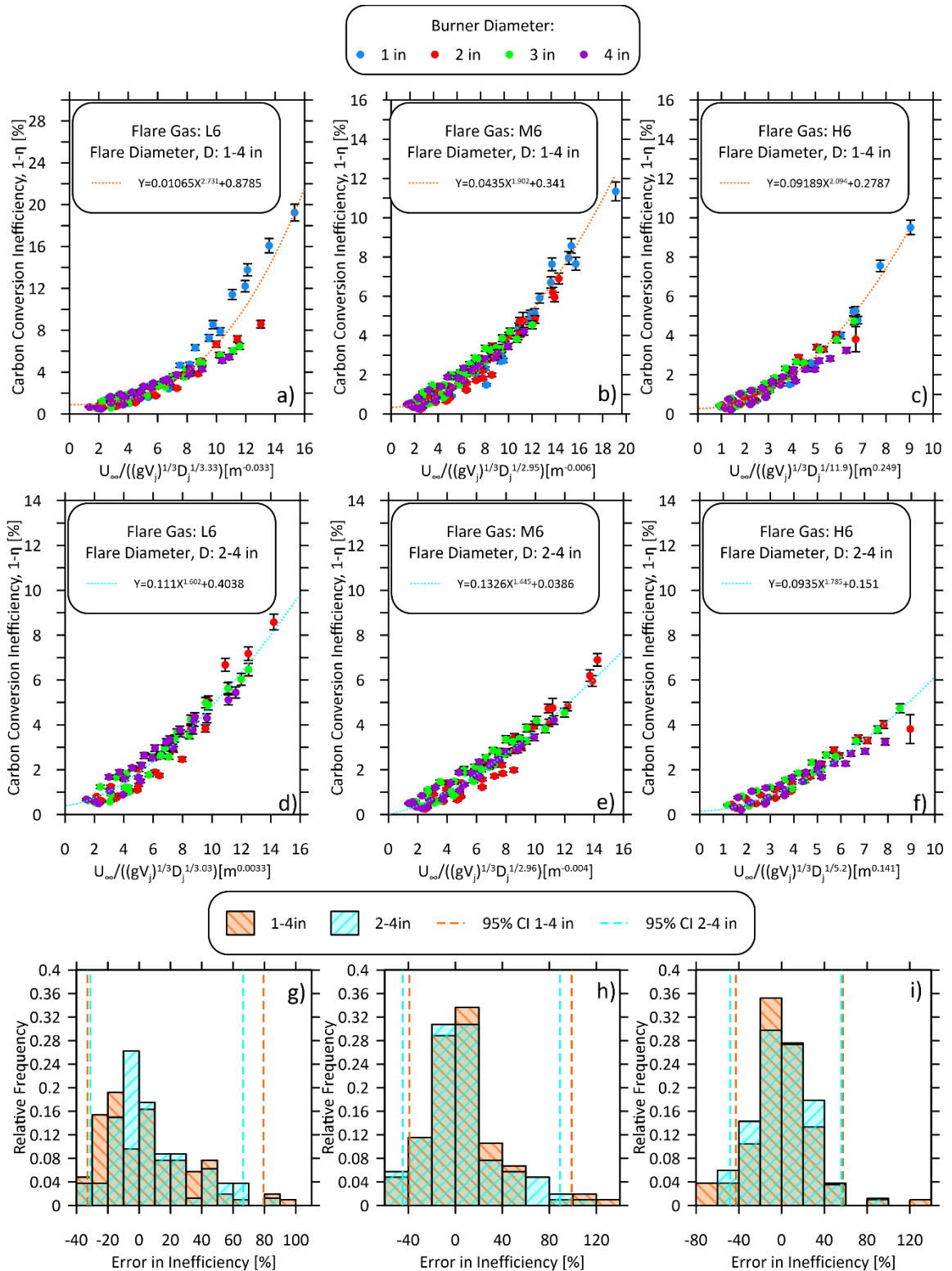


Figure 5.9: Efficiency of a)-c) 1-4 inch and d)-f) 2-4 inch burners, burning flare gas (L6, M6 and H6), plotted against $\frac{U_{\infty}}{(gV_j)^{1/3} D_j^n}$ developed by Kostiuik et al. (2000) where n has been optimized to minimize the summed square of residuals. Figures g), h) and i) present histograms of the errors in the empirical fit errors when predicting individual data points.

5.5.3 Correlation of Flare Gas Composition

Johnson and Kostiuk (2002) also suggested a parametric model to estimate flare efficiency for multiple flare diameters and fuel compositions:

$$1 - \eta = A \frac{\exp \left(B \frac{U_{\infty}}{(gV_j D)^{1/3}} \right)}{LHV_m^3} \quad 5.5$$

This practically-motivated model used heating value as an easily obtainable parameter to represent flare gas compositions, to scale data in combination with the empirical relationship of Kostiuk et al. (2000). Separate empirical coefficients A and B were used for either natural gas or propane-based fuels. Their attempts to incorporate heating value in the term show that while heating value may be a property that impacts flare efficiency, that the connection between inefficiency and different fuel compositions is not a simple-power law relationship that may be accurately described by a single model for all conditions. Johnson and Kostiuk (2002) acknowledged the fact that since different coefficients were needed for different fuels, that underlying mechanisms of flare inefficiency exist that were not captured in their analysis.

Figure 5.10 plots the heating value model developed by Johnson and Kostiuk (2002) using the coefficient proposed for natural-gas based flames overtop the current experimental data. Noting that Johnson and Kostiuk (2002) considered low-turbulence crosswind only in their model, it is evident that the present flare inefficiency data (encompassing both larger diameters and turbulent crosswinds) follow a different trend. Errors in predicting inefficiency using Johnson and Kostiuk (2002)'s model range from -80% to +197%, which are skewed towards underestimating inefficiency while tailing towards overestimation. It is evident that the exponential trend measured by Johnson and Kostiuk (2002) on 0.5- to 2-inch flare diameters is not present in current experimental data, which may partially explain these large overestimations as the value of the non-dimensional parameter on the x-axis increases. While heating value provides an approximation of emissions, it does not capture the underlying mechanism of flare inefficiency. This highlights the need of a model that will accurately predict low heating value fuels.

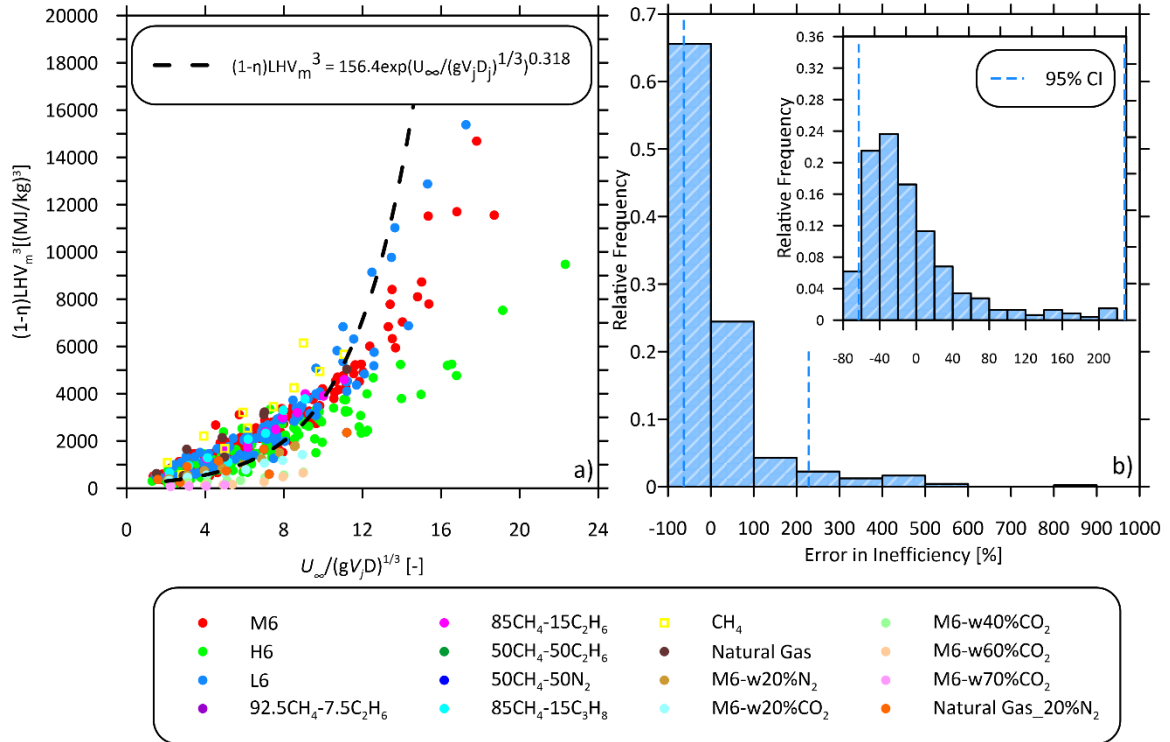


Figure 5.10: Comparing experimental data to the heating value model for natural gas flares developed by Johnson and Kostiuik (2002) and b) histograms of model error in predicting individual data points.

Goglek et al. (2012) also proposed a non-dimensional parameter called the Power Factor, PF, for correlating flare efficiency data:

$$PF = \left(\frac{\rho_\infty U_\infty^3 D^2}{\rho_j A_j V_j LHV_m} \right)^{1/3} \quad 5.6$$

However, with this parameter, the inclusion of the squared diameter in the numerator and the jet cross-sectional area in the denominator is redundant, while the density ratio between air and jet densities does not vary significantly for CH₄-dominant fuel compositions typical of the upstream oil and gas industry. This leaves the $\frac{U_\infty^3}{V_j}$ term, which is directly analogous to $U_\infty/V_j^{1/3}$ from Eq. 5.2 as proposed by (Johnson and Kostiuik 2000) who noted that this arrangement was “chosen to maintain the same general shape” of the presented inefficiency curves. Johnson and Kostiuik (2000) also noted that the velocity ratios were the dominant factor in their comparison of buoyant and momentum forces, while density differences were not significant given the small density differences between ambient and flare gases. Similarly, $PF \propto LHV_m^{-1/3}$ replicates the form proposed by Johnson and Kostiuik (2002) in identifying mass-based heating value as an important parameter in flare efficiency, while failing to extend the analysis any further.

Regardless, based on results from Gogolek and Hayden (2004) conducted at the CanmetENERGY Flare Test Facility and from (Howell 2004), Gogolek et al. (2012) deemed the inefficiency of flares greater than 3 inches were correlated by the following equation:

$$1 - \eta = 0.1 + \frac{100PF}{1 + \left(\frac{0.06}{PF}\right)^2} \quad 5.7$$

Gogolek et al. (2012) suggested that the power factor was also unable to correlate 1- and 2-inch burner diameters, which they deemed to be unrepresentative of larger-scale burner diameters. Figure 5.11a-b plots current, 1–4-inch burner diameters in terms in terms of the power factor, where the power factor consistently underpredicts inefficiencies between 64-97%. Even if only 3–4-inch burner diameters are considered (Figure 5.11c-d), inefficiencies are underpredicted by 58-90% such that it is evident the power factor unable to describe flare inefficiencies of current experimental data for 1–4-inch burner diameters.

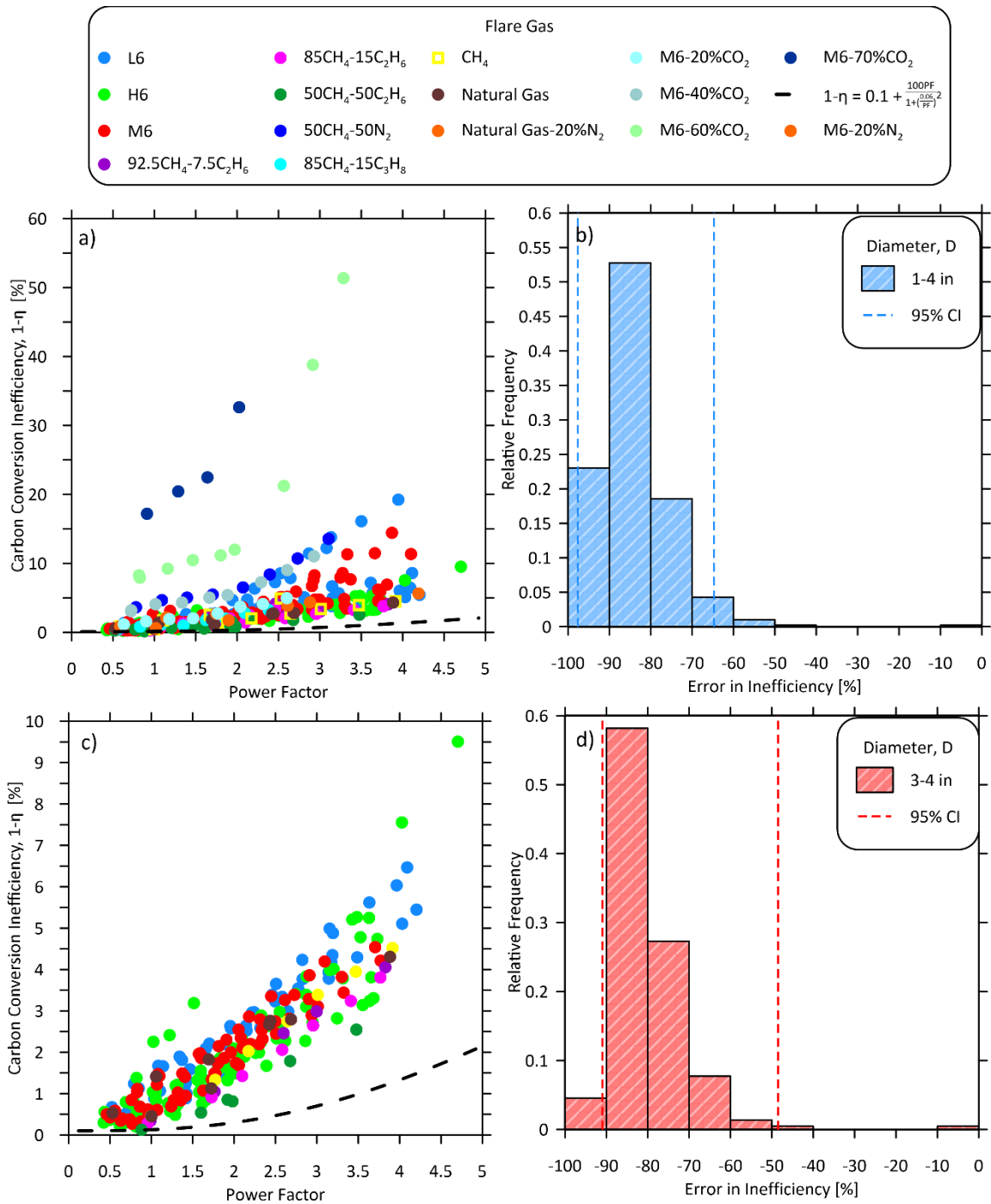


Figure 5.11: a) Comparing 1-4 inch experimental data to the Power Factor model from Gogolek et al. (2012) and b) error in predicted inefficiency, and c) comparing 3-4 inch experimental data to the Power Factor model from Gogolek et al. (2012) and d) error in predicted inefficiency using the Power Factor.

This chapter examined several important parameters affecting flare inefficiency, including flare gas exit velocity, burner diameter, and fuel composition. A previously developed velocity ratio of the flare gas to crosswind was shown to effectively correlate multiple exit velocities of a single

flare gas at a single burner diameter. A non-dimensional parameter based on the Richardson number was also shown to correlate a single flare gas for multiple exit velocities and burner diameters. However, various flare gases typical of the upstream oil and gas industry were shown to correlate with different exponents of the burner diameter, particularly at a burner diameter of 1 inch, which may represent a scaling limit in the current experiments. Furthermore, models correlating flare gas compositions using heating value were evaluated, which were shown to have difficulty in accurately predicting flare inefficiency, which presents a gap in knowledge which will be addressed in Chapter 6.

Chapter 6 Empirical Modelling

Chapter 5 presented experimental results for several flare gas compositions typical of the upstream oil and gas industry in Western Canada. Results suggest inefficiencies are affected by wind speed, flare gas exit velocity, burner diameter, and flare gas composition, where the latter has an especially strong impact on inefficiency. Previously developed models were evaluated using current experimental data. Although the models of (Johnson and Kostiuik 2002b) reasonably captured the influence of the first three parameters with the parameter $U_{\infty}/(gV_jD)^{1/3}$, no model was able to accurately predict inefficiencies of flares with differing flare gas compositions. This chapter attempts to understand flare performance in terms of operating conditions and chemical properties of the flare gas with the goal of developing a practical, empirical model that could be useful in predicting both flare inefficiency and methane emissions over a broader range of conditions.

6.1 Effects of Flare Gas Composition on Flare Inefficiency

The results presented in Chapter 5, Section 5.4 demonstrate that fuel composition has a critical role in determining flare inefficiency; however, the specific drivers of these effects are unknown. To further elucidate the role of flare gas composition on flare inefficiency, twelve different flare gas compositions were tested at comparable operating conditions. Figure 6.1 plots the associated inefficiency curves as a function of wind speed at two common conditions: a 4-inch burner with an exit velocity of 0.5 m/s (Figure 6.1a), and a 2-inch burner with an exit velocity of 2 m/s (Figure 6.1b). These two conditions span the range of the experimental data while having similar total gas flow rates of 246 SLPM ($V_j = 2$ m/s) for the 2-inch flare and 259 SLPM ($V_j = 0.5$ m/s) for the 4-inch flare. Table 6.1 lists key properties of these flare gases, approximately ordered by decreasing inefficiency as plotted in Figure 6.1.

Inefficiencies of 2-inch, 2 m/s exit velocity flares range from 0.26% to 1.13% at a wind speed of 2 m/s, and from 2% to 4.95% at a wind speed of 9 m/s. Inefficiencies of 4-inch, 0.5 m/s exit velocity flares range from 0.13% to 2.72% at a wind speed of 2 m/s, and from 2.54% to 5.62% at a wind speed of 9 m/s. There are no obvious simple trends between inefficiencies of various flare gases and the properties listed in Table 6.1.

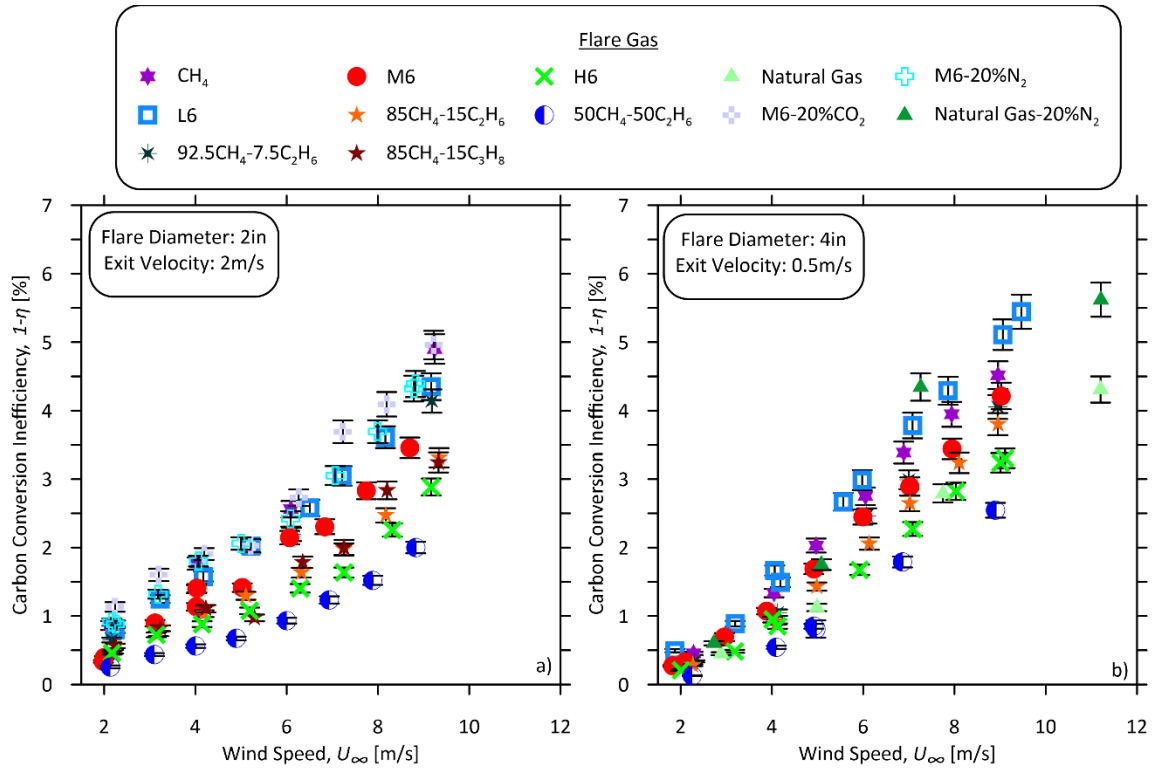


Figure 6.1: Inefficiency curves for twelve different flare gas compositions burning on a) a 2-inch flare with an exit velocity of 2 m/s flares and b) a 4-inch flare with an exit velocity of 0.5 m/s.

Table 6.1: Properties of gas mixtures in Figure 6.1. Properties are calculated at 15°C and 1 atm unless otherwise specified

Flare Gas	X_{CH_4} [-]	MW [kg/kmol]	Density [kg/m ³] (15°C, 1 atm)	Molar AF ratio [-]	Mass AF ratio [-]	HHV [MJ/kg]	LHV [MJ/kg]	Specific Heat Capacity [kJ/kgK] (25°C, 1 atm)	Tad [K] (15°C, 1 atm)	Dynam. Viscosity [N-s/m ²] (15°C, 1 atm)	S_i (15°C, 1 atm) [m/s]	C# [-]
Natural Gas_w20%N ₂	74.15	19.33	0.82	7.94	11.90	38.43	34.69	1.83	2203.6	1.18E-05	0.324	0.85
AB-M6_w20%CO ₂	69.67	23.78	1.01	8.50	10.36	33.44	30.26	1.63	2188.8	1.21E-05	0.290	0.93
AB-M6_w20%N ₂	69.67	20.79	0.88	8.50	11.85	38.25	34.62	1.79	2208.1	1.16E-05	0.314	0.93
CH ₄	100	16.04	0.68	9.52	17.19	55.51	50.03	2.23	2224.3	1.11E-05	0.359	1.00
NATURAL GAS	92.68	17.16	0.73	9.93	16.75	54.11	48.85	2.15	2228.2	1.06E-05	0.347	1.06
AB_L6	93.30	17.69	0.75	9.04	14.81	47.81	43.10	2.04	2214.0	1.15E-05	0.308	0.95
92.5CH ₄ -7.5C ₂ H ₆	92.5	17.09	0.72	10.06	17.04	55.04	49.70	2.17	2229.8	1.06E-05	0.363	1.08
AB_M6	86.03	19.03	0.80	10.50	15.99	51.60	46.70	2.05	2229.1	1.09E-05	0.334	1.15
85CH ₄ -15C ₂ H ₆	85.00	18.15	0.77	10.59	16.91	54.62	49.40	2.11	2227.7	1.04E-05	0.368	1.15
85CH ₄ -15C ₃ H ₈	85.00	20.25	0.86	11.66	16.68	53.82	48.82	2.05	2232.1	1.02E-05	0.396	1.30
AB_H6	75.2	21.76	0.92	11.88	15.82	51.03	46.35	1.97	2236.6	1.05E-05	0.348	1.34
50CH ₄ -50C ₂ H ₆	50.00	23.06	0.98	13.09	16.45	53.16	48.38	1.92	2241.5	9.72E-06	0.385	1.50

Figure 6.2 plots a reduced dataset of Figure 6.1, including only simple flare gas mixtures of CH_4 and C_2H_6 . Inefficiencies decrease with the addition of higher volume fractions of C_2H_6 , regardless of crosswind speed. Wind speed has a stronger adverse effect on inefficiency for flares with higher CH_4 content, which appears to be dampened by the introduction of more C_2H_6 . This may suggest that the addition of heavier hydrocarbons results in lower inefficiencies. For example, a flare burning CH_4 subject to a crosswind speed of 9 m/s results in an inefficiency of 4.5%, whereas the inefficiency of a 92.5% CH_4 and 7.5% C_2H_6 flare drops by $\sim 11\%$ (to 4%), an 85% CH_4 and 15% C_2H_6 flare drops by $\sim 16\%$ (to 3.8%), and a 50% CH_4 , 50% C_2H_6 flare drops by 45% (to 2.5%). Results for the 2-inch flare are similar with higher fractions of C_2H_6 resulting in lower inefficiencies. This suggests that the volume fraction of CH_4 plays an important role in inefficiency, where even slight additions of C_2H_6 have significant effects on the sensitivity to crosswinds.

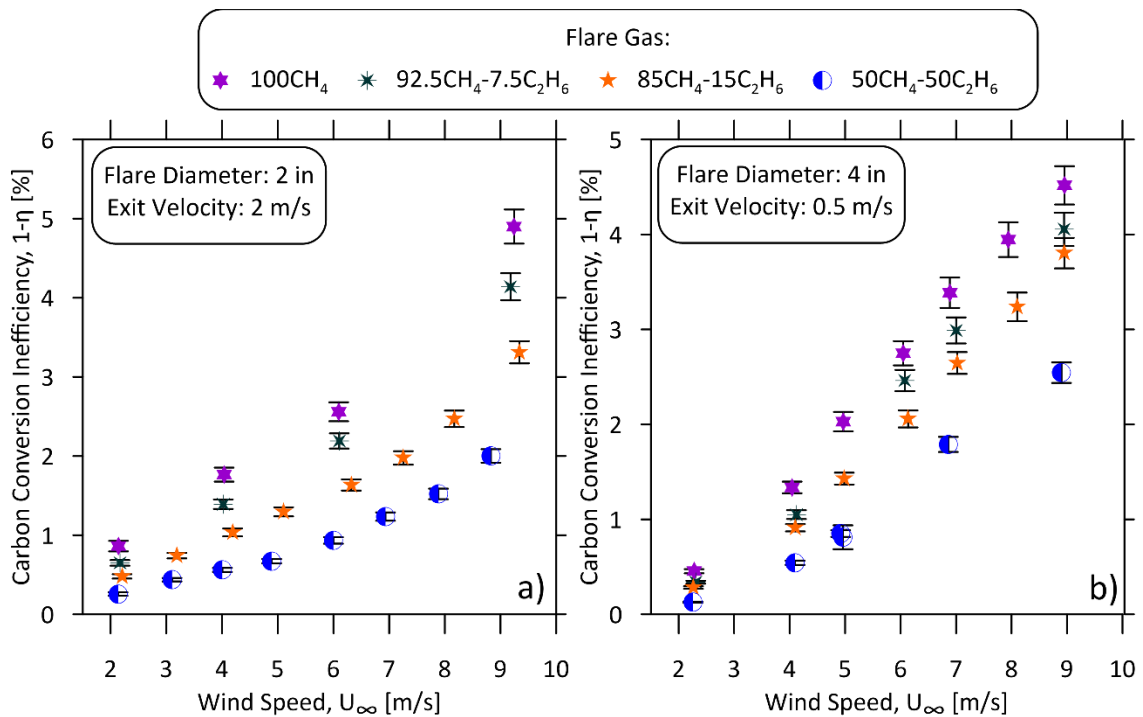


Figure 6.2: Inefficiency curves for flares burning various $\text{CH}_4/\text{C}_2\text{H}_6$ blends from a) 4-inch burners with an exit velocity of 0.5 m/s and b) 2-inch burners with an exit velocity of 2 m/s at crosswind speeds between 2 and 9 m/s.

Figure 6.3 compares 2-inch flares burning 85% CH_4 blended with either 15% C_2H_6 or C_3H_8 . By overlaying empirical power fits for visualization, it is evident that the inefficiency curves are practically identical, and that the individual error bars of both inefficiency curves overlap.

Referring again to Table 6.1, it is difficult to make any definite conclusions from this dataset alone, as all displayed properties vary between mixtures, while significant differences in inefficiencies are not obvious. While the natural progression would be to perform this comparison of heavier hydrocarbons at larger volume fractions than 15%, this was not possible due to available flow rates from MFCs, since Joule-Thomson cooling at higher flow rates restricted the available gas flow as the cylinder began to freeze. However, the available data in Figure 6.3 suggest that the amount of CH₄ in the flare gas is a stronger indicator of inefficiency than the specific form of the heavier hydrocarbons (i.e., C₂H₆ or C₃H₈).

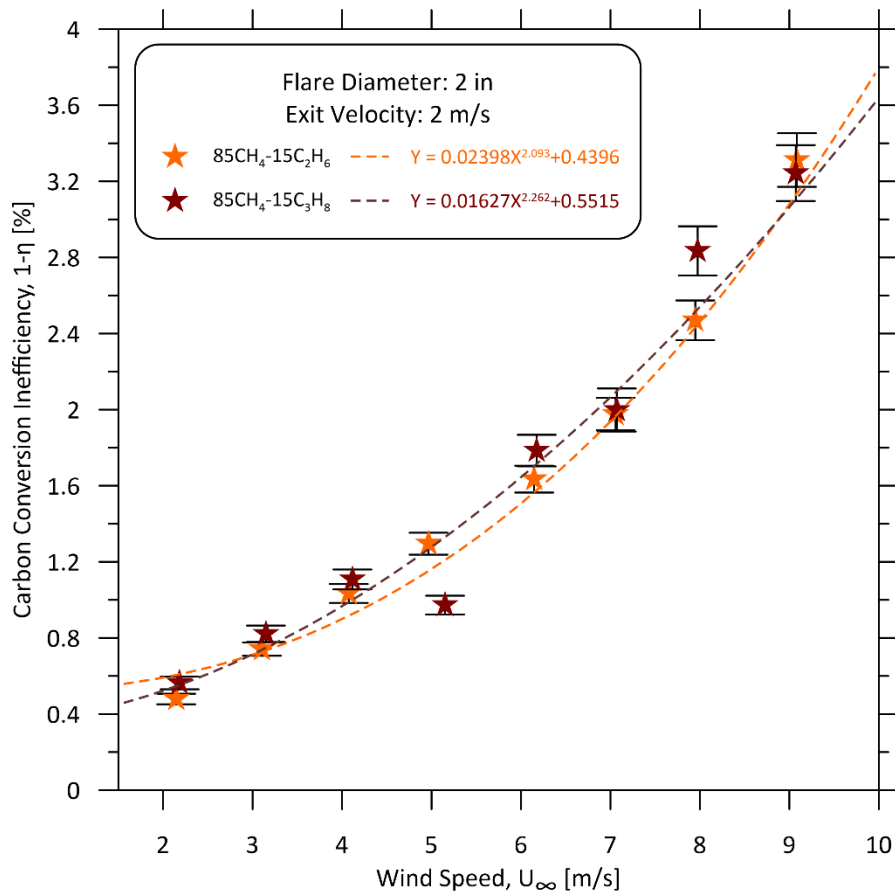


Figure 6.3: Inefficiency curves for a 2-inch flare burning various 85% CH₄ with either 15% C₂H₆ or C₃H₈ with an exit velocity of 2 m/s at crosswind speeds between 2 and 9 m/s.

Further insight into the effects of flare gas composition may be gleaned by comparing inefficiencies of various flare gas mixtures at a single wind speed, flare diameter, and exit velocity. Selecting data from Figure 6.1 for the 2-inch flare with a 2 m/s exit velocity in 4 m/s crosswind, Figure 6.4 plots inefficiencies for the different fuel mixtures as a function of flare gas properties

including a) molecular weight, b) mass stoichiometric air to fuel ratio $AF_{mass,stoic}$, c) laminar flame speed, d) adiabatic flame temperature (T_{ad}), e) mass lower heating value (LHV_{mass}), f) volumetric lower heating value (LHV_{vol}), mean carbon number ($C_{\#}$), and g) molar stoichiometric air to fuel ratio ($AF_{vol,stoic}$). Mean carbon number of the flare gas was calculated as:

$$C_{\#} = \frac{c_i X_{i,HC}}{\sum X_{i,HC}} \quad 6.1$$

where, c_i is the number of carbon atoms in the i^{th} hydrocarbon species and $X_{i,HC}$ is the mole fraction of that species in the hydrocarbons within the fuel mixture (i.e., inerts CO_2 and N_2 are excluded in the calculation). The reference stoichiometric laminar flame speed, S_L , of each mixture was simulated using Cantera 2.5.1. at temperature of 288.15K and pressure of 1 atmosphere (101325 Pa) (see Appendix F).

Figure 6.5a-c show that correlations are poor between flare inefficiency and either MW, $AF_{mass,stoic}$, S_L , or T_{ad} . Previous studies (Johnson and Kostiuik 2002a, Gogolek et al. 2012) have proposed that energy density, described by LHV_{mass} , may be used to correlate various flare gas compositions. However, Figure 6.5e,f show that although the volumetric heating value (LHV_{vol}) provides reasonable correlation, LHV_{mass} does not, especially above ~ 48 MJ/kg. Of the individual variables considered, LHV_{vol} , $C_{\#}$, and $AF_{vol,stoic}$ show the best correlation, with nearly identical trends for each. This is expected since $AF_{vol,stoic}$ and LHV_{vol} both scale with the mean carbon number for simple mixtures of alkane hydrocarbons. However, as shown in Figure E of Appendix E, if the range of flare gas mixtures is extended to include gases with $>20\%$ inert species by volume, then inefficiency is no longer simply correlated with $C_{\#}$ and results are best scaled with either $AF_{vol,stoic}$ or LHV_{vol} .

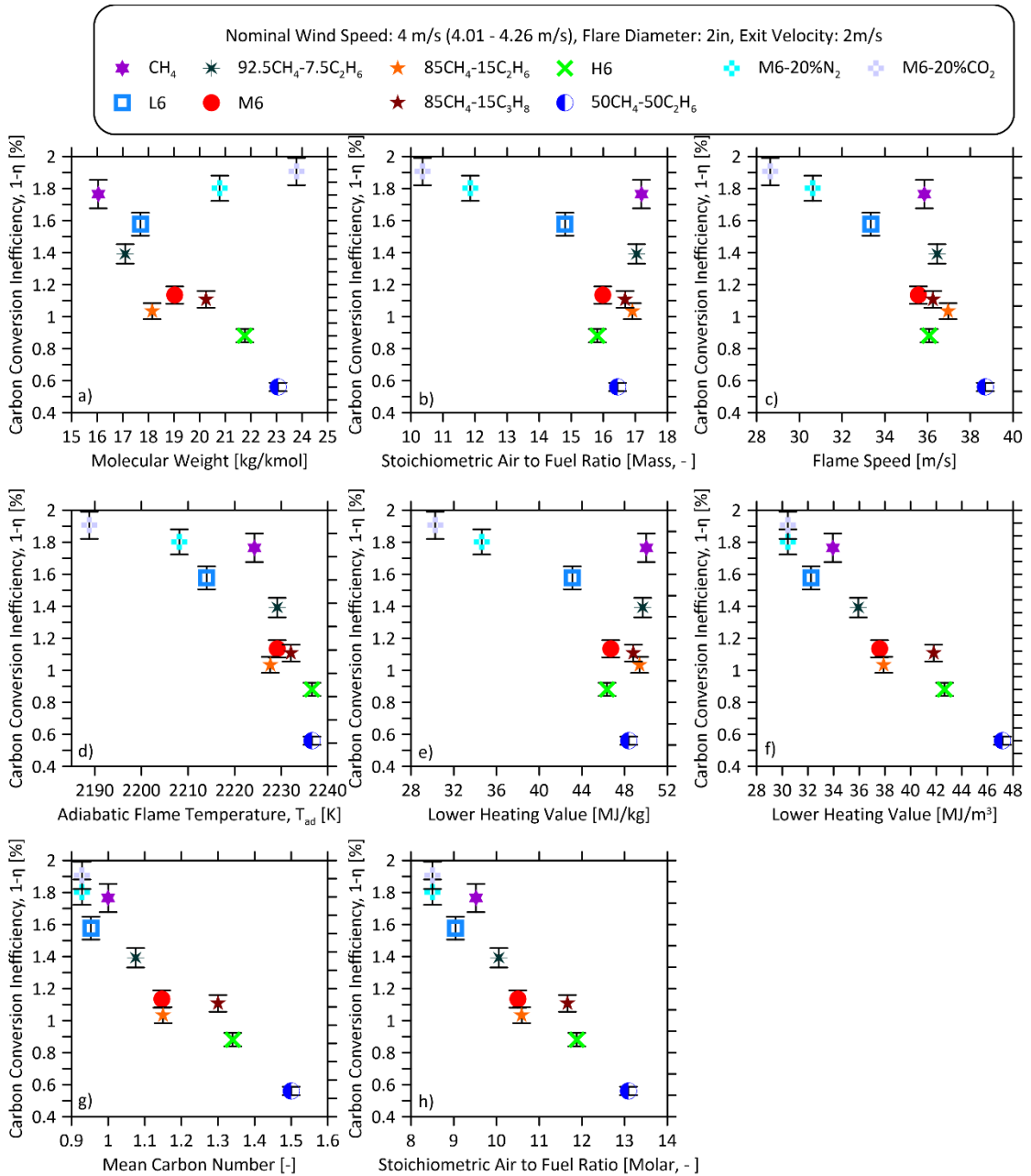


Figure 6.4: Inefficiency as a function of several parameters for 2-inch flares burning flare gases with less than 20% inert dilution at an exit velocity of 2 m/s at a nominal crosswind speed of 4 m/s.

Beyond predicting flare inefficiency, it is potentially even more important from a greenhouse gas perspective to be able to predict methane yields, Y_{CH_4} , defined as the emitted mass methane per mass of hydrocarbons in the flare gas ($g\ CH_4 / kg\ HC_{fg}$). Figure 6.5 plots methane yield in terms of the same flare gas properties as in Figure 6.4. Similar to inefficiency, methane yields are poorly

correlated with molecular weight, $AF_{mass,stoic}$, S_L , T_{ad} , and LHV_{mass} . Although inefficiency data were simply correlated with LHV_{vol} , $C_{\#}$, or $AF_{vol,stoic}$, the trends with methane yields are less clear, particularly for more inefficient flare gases. As discussed in Chapter 5, it is likely that there is more than one mechanism responsible for methane emissions in flares in crossflow that are not readily captured by these parameters in isolation. Appendix E, Figure E2 shows further plots of methane yields versus the various flare gas properties for all flare gas mixtures considered in this thesis, including fuels with >20% high diluent-fraction. Over this broader range of conditions, methane yields appear similarly correlated with either LHV_{vol} , $C_{\#}$, or $AF_{vol,stoic}$.

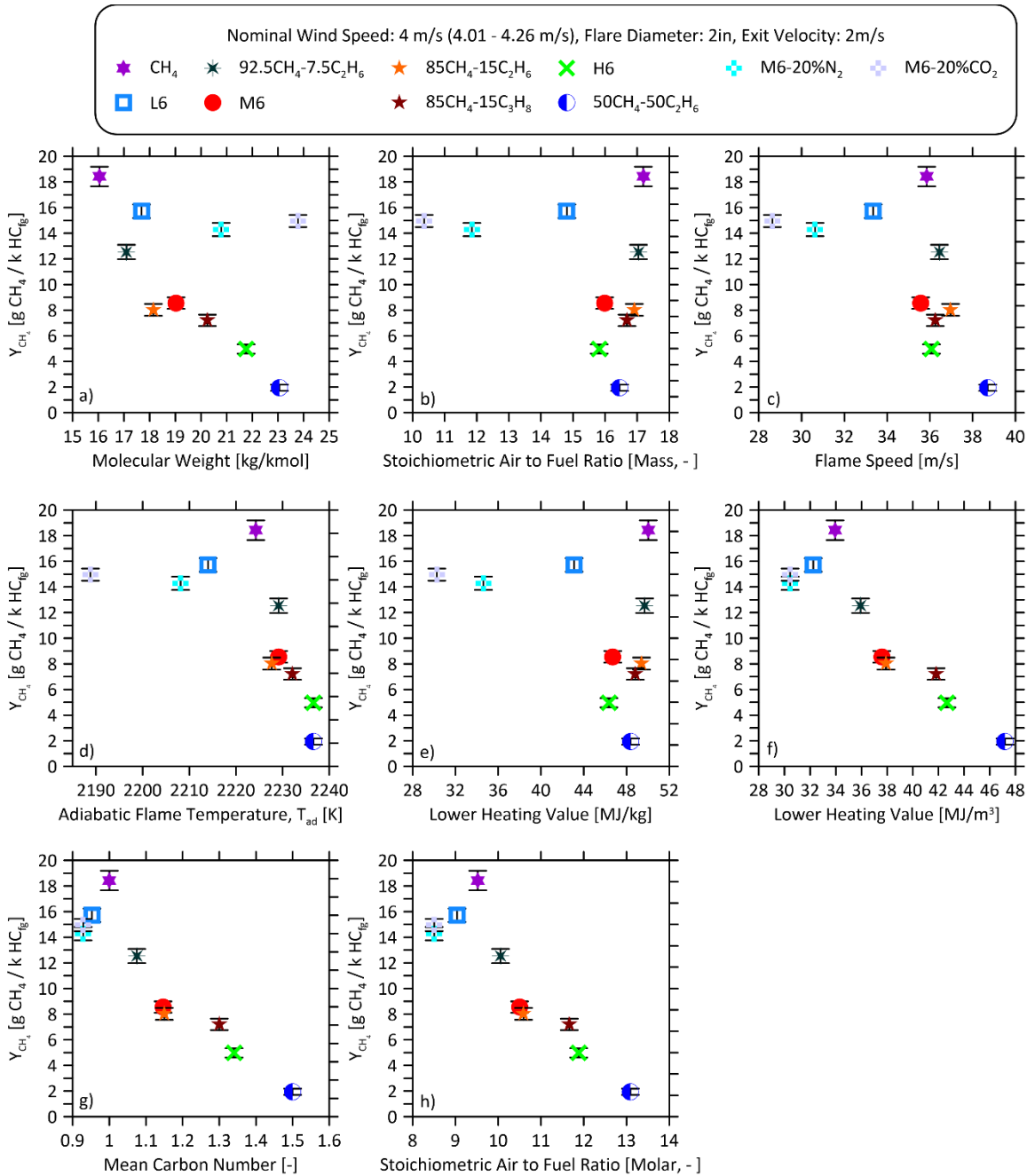


Figure 6.5: Methane yield as a function of several parameters for 2-inch flares burning flare gases with less than 20% inert dilution at an exit velocity of 2 m/s at a nominal crosswind speed of 4 m/s.

6.2 Empirical models for inefficiencies of upstream oil and gas flares

Results presented thus far highlight the complexity of predicting flare emissions for a broad range of operating conditions, especially over a range of flare gas compositions. Although the discussion in Chapter 5 was encouraging for correlating carbon conversion inefficiency in terms of flare burner diameter and exit velocity for a single fuel mixture over a range of wind speeds, the results

presented in Section 5.4 highlight how even among methane-dominated flare gas mixtures small changes in the composition of other species can dramatically affect emissions. Although previous models have attempted to use energy density to correlate inefficiencies, the results presented in Section 5.5 and Section 6.1 suggest these models do not extend well to the present data set. The effects of fuel chemistry are likely too complex to be easily described by single parameters as explored in Figure 6.4 and Figure 6.5 (and in Appendix E), and ultimately further research will be required to gain insight into the exact mechanisms driving flare inefficiency, and how these may vary with fuel composition.

Nevertheless, flaring remains as a globally significant problem with important climate and air quality concerns as noted in Chapter 1. Thus, in the absence of a detailed understanding of the physical and chemical mechanisms controlling flare emissions, there is still an obligation to use this unique, global-first data set to attempt to develop practical models that might be used to estimate emissions. With this primary objective in mind, the newly available experimental data will be used in an attempt to create updated, practically implementable, semi-empirical relationships/models that describes flare inefficiency and methane emissions for pipe flares typical of those in the upstream oil and gas sector burning a representative range of methane-dominated flare gas compositions. It must be reiterated that the models presented below are empirical, and the mechanisms that cause flare inefficiency are not fully understood and are unlikely to be completely captured. Further experiments, model development research, and validation work are expected to continue beyond this thesis.

While initial attempts were made to correlate experimental data using momentum, no suitable correlations were determined in the present work. The empirical models presented below consider simple hydrocarbon flare gas mixtures with less than 20% inert diluents, including the three main flare gas mixtures considered in this thesis (i.e., L6, M6 and H6) which were chosen to represent the range of likely flare gas mixtures in Alberta, Canada. Empirical models build upon correlating exit velocity and burner diameters as outlined in Chapter 5, Section 5.5.3. Given that the 1-inch burner diameter may not be relevant to full scale flares, and the added complexity of different flare gases being sensitive to exponent n in D^n in Eq. 5.3 (See Chapter 5, Section 5.5.3), the 1-inch diameter experiments were omitted from correlations. Several simple parameters were considered to correlate data for different fuel mixtures, including $AF_{mass,stoic}$, S_L , LHV_{mass} , LHV_{vol} , $C_{\#}$ and $AF_{vol,stoic}$. Power law fits in the form of $f(x) = ax^b + c$ were applied, and fit

coefficients of the parameters were optimized by minimizing absolute errors in the predicted inefficiencies. Table 6.2 presents summarized 95% confidence intervals for candidate models. See Appendix C for a complete summary of tested empirical models. Error analysis summarized in Table 6.2 suggests that empirical models using any one of the considered parameters are capable of predicting carbon conversion inefficiency to within 2% absolute uncertainty at 95% confidence, while models based on either LHV_{vol} , $C_{\#}$, or $AF_{vol,stoic}$ provide the best estimates.

Table 6.2: Comparison of candidate empirical models in predicting flare inefficiency of 2–4 inch diameter pipe flares burning C1–C4 alkane flare gas mixtures with <20% inert fraction (N₂ and CO₂).

Correlating Parameter	Empirical Model Equation	R ²	Confidence Interval on Model Error when Predicting Experimental Data		
			2.50%	97.50%	Range [%]
$AF_{mass,stoic}$	$(1 - \eta)AF_m^{1.3} = 2.822 \left(\frac{U_{\infty}}{(gV_j D)^{1/3}} \right)^{1.65} + 8.74$	0.8572	-1.0137	1.0474	2.0611
S_L	$(1 - \eta) \left(\frac{S_L}{S_{L,CH_4}} \right)^{3.6} = 0.08468 \left(\frac{U_{\infty}}{(gV_j D)^{1/3}} \right)^{1.593} + 0.2056$	0.9005	-0.7787	0.8755	1.6542
LHV_{mass}	$(1 - \eta) \left(\frac{LHV_m}{LHV_{m,CH_4}} \right)^{1.2} = 0.086 \left(\frac{U_{\infty}}{(gV_j D)^{1/3}} \right)^{1.576} + 0.1867$	0.8602	-0.9986	0.9886	1.9872
LHV_{vol}	$(1 - \eta) \left(\frac{LHV_v}{LHV_{v,CH_4}} \right)^{2.7} = 0.0985 \left(\frac{U_{\infty}}{(gV_j D)^{1/3}} \right)^{1.625} + 0.3071$	0.9294	-0.691	0.628	1.319
$C_{\#}$	$(1 - \eta)C_{\#}^{1.6} = 0.1155 \left(\frac{U_{\infty}}{(gV_j D)^{1/3}} \right)^{1.575} + 0.2756$	0.9281	-0.6566	0.7519	1.4085
$AF_{vol,stoic}$	$(1 - \eta)AF_v^{1.7} = 4.54 \left(\frac{U_{\infty}}{(gV_j D)^{1/3}} \right)^{1.615} + 13.53$	0.9292	-0.679	0.6907	1.3697

As described by Johnson et al. (2001), wake stabilized flares in crossflow may be described by 3 zones: a planar recirculation zone (standing vortex) on the lee-side of the stack (Zone 1), the

axisymmetric main tail of the flame (Zone 3) and a junction between the recirculation zone and flame tail (Zone 2). While most of fuel is drawn into the flame and either burns in Zone 1 or Zone 3, sporadic pockets of unburned fuel may be drawn through the intermediate Zone 2 and ejected on the underside of the flame without reacting. This mechanism allows fuel to be stripped from the flame and escape combustion as it is carried downstream. This description was verified by FFID measurements (Johnson et al. 2001) and flow visualization (Johnson and Kostiuik 2002a).

Since the volumetric air to fuel ratio is proportional to flame length, it is presumably related to the relative amounts of flame in each zone. Thus, following the mechanism proposed by Johnson et al. (2001), it is reasonable to expect that emissions from the flare may correlate with the volumetric air to fuel ratio, which acts as a surrogate chemical mechanism to fuel stripping. However, comprehensive flame observations were not logged in the current experimental dataset to confirm these assumptions.

Figure 6.6 plots the suggested empirical model for scaling carbon conversion inefficiency data using $AF_{vol,stoic}$. The 95% confidence interval on the predicted inefficiency is -0.679% to $+0.6907\%$ (absolute) and the R^2 value of the empirical power-law fit is 0.9292. Similar results are possible by using mean carbon number (See Figure C5 in Appendix C) instead of $AF_{vol,stoic}$ to correlate the data (95% confidence interval in predicted inefficiency from -0.656% to $+0.752\%$ and an R^2 value of 0.9281). This simply shows that these two parameters are directly correlated when the flare gas does not include significant inerts and the combustible species are exclusively alkanes.

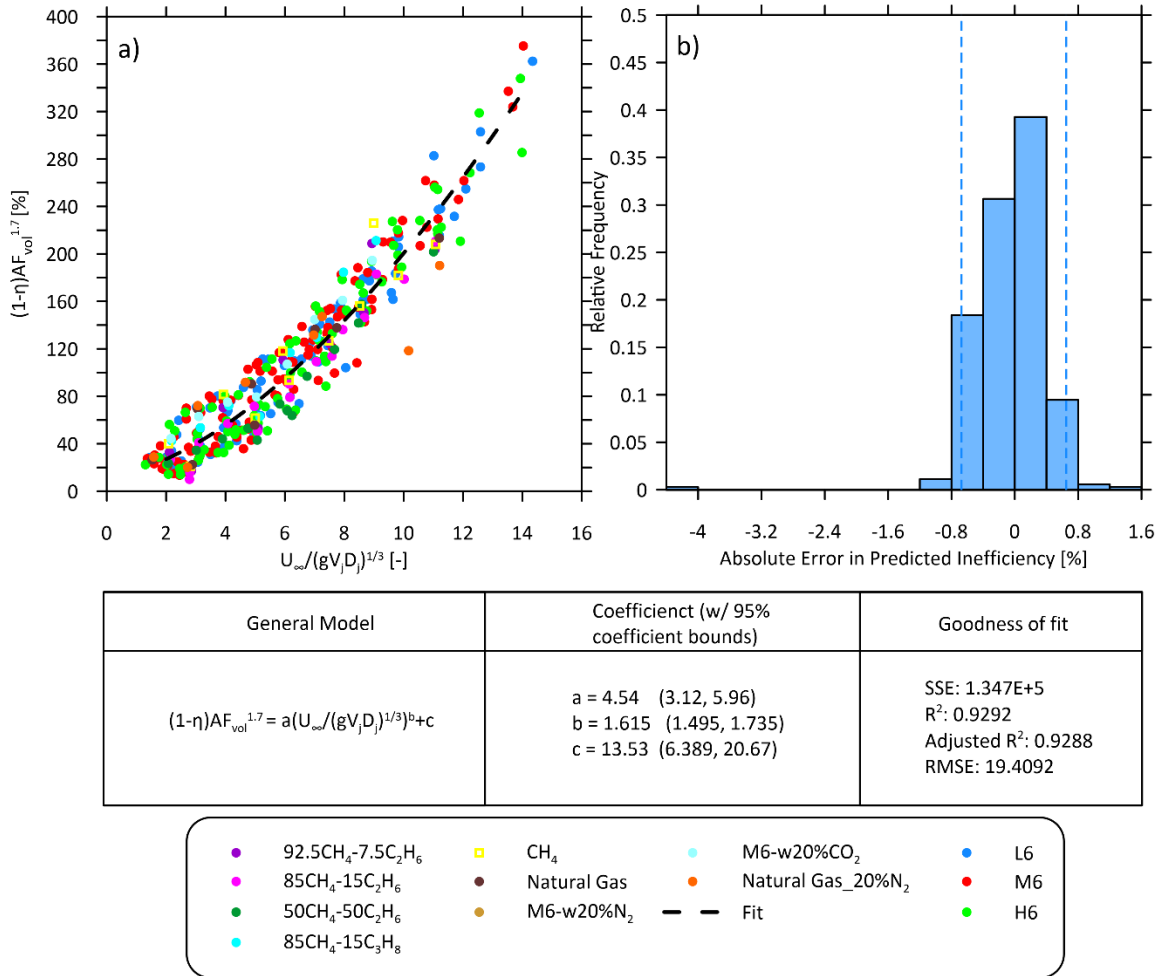


Figure 6.6: a) Suggested empirical model for predicting carbon conversion inefficiency of 2–4 inch diameter pipe flares burning C1–C4 alkane-based flare gas mixtures with less than 20% inert fraction (CO₂ and N₂) and b) corresponding histograms of the errors in the predicted inefficiency.

Flares in certain applications, such as those associated with gas treatment processes, may include large amounts of inert species in the flare gas. For these cases, the presented empirical models can be recalculated to include data for flare gas mixtures with up to 70% inert species (i.e., CO₂ or N₂). As shown in Table 6.3, a model based on $AF_{vol,stoic}$ is again applicable, predicting the flare inefficiency within an absolute difference of -1.697% to $+1.216\%$ at 95% confidence and with an R² value of 0.9974. Although models using S_L or LHV_{vol} to correlate the data provide marginally better confidence intervals and similar R² values (see Table 6.3), the model based on $AF_{vol,stoic}$ is suggested for consistency with the discussion above and the expected link between $AF_{vol,stoic}$ and the potential mechanism of fuel stripping. It must be noted the model is based only on the available data for diluted fuels and is not recommended for use outside of the tested criteria.

Future improvements on this model could be made by further testing of alternative diluted fuels with various inert species at multiple diameters and exit velocities.

Table 6.3: Comparison of candidate empirical models in predicting flare inefficiency of 2–4 inch diameter pipe flares burning C1–C4 alkane flare gas mixtures with up to 70% inert fraction (N₂ and CO₂).

Correlating Parameter	Empirical Model Equation	R ²	Confidence Interval on Model Error when Predicting Experimental Data		
			2.50%	97.50%	Range [%]
$AF_{mass,stoic}$	$(1 - \eta)AF_m^{1.9} = 13.49 \left(\frac{U_\infty}{(gV_j D)^{1/3}} \right)^{1.693} + 47.7$	0.9956	-0.9633	4.0695	5.0328
S_L	$(1 - \eta) \left(\frac{S_L}{S_{L,CH_4}} \right)^{3.6} = 0.06603 \left(\frac{U_\infty}{(gV_j D)^{1/3}} \right)^{1.691} + 0.2574$	0.9973	-0.8569	3.5331	4.39
LHV_{mass}	$(1 - \eta) \left(\frac{LHV_m}{LHV_{m,CH_4}} \right)^{1.9} = 0.05429 \left(\frac{U_\infty}{(gV_j D)^{1/3}} \right)^{1.734} + 0.2354$	0.9958	-0.9689	3.9252	4.8941
LHV_{vol}	$(1 - \eta) \left(\frac{LHV_v}{LHV_{v,CH_4}} \right)^{2.6} = 0.09189 \left(\frac{U_\infty}{(gV_j D)^{1/3}} \right)^{1.677} + 0.3677$	0.8908	-1.1472	1.4662	2.6134
$C_\#$	$(1 - \eta)C_\#^{2.4} = 0.08941 \left(\frac{U_\infty}{(gV_j D)^{1/3}} \right)^{1.717} + 0.4273$	0.9965	-1.4038	1.8008	3.2046
$AF_{vol,stoic}$	$(1 - \eta)AF_v^{2.5} = 25.13 \left(\frac{U_\infty}{(gV_j D)^{1/3}} \right)^{1.678} + 100.3$	0.9974	-1.6967	1.216	2.9127

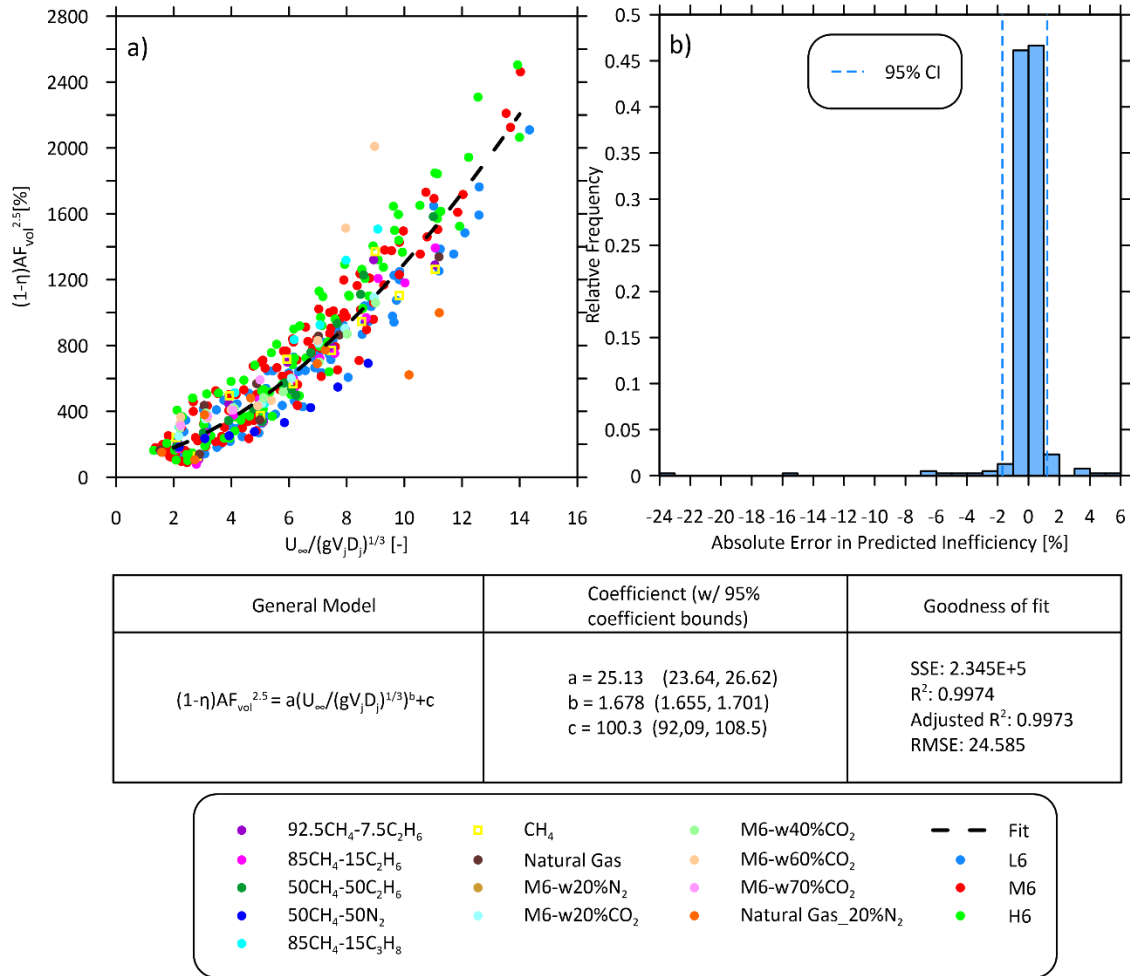


Figure 6.7: a) Empirical model for predicting carbon conversion inefficiency of 2–4 inch diameter pipe flares burning C1–C4 alkane flare gas mixtures including data for mixture with higher inert fraction (up to 70% CO₂ or N₂) and b) corresponding histograms of the errors in the predicted inefficiency.

6.3 Empirical models for methane emission from upstream oil and gas flares

Chapter 5 introduced several models that attempted to predict flare inefficiency, which drove the investigation of alternate, improved models in Section 6.2. However, from a greenhouse gas perspective, a model to specifically predict methane emissions rather than bulk inefficiency is also desirable. The same correlating parameters considered in the empirical model for inefficiency ($AF_{vol,stoic}$, S_L , LHV_{vol} , $C_{\#}$, and $AF_{vol,stoic}$) were again evaluated, and separate empirical models were created for flare gas compositions with less than 20% inert fraction and for all tested cases (with up to 70% inert fraction). Power-law fits in the form of $f(x) = ax^b + c$ were applied to the correlated data and the fit coefficients on the parameters of interest were optimized to minimize absolute errors in the predicted methane yield.

Table 6.4 summarizes the 95% confidence intervals of the candidate empirical models in predicting methane yields and again suggests that LHV_{vol} , $C_{\#}$, and $AF_{vol,stoic}$ are the best performing among the considered correlating parameters. Curiously, although the R^2 values of these models ($R^2 = 0.8874$ to 0.9014) were lower than candidate models using $AF_{mass,stoic}$, S_L , or LHV_{mass} ($R^2 = 0.9876$ to 0.9931), the range of predicted errors in methane emissions was much larger for the latter. It is noted however that R^2 represents the proportion of the variation in the dependent variable that is predictable from the independent variable. Since the regression only looks at the deviations of the points in the vertical direction, swapping variables from one axis to another will result in a different regression and therefore a different coefficient of determination, where applying the correlating parameter may also stretch data points on the y-axis. Analysis was performed by moving correlating $AF_{vol,stoic}$ parameters to the x-axis, which improved the R^2 to 0.9965 ; however, confidence intervals worsened. Thus, coefficient of determination was not taken as a deciding factor in selecting candidate models.

Figure 6.8 plots the suggested empirical model for predicting methane yield (Y_{CH_4} , defined as g CH_4 per kg of hydrocarbons in the flare gas) scaled using $AF_{vol,stoic}$. The adjacent histogram shows the relative error of the model in predicting experimentally measured methane yields. While it must be underscored that the mechanisms that cause methane emissions are still not fully understood, this model is shared as a current best attempt to predict methane yields recognizing the significance of global gas flaring and the urgent need for practical models to guide policy decisions in the absence of other available data.

Table 6.4: Comparison of candidate empirical models in predicting methane yields of 2–4 inch diameter pipe flares burning C1–C4 alkane flare gas mixtures with <20% inert fraction (N₂ and CO₂).

Correlating Parameter	Empirical Model Equation	R ²	Confidence Interval on Model Error when Predicting Experimental Data		
			2.50%	97.50%	Range [%]
$AF_{mass,stoic}$	$Y_{CH_4} AF_m^{1.8} = 56.6 \left(\frac{U_\infty}{(gV_j D)^{1/3}} \right)^{1.864} + 352$	0.9912	-55.7921	264.589	320.3811
S_L	$Y_{CH_4} \left(\frac{S_L}{S_{L,CH_4}} \right)^{5.1} = 0.4483 \left(\frac{U_\infty}{(gV_j D)^{1/3}} \right)^{1.796} + 1.306$	0.9931	-52.5082	191.6549	244.1631
LHV_{mass}	$Y_{CH_4} \left(\frac{LHV_m}{LHV_{m,CH_4}} \right)^{1.8} = 0.358 \left(\frac{U_\infty}{(gV_j D)^{1/3}} \right)^{1.839} + 2.063$	0.9876	--56.234	255.088	311.322
LHV_{vol}	$Y_{CH_4} \left(\frac{LHV_v}{LHV_{v,CH_4}} \right)^3 = 0.06403 \left(\frac{U_\infty}{(gV_j D)^{1/3}} \right)^{1.779} + 2.698$	0.8874	-44.6896	142.9127	187.6023
$C_\#$	$Y_{CH_4} C_\#^{2.7} = 0.7071 \left(\frac{U_\infty}{(gV_j D)^{1/3}} \right)^{1.755} + 2.792$	0.9014	-43.8467	134.8377	178.6844
$AF_{vol,stoic}$	$Y_{CH_4} AF_v^{3.2} = 911.3 \left(\frac{U_\infty}{(gV_j D)^{1/3}} \right)^{1.757} + 3283$	0.8892	-44.8106	142.1017	186.9123

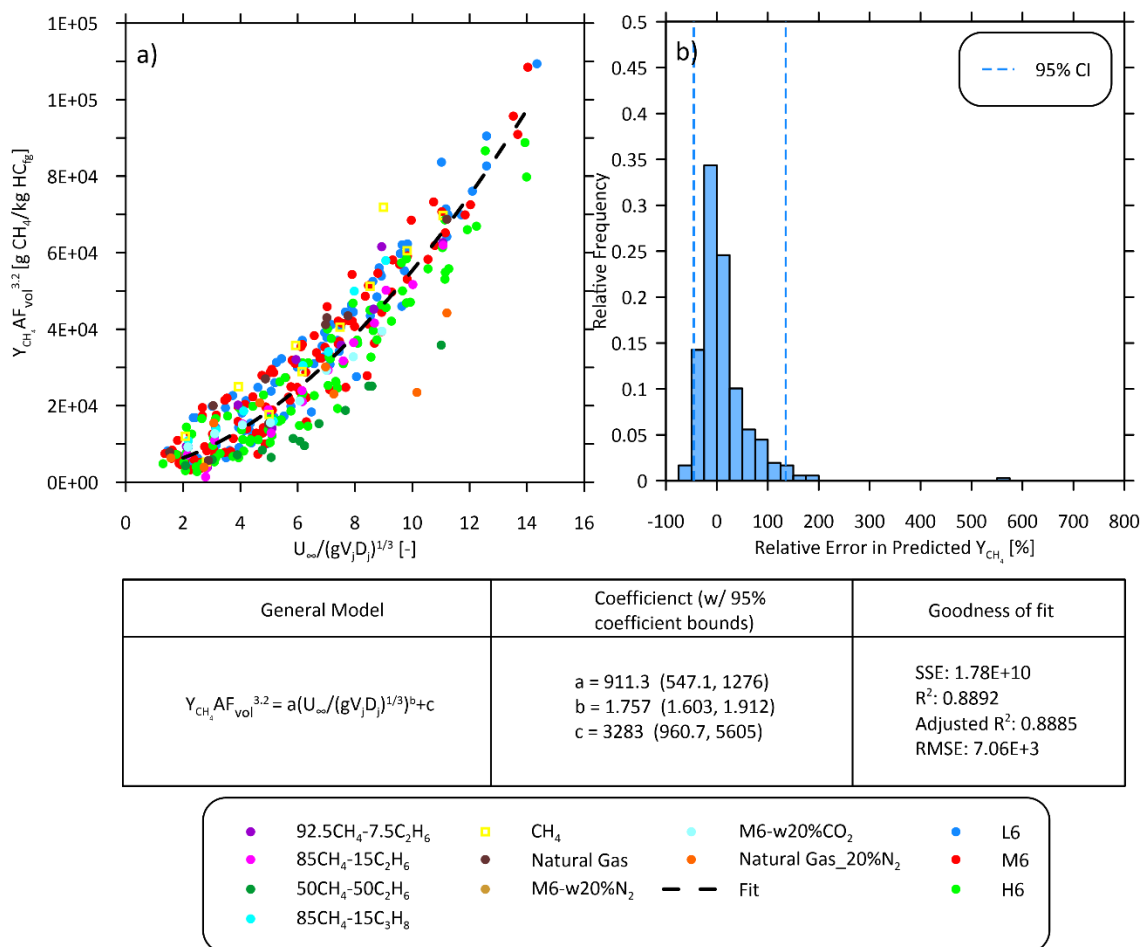


Figure 6.8: a) Empirical model for predicting methane yield of 2–4 inch diameter pipe flares burning C1–C4 alkane flare gas mixtures with <20% inert fraction (CO₂ and N₂) and b) corresponding histogram of the errors in the predicted methane yield.

As with the empirical models for flare inefficiency, an alternative methane emissions model for flares burning mixtures with large fractions of inert species was also considered as summarized in Table 6.5. The suggested model, plotted in Figure 6.9, again uses $AF_{vol,stoic}$ as a correlating parameter and predicts methane yields within –43.1% to +143.5% at 95% confidence (R² value of 0.8633). It is important to acknowledge the model is purely empirical since the mechanisms that cause methane emissions are not fully understood, and models using different correlating parameters result in similar errors as summarized in Table 6.5. Therefore, it is not advised to apply the model outside of the bounds of tested conditions. Future experiments are advised to try to extend the range of test conditions in an effort to improve these models and better understand underlying mechanisms of methane emissions.

Table 6.5: Comparison of candidate empirical models in predicting methane yields of 2–4 inch diameter pipe flares burning C1–C4 alkane flare gas mixtures with up to 70% inert fraction (CO₂ or N₂)

Correlating Parameter	Empirical Model Equation	R ²	Confidence Interval on Model Error when Predicting Experimental Data		
			2.50%	97.50%	Range [%]
$AF_{mass,stoic}$	$Y_{CH_4} AF_m^{1.8} = 55.29 \left(\frac{U_\infty}{(gV_j D)^{1/3}} \right)^{1.872} + 368.6$	0.9919	-55.88	265.64	321.52
S_L	$Y_{CH_4} \left(\frac{S_L}{S_{L,CH_4}} \right)^{3.5} = 0.3874 \left(\frac{U_\infty}{(gV_j D)^{1/3}} \right)^{1.849} + 2.333$	0.9935	-52.11	191.66	243.77
LHV_{mass}	$Y_{CH_4} \left(\frac{LHV_m}{LHV_{m,CH_4}} \right)^{1.8} = 0.327 \left(\frac{U_\infty}{(gV_j D)^{1/3}} \right)^{1.878} + 2.233$	0.9920	-55.83	261.03	316.86
LHV_{vol}	$Y_{CH_4} \left(\frac{LHV_v}{LHV_{v,CH_4}} \right)^{2.7} = 0.5259 \left(\frac{U_\infty}{(gV_j D)^{1/3}} \right)^{1.839} + 3.265$	0.8689	-45.14	137.60	182.74
$C_\#$	$Y_{CH_4} C_\#^{2.7} = 0.6271 \left(\frac{U_\infty}{(gV_j D)^{1/3}} \right)^{1.799} + 3.404$	0.8939	-41.17	134.48	175.65
$AF_{vol,stoic}$	$Y_{CH_4} AF_v^{2.7} = 229.1 \left(\frac{U_\infty}{(gV_j D)^{1/3}} \right)^{1.834} + 1414$	0.9959	-43.10	143.58	186.69

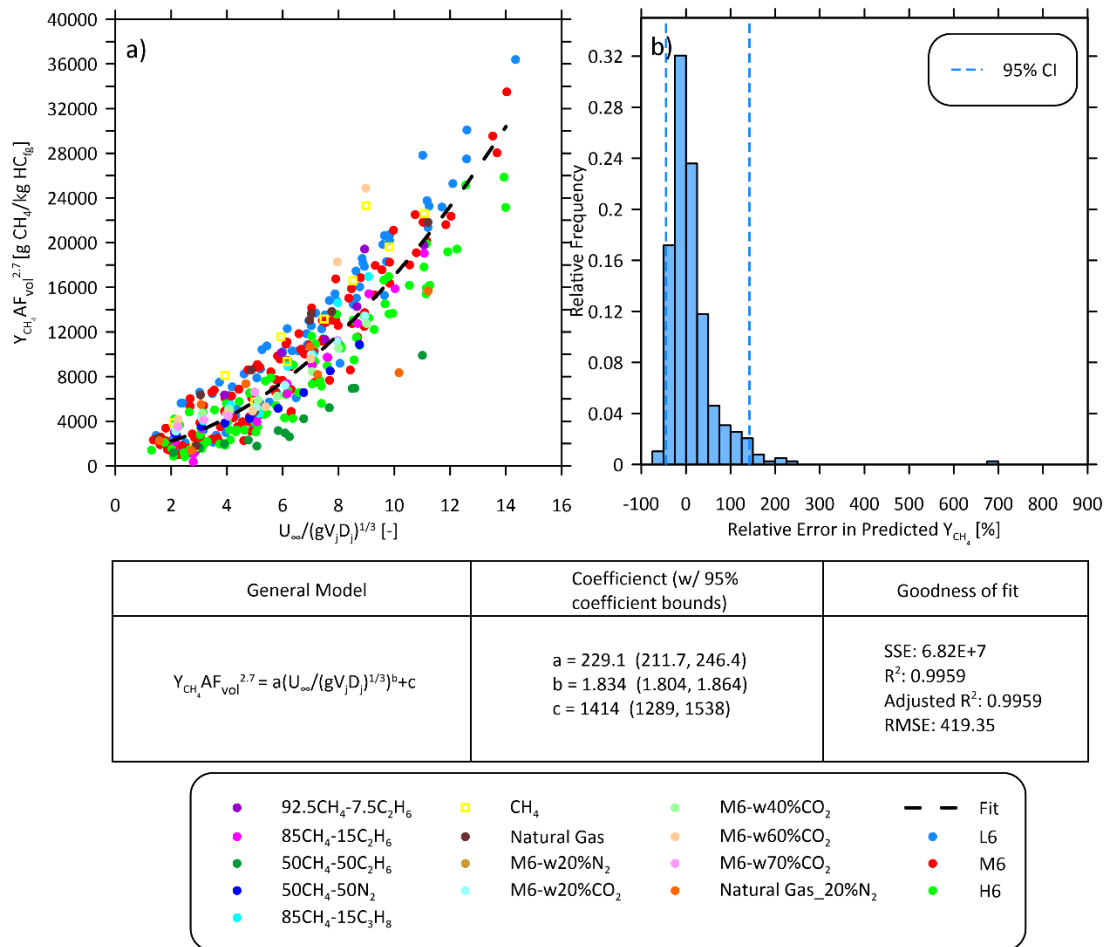


Figure 6.9: a) Empirical model for predicting methane yield of 2–4 inch diameter pipe flares burning C1–C4 alkane flare gas mixtures with up to 70% inert fraction (CO₂ or N₂) and b) corresponding histogram of the errors in the predicted methane yield.

Chapter 7 Conclusions and Future Work

7.1 Conclusions

The objectives of this thesis were to investigate the impacts of turbulent crosswinds on unassisted pipe flares representative of those found in the upstream oil and gas industry. A detailed method was first developed to quantify flare performance using a closed-loop wind tunnel to relate the accumulation rates of species concentrations to emission rates and carbon conversion efficiency. The method is assessed with a comprehensive Monte Carlo uncertainty and sensitivity analysis and demonstrated that carbon conversion inefficiency could be measured within $\lesssim \pm 0.5\%$, and methane emission rates quantified within $\pm 3.5\%$ at 95% confidence. The method has been published as a peer-review journal article co-authored by the author of this thesis.

Experiments were subsequently performed in a closed-loop wind tunnel which was retrofitted to allow for controlled experiments of flares subject to a turbulent crosswind, as generated from a passive turbulence grid placed upstream of the flare. The generated turbulence approached the expected intensity and scales of atmospheric turbulence expected in a field scenario, with a fall-off in energy at scales smaller than the burner diameter. A comprehensive dataset of experimentally measured flare efficiencies and species emission rates was collected which comprised 1–4-inch diameter flares, burning a variety of methane-dominated flare gas compositions representative of the upstream oil and gas industry, at flare gas exit velocities between 0.5 and 2 m/s, and at crosswind speeds between 2 and 9 m/s. Importantly, these experiments partially overlap with field-scale conditions for flares in Western Canada. To the author's knowledge, this is the first experimental dataset which considers simple pipe flares subjected to a turbulent crosswind at scales approaching real-world scenarios.

Consistent with data for previous, smaller-scale experiments in the literature, wind speed, exit velocity, and diameter were each found to affect flare efficiency. Results also demonstrated that flare inefficiency and methane emission rates are highly sensitive to even small variations in flare gas compositions. Efficiencies frequently fell below the common assumption that normally-operating flares have a combustion efficiency of 98%, especially at higher wind speeds.

Comparison of these new experimental dataset with models proposed in the prior literature suggests that no currently available model is capable of predicting inefficiency with any level of

certainty over a broad range of conditions. Further analysis attempted to elucidate independent effects of different parameters on flare efficiency and emissions, including parameters that might correlate effects of varied fuel composition within a narrow range of methane dominated alkane mixtures. Recognizing the global significance of flare emissions, an attempt was then made to develop useful empirical models, recognizing the practical need to predict flare emissions for regulations, emission inventories, and mitigation. Candidate models were developed by first correlating wind speed, flare gas exit velocity, and burner diameter using a non-dimensional parameter first proposed by Kostiuk et al. (2000), coupled with different parameters to represent the effects of changing flare gas compositions. While several parameters offer similar confidence in predicting inefficiency and methane yield, the models proposed in this thesis are based on correlating flare gas compositions using a stoichiometric molar air-fuel ratio. It is hypothesized that air to fuel ratio may be important in determining the relative sizes of flame zones in the wake of the stack that drive the fuel-stripping mechanism described by (Johnson 2001). The final empirical models are applicable over the range of experimental conditions, with separate coefficients for methane-dominated mixtures with low (<20%) and high (up to 70%) volume fractions of CO₂ or N₂. For the typical case with <20% inert species, these models can predict inefficiency of 2–4-inch diameter flares within -0.68% to 0.69% absolute uncertainty at 95% confidence, and methane yield to within -44.8% to 142% relative uncertainty at 95% confidence.

It must be acknowledged that the exact mechanisms causing flare emissions remain elusive, but flare emissions are a nevertheless a globally important problem. Thus, the presented experimental data set is a significant advance, and in the absence of a more clear understanding of the underlying mechanisms of flare emissions, the developed empirical models offer a valuable new tool for estimate emissions and impacts of flares.

7.2 Future Work

The empirical models presented in Chapter 6 suggest fuel chemistry has a complex influence on flare performance even over a relatively narrow range of methane-dominated flare gas mixtures. Current experimental conditions approach the limit of capabilities of the present infrastructure, with flow rates approaching 1000 SLPM and burner diameters up to 4 inches in diameter; however, there remains significant capacity to expand experimental conditions. Specifically, experiments are recommended for a broader range of fuel mixtures with higher hydrocarbon component (up to C7+) as are commonly present in flare gas at upstream production sites. While

it is noted in Chapter 1 that BC and NO_x emissions are expected to be reduced in crosswind conditions, future experiments should include these measurements. The necessary liquid fuel handling systems to enable these experiments are currently being tested at the wind tunnel. In addition, models for diluted fuels were shown in Chapter 6 to have less confidence in predicting both inefficiency and methane yield, and the greater inefficiencies for CO₂ than N₂ are unexplained with the limited tests comparing inert diluent selection. Further experiments with high diluent-content flare gases (especially N₂ which was limited to 20% volume fraction in the current experiments) are recommended. Diluted fuels should also be studied by varying flare diameter and exit velocity to compare inefficiency trends to those at multiple operating conditions.

Another recommendation is to study flares subject to a crosswind with turbulence at scales approaching the shear layer scale, which has been hypothesized as the cause of fuel stripping, and as such should be prioritized. Currently, a passive grid generates turbulence at the burner diameter scale, with energy rapidly falling off below this limit. Turbulence at the shear layer scale may be produced by way of an active grid, which consists of continuously rotating horizontal and vertical bars with attached obstructions. Operating conditions using the passive grid should be replicated using the active grid, particularly for the L6, M6 and H6 flare gas compositions, to study the viability of a fuel stripping mechanism that results in significant emissions, particularly as crosswind increases.

While accompanying flame observations are not included in the present experiments, this work could also be complemented by flow visualization, which can be achieved by seeding the flare gas with small oil droplets of oil and using a laser to identify regions of unburnt fuel in the flame. This could help better understand the role of fuel stripping of flare emissions and possibly give other insights into the variation of emissions patterns with condition. Furthermore, given that the stoichiometric molar air-fuel ratio has been identified as a potential correlating parameter for flare inefficiency and methane yield, and this ratio is directly related to flame length, flame length measurements could provide useful insight into the current, poor understanding of the mechanisms that cause inefficiencies.

References

- Aboje, A.A., Umar Garba, M., Abdulkareem, A.S., Muzenda, E., and Faruq, A.A. (2017). Numerical modelling of pollutant formation in a lifted methane–air vertical diffusion flame. *Cogent Environ. Sci.* 3 (1). doi:10.1080/23311843.2017.1302543.
- Ahsan, A., Ahsan, H., Olfert, J.S., and Kostiuk, L.W. (2019a). Quantifying the carbon conversion efficiency and emission indices of a lab-scale natural gas flare with internal coflows of air or steam. *Exp. Therm. Fluid Sci.* 103 (December 2018):133–142. doi:10.1016/j.expthermflusci.2019.01.013.
- Ahsan, A., Ahsan, H., Olfert, J.S., and Kostiuk, L.W. (2019b). Carbon conversion efficiency and emission indices from a lab-scale flare with air or steam assist., in *Combustion Institute Canadian Section Spring Technical Meeting*, Kelowna, BC, p. 6.
- Allen, D.T. and Torres, V.M. (2011). TCEQ 2010 Flare study final report (No. PGA No. 582-8-862-45-FY09-04). Texas Commission on Environmental Quality (TCEQ), Austin, TX.
- Barlow, R.S. and Carter, C.D. (2000). Radiation and Nitric Oxide Formation in Turbulent Non-Premixed Jet Flames. *Proc. Combust. Inst.* 28:447–454.
- Becker, H.A. and Liang, D. (1982). Total emission of soot and thermal radiation by free turbulent diffusion flames. *Combust. Flame* 44 (1–3):305–318. doi:10.1016/0010-2180(82)90080-3.
- Bello, O.W., Zamani, M., Abbasi-Atibeh, E., Kostiuk, L.W., and Olfert, J.S. (2021). Comparison of emissions from steam- and water-assisted lab-scale flames. *Fuel* 302 (May):121107. doi:10.1016/j.fuel.2021.121107.
- Blackwood, T.R. (2000). An evaluation of flare combustion efficiency using open-path Fourier transform infrared technology. *J. Air Waste Manage. Assoc.* 50 (10):1714–22.
- Boden, J.C., Tjessem, K., Wootton, A.G., and Moncrieff, J.T.M. (1996). Elevated flare emissions measured by remote sensing. *Pet. Rev.* 50 (598):524–8.
- Bond, T.C., Doherty, S.J., Fahey, D.W., Forster, P.M., Berntsen, T.K., DeAngelo, B.J., Flanner, M.G., Ghan, S., Kärcher, B., Koch, D., Kinne, S., Kondo, Y., Quinn, P.K., Sarofim, M.C., Schultz, M.G., Schulz, M., Venkataraman, C., Zhang, H., Zhang, S., Bellouin, N., Guttikunda, S.K., Hopke, P.K., Jacobson, M.Z., Kaiser, J.W., Klimont, Z., Lohmann, U., Schwarz, J.P., Shindell, D.T., Storelvmo, T., Warren, S.G., and Zender, C.S. (2013). Bounding the role of black carbon in the climate system: A scientific assessment. *J. Geophys. Res. Atmos.* 118 (11):5380–5552. doi:10.1002/jgrd.50171.
- Bourguignon, E., Johnson, M.R., and Kostiuk, L.W. (1999). The use of a closed-loop wind tunnel for measuring the combustion efficiency of flames in a cross flow. *Combust. Flame* 119 (3):319–334. doi:10.1016/S0010-2180(99)00068-1.
- Castiñeira, D. and Edgar, T.F. (2006). CFD for simulation of steam-assisted and air-assisted flare combustion systems. *Energy and Fuels* 20 (3):1044–1056. doi:10.1021/ef050332v.
- Caulton, D.R., Shepson, P.B., Cambaliza, M.O.L., McCabe, D., Baum, E., and Stirn, B.H. (2014). Methane destruction efficiency of natural gas flares associated with shale formation wells. *Environ. Sci. Technol.* 48 (16):9548–54. doi:10.1021/es500511w.
- Conley, S.A., Faloona, I., Mehrotra, S., Suard, M., Lenschow, D.H., Sweeney, C., Herndon, S.,

- Schwietzke, S., Pétron, G., Pifer, J., Kort, E.A., and Schnell, R. (2017). Application of Gauss's theorem to quantify localized surface emissions from airborne measurements of wind and trace gases. *Atmos. Meas. Tech.* 10:3345–3358. doi:10.5194/amt-10-3345-2017.
- Conrad, B.M. and Johnson, M.R. (2019). Mass absorption cross-section of flare-generated black carbon: Variability, predictive model, and implications. *Carbon N. Y.* 149:760–771. doi:10.1016/j.carbon.2019.04.086.
- Conrad, B.M. and Johnson, M.R. (2017). Field measurements of black carbon yields from gas flaring. *Environ. Sci. Technol.* 51 (3):1893–1900. doi:10.1021/acs.est.6b03690.
- Corbin, D.J. (2014). Methodology and experiments to determine soot and NO_x yields from a vertical lab-scale flare burning alkane-mixtures and ethylene (M.A.Sc. Thesis). Carleton University.
- Corbin, D.J. and Johnson, M.R. (2014). Detailed Expressions and Methodologies for Measuring Flare Combustion Efficiency, Species Emission Rates, and Associated Uncertainties. *Ind. Eng. Chem. Res.* 53 (49):19359–19369. doi:10.1021/ie502914k.
- Cushing, L.J., Chau, K., Franklin, M., and Johnston, J.E. (2021). Up in smoke: Characterizing the population exposed to flaring from unconventional oil and gas development in the contiguous US. *Environ. Res. Lett.* 16 (3). doi:10.1088/1748-9326/abd3d4.
- Cushing, L.J., Vavra-Musser, K., Chau, K., Franklin, M., and Johnston, J.E. (2020). Flaring from Unconventional Oil and Gas Development and Birth Outcomes in the Eagle Ford Shale in South Texas. *Environ. Health Perspect.* 128 (7):077003. doi:10.1289/EHP6394.
- Cusworth, D.H., Duren, R.M., Thorpe, A.K., Olson-Duvall, W., Heckler, J., Chapman, J.W., Eastwood, M.L., Helmlinger, M.C., Green, R.O., Asner, G.P., Dennison, P.E., and Miller, C.E. (2021). Intermittency of Large Methane Emitters in the Permian Basin. *Environ. Sci. Technol. Lett.* 8 (7):567–573. doi:10.1021/acs.estlett.1c00173.
- Czolowski, E.D., Santoro, R.L., Srebotnjak, T., and Shonkoff, S.B.C. (2017). Toward consistent methodology to quantify populations in proximity to oil and gas development: A national spatial analysis and review. *Environ. Health Perspect.* 125 (8):1–11. doi:10.1289/EHP1535.
- Davis, S.G. and Law, C.K. (1998). Determination of and Fuel Structure Effects on Laminar Flame Speeds of C 1 to C 8 Hydrocarbons. *Combust. Sci. Technol.* 140:427–449. doi:10.1080/00102209808915781.
- Ellzey, J.L., Berbe, J.G., Tay, Z.F., and Foster, D.E. (1990). Total Soot Yield from a Propane Diffusion Flame in Cross-Flow. *Combust. Sci. Technol.* 71 (1–3):41–52. doi:10.1080/00102209008951623.
- EOG (2021). Global Gas Flaring Observed from Space. Available at https://eogdata.mines.edu/download_global_flare.html (Accessed 11 March 2021).
- EPA (2000). Section 3.2 VOC Destruction Controls Chapter 1 Flares.
- ESDU (1993). ESDU 85020: Characteristics of Atmospheric Turbulence Near the Ground - 2. Single Point Data for Strong Winds (Neutral Atmosphere). *ESDU Data Items (74031)*:42.
- Forster, P., Storelvmo, T., Armour, K., Collins, W., Dufresne, J.-L., Frame, D., Lunt, D.J., Mauritsen, T., Palmer, M.D., Watanabe, M., Wild, M., and Zhang, H. (2021). Chapter 7: The Earth's Energy Budget, Climate Feedbacks, and Climate Sensitivity., in *Climate Change 2021: The Physical Science Basis. Contribution of Working Group I to the Sixth Assessment*

- Report of the Intergovernmental Panel on Climate Change, V. Masson-Delmotte, P. Zhai, A. Pirani, S.L. Connors, C. Péan, S. Berger, N. Caud, Y. Chen, L. Goldfarb, M.I. Gomis, M. Huang, K. Leitzell, E. Lonnoy, J.B.R. Matthews, T.K. Maycock, T. Waterfield, O. Yelekçi, R. Yu, B. Zhou, eds, Cambridge University Press.*
- Fortner, E.C., Brooks, W.A., Onasch, T.B., Canagaratna, M.R., Massoli, P., Jayne, J.T., Franklin, J.P., Knighton, W.B., Wormhoudt, J., Worsnop, D.R., Kolb, C.E., and Herndon, S.C. (2012). Particulate emissions measured during the TCEQ comprehensive flare emission study. *Ind. Eng. Chem. Res.* 51 (39):12586–12592. doi:10.1021/ie202692y.
- Frank, J.H. and Barlow, R.S. (1998). Effects of turbulence on species mass fractions in methane/air jet flames. *Symp. Combust.* 1087–1095.
- Gogolek, P.E.G., Caverly, A., Balderson, C., Caravaggio, G., Seebold, J., and Pohl, J.H. (2012). Highlights of IFC Experimental Program. *17th Int. IFRF Memb. Conf. – Clean Effic. Fuel Convers. Ind.*
- Gogolek, P.E.G. and Hayden, A.C.S. (2004). Performance of Flare Flames in a Crosswind With Nitrogen Dilution. *J. Can. Pet. Technol.* 43 (8):43–47.
- Gollahalli, S.R., Brzustowski, T.A., and Sullivan, M.H.F. (1975). Characteristics of a turbulent propane diffusion flame in a cross-Wind. *Trans. CSME* 3 (4):205–214.
- Gvakharia, A., Kort, E.A., Brandt, A.R., Peischl, J., Ryerson, T.B., Schwarz, J.P., Smith, M.L., and Sweeney, C. (2017). Methane, black carbon, and ethane emissions from natural gas flares in the Bakken Shale, North Dakota. *Environ. Sci. Technol.* 51 (9):5317–5325. doi:10.1021/acs.est.6b05183.
- Herndon, S.C., Nelson, D.D., Wood, E.C., Knighton, W.B., Kolb, C.E., Kodesh, Z., Torres, V.M., and Allen, D.T. (2012). Application of the Carbon Balance Method to Flare Emissions Characteristics. *Ind. Eng. Chem. Res.* 51 (39):12577–12585. doi:10.1021/ie202676b.
- Hossain, M. (2019). The effects of turbulent cross-winds on combusting jets at low velocity ratios.
- Howell, L.W. (2004). Flare stack diameter scaling and wind tunnel ceiling and floor effects on model flares. University of Alberta, Edmonton, AB, Canada.
- Huang, R.F. and Wang, S.M. (1999). Characteristic flow modes of wake-stabilized jet flames in a transverse air stream. *Combust. Flame* 117 (1–2):59–77. doi:10.1016/S0010-2180(98)00070-4.
- IPCC (2021). Summary for Policy Makers., in *Climate Change 2021: The Physical Science Basis. Contribution of Working Group I to the Intergovernmental Panel on Climate Change 6th Assessment Report, V. Masson-Delmotte, P. Zhai, A. Pirani, S.L. Connors, C. Péan, S. Berger, N. Caud, Y. Chen, L. Goldfarb, M.I. Gomis, M. Huang, K. Leitzell, E. Lonnoy, J.B.R. Matthews, T.K. Maycock, T. Waterfield, O. Yelekçi, R. Yu, B. Zhou, eds, Cambridge University Press, p. 42.*
- Irakulis-Loitxate, I., Guanter, L., Liu, Y.-N., Varon, D.J., Maasackers, J.D., Zhang, Yuzhong, Chulakadabba, A., Wofsy, S.C., Thorpe, A.K., Duren, R.M., Frankenberg, C., Lyon, D.R., Hmiel, B., Cusworth, D.H., Zhang, Yongguang, Segl, K., Gorroño, J., Sánchez-García, E., Sulprizio, M.P., Cao, K., Zhu, H., Liang, J., Li, X., Aben, I., and Jacob, D.J. (2021). Satellite-based survey of extreme methane emissions in the Permian basin. *Sci. Adv.* 7

(27):eabf4507. doi:10.1126/sciadv.abf4507.

- Janssen, N.A.H., Hoek, G., Simic-Lawson, M., Fischer, P., van Bree, L., ten Brink, H., Keuken, M., Atkinson, R.W., Anderson, H.R., Brunekreef, B., and Cassee, F.R. (2011). Black Carbon as an Additional Indicator of the Adverse Health Effects of Airborne Particles Compared with PM 10 and PM 2.5. *Environ. Health Perspect.* 119 (12):1691–1699. doi:10.1289/ehp.1003369.
- Jatale, A., Smith, P.J., Thornock, J.N., Smith, S.T., and Hradisky, M. (2016). A Validation of Flare Combustion Efficiency Predictions From Large Eddy Simulations. *J. Verif. Valid. Uncertain. Quantif.* 1 (2):1–8. doi:10.1115/1.4031141.
- Johnson, M.R. (2001). Wake-Stabilized Diffusion Flames in Crossflow: Application to the Efficiencies of Gas Flares. University of Alberta.
- Johnson, M.R. and Coderre, A.R. (2012). Compositions and greenhouse gas emission factors of flared and vented gas in the western Canadian sedimentary basin. *J. Air Waste Manage. Assoc.* 62 (9):992–1002. doi:10.1080/10962247.2012.676954.
- Johnson, M.R. and Coderre, A.R. (2011). An Analysis of Flaring and Venting Activity in the Alberta Upstream Oil and Gas Industry. *J. Air Waste Manage. Assoc.* 61 (2):190–200. doi:10.3155/1047-3289.61.2.190.
- Johnson, M.R., Devillers, R.W., and Thomson, K.A. (2013). A generalized sky-LOSA method to quantify soot/black carbon emission rates in atmospheric plumes of gas flares. *Aerosol Sci. Technol.* 47 (9):1017–1029. doi:10.1080/02786826.2013.809401.
- Johnson, M.R., Devillers, R.W., and Thomson, K.A. (2011). Quantitative field measurement of soot emission from a large gas flare using sky-LOSA. *Environ. Sci. Technol.* 45 (1):345–350. doi:10.1021/es102230y.
- Johnson, M.R. and Kostiuik, L.W. (2002a). Visualization of the fuel stripping mechanism for wake-stabilized diffusion flames in a crossflow., in *IUTAM Symposium on Turbulent Mixing and Combustion, Fluid Mechanics and Its Applications*, A. Pollard, S. Candel, eds, Springer Netherlands, Dordrecht, pp. 295–303.
- Johnson, M.R. and Kostiuik, L.W. (2002b). A parametric model for the efficiency of a flare in crosswind. *Proc. Combust. Inst.* 29 (2):1943–1950. doi:10.1016/S1540-7489(02)80236-X.
- Johnson, M.R. and Kostiuik, L.W. (2000). Efficiencies of low-momentum jet diffusion flames in crosswinds. *Combust. Flame* 123 (1–2):189–200. doi:10.1016/S0010-2180(00)00151-6.
- Johnson, M.R., Wilson, D.J., and Kostiuik, L.W. (2001). A fuel stripping mechanism for wake-stabilized jet diffusion flames in crossflow. *Combust. Sci. Technol.* 169 (1):155–174. doi:10.1080/00102200108907844.
- Johnston, J.E., Chau, K., Franklin, M., and Cushing, L. (2020). Environmental Justice Dimensions of Oil and Gas Flaring in South Texas: Disproportionate Exposure among Hispanic communities. *Environ. Sci. Technol.* 54 (10):6289–6298. doi:10.1021/acs.est.0c00410.
- Kalghatgi, G.T. (1981a). Blow-Out Stability of Gaseous Jet Diffusion Flames. Part I In Still Air. *Combust. Sci. Technol.* 26 (5–6):233–239. doi:10.1080/00102208108946964.
- Kalghatgi, G.T. (1981b). Blow-Out stability of gaseous jet diffusion flames part II: effect of cross wind. *Combust. Sci. Technol.* 26 (5–6):241–244. doi:10.1080/00102208108946965.
- Knighton, W.B., Herndon, S.C., Franklin, J.F., Wood, E.C., Wormhoudt, J., Brooks, W., Fortner,

- E.C., and Allen, D.T. (2012). Direct measurement of volatile organic compound emissions from industrial flares using real-time online techniques: Proton Transfer Reaction Mass Spectrometry and Tunable Infrared Laser Differential Absorption Spectroscopy. *Ind. Eng. Chem. Res.* 51 (39):12674–12684. doi:10.1021/ie202695v.
- Kopp, G.A., Morrison, M.J., Gavanski, E., Henderson, D.J., and Hong, H.P. (2010). “Three Little Pigs” Project: Hurricane Risk Mitigation by Integrated Wind Tunnel and Full-Scale Laboratory Tests. *Nat. Hazards Rev.* 11 (4):151–161. doi:10.1061/(asce)nh.1527-6996.0000019.
- Kostiuk, L.W., Majeski, A.J., Poudenx, P., Johnson, M.R., and Wilson, D.J. (2000). Scaling of wake-stabilized jet diffusion flames in a transverse air stream. *Proc. Combust. Inst.* 28 (1):553–559. doi:10.1016/S0082-0784(00)80255-6.
- Krause, D.F. and Leirvik, F. (2018). Field Measurement of BC Emissions from Rolvsnes Well Test Flare.
- Kuipers, E.W., Jarvis, B., Bullman, S.J., Cook, D.K., and McHugh, D.R. (1996). Combustion efficiency of natural gas flares; effect of wind speed, flow rate and pilots., in *The Emission Inventory: Key to Planning, Permit, Compliance and Reporting*, pp. 361–374.
- Lawal, M.S., Fairweather, M., Gogolek, P.E.G., Ingham, D.B., Ma, L., Pourkashanian, M., and Williams, A. (2013). CFD predictions of wake-stabilised jet flames in a cross-flow. *Energy* 53:259–269.
- Li, Y., Henze, D.K., Jack, D., Henderson, B.H., and Kinney, P.L. (2016). Assessing public health burden associated with exposure to ambient black carbon in the United States. *Sci. Total Environ.* 539:515–525. doi:10.1016/j.scitotenv.2015.08.129.
- Luben, T.J., Nichols, J.L., Dutton, S.J., Kirrane, E., Owens, E.O., Datko-Williams, L., Madden, M., and Sacks, J.D. (2017). A systematic review of cardiovascular emergency department visits, hospital admissions and mortality associated with ambient black carbon. *Environ. Int.* 107 (January):154–162. doi:10.1016/j.envint.2017.07.005.
- Lyon, D.R., Hmiel, B., Gautam, R., Omara, M., Roberts, K., Barkley, Z.R., Davis, K.J., Miles, N.L., Monteiro, V.C., Richardson, S.J., Conley, S.A., Smith, M.L., Jacob, D.J., Shen, L., Varon, D.J., Deng, A., Rudelis, X., Sharma, N., Story, K.T., Brandt, A.R., Kang, M., Kort, E.A., Marchese, A.J., and Hamburg, S.P. (2021). Concurrent variation in oil and gas methane emissions and oil price during the COVID-19 pandemic. *Atmos. Chem. Phys.* 21 (9):6605–6626. doi:10.5194/acp-21-6605-2021.
- McDaniel, M. (1983). Flare efficiency study (No. EPA-600/2-83-052). United States Environmental Protection Agency, Research Triangle Park, NC.
- McEwen, J.D.N. and Johnson, M.R. (2012). Black carbon particulate matter emission factors for buoyancy-driven associated gas flares. *J. Air Waste Manage. Assoc.* 62 (3):307–321. doi:10.1080/10473289.2011.650040.
- Mehr, P. (2020). Experimental Modelling of Black Carbon Emissions from Gas Flares in the Oil and Gas Sector. Carleton University.
- Miguel, R.B., Talebi-Moghaddam, S., Zamani, M., Turcotte, C., and Daun, K. (2021). Assessing Flare Combustion Efficiency using Imaging Fourier Transform Spectroscopy. *J. Quant. Spectrosc. Radiat. Transf.* 273:107835. doi:10.1016/j.jqsrt.2021.107835.

- Mølhave, L., Clausen, G., Berglund, B., De Ceaurriz, J., Kettrup, A., Lindvall, T., Maroni, M., Pickering, A.C., Risse, U., Rothweiler, H., Seifert, B., and Younes, M. (1997). Total Volatile Organic Compounds (TVOC) in indoor air quality investigations. *Indoor Air* 7 (4):225–240. doi:10.1111/j.1600-0668.1997.00002.x.
- Mydlarski, L. (2017). A turbulent quarter century of active grids: From Makita (1991) to the present. *Fluid Dyn. Res.* 49 (6). doi:10.1088/1873-7005/aa7786.
- Ohio EPA (2012). Understanding the Basics of Gas Flaring. Ohio Environmental Protection Agency, Columbus, OH.
- Pohl, J.H. and Soelberg, N.R. (1985). Evaluation of the efficiency of industrial flares: Flare head design and gas composition (No. EPA-600/2-85-106). United States Environmental Protection Agency, Research Triangle Park, NC.
- Pohl, J.H., Tichenor, B.A., Lee, J., and Payne, R. (1986). Combustion Efficiency of Flares. *Combust. Sci. Technol.* 50 (4–6):217–231. doi:10.1080/00102208608923934.
- Poudenx, P. (2000). Plume sampling of a flare in crosswind: structure and combustion efficiency (M.Sc. Thesis). University of Alberta, Edmonton, AB, Canada, Edmonton.
- Saffaripour, M., Kholghy, M., Dworkin, S.B., and Thomson, M.J. (2013). A numerical and experimental study of soot formation in a laminar coflow diffusion flame of a Jet A-1 surrogate. *Proc. Combust. Inst.* 34 (1):1057–1065. doi:10.1016/j.proci.2012.06.176.
- Sand, M., Berntsen, T.K., Von Salzen, K., Flanner, M.G., Langner, J., and Victor, D.G. (2016). Response of Arctic temperature to changes in emissions of short-lived climate forcers. *Nat. Clim. Chang.* 6 (3):286–289. doi:10.1038/nclimate2880.
- Seymour, S.P. and Johnson, M.R. (2021). Species correlation measurements in turbulent flare plumes: considerations for field measurements. *Atmos. Meas. Tech.* 14 (7):5179–5197. doi:10.5194/amt-14-5179-2021.
- Siegel, K.D. (1980). Degree of conversion of flare gas in refinery high flares (Ph.D. Thesis). Fridericiana University Karlsruhe, Germany.
- Sorrels, J.L. and Coburn, J. (2019). Section 3 VOC Controls. *EPA Air Pollut. Control Cost Man.* 71.
- Spellicy, R.L., Phillips, W.J., Crow, W.L., Stopper, B.E., and Olsen, K.N.T. (2006). Passive FTIR Measurements of Flare Combustion Efficiencies By., in *Proceedings of the Air and Waste Management Association's Annual Conference and Exhibition*, .
- Stroscher, M.T. (2000). Characterization of emissions from diffusion flare systems *J. Air Waste Manage. Assoc.*
- Stroscher, M.T. (1996). Investigation of Flare Gas Emissions in Alberta. Calgary, Alberta.
- Talebi, A., Fatehifar, E., Alizadeh, R., and Kahforoushan, D. (2014). The Estimation and Evaluation of New CO, CO₂, and NO_x Emission Factors for Gas Flares Using Pilot Scale Flare. *Energy Sources, Part A Recover. Util. Environ. Eff.* 36 (7):719–726. doi:10.1080/15567036.2011.584117.
- Torres, V.M., Herndon, S.C., and Allen, D.T. (2012a). Industrial flare performance at low flow conditions. 2. Steam- and air-assisted flares. *Ind. Eng. Chem. Res.* 51 (39):12569–12576. doi:10.1021/ie202675f.
- Torres, V.M., Herndon, S.C., Kodesh, Z., and Allen, D.T. (2012b). Industrial flare performance at

- low flow conditions. 1. Study overview. *Ind. Eng. Chem. Res.* 51 (39):12559–12568. doi:10.1021/ie202674t.
- Torres, V.M., Herndon, S.C., Wood, E., Al-Fadhli, F.M., and Allen, D.T. (2012c). Emissions of Nitrogen Oxides from Flares Operating at Low Flow Conditions. *Ind. Eng. Chem. Res.* 51 (39):12600–12605. doi:10.1021/ie300179x.
- Tyner, D.R. and Johnson, M.R. (2020). Improving Upstream Oil and Gas Emissions Estimates with Updated Gas Composition Data. Carleton University Energy & Emissions Research Lab., Ottawa, ON.
- U.S. EPA (2018). AP 42 - Compilation of Air Pollutant Emission Factors, Volume I, Section 13.5 Industrial Flares. Research Triangle Park, NC.
- UCSD (2016). Chemical-Kinetic Mechanisms for Combustion Applications *San Diego Mech. web page*.
- Vagelopoulos, C.M. and Egolfopoulos, F.N. (1998). Direct experimental determination of laminar flame speeds. *Symp. Combust.* 27 (1):513–519. doi:10.1016/S0082-0784(98)80441-4.
- Weyant, C.L., Shepson, P.B., Subramanian, R., Cambaliza, M.O.L.L., Heimbürger, A., McCabe, D., Baum, E., Stirm, B.H., and Bond, T.C. (2016). Black carbon emissions from associated natural gas flaring. *Environ. Sci. Technol.* 50 (4):2075–2081. doi:10.1021/acs.est.5b04712.
- Wormhoudt, J., Herndon, S.C., Franklin, J., Wood, E.C., Knighton, B., Evans, S., Laush, C., Sloss, M., and Spellicy, R. (2012). Comparison of remote sensing and extractive sampling measurements of flare combustion efficiency. *Ind. Eng. Chem. Res.* 51 (39):12621–12629. doi:10.1021/ie202783m.
- Yang, J. and Chang, P. (2006). Evaluating Flare Abatement Efficiencies by Open-Path and Extractive Fourier Transform Infrared Technology., in *Proceedings of the Air & Waste Management Association Annual Meeting & Exhibition*, .
- Zamani, M., Abbasi-Atibeh, E., Mobaseri, S., Ahsan, H., Ahsan, A., Olfert, J.S., and Kostjuk, L.W. (2021). An experimental study on the carbon conversion efficiency and emission indices of air and steam co-flow diffusion jet flames. *Fuel* 287 (August 2020):119534. doi:10.1016/j.fuel.2020.119534.
- Zang, K., Zhang, G., and Wang, J. (2020). Methane emissions from oil and gas platforms in the Bohai Sea, China. *Environ. Pollut.* 263:114486. doi:10.1016/j.envpol.2020.114486.
- Zavala-Araiza, D., Omara, M., Gautam, R., Smith, M.L., Pandey, S., Aben, I., Almanza-Veloz, V., Conley, S., Houweling, S., Kort, E.A., Maasackers, J.D., Molina, L.T., Pusuluri, A., Scarpelli, T., Schwietzke, S., Shen, L., Zavala, M., and Hamburg, S.P. (2021). A tale of two regions: Methane emissions from oil and gas production in offshore/onshore Mexico. *Environ. Res. Lett.* 16 (2). doi:10.1088/1748-9326/abceeb.
- Zeng, Y., Morris, J., and Dombrowski, M. (2016). Validation of a new method for measuring and continuously monitoring the efficiency of industrial flares. *J. Air Waste Manage. Assoc.* 66 (1):76–86. doi:10.1080/10962247.2015.1114045.

Appendix A Supporting Information for Quantifying Combustion Efficiencies and Species Emission Rates of Flares Subjected to Crosswind

This Appendix is included as the Supplementary Information (SI) to the article from Chapter 4 submitted for peer review to Journal of the Energy Institute on April 17, 2022. This paper was co-authored by the thesis author, Damon Burt and his M.A.Sc. supervisor Prof. Matthew Johnson, with contributions from Darcy Corbin, Joshua Armitage, Brian Crosland, Melina Jefferson, Gregory Kopp and Larry Kostiuk. Mr. Burt produced the synthetic data and calculated the associated uncertainties via Monte Carlo Uncertainty Analysis. Retrofitting of the closed-loop wind tunnel and subsequent instrumentation to perform controlled combustion experiments was led by Darcy Corbin and Matthew Johnson. Experimental validation measurements, as well as writing and editing of the manuscript were performed jointly.

This Appendix should be cited as:

D.C. Burt, D.J. Corbin, J.R. Armitage, B.M. Crosland, A.M. Jefferson, G.A. Kopp, L.W. Kostiuk, M.R. Johnson (2022), A Methodology for Quantifying Combustion Efficiencies and Species Emission Rates of Flares Subjected to Crosswind, Journal of the Energy Institute, submitted April 17, 2022 (manuscript id: JOTEI-D-22-00359)

A.1 Derivation of the Simplified Species Balance Equation

This section shows the detailed derivation of the simplified species balance, Eq. (4.5 of the main text). For a fixed-volume control volume (CV, Figure 4.1 in the main text), consisting of the internal volume of a closed-loop wind tunnel but excluding the flame, the species mass balance can be written as:

$$\frac{dm_{i,cv}}{dt} = \dot{m}_{i,prod,comb} + \dot{m}_{i,inert,f} + \dot{m}_{i,in} - \dot{m}_{i,ex} \pm \dot{m}_{i,r} \quad \text{B.1}$$

As in the main text, terms in Eq. B.1 are defined as follows:

$m_{i,cv}$ is the mass of species i in the CV,

$\dot{m}_{i,prod,comb}$ is the mass emission rate of species i produced from combustion (including any amount of species i emitted as un-combusted hydrocarbon material originating in the flare gas) and entering the CV,

$\dot{m}_{i,inert}$ is the mass emission rate of species i originating as an inert species in the flare gas (e.g. non-reacting CO₂ in the flare gas) and entering the CV,

$\dot{m}_{i,in}$ is the mass infiltration rate of species i transported as a component of the ambient air leaking into the CV,

$\dot{m}_{i,ex}$ is the mass exfiltration rate of species i from the CV, which includes exfiltration driven by static pressure differences between the interior of the CV and the surrounding environment as well as exfiltration driven by thermal expansion as the CV warms (due to heat transfer from the CV drive system as well as from the flare), and

$\dot{m}_{i,r}$ is the rate of creation or destruction of mass of species i due to reburning of species in the CV that exit the CV and subsequently enter the flame as a component of the combustion air. The sign (\pm) on this term is species specific, where a fraction of the accumulated hydrocarbons (denoted by the subscript HC) in the CV could be destroyed in the flame (e.g. $-\dot{m}_{HC,r}$) and additional products could be formed from this reburning (e.g. $+\dot{m}_{CO_2,r}$) and emitted back into the CV.

Although the reburning term, $\dot{m}_{i,r}$ is potentially relevant as a sink for hydrocarbons and as a source for CO₂, H₂O, or possibly CO, it will be shown to be negligible in a practical experiment. Thus, for simplicity when considering this term, it can be assumed that the flame is 100% efficient in consuming hydrocarbons in the combustion air and converting them to CO₂. Since the concentration of hydrocarbons in the CV will always be small during experiments, the implications of assuming perfect combustion during reburning are negligible. For a species mass balance on CO₂ in the CV, the reburning term can then be written as:

$$+\dot{m}_{CO_2,r} = +\rho_{CO_2}^o x X_{HC,cv} \dot{V}_{air,comb} \quad \text{B.2}$$

where:

$X_{HC,cv}$ is the mole fraction of hydrocarbons contained in the CV air,

x is the average number of carbon atoms in the hydrocarbons in the CV,

$\dot{V}_{air,comb}$ is the volume of CV air required for combustion of the flare gas (where it is further noted that $\dot{V}_{air,comb}$ will be reduced accordingly relative to the theoretical stoichiometric value if the flare combustion is incomplete), and

$\rho_{CO_2}^o$ is the density of pure CO₂ (calculated at the same temperature and pressure conditions as $\dot{V}_{air,comb}$).

Similarly for each specific hydrocarbon species in the CV, the reburning term can be written as:

$$-\dot{m}_{i,r}|_{i=HC} = -[\rho_i^o X_i]_{i=HC} \dot{V}_{air,comb} \quad B.3$$

where:

X_i is the mole fraction of the hydrocarbon of interest within the CV, and

ρ_i^o is pure species density of the hydrocarbon of interest calculated at the same temperature and pressure conditions as $\dot{V}_{air,comb}$.

The mass of species i emitted in the plume of the flare, $\dot{m}_{i,p}$, may be defined as the sum of the mass emission rate of species i produced through combustion and any mass flow rate of species i originating as an inert component of the flare gas that passes through the flame and is released into the combustion plume.

$$\dot{m}_{i,prod,comb} + \dot{m}_{i,inert,f} = \dot{m}_{i,p} \quad B.4$$

Eq. B.1 can then be simplified to Eq. (4.1) of the main text:

$$\frac{dm_{i,cv}}{dt} = \dot{m}_{i,p} + \dot{m}_{i,in} - \dot{m}_{i,ex} \pm \dot{m}_{i,r} \quad (4.1)$$

Applying the following form of the ideal gas law converts mass flows to volume flows:

$$\dot{m}_i = \frac{M_i \dot{V} X_i P}{R_u T} \quad B.5$$

where:

X_i denotes the mole fraction of species i ,

M_i is the molar mass of species i ,

T is temperature,

P is pressure, and

R_u is the universal ideal gas constant.

Assuming the volume of the CV (V_{cv}) is constant, the constituents within the CV are well-mixed, and the mean pressure within the CV (P_{cv}) is constant and equal to the ambient pressure outside the CV (P_∞), while acknowledging the existence of a small pressure gradient within the CV, Eq. (4.1) can be written as:

$$\begin{aligned} \left(\frac{M_i P_\infty}{R_u}\right) V_{cv} \frac{d}{dt} \left(\frac{X_{i,cv}}{T_{cv}}\right) &= \frac{M_i P_p X_{i,p} \dot{V}_p}{R_u T_p} + \frac{M_i P_\infty X_{i,\infty} \dot{V}_{in}}{R_u T_\infty} - \frac{M_i P_\infty X_{i,cv} \dot{V}_{ex}}{R_u T_{cv}} \\ &- \left\{ \frac{M_i P_p X_{i,cv} \dot{V}_{air,comb}}{R_u T_p} \right\}_{i=HC} + \left\{ \frac{M_i P_p X_{HC,cv} \dot{V}_{air,comb}}{R_u T_p} \right\}_{i=CO_2} \end{aligned} \quad B.6$$

where:

T_{cv} is the temperature of the well-mixed gases within the CV,

T_p is the temperature of the hot gases emitted from the flare gas combustion,

T_∞ is the ambient temperature of the air outside the CV,

P_p is the ambient pressure in the CV at the flare location,

$X_{i,cv}$ is the mole fraction of species i within the CV,

$X_{i,p}$ is the mole fraction of species i in the hot gases emitted from the flare gas combustion including any inert species present in the fuel and emitted with the combustion products,

$X_{i,\infty}$ is the mole fraction of species i in the ambient air,

\dot{V}_p is the volume flow rate of the products from combustion of the flare stream,

\dot{V}_{in} is the volume flow rate of ambient air leaking into the CV, and

\dot{V}_{ex} is volume flow rate of CV air leaking out of the CV.

However, since $\frac{\dot{V}_p P_p}{T_p}$ is difficult to measure, the ideal gas law can be used to redefine this ratio at any chosen temperature and pressure. In this case, it is convenient to choose ambient conditions:

$$\frac{\dot{V}_p P_p}{T_p} = \frac{\dot{m}_p R_u}{M_p} = \text{constant} = \frac{\dot{V}_{p,\infty} P_\infty}{T_\infty} \quad \text{B.7}$$

Applying Eq. B.7 and simplifying allows Eq. B.6 to be written as Eq. (4.2) in the main text:

$$V_{cv} \frac{d}{dt} \left(\frac{X_{i,cv}}{T_{cv}} \right) = \frac{X_{i,p} \dot{V}_{p,\infty}}{T_\infty} + \frac{X_{i,\infty} \dot{V}_{in}}{T_\infty} - \frac{X_{i,cv} \dot{V}_{ex}}{T_{cv}} - \left\{ \frac{X_{i,cv} \dot{V}_{air,comb,\infty}}{T_\infty} \right\}_{i=HC} \quad (4.2)$$

$$+ \left\{ \frac{x X_{HC,cv} \dot{V}_{air,comb,\infty}}{T_\infty} \right\}_{i=CO_2}$$

The left-hand side of Eq. (4.2) can be expanded using the quotient rule:

$$\frac{V_{cv}}{T_{cv}} \frac{dX_{i,cv}}{dt} - X_{i,cv} \frac{V_{cv}}{T_{cv}^2} \frac{dT_{cv}}{dt} = \frac{X_{i,p} \dot{V}_{p,\infty}}{T_\infty} + \frac{X_{i,\infty} \dot{V}_{in}}{T_\infty} - \frac{X_{i,cv} \dot{V}_{ex}}{T_{cv}} \quad \text{B.8}$$

$$- \left\{ \frac{X_{i,cv} \dot{V}_{air,comb,\infty}}{T_\infty} \right\}_{i=HC} + \left\{ \frac{x X_{HC,cv} \dot{V}_{air,comb,\infty}}{T_\infty} \right\}_{i=CO_2}$$

Since \dot{V}_{ex} is unknown and difficult to measure, an overall mass balance expression for the CV can be used to determine the exfiltration flow rate as a function of the remaining flow rates. As shown in the main text, the overall mass balance can be written as follows:

$$\frac{dm_{cv}}{dt} = \dot{m}_p + \dot{m}_{in} - \dot{m}_{ex} - \dot{m}_{air,comb} = \dot{m}_f + \dot{m}_{in} - \dot{m}_{ex} \quad (4.3)$$

where:

\dot{m}_p is the mass flow rate of emitted products formed via combustion of the flare stream (which includes mass emission of any inert components in the flare gas passing through the

flame, but specifically excludes and species produced via reburning of hydrocarbon species present in the combustion air as shown in Figure 1 of the main text),

$\dot{m}_{air,comb}$ is the mass flow rate of air required for combustion of the flare stream, which is defined to specifically exclude the mass of any hydrocarbons involved in reburning again as shown in Figure 4.1, and

\dot{m}_f is the mass flow rate of flare gas (including any inert species) which is thus equal to $\dot{m}_p - \dot{m}_{air,comb}$.

As also illustrated in Figure 4.1, the mass flow rate of any potentially reactive species in the CV (e.g. hydrocarbons in the combustion air, $\dot{m}_{HC,r}$) leaving the CV as part of the combustion air, plus any extra oxygen (\dot{m}_{O_2}) required to reburn them, is exactly balanced by the mass flow rate of reburned products re-entering the CV (e.g. $\dot{m}_{CO_2,r}$, $\dot{m}_{H_2O,r}$, $\dot{m}_{CO,r}$). Thus, none of these terms appear in Eq. (4.3).

Similar to the species mass balance, the total mass within the CV can be written in terms of the ideal gas law. Assuming that the average pressure within the CV remains effectively constant and equal to the ambient pressure outside the tunnel, P_∞ , and that the mean molecular mass of the gases within the CV, M_{cv} , is effectively constant (i.e. noting that the volume of the CV is 200-5000 times larger than the total volume of products introduced during an experiment), then the left side of Eq. (4.3) becomes:

$$\frac{dm_{cv}}{dt} = \frac{d}{dt} \left(\frac{P_\infty V_{cv} M_{cv}}{R_u T_{cv}} \right) = \frac{P_\infty V_{cv} M_{cv}}{R_u} \frac{d}{dt} \left(\frac{1}{T_{cv}} \right) \quad \text{B.9}$$

Manipulating Eq. B.9 using the quotient rule gives:

$$\frac{dm_{cv}}{dt} = - \frac{P_\infty V_{cv} M_{cv}}{R_u T_{cv}^2} \frac{dT_{cv}}{dt} \quad \text{B.10}$$

Substituting this result back into Eq. (4.3) and rewriting the remaining terms on the right side using the ideal gas law provides Eq. (4.4) in the main text:

$$- \frac{P_\infty V_{cv} M_{cv}}{R_u T_{cv}^2} \frac{dT_{cv}}{dt} = \frac{P_\infty}{R_u} \left(\frac{M_f \dot{V}_{f,\infty}}{T_\infty} + \frac{M_\infty \dot{V}_{in}}{T_\infty} - \frac{M_{cv} \dot{V}_{ex}}{T_{cv}} \right) \quad (4.4)$$

where $\dot{V}_{f,\infty}$ is the volume flow rate of flare gas referenced at ambient conditions, M_f is the molecular weight of the flare gas, and M_∞ is the molecular weight of the ambient air.

Cancelling the $\frac{P_\infty}{R_u}$ terms and solving for \dot{V}_{ex} :

$$\dot{V}_{ex} = \frac{T_{cv}}{M_{cv}} \left(\frac{V_{cv} M_{cv}}{T_{cv}^2} \frac{dT_{cv}}{dt} + \frac{M_f \dot{V}_{f,\infty}}{T_\infty} + \frac{M_\infty \dot{V}_{in}}{T_\infty} \right) \quad \text{B.11}$$

Substituting Eq. B.11 into Eq. B.8, eliminating \dot{V}_{ex} in the species balance:

$$\begin{aligned} \frac{V_{cv}}{T_{cv}} \frac{dX_{i,cv}}{dt} - X_{i,cv} \frac{V_{cv}}{T_{cv}^2} \frac{dT_{cv}}{dt} &= \frac{X_{i,p} \dot{V}_{p,\infty}}{T_\infty} + \frac{X_{i,\infty} \dot{V}_{in}}{T_\infty} - \\ \frac{X_{i,cv}}{M_{cv}} \left(\frac{V_{cv} M_{cv}}{T_{cv}^2} \frac{dT_{cv}}{dt} + \frac{M_f \dot{V}_{f,\infty}}{T_\infty} + \frac{M_\infty \dot{V}_{in}}{T_\infty} \right) &- \left\{ \frac{X_{i,cv} \dot{V}_{air,comb,\infty}}{T_\infty} \right\}_{i=HC} \\ &+ \left\{ \frac{x X_{HC,cv} \dot{V}_{air,comb,\infty}}{T_\infty} \right\}_{i=CO_2} \end{aligned} \quad B.12$$

Expanding the bracketed term on the right-hand side of Eq. B.12 reveals that the term containing the temperature-time derivative appears on both sides of the equation and cancel:

$$\begin{aligned} \frac{V_{cv}}{T_{cv}} \frac{dX_{i,cv}}{dt} &= \frac{X_{i,p} \dot{V}_{p,\infty}}{T_\infty} + \frac{X_{i,\infty} \dot{V}_{in}}{T_\infty} - X_{i,cv} \frac{M_f \dot{V}_{f,\infty}}{M_{cv} T_\infty} - X_{i,cv} \frac{M_\infty \dot{V}_{in}}{M_{cv} T_\infty} - \left\{ \frac{X_{i,cv} \dot{V}_{air,comb,\infty}}{T_\infty} \right\}_{i=HC} \\ &+ \left\{ \frac{x X_{HC,cv} \dot{V}_{air,comb,\infty}}{T_\infty} \right\}_{i=CO_2} \end{aligned} \quad B.13$$

Multiplying both sides of Eq. B.13 by T_{cv} gives Eq. (4.5) in the main text:

$$\begin{aligned} V_{cv} \frac{dX_{i,cv}}{dt} &= \frac{X_{i,p} \dot{V}_{p,\infty} T_{cv}}{T_\infty} + \frac{X_{i,\infty} \dot{V}_{in} T_{cv}}{T_\infty} - X_{i,cv} \frac{M_f \dot{V}_{f,\infty} T_{cv}}{M_{cv} T_\infty} - X_{i,cv} \frac{M_\infty \dot{V}_{in} T_{cv}}{M_{cv} T_\infty} \\ &- \left\{ \frac{X_{i,cv} \dot{V}_{air,comb,\infty} T_{cv}}{T_\infty} \right\}_{i=HC} + \left\{ \frac{x X_{HC,cv} \dot{V}_{air,comb,\infty} T_{cv}}{T_\infty} \right\}_{i=CO_2} \end{aligned} \quad (4.5)$$

A.2 Limit Approach to Determine Species Emission Rates

Eq. (4.5) is valid for all times during a simulation. To simplify further, as noted in Section 4.3.2 of the manuscript, it is useful to consider limiting conditions near the start of an experiment ($t \rightarrow t_0$) when all properties in the CV approach ambient conditions, such that $X_{i,cv} \rightarrow X_{i,\infty}$, $T_{cv} \rightarrow T_\infty$, $M_{cv} \rightarrow M_\infty$, $X_{HC,cv} \rightarrow X_{HC,\infty}$. In this limit, Eq. (4.5) becomes:

$$\begin{aligned} V_{cv} \left. \frac{dX_{i,cv}}{dt} \right|_{t \rightarrow t_0} &= X_{i,p} \dot{V}_{p,\infty} + X_{i,\infty} \dot{V}_{in} - X_{i,\infty} \frac{M_f}{M_\infty} \dot{V}_{f,\infty} - X_{i,\infty} \dot{V}_{in} \\ &- \left\{ X_{i,\infty} \dot{V}_{air,comb,\infty} \right\}_{i=HC} + \left\{ x X_{HC,\infty} \dot{V}_{air,comb,\infty} \right\}_{i=CO_2} \end{aligned} \quad B.14$$

The terms containing \dot{V}_{in} on the right-hand side cancel and Eq. B.14 can be rearranged as follows to give Eq. (4.6) in the main text:

$$\begin{aligned} V_{cv} \left. \frac{dX_{i,cv}}{dt} \right|_{t \rightarrow t_0} &= X_{i,p} \dot{V}_{p,\infty} - X_{i,\infty} \frac{M_f}{M_\infty} \dot{V}_{f,\infty} - \left\{ X_{i,\infty} \dot{V}_{air,comb,\infty} \right\}_{i=HC} \\ &+ \left\{ x X_{HC,\infty} \dot{V}_{air,comb,\infty} \right\}_{i=CO_2} \end{aligned} \quad (4.6)$$

Table A1 shows the expected order of magnitude of the remaining four terms appearing on the right side of Eq. (4.6). The values shown were calculated for a flare burning CH₄ at different assumed carbon conversion efficiencies (defined as the percentage of carbon in the fuel that is fully converted to CO₂). For cases with assumed efficiencies less than 100%, the unconverted fuel carbon is assumed in this simulation to be split equally between emissions of CO and CH₄. The calculations assume combustion with air (79% N₂, 21% O₂) containing typical background volume fractions of CO₂ at 400 ppm, CH₄ at 2 ppm, and CO at 1 ppm. As shown in the table, the reburning term for CO₂ is negligible in all cases, with a magnitude less than 0.002% of the first term (plume term) on the right side of Eq.(4.6). Similarly, the second term on the right of Eq. (4.6) (related to the infiltration of ambient air into the CV) should be negligible in all cases.

The reburning term in a species balance on methane (third term on right side of Eq. (4.6)) is more nuanced. At an assumed efficiency of 100%, the plume term would be zero, leaving the reburning term as the only relevant term, suggesting that in principle, the flame could destroy methane present in the ambient air. However, for flare carbon conversion efficiencies below 99.96%, the magnitude of the reburning term falls to less than 10% of that of the plume term, and less than the 1% of the plume term as efficiencies decrease beyond 99.6%. Keeping the hydrocarbon reburning term in place, Eq. (4.6) can be simplified to represent the volumetric emission rate of any species *i* in the CV, defined as $X_{i,p}\dot{V}_{p,\infty}$:

$$X_{i,p}\dot{V}_{p,\infty} = V_{cv} \left. \frac{dX_{i,cv}}{dt} \right|_{t \rightarrow t_0} + X_{i,\infty} \frac{M_f}{M_\infty} \dot{V}_{f,\infty} + \{X_{i,\infty} \dot{V}_{air,comb,\infty}\}_{i=HC} \quad (4.7)$$

An emission rate on a mass basis can then be calculated using:

$$\dot{m}_{i,p} = \rho_{i,\infty}^o X_{i,p} \dot{V}_{p,\infty} = \rho_{i,\infty}^o \left(V_{cv} \left. \frac{dX_{i,cv}}{dt} \right|_{t \rightarrow t_0} + X_{i,\infty} \frac{M_f}{M_\infty} \dot{V}_{f,\infty} + \{X_{i,\infty} \dot{V}_{air,comb,\infty}\}_{i=HC} \right) \quad (4.8)$$

Table A1: Estimated relative order of magnitude of terms on right side of Eq. (4.6) when written for different species calculated for a flare burning CH₄ at a nominal reference flow rate of 1 m³/s at various carbon conversion efficiencies. All terms have units of m³/s unless otherwise specified. Values in parentheses indicate percentage of Term 1 on right side of Eq. (4.6).

Species	CO ₂		CO		CH ₄				
Carbon Conversion Efficiency, η [%]	100	70	99.96	70	99.96	99.9	99.6	90	70
$\dot{V}_{air,comb,\infty}$	9.520	7.735	9.518	7.735	9.518	9.514	9.496	8.925	7.735
$X_{i,p}$ [-]	0.0951	0.0801	1.90×10^{-5}	0.0172	1.90×10^{-5}	4.76×10^{-5}	1.91×10^{-4}	5.04×10^{-3}	1.72×10^{-2}
$X_{i,\infty}$ [-]	4.00×10^{-4}	4.00×10^{-4}	1.00×10^{-6}	1.00×10^{-6}	2.00×10^{-6}				
$\dot{V}_{f,\infty}$	1	1	1	1	1	1	1	1	1
$\dot{V}_{p,\infty}$	10.52	8.74	10.52	8.74	10.52	10.51	10.50	9.93	8.74
Term 1, $\dot{V}_{p,\infty} X_{i,p}$	1.00 (100%)	0.70 (100%)	2.00×10^{-4} (100%)	0.150 (100%)	2.00×10^{-4} (100%)	5.00×10^{-4} (100%)	2.00×10^{-3} (100%)	5.00×10^{-2} (100%)	1.50×10^{-1} (100%)
Term 2, $X_{i,\infty} \frac{M_f}{M_\infty} \dot{V}_{f,\infty}$	2.22×10^{-4} (0.022%)	2.22×10^{-4} (0.032%)	5.54×10^{-7} (0.277%)	5.54×10^{-7} (0.000%)	1.11×10^{-6} (0.554%)	1.11×10^{-6} (0.222%)	1.11×10^{-6} (0.055%)	1.11×10^{-6} (0.002%)	1.11×10^{-6} (0.001%)
Term 3, $\{X_{i,\infty} \dot{V}_{air,comb,\infty}\}_{i=HC}$	n/a	n/a	n/a	n/a	1.90×10^{-5} (9.52%)	1.90×10^{-5} (3.81%)	1.90×10^{-5} (0.95%)	1.79×10^{-5} (0.04%)	1.55×10^{-5} (0.01%)
Term 4, $\{x X_{HC,\infty} \dot{V}_{air,comb,\infty}\}_{i=CO_2}$	1.90×10^{-5} (0.002%)	1.55×10^{-5} (0.002%)	n/a						

A.2.1 Evaluation of $\dot{V}_{air,comb,\infty}$

In principle the required combustion air in the hydrocarbon reburning term, $\dot{V}_{air,comb,\infty}$, depends on the carbon conversion efficiency of the flare and the relative amounts of CO, unburned fuel, or other carbon species in the products. However, as the carbon conversion efficiency approaches 100%, $\dot{V}_{air,comb,\infty}$ approaches its readily calculated stoichiometric value for complete combustion. Conveniently, as shown in Table A1, the magnitude of the reburning term is largest (and its relevance in Eq. (4.7) and (4.8) maximized) as a calculation of $\dot{V}_{air,comb,\infty}$ assuming complete combustion approaches perfect accuracy. Conversely, as the carbon conversion efficiency drops, the magnitude and relevance of the reburning term rapidly falls. Thus, $\dot{V}_{air,comb,\infty}$ within the reburning term may be assumed equal to its stoichiometric value for complete combustion in all cases. This assumption was further verified by calculating methane emission rates assuming either the stoichiometric value for $\dot{V}_{air,comb,\infty}$ or its actual value given

the composition of combustion products for all cases shown in Table A1. Results showed that the two sets of values agreed within 0.00238% in all cases.

A.3 General Fitting Solution to Calculate Species Accumulation Rates

A.3.1 Mathematical Form of Concentration Rise in the Tunnel

As discussed in Section 4.3.2 of the main text, the initial accumulation rate of a species of interest can be accurately determined by fitting the expected functional form to the measured trend of the time-varying concentration rise in the CV. The expected form is the solution to a non-linear ordinary differential equation with two time-varying coefficients (concentration and temperature), which can be obtained by first collecting like terms in Eq. (4.5):

$$\frac{dX_{i,cv}(t)}{dt} = T_{cv}(t) \left(\frac{(X_{i,p}\dot{V}_{p,\infty} + X_{i,\infty}\dot{V}_{in})}{V_{cv}T_{\infty}} - X_{i,cv}(t) \frac{\left(\frac{M_f}{M_{cv}}\dot{V}_{f,\infty} + \frac{M_{\infty}}{M_{cv}}\dot{V}_{in}\right)}{V_{cv}T_{\infty}} - \left\{ X_{i,cv}(t) \frac{\dot{V}_{air,comb,\infty}}{V_{cv}T_{\infty}} \right\}_{i=HC} + \left\{ x(t)X_{HC,cv}(t) \frac{\dot{V}_{air,comb,\infty}}{V_{cv}T_{\infty}} \right\}_{i=CO_2} \right) \quad \text{B.15}$$

Table A2 summarizes the estimated order of magnitudes of each term on the right-hand side of Eq. B.15 at the end of a 10-minute experiment for a flare burning CH₄ at flow rates of up to 1000 SLPM. The fourth term, which accounts for the additional CO₂ produced from reburning, is shown to account for less than 0.3% of the right-hand side of Eq. B.15 for all considered scenarios and is much smaller for most cases. A similar analysis considering flares burning propane also demonstrated the CO₂ reburning term as negligible, accounting for less than 0.8% of the right-hand side of Eq. B.15 in all cases. Thus, for the purpose of fitting experimental data, this term is ignored due to the added complexity of the ordinary differential equation solution caused by the $X_{HC,cv}(t)$ term varying with respect to time, and the species balance is simplified to:

$$\frac{dX_{i,cv}(t)}{dt} = T_{cv}(t) \left(\frac{(X_{i,p}\dot{V}_{p,\infty} + X_{i,\infty}\dot{V}_{in})}{V_{cv}T_{\infty}} - X_{i,cv}(t) \frac{\left(\frac{M_f}{M_{cv}}\dot{V}_{f,\infty} + \frac{M_{\infty}}{M_{cv}}\dot{V}_{in}\right)}{V_{cv}T_{\infty}} - \left\{ X_{i,cv}(t) \frac{\dot{V}_{air,comb,\infty}}{V_{cv}T_{\infty}} \right\}_{i=HC} \right) \quad (4.6)$$

Table A2: Estimated order of magnitude of terms in Eq. B.15 when $i = \text{CO}_2$ for a flare burning CH_4 for 10 minutes at various flow rates and carbon conversion efficiencies.

Fuel Flow Rates (L/min)	20				100				1000			
Carbon Conversion Efficiency, η (%)	99	90	80	70	99	90	80	70	99	90	80	70
$X_{i,p}$ [-]	0.0946	0.0905	0.0853	0.0795	0.0946	0.0905	0.0853	0.0795	0.0946	0.0905	0.0853	0.0795
$X_{i,\infty}$ [ppm _v]	400											
$\dot{V}_{f,\infty} \times 10^3$ [m ³ /s]	0.333				1.67				16.7			
$\dot{V}_{air,comb,\infty} \times 10^3$ [m ³ /s]	3.15	2.98	2.78	2.58	15.8	14.9	13.9	12.9	1578	149	139	129
$\dot{V}_{p,\infty} \times 10^3$ [m ³ /s]	3.49	3.32	3.13	2.94	17.4	16.6	15.6	14.7	174	166	156	147
M_∞ and M_{cv} [kg/kmol]	28.97											
M_f [kg/kmol]	16.04											
$X_{i,cv}(t)^a$ [ppm _v]	468	462	455	448	739	708	674	639	3783	3476	3134	2792
V_{cv} [m ³]	2000											
T_∞ [K]	293.15											
\dot{V}_{in} [air changes per hour]	5.00											
$x(t)^a$ [-]	1.00											
$X_{HC,cv}(t)^a$ [ppm _v]	2.34	5.42	8.84	12.3	3.70	19.1	36.2	53.2	18.7	170	338	506
Term 1 $\times 10^9$	2.46 52.6%	4.71 57.4%	2.35 52.2%	2.29 51.9%	4.71 57.4%	4.45 57.0%	4.17 56.6%	3.89 56.2%	30.0 62.5%	27.5 62.4%	24.6 62.2%	21.8 62.0%
Term 2 $\times 10^9$	2.22 47.4%	3.50 42.6%	2.15 47.8%	2.12 48.1%	3.50 42.6%	3.36 43.0%	3.19 43.4%	3.03 43.8%	18.0 37.4%	16.5 37.5%	14.9 37.6%	13.3 37.7%
Term 4 $\times 10^{14}$	1.26 0.00%	9.95 0.00%	4.19 0.00%	5.39 0.00%	9.95 0.00%	48.4 0.01%	85.6 0.01%	117 0.02%	502 0.01%	4302 0.10%	7995 0.20%	11129 0.32%

^a Evaluated near the end of an experiment at $t=600$ s

Eq. (4.6) can be rearranged by separating concentration and temperature and integrating from t_0 to t ,

$$\int_{t_0}^t \frac{dX_{i,cv}(t)}{A_i - B_i X_{i,cv}(t)} dt = \int_{t_0}^t T_{cv}(t) dt \quad \text{B.16}$$

$$\text{where: } A_i = \frac{X_{i,p} \dot{V}_{p,\infty} + X_{i,\infty} \dot{V}_{in}}{V_{cv} T_\infty},$$

$$B_i = \frac{\left(\frac{M_f}{M_{cv}} \dot{V}_{f,\infty} + \frac{M_\infty}{M_{cv}} \dot{V}_{in} + \{ \dot{V}_{air,comb,\infty} \}_{i=HC} \right)}{V_{cv} T_\infty}$$

Applying u-substitution, where

$$u = A_i - B_i X_{i,cv}(t) \quad \text{B.17}$$

$$\frac{du}{dt} = -B_i \frac{dX_{i,cv}(t)}{dt} \quad \text{B.18}$$

Eq. B.16 can be rewritten as:

$$-\frac{1}{B_i} \int_{t_0}^t \frac{du}{u} = \int_{t_0}^t T_{cv}(t) dt \quad \text{B.19}$$

Integration and subsequent substitution of Eq. B.17 and Eq. B.18 yields:

$$-\frac{1}{B_i} \ln|A_i - B_i X_{i,cv}(t)| + C = \int_{t_0}^t T_{cv}(t) dt \quad \text{B.20}$$

Taking the exponential of both sides of Eq. B.20 and rearranging,

$$e^{-B_i \left(\int_{t_0}^t T_{cv}(t) dt + C \right)} = A_i - B_i X_{i,cv}(t) \quad \text{B.21}$$

Solving B.21 for $X_{i,cv}(t)$,

$$X_{i,cv}(t) = \frac{A_i - e^{-B_i \left(\int_{t_0}^t T_{cv}(t) dt + C \right)}}{B_i} \quad \text{B.22}$$

Applying the product rule to Eq. B.22,

$$X_{i,cv}(t) = \frac{A_i - e^{C_i} e^{-B_i \left(\int_{t_0}^t T_{cv}(t) dt \right)}}{B_i} \quad \text{B.23}$$

Simplifying Eq. B.23 yields the solution to the ordinary differential equation in Eq. (4.6):

$$X_{i,cv}(t) = \frac{A_i - C_i e^{-B_i \left(\int_{t_0}^t T_{cv}(t) dt \right)}}{B_i} \quad (4.7)$$

where $C_i = A_i - B_i X_{i,\infty}$.

The integral containing the $T_{cv}(t)$ term can be explicitly evaluated from the start of a test, t_0 , to time t , while the parameters A_i , B_i , and C_i can be measured empirically by curve fitting the measured species concentrations using the Levenberg-Marquardt or similar algorithm. The slope of the concentration at time zero represents the accumulation rate at the start of the test, t_0 , and can be calculated by differentiating Eq. (4.7) and applying limiting conditions near the start of an experiment as $t \rightarrow t_0$:

$$\left. \frac{dX_{i,cv}}{dt} \right|_{t \rightarrow t_0} = -\frac{C_i}{B_i} \left(-B_i T_{cv}(t_0) e^{-B_i \left(\int_{t_0}^{t_0} T_{cv}(t) dt \right)} \right) \quad \text{B.24}$$

where the temperature integral evaluated from t_0 to t_0 is simply 0, while the B_i coefficients cancel out. The accumulation rate in Eq. B.24 can be simplified to Eq. (4.8) in the main text:

$$\left. \frac{dX_{i,cv}}{dt} \right|_{t \rightarrow t_0} = T_{cv}(t_0) (C_i) \quad (4.8)$$

A.3.2 Determining Test Start Time, t_0

A.3.2.1 Accounting for Analyzer Time Response

Accurate determination of the initial accumulation rate (slope) of the species mole fractions requires an objective determination of the test start time, t_0 , which depends on several factors. These are i) the time it takes fuel to travel from the mass flow controllers to the outlet of the burner; ii) the time it takes for new products of combustion to travel around the wind tunnel and reach the gas sample probe; iii) the time required for gas to travel from the gas probe to the gas analyzers; and iv) the response time of each gas analyzer. For this reason, the concentration trace of each measured gas species was analyzed independently to determine a nominal value for t_0 . This nominal value was then allowed to vary during the Monte Carlo uncertainty analysis to account for the effects of an uncertain value of t_0 .

Example gas analyzer readings (CO_2) for an experiment are shown in Figure A1. The pre-test ambient reading of about 440 ppm is visible on the far left, followed by a measured step increase starting at about 70 s when the first products of combustion are measured by the analyzer. The steps smooth out by the ~280 s mark due to the accumulated effects of mixing in the streamwise flow direction. Importantly, for each gas analyzer, the delay between the arrival of products at the probe and the measurement of these gases within the analyzer itself is effectively fixed, and is self-canceling when considering *durations* of time between two events. Thus, for simplicity, it can be assumed that the time at which the step increase occurs represents the moment when the products of combustion arrived at the sample probe, labelled as t_0^* in Figure A1.

However, the $1/e$ time-response of each analyzer (considering its internal sample cell volume and sample flow rate) must still be considered when interpreting data. In the present experiment, the measured quantity of interest is the time rate of change (i.e., the slope, k) of concentration within the wind tunnel. At the beginning of an experiment, the average mole fraction of an emitted species from the flare in the wind tunnel starts from a steady background value, $X_{i,\infty}$, and then undergoes an initially linear rise, $X_i(t)$, such that $X_i(t) = kt + X_{i,\infty}$. Considering the specified $1/e$ response time for each analyzer, it can readily be shown that rate of change in mole fraction measured by the analyzer $\frac{dX_i}{dt}$ relates to the actual slope k as follows:

$$\frac{dX_i}{dt} = k \left(1 - e^{-\frac{t}{\tau_{1/e}}} \right) \quad \text{B.25}$$

where t is the time since the linear increase in the tunnel began and $t_{1/e}$ is the effective 1/e time response of the analyzer. For the present experiments, the manufacturer-specified $t_{1/e}$ was 0.7 s and 1 s for the CO₂/CO and CH₄/C₂H₆ analyzers respectively. Substituting these values into Eq. B.25 suggests the measured slope will be within 1% of the true slope after 5 s. However, in practice the 1/e times of the analyzers were estimated to be closer to 4 s considering the added input sample tubing and the measured sample flow rates, such that the measured slopes would be safely within 1% of the true slope after 17 s. As elaborated below, the final analysis protocol used data for fitting starting from the next integer lap time after the start of the experiment that was greater than 17 s after the first step change detected by each analyzer.

A.3.2.2 Defining Test Start Time, t_0

Because the wind tunnel volume is large, the time required for a parcel of gas to travel around the tunnel (“lap time”, t_{lap}) can be up to ~70 s depending on wind speed (See Figure A1). Conceptually, the sample probe would be ideally located if it were exactly half-way around the closed loop tunnel from the flare, such that half of the wind tunnel volume was between the flare and the probe. In this case, during the first lap after the flare is ignited, the half-height of arriving step function would represent the wind-tunnel-averaged concentration at that moment in time. At this instant, t_0^* , 50% of the wind tunnel volume upstream of the probe would be filled with the fresh products of combustion, while the other 50% downstream of the probe would still be at ambient conditions. As the experiment progressed, the gases sampled at this location would, on average, continue to represent the mean concentration within the wind tunnel, consistent with the assumption of a fully-mixed control volume. The test start time, t_0 , defined as when the flare is ignited and combustion products start to be emitted into the tunnel, would then be exactly one-half lap time prior to the arrival of the initial step function in concentration at the sample probe (i.e., $t_0 = t_0^* - \frac{1}{2}t_{lap}$).

Importantly, the actual position of the probe within the tunnel is not critical, since the measured trends at any location would be identical except phase shifted earlier or later in time depending on whether the probe was further upstream or downstream. Thus, for any probe location, the test start time, t_0 , can be defined as exactly one-half lap time prior to the arrival of the first detected increase in concentration *at that location*. In the present experiments, the probe was installed at the centerline of the tunnel, 5.08 m upstream of the flare, on the upstream side of the

turbulence-generating grid (where it would not disrupt the flow to the flare). Referring to Figure A1, the test start time, t_0 , was thus determined in three steps by: i) recording the arrival time of the fresh gases at the probe (t_0^* , which is easily found by locating the last point at time at which the concentration is less than the five standard deviations above the mean of the background); ii) determining the amount of time it takes for gases to complete one lap of the wind tunnel (t_{lap}); and iii) calculating $t_0 = t_0^* - \frac{1}{2}t_{lap}$. When fitting the concentration data in the tunnel (See Section A.3.1), data beginning at $t_{fit,0}$ were used, where $t_{fit,0}$ was specified as the next integer lap time after t_0^* that was at least 17 s after t_0^* as noted above to account for any effects of the $1/e$ time response of the analyzers.

Finally, it should be noted that the fitted concentration rise of species in the tunnel is approximately linear near the start of each test. Thus, although this approach gives a robust methodology for determining t_0 , the final calculation of efficiency and emission rates are insensitive to the precision of t_0 . Nevertheless, both t_0 and $t_{fit,0}$ were independently varied by $\pm 25\%$ of the lap time (uniform random distribution) during the Monte Carlo analysis as summarized in Table A4 to account for any impacts on the final uncertainties of the measurements.

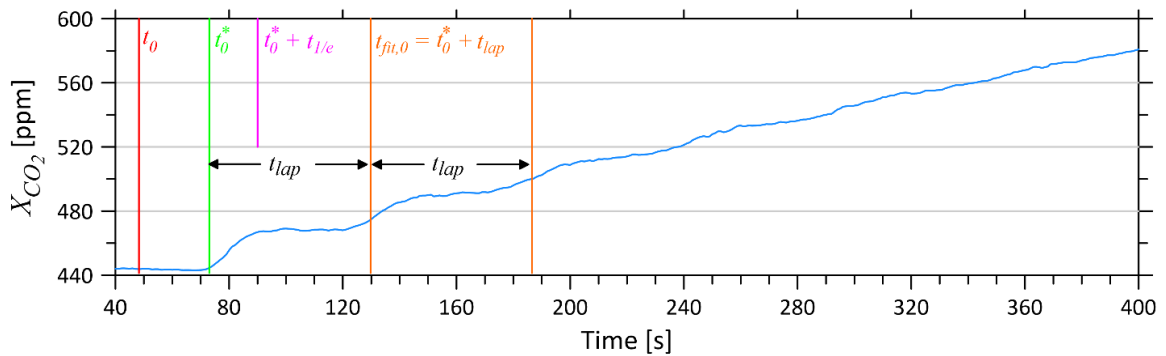


Figure A1: Example measured CO₂ volume fraction during a test with labels indicating how test start time t_0 is determined.

A.3.2.3 Determining Wind Tunnel Lap Time

The lap time (i.e., the time for a gas parcel to travel one full circuit around the tunnel) was measured for a range of test conditions by computing the fast Fourier transform (FFT) of the first derivative of the concentration measurement signal as shown by example in Figure A2. The frequency of the peak corresponding to the initial step increases in concentration after the

experiment begins is equal to the inverse of the lap time. For most cases, this was the lowest non-DC frequency peak and was also the most prominent peak. However in some cases, especially at higher wind speeds, better mixing resulted in less prominent steps, which made the FFT difficult to interpret. For this reason, it was necessary to develop a robust empirical relation to estimate lap time as a function of wind speed which was then used in all subsequent experiments and calculations.

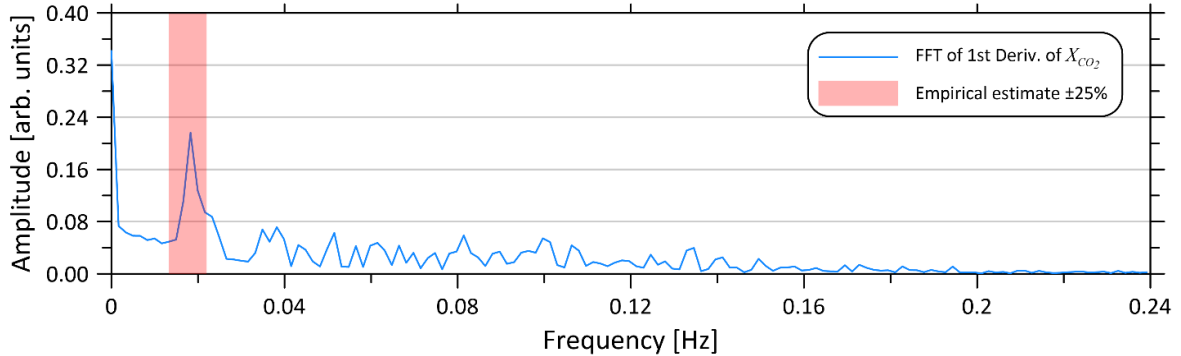


Figure A2: Example use of the Fast Fourier Transform (FFT) of measured CO₂ volume fraction to determine the wind tunnel lap time.

As plotted in Figure A3, the measured lap times from the FFT analysis of the CO₂, CO, and CH₄ concentrations were modeled as an inverse function of wind speed via least squares regression. Three different fits are shown: a fit derived from “cold flow” tests where the flare remained unlit (see Section A.7.2), a fit derived from “hot flow” tests with the flare lit, and a fit derived from the combined data. Statistical analysis indicated that the inclusion of a constant was justified, resulting in an equation of the form $t_{lap} = a + b/U_{\infty}$.

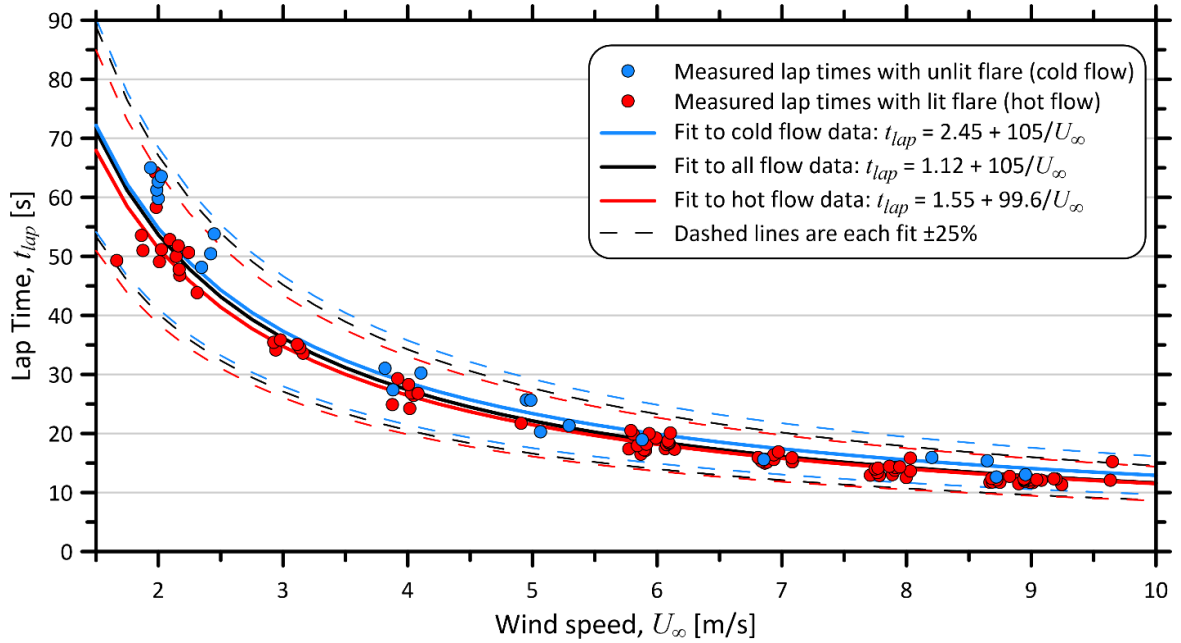


Figure A3: Effective lap time of the wind tunnel as a function of wind speed.

A.3.3 Measuring Emissions of Batch Sampled Species without Time Resolved Concentrations

The emission rates of species that are not accompanied by time-resolved concentration measurements can still be determined using batch-samples at the start and end of the combustion test. To accomplish this, Eq. (4.7) can be manipulated to represent the start of a test as:

$$X_{i,cv}(t_0) = \frac{A_i - C_i e^{-(B_i \int_{t_0}^{t_0} T_{cv}(t) dt)}}{B_i} \quad \text{S26}$$

which reduces to

$$X_{i,cv}(t_0) = \frac{A_i - C_i}{B_i} \quad \text{S27}$$

Similarly, Eq (4.7) can be modified to represent the end of the test, t_{end} , when the second grab sample is taken, and can be expressed as

$$X_{i,cv}(t_{end}) = \frac{A_i - C_i e^{-(B_i \int_{t_0}^{t_{end}} T_{cv}(t) dt)}}{B_i} \quad \text{S28}$$

Subbing Eq. S27 into Eq. S28 eliminates A_i , and solving for C_i ,

$$C_i = \frac{B_i (X_{i,cv}(t_{end}) - X_{i,cv}(t_0))}{1 - e^{-(B_i \int_{t_0}^{t_{end}} T_{cv}(t) dt)}} \quad S29$$

The B_i coefficient, which is common for all non-hydrocarbon species or for all hydrocarbon species, can be calculated using an average of the known B_i coefficients from other measured hydrocarbon or non-hydrocarbon species involved in the combustion process as appropriate. Accumulation rates at the start of a test can be calculated by substituting Eq. S29 into Eq. (4.8):

$$\left. \frac{dX_{i,cv}}{dt} \right|_{t \rightarrow t_0} = T_{cv}(t_0) \frac{B_i [X_{i,cv}(t_{end}) - X_{i,cv}(t_0)]}{1 - e^{-B_i \int_{t_0}^{t_{end}} T_{cv}(t) dt}} \quad S30$$

Similarly, the emission rate can be calculated by substituting Eq. S30 into Eq. (4.7):

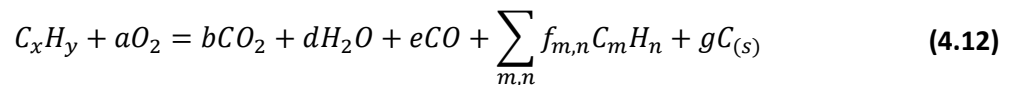
$$X_{i,p} \dot{V}_{p,\infty} = V_{cv} T_{cv}(t_0) \frac{B_i [X_{i,cv}(t_{end}) - X_{i,cv}(t_0)]}{1 - e^{-B_i \int_{t_0}^{t_{end}} T_{cv}(t) dt}} + X_{i,\infty} \frac{M_f}{M_\infty} \dot{V}_{f,\infty} + \{X_{i,\infty} \dot{V}_{air,comb,\infty}\}_{i=HC} \quad S31$$

A.4 Methods to Determine Wind Tunnel Volume

The effective volume, V_{cv} , in Eq. (4.7) is unknown. In principle the volume could be directly measured; however, the presence of contraction sections, varying width walls and ceilings, and equipment including turbulence grids, turning vanes, driving fan, and measurement apparatus means the volume is difficult to measure accurately. Moreover, the participating volume of the CV may vary under different test conditions. Therefore, two different methods were considered for calculating V_{cv} as part of each experiment: a carbon balance method and a tracer-dilution method. Ultimately, the carbon balance approach was found to be more accurate as shown in Figure A6 and was subsequently used in all tests; however, the tracer method is also detailed here for completion.

A.4.1 Carbon Balance Approach to Determine V_{cv}

Incomplete combustion of a general hydrocarbon fuel (C_xH_y) may be summarized by Eq. (4.12) from the main text:



As discussed in Section 4.4.1 of the main text, the relative mass of soot in the plume is expected to be small in all cases and its influence on the plume volume is negligible. Equating the mass of

carbon in the fuel to the mass of carbon in the products (i.e., a carbon balance) in Eq. (4.12) provides an additional equation:

$$\dot{m}_{C,f} = \dot{m}_{C,p} \quad \text{B.32}$$

where: $\dot{m}_{C,f}$ is the mass flow of carbon in the fuel, and

$\dot{m}_{C,p}$ is the mass flow of carbon in the products in both gaseous and solid form.

By expressing carbon in terms of a molar flow using $\dot{m} = M\dot{n}$, where M is the molecular mass of carbon and \dot{n} is the molar flow rate, Eq. B.32 can be expressed as:

$$xX_{C_xH_y}\dot{n}_f = \dot{n}_p \sum_i (\#_{C,i}X_{i,p}) \quad \text{B.33}$$

where: $X_{C_xH_y}$ is the mole fraction of hydrocarbons in the fuel,

\dot{n}_f is the molar flow rate of flare gas,

\dot{n}_p is the molar flow rate of products, and

$\#_{C,i}$ is the carbon number of species i (i.e., the number of carbon atoms in molecule i).

Eq. B.33 can be generalized to account for the possibility of inert species in the flare gas mixture:

$$\sum_i (\#_{C,i}\dot{n}_f X_{i,f}) = \sum_i (\#_{C,i}\dot{n}_p X_{i,p}) \quad \text{B.34}$$

where $X_{i,f}$ is the mole fraction of species i in the flare gas. Considering gaseous species only, Eq.

B.34 can then be expressed in terms of volume,

$$\sum_i (\#_{C,i}\dot{V}_{f,\infty} X_{i,f}) = \sum_i (\#_{C,i}\dot{V}_{p,\infty} X_{i,p}) \quad (4.13)$$

A.4.1.1 Assumption of Fuel Stripping to Quantify Unmeasured Hydrocarbons

Real time measurements in the present test apparatus are limited to the major carbon-containing species CO_2 , CO , CH_4 , and C_2H_6 . Thus, although Eq. (4.13) may be used directly in cases where the accumulation rates of all relevant carbon species can be measured, more generally it may be expanded to distinguish carbon in measured and unmeasured hydrocarbons (*UMHC*), as well as in non-hydrocarbon products of combustion:

$$\sum_i (\#_{C,i} \dot{V}_{f,\infty} X_{i,f}) = \sum_{i=HC} (\#_{C,i} \dot{V}_{p,\infty} X_{i,p}) + \sum_{i=UMHC} (\#_{C,i} \dot{V}_{p,\infty} X_{i,p}) + \sum_{i \neq HC} (\#_{C,i} \dot{V}_{p,\infty} X_{i,p}) \quad \text{B.35}$$

Recognizing that flare emissions are thought to be driven primarily by stripping of unburned fuel (Johnson and Kostiuik 2002a; Johnson et al. 2001), it is possible to estimate the mole fractions of unmeasured hydrocarbons in the plume from measured species by assuming the relative fractions of unburned hydrocarbons are the same as in the flare gas. For methane-dominated fuels, as are typical of flares in the upstream oil and gas sector (Conrad and Johnson 2019; Johnson and Coderre 2012), the concentration of any unmeasured hydrocarbon in the plume can be inferred based on measured CH₄ concentration as follows:

$$\left\{ X_{i,p} = \frac{X_{i,f}}{X_{CH_4,f}} X_{CH_4,p} \right\}_{i=UMHC} \quad (4.14)$$

where $X_{i,f}$ and $X_{CH_4,f}$ indicate the mole fractions of hydrocarbon i and CH₄ in the flare gas and $X_{i,p}$ and $X_{CH_4,p}$ indicate the mole fractions in the plume. Eq. (4.14) can be recast in terms of volumetric emission rates by multiplying both sides by $\dot{V}_{p,\infty}$,

$$\left\{ X_{i,p} \dot{V}_{p,\infty} = \frac{X_{i,f}}{X_{CH_4,f}} X_{CH_4,p} \dot{V}_{p,\infty} \right\}_{i=UMHC} \quad \text{B.36}$$

Substituting Eq. (4.7) and Eq. B.36 into Eq. B.35 gives,

$$\begin{aligned} & \sum_i (\#_{C,i} \dot{V}_{f,\infty} X_{i,f}) \\ &= \sum_{i \neq HC} \left(\#_{C,i} \left(V_{cv} \frac{dX_{i,cv}}{dt} \Big|_{t \rightarrow t_0} + X_{i,\infty} \frac{M_f}{M_\infty} \dot{V}_{f,\infty} \right) \right) \\ &+ \sum_{i=HC} \left(\#_{C,i} \left(V_{cv} \frac{dX_{i,cv}}{dt} \Big|_{t \rightarrow t_0} + X_{i,\infty} \frac{M_f}{M_\infty} \dot{V}_{f,\infty} + X_{i,\infty} \dot{V}_{air,comb,\infty} \right) \right) \\ &+ \sum_{i=UMHC} \left(\#_{C,i} \frac{X_{i,f}}{X_{CH_4,f}} \left(V_{cv} \frac{dX_{CH_4,cv}}{dt} \Big|_{t \rightarrow t_0} + X_{CH_4,\infty} \frac{M_f}{M_\infty} \dot{V}_{f,\infty} \right. \right. \\ &\left. \left. + X_{CH_4,\infty} \dot{V}_{air,comb,\infty} \right) \right) \end{aligned} \quad \text{B.37}$$

Finally, expanding and collecting like terms in Eq. B.37 allows a direct calculation of the volume of the CV,

$$V_{cv} = \left[\begin{array}{l} \sum_i (\#_{C,i} \dot{V}_{f,\infty} X_{i,f}) - \sum_{i \neq HC} \#_{C,i} X_{i,\infty} \frac{M_f}{M_\infty} \dot{V}_{f,\infty} \\ - \sum_{i=HC} \#_{C,i} X_{i,\infty} \frac{M_f}{M_\infty} \dot{V}_{f,\infty} - \sum_{i=UMHC} \#_{C,i} \frac{X_{i,f}}{X_{CH_4,f}} X_{CH_4,\infty} \frac{M_f}{M_\infty} \dot{V}_{f,\infty} \\ - \sum_{i=HC} \#_{C,i} X_{i,\infty} \dot{V}_{air,comb,\infty} - \sum_{i=UMHC} \#_{C,i} \frac{X_{i,f}}{X_{CH_4,f}} X_{CH_4,\infty} \dot{V}_{air,comb,\infty} \end{array} \right] \quad (4.15)$$

$$/ \left[\sum_{i \neq HC} \#_{C,i} \frac{dX_{i,cv}}{dt} \Big|_{t \rightarrow t_0} + \sum_{i=HC} \#_{C,i} \frac{dX_{i,cv}}{dt} \Big|_{t \rightarrow t_0} \right.$$

$$\left. + \sum_{i=UMHC} \#_{C,i} \frac{X_{i,f}}{X_{CH_4,f}} \frac{dX_{CH_4,cv}}{dt} \Big|_{t \rightarrow t_0} \right]$$

Importantly, Eq. (4.15) is generally applicable, such that if all relevant hydrocarbon species are measured, then terms in the $i = UMHC$ summation term reduces to zero.

As shown in Figure 4.5b of the main text, measured CH₄ to C₂H₆ ratios in the plume demonstrate that the fuel stripping assumption is a fair approximation at higher wind speeds, but may overestimate the C₂H₆ fraction at wind speeds below ~4 m/s. To examine this further, canister samples were collected from the wind tunnel (CV) at the end of the experiment and sent to an off-site, third-party lab for gas chromatography-mass spectrometry (GC-MS) analysis according to EPA Method TO-15. Table A3 shows the measured hydrocarbon species for several experiments at lower wind speeds, i.e., when the results of Figure 4.5b suggest the fuel stripping assumption is least accurate. The measured carbon conversion efficiency in these experiments ranged from 99.13 to 99.51%. High concentrations of species in the TO-15 analysis would indicate that the flare was emitting reformed or partially combusted hydrocarbons. Instead, the range of tests show that the carbon within the measured species in the TO-15 analysis was consistently less than 1.14% of the carbon in CH₄ plus C₂H₆, and typically less than 0.6%. Even in an extreme scenario where all VOC species below their detectable limits were postulated to be present at their detectable limits in the sample and at zero concentration in the ambient background, the fraction of carbon in VOCs would still be less than 2.93% of the total carbon emitted (VOCs as well as CH₄ and C₂H₆). This suggests the mass of carbon contained in emissions of reformed hydrocarbon species is likely negligible as further explored below.

Table A3: Volume fractions of hydrocarbons and VOCs in CV at the end of a flare experiment burning different natural gas mixtures (M6 and H6), in 2- and 4-inch diameter flares at exit velocities of 0.5–2 m/s while subjected to crosswinds of 3–4 m/s.

Species Detection Limit, DL [ppb(V)]	Volume Fraction [ppbv]				
	Test 1 $d_f=0.102$ m, $V_j=0.5$ m/s, $U_\infty=3$ m/s, Flare gas M6 [†]	Test 2 $d_f=0.102$ m, $V_j=1$ m/s, $U_\infty=3$ m/s, Flare gas M6 [†]	Test 3 $d_f=0.102$ m, $V_j=2$ m/s, $U_\infty=3$ m/s, Flare gas M6 [†]	Test 4 $d_f=0.102$ m, $V_j=0.5$ m/s, $U_\infty=4$ m/s, Flare gas H6	Test 5 $d_f=0.0525$ m, $V_j=1$ m/s, $U_\infty=4$ m/s, Flare gas H6 ^{††}
Measured using Aeris Analyzer					
Methane	4800 (88.88% / 88.26%)	9600 (88.6% / 88.27%)	27350 (87.62% / 87.5%)	5500 (79.34% / 78.4%)	2270 (80.32% / 78.86%)
Ethane	570 (10.55% / 10.48%)	1194 (11.02% / 10.98%)	3788 (12.14% / 12.12%)	1390 (20.05% / 19.81%)	524 (18.54% / 18.2%)
Measured via GC-MS according to EPA TO-15					
Combined fraction of total carbon (as measured / assuming DL when reported as <DL)	(0.56% / 1.26%)	(0.38% / 0.75%)	(0.24% / 0.39%)	(0.60% / 1.79%)	(1.14% / 2.93%)
Acetone	<32	8.9	8.3	3.79	10.9
Allyl chloride	<0.20	<0.20	<0.20	<0.20	<0.20
Benzene	2.02	2.50	3.330	2.57	1.14
Benzyl chloride	<0.20	<0.20	<0.20	<0.20	<0.20
Bromodichloromethane	<0.20*	<0.20*	<0.20*	<0.20*	<0.20*
Bromoform	<0.20*	<0.20*	<0.20*	<0.20*	<0.20*
Bromomethane	<0.20	<0.20	<0.20	<0.20	<0.20
1,3-Butadiene	0.44	<1.3	<2.8	<1.5*	<0.20*
Carbon Disulfide	<0.20	0.30	<0.20	0.33	0.39
Carbon Tetrachloride	<0.20	<0.20	<0.20	<0.20	<0.20
Chlorobenzene	<0.20	<0.20	<0.20	<0.20	<0.20
Dibromochloromethane	<0.20	<0.20	<0.20	<0.20	<0.20
Chloroethane	<0.20	<0.20	<0.20	<0.20	<0.20
Chloroform	<0.20	<0.20*	<0.20*	<0.20*	<0.20*
Chloromethane	0.61	0.55	0.41	0.39	0.36
Cyclohexane	<0.20	<0.20	<0.20	<0.20	<0.20
1,2-Dibromoethane	<0.20*	<0.20*	<0.20*	<0.20*	<0.20*
1,2-Dichlorobenzene	<0.20	<0.20	<0.20	<0.20	<0.20
1,3-Dichlorobenzene	<0.20	<0.20	<0.20	<0.20	<0.20
1,4-Dichlorobenzene	<0.20*	<0.20*	<0.20*	<0.20*	<0.20*
Dichlorodifluoromethane	1.37	1.07	0.89	0.59	0.69
1,1-Dichloroethane	<0.20	<0.20	<0.20	<0.20	<0.20
1,2-Dichloroethane	<0.20	<0.20	<0.20	<0.20*	<0.20*
1,1-Dichloroethene	<0.20	<0.20	<0.20	<0.20	<0.20
cis-1,2-Dichloroethene	<0.20	<0.20	<0.20	<0.20	<0.20
trans-1,2-Dichloroethene	<0.20	<0.20	<0.20	<0.20	<0.20
Methylene chloride	2.97	0.30	0.22	<0.20	2.16

1,2-Dichloropropane	<0.20*	<0.20*	<0.20*	<0.20*	<0.20*
cis-1,3-Dichloropropene	<0.20*	<0.20*	<0.20*	<0.20*	<0.20*
trans-1,3-Dichloropropene	<0.20*	<0.20*	<0.20*	<0.20*	<0.90*
1,4-Dioxane	<0.20	<0.20	<0.20	<0.20*	<0.20*
Ethyl acetate	<0.20	<0.20	<0.20	<0.20	<0.20
Ethylbenzene	<0.20	<0.20	<0.20	<0.20	<0.20
4-Ethyltoluene	<0.20	<0.20	<0.20	<0.20	<0.20
n-Heptane	<0.20	<0.20	<0.20	<0.20	<0.20
Hexachlorobutadiene	<0.20*	<0.20*	<0.20*	<0.20	<0.20
n-Hexane	<0.20	0.29	<0.20	<0.20*	<0.20*
2-Hexanone	<1.0	<1.0	<1.0	3.82	0.22
Isooctane	<0.20	<0.20	<0.20	<1.0	<1.0
Isopropylbenzene	<0.20	<0.20	<0.20	<0.20	<0.20
Methyl ethyl ketone	1.72	1.22	5.00	<0.20	<0.20
Methyl isobutyl ketone	<0.20	<0.20	1.5	0.89	3.42
MTBE	<0.20	<0.20	<0.20	<0.20	<0.20
Naphthalene	<0.20*	<0.20	<0.20*	<0.20	<0.20
Propylene	<33*	<76*	<220*	<0.20*	<0.20*
Styrene	<0.20	<0.20	<0.20	<160*	<35*
1,1,1,2-Tetrachloroethane	<0.20*	<0.20*	<0.20*	<0.20	<0.20
1,1,2,2-Tetrachloroethane	<0.20*	<0.20*	<0.20*	<0.20*	<0.20*
Tetrachloroethylene	<0.20	<0.20	<0.20	<0.20*	<0.20*
Tetrahydrofuran	<0.20	0.22	0.63	<0.20	<0.20
Toluene	0.42	0.69	0.44	0.31	<0.20
Freon 113	<0.20	<0.20	<0.20	0.21	<0.20
1,2,4-Trichlorobenzene	<0.20	<0.20	<0.20	<0.20	<0.20
1,1,1-Trichloroethane	<0.20	<0.20	<0.20	<0.20	<0.20
1,1,2-Trichloroethane	<0.20*	<0.20*	<0.20*	<0.20*	<0.20*
Trichloroethylene	<0.20*	<0.20*	0.3	<0.20*	<0.20*
Trichlorofluoromethane	0.24	<0.20	<0.20	<0.20	<0.20
Freon 114	<0.20	<0.20	<0.20	<0.20	<0.20
1,2,4-Trimethylbenzene	0.30	0.26	0.38	<0.20	<0.20
1,3,5-Trimethylbenzene	<0.20	<0.20	<0.20	<0.20	<0.20
Vinyl acetate	0.95	0.94	0.61	<0.50	<0.50
Vinyl bromide	<0.20	<0.20	<0.20	<0.20	<0.20
Vinyl chloride	<0.20*	<0.20*	<0.20*	<0.20*	<0.20*
o-Xylene	0.22	0.25	0.83	<0.20	<0.20
m&p-Xylene	0.61	0.69	0.50	<0.40	<0.40

† 75% and 12% of the carbon within the hydrocarbons in M6 is in the form of CH₄ and C₂H₆, respectively.

‡ 55% and 17% of the carbon within the hydrocarbons in H6 is in the form of CH₄ and C₂H₆, respectively.

* Below detectable limit in both sample and background, but detection limits were different between the background and sample due to interference from other species. Sample detection limit was thus used when assuming species were at DL.

Looking more closely at the measured CH₄ and C₂H₆ in Table A3, in each case the measured mass of carbon in CH₄ is much higher than it is in the raw fuel, and the measured C₂H₆ lower. Specifically, for fuel M6, methane accounted for 87.5–88.9% of the emitted carbon in hydrocarbons in Table A3 across all scenarios versus 75% in the raw flare gas. Similarly, for fuel H6, methane accounted for 78.4–80.3% of the emitted carbon in hydrocarbons across all scenarios versus 55% in the raw flare gas. This is consistent with Figure 5b of the main text which suggests that if anything, the CH₄ fraction in the combustion plume tends to be higher than would be expected based on an assumption of fuel stripping. Combined with the lack of reformed hydrocarbon species, in the extreme, this suggests an alternate “heavy-first” limit on the form of emitted hydrocarbons in which the heavier hydrocarbon species in the fuel are assumed to burn first leaving only CH₄ in the products.

As summarized in Figure A4, an analysis was completed using this “heavy-first” limit to bound the maximum expected uncertainty that might be introduced by the fuel stripping assumption. Synthetic data were first created for a flare burning H6 in which the permitted products were limited to CH₄, CO, and CO₂. Then, the method developed in this paper – invoking the fuel-stripping assumption – was applied to calculate V_{cv} as well as carbon conversion efficiency and CH₄ emission rate. The differences between the calculated values of each parameter assuming fuel-stripping vs. the synthetic values generated using the alternate “heavy-first” assumption (which assumed heavy species burn preferentially leaving only CH₄, CO, and CO₂ in the products) provides an upper bound estimate of the uncertainty in using the fuel-stripping assumption.

The results of Figure A4 show that the maximum expected uncertainties in V_{cv} , efficiency, and methane emission rate from the use of the fuel stripping assumption share the same linear relationship with carbon conversion efficiency. It is noted that this analysis considers an extreme limiting case in which the ratio of emitted methane to ethane goes to infinity, whereas the data in Figure 5b of the main text show this ratio remaining below 1.8. Nevertheless, the maximum error incurred when using the fuel stripping assumption is less than 5% for efficiencies between 80–100%, and much lower for the lighter fuels with higher methane content. More importantly, the low wind speed conditions at which the methane to ethane ratios deviate the most from a fuel-stripping scenario are also the conditions that produce the highest efficiency flares as shown in Figure 5b of the main text. Once this is taken into consideration, i.e., only looking at efficiencies above 98%, the maximum expected error in both calculated efficiency and methane emission rate

is <0.5%. Overall, this analysis demonstrates that the fuel stripping assumption is a robust method for closing the equations to calculate V_{cv} . Nevertheless, for the purpose of estimating conservative uncertainty bounds, the Monte Carlo analysis presented in Section A.6 allows mole fractions of emitted unmeasured hydrocarbons to vary uniformly between these two limits (i.e. unmeasured hydrocarbons are permitted to vary between zero, assuming that heavy hydrocarbons burn first, and their mole fractions in the raw flare gas corresponding to expected values from fuel stripping).

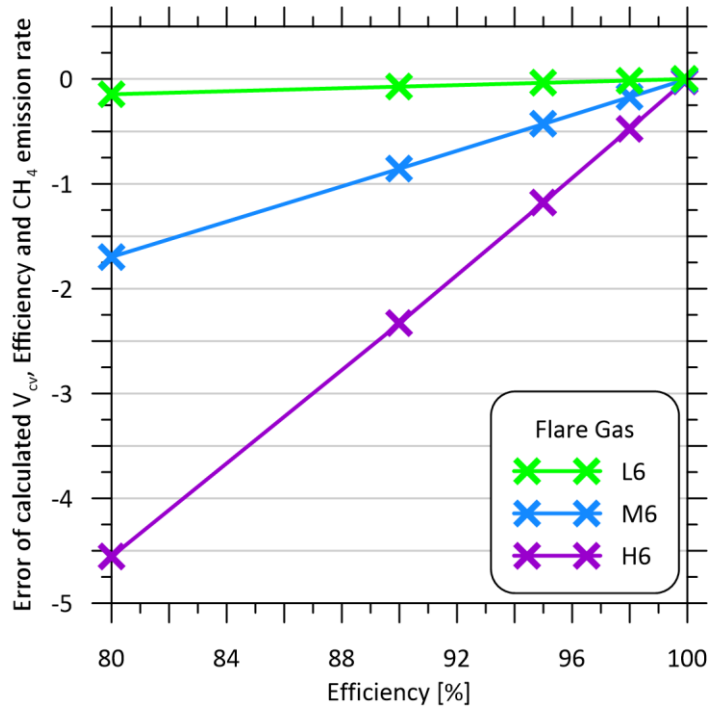


Figure A4: Relative error (expressed as a percentage of the actual value) in calculated wind tunnel volume, V_{cv} , carbon conversion efficiency, or CH_4 emission rate when calculated using the fuel stripping assumption (Eq. (4.14)) for a synthetic data set generated burning flare gas L6, M6 and H6 that assumed heavy hydrocarbons burn preferentially and only CH_4 is emitted as a hydrocarbon. The induced error as a function of efficiency is independent of flare gas flow rate.

A.4.2 Tracer-Dilution Approach to Measure V_{cv}

Alternatively, an additional equation to determine the volume of the CV can be obtained by injecting an inert tracer into the CV at a separate location near the flare and measuring its rate of concentration rise in the CV. For a chosen inert tracer species (denoted by subscript tr) that is not otherwise emitted or destroyed by the flame, Eq. B.15 can be modified to:

$$\frac{dX_{tr,cv}(t)}{dt} = T_{cv}(t) \left(\frac{(\dot{V}_{tr,\infty} + X_{tr,\infty}\dot{V}_{in})}{V_{cv}T_{\infty}} - X_{tr,cv}(t) \frac{\left(\frac{M_{tr}}{M_{cv}}\dot{V}_{tr} + \frac{M_f}{M_{cv}}\dot{V}_{f,\infty} + \frac{M_{\infty}}{M_{cv}}\dot{V}_{in}\right)}{V_{cv}T_{\infty}} \right) \quad \text{B.38}$$

Rearranging Eq. B.38 to solve for V_{cv} ,

$$V_{cv} = \frac{\frac{T_{cv}(t)}{T_{\infty}} \left(\dot{V}_{tr,\infty} + X_{tr,\infty}\dot{V}_{in} - X_{tr,cv}(t) \left(\frac{M_{tr}}{M_{cv}}\dot{V}_{tr} + \frac{M_f}{M_{cv}}\dot{V}_{f,\infty} + \frac{M_{\infty}}{M_{cv}}\dot{V}_{in} \right) \right)}{\frac{dX_{tr,cv}(t)}{dt}} \quad \text{B.39}$$

Using the limit approach first introduced in Eq. B.14, where conditions in the CV approach ambient conditions near the start of an experiment ($t \rightarrow t_0$), Eq. B.39 can be simplified to

$$V_{cv} = \frac{\dot{V}_{tr,\infty} - X_{tr,\infty} \frac{M_f}{M_{\infty}} \dot{V}_{f,\infty} - X_{tr,\infty} \frac{M_{tr}\dot{V}_{tr,\infty}}{M_{\infty}}}{\left. \frac{dX_{tr,cv}}{dt} \right|_{t \rightarrow t_0}} \quad \text{B.40}$$

To solve for the accumulation rate of tracer gas at the start of the experiment, integration of Eq. B.38 following a similar method as between Eq. (4.6) and Eq. (4.7) yields the following expression for the tracer species concentration as a function of time:

$$X_{tr,cv}(t) = \frac{A_{tr} - C_{tr} e^{-B_{tr} \int_{t_0}^t T_{cv}(t) dt}}{B_{tr}} \quad \text{B.41}$$

where $A_{tr} = \frac{\dot{V}_{tr,\infty} + X_{tr,\infty}\dot{V}_{in}}{V_{cv}T_{\infty}}$,

$$B_{tr} = \frac{\left(\frac{M_{tr}}{M_{cv}}\dot{V}_{tr} + \frac{M_f}{M_{cv}}\dot{V}_{f,\infty} + \frac{M_{\infty}}{M_{cv}}\dot{V}_{in}\right)}{V_{cv}T_{\infty}}, \text{ and}$$

$$C_{tr} = A_{tr} - B_{tr}X_{tr,\infty}$$

The term $T_{cv}(t)dt$ can be integrated from t_0 to t at each time step as the temperature of the CV is measured. It is possible to then fit a curve to the measured tracer concentration using the Levenberg-Marquardt or similar algorithm to solve for the coefficients A , B , and C , and the accumulation rate at t_0 can be calculated using Eq. (4.8).

A.5 Carbon Conversion Efficiency Assuming Gas-Phase Products of Combustion Only and Assuming Emitted Hydrocarbons Have Same Form as Raw Fuel

From the expression developed for a species emission rate in Eq. (4.7), the combustion efficiency can also be calculated. From the definition of η in Eq. (4.16) of the main text, η may be written as:

$$\eta = \frac{\dot{V}_{p,\infty} X_{CO_2,p} - \dot{V}_{f,\infty} X_{CO_2,f}}{\sum_{i=HC} (\#_{C,i} \dot{V}_{f,\infty} X_{i,f})} \quad B.42$$

Substituting an expression for $\dot{V}_{p,\infty} X_{CO_2,p}$ using Eq. (4.7) into Eq. B.42 gives:

$$\eta = \frac{V_{cv} \left. \frac{dX_{CO_2,cv}}{dt} \right|_{t \rightarrow t_0} + X_{CO_2,\infty} \frac{M_f}{M_\infty} \dot{V}_{f,\infty} - \dot{V}_{f,\infty} X_{CO_2,f}}{\sum_{i=HC} (\#_{C,i} \dot{V}_{f,\infty} X_{i,f})} \quad (4.17)$$

The expression for V_{cv} in Eq. (4.15) can then be substituted into Eq. (4.17) to express carbon conversion efficiency as:

$$\eta = \frac{\left[\begin{array}{l} \sum_i (\#_{C,i} \dot{V}_{f,\infty} X_{i,f}) - \sum_{i \neq HC} \#_{C,i} X_{i,\infty} \frac{M_f}{M_\infty} \dot{V}_{f,\infty} \\ - \sum_{i=HC} \#_{C,i} X_{i,\infty} \frac{M_f}{M_\infty} \dot{V}_{f,\infty} - \sum_{i=UMHC} \#_{C,i} \frac{X_{i,f}}{X_{CH_4,f}} X_{CH_4,\infty} \frac{M_f}{M_\infty} \dot{V}_{f,\infty} \\ - \sum_{i=HC} \#_{C,i} X_{i,\infty} \dot{V}_{air,comb,\infty} - \sum_{i=UMHC} \#_{C,i} \frac{X_{i,f}}{X_{CH_4,f}} X_{CH_4,\infty} \dot{V}_{air,comb,\infty} \end{array} \right] \left. \frac{dX_{CO_2,cv}}{dt} \right|_{t \rightarrow t_0}}{\left[\begin{array}{l} \sum_{i=HC} \#_{C,i} \left. \frac{dX_{i,cv}}{dt} \right|_{t \rightarrow t_0} + \\ \left[\sum_{i=HC} \#_{C,i} \left. \frac{dX_{i,cv}}{dt} \right|_{t \rightarrow t_0} + \sum_{i=UMHC} \#_{C,i} \frac{X_{i,f}}{X_{CH_4,f}} \left. \frac{dX_{CH_4,cv}}{dt} \right|_{t \rightarrow t_0} \right] \\ + X_{CO_2,\infty} \frac{M_f}{M_\infty} \dot{V}_{f,\infty} - \dot{V}_{f,\infty} X_{CO_2,f} \end{array} \right] \sum_{i=HC} (\#_{C,i} \dot{V}_{f,\infty} X_{i,f})} \quad B.43$$

A.6 Uncertainty Analysis

A.6.1 Monte Carlo Simulation of Systematic Uncertainties

The systematic uncertainties, or bias, of carbon conversion efficiency and species emission rates obtained using the methodology derived in this paper were assessed via Monte Carlo simulations. For each simulated condition, values of all input variables were drawn from representative distributions as summarized in Table A4. For variables such as ambient concentrations and temperatures, typical average values were used with representative normally distributed

uncertainties based on specifications of the measurement equipment. Gas cylinder purities were based on manufacturer specifications, where different gas bottles typically include a small fraction of impurities in the form of total hydrocarbons (THC) and inerts, often CO₂ or N₂. For gas-phase cylinders, THCs are assumed to be distributed based on flare gas M6 fractions, while for the two liquid-phase cylinders (C₃H₈ and C₄H₁₀) impurities are assumed to be comprised of the alternative species: for example, THC impurities in C₃H₈ are assumed to be C₄H₁₀ and vice versa. Flare gas release rates were based on both the full-scale and relative uncertainties of mass flow controller manufacturer specifications. For combustion properties such as the form of the unmeasured hydrocarbons in the plume, mole fractions were varied uniformly between the limits outlined in Section A.4.1.1, while the uncertainty in volume of combustion air was drawn from a uniform distribution bounded by the stoichiometric volume and the assumption that heaviest hydrocarbons burn first for a flare burning H6. For time-varying parameters such as mole fractions of accumulating species within the CV analyzer precision, calibration, and linearity errors were introduced to produce an independently corrupted measurement signal for each species in each Monte Carlo draw. The method used to introduce linearity errors is described in section A.6.3.

Table A4: Summary input parameters and associated uncertainties considered in the Monte Carlo analysis.

Variable Group	Variable Name	Symbol [Unit]	Value	2 σ Uncertainty
Test times ^a	Test start time	t_0	0	Uniform Distribution, $\pm 25\%$ of the estimated tunnel lap time
	Earliest time to include in the fits to X_i	$t_{fit,0}$	>17 s	Uniform Distribution, $\pm 25\%$ of the estimated tunnel lap time
Concentration	Ambient Concentration	CH ₄	$X_{i,\infty}$ [-]	2.00E-06 Normal Distribution, Analyzer Prec. [$2\sigma = 3e-9$] +0.1 $X_{i,\infty}$
		C ₂ H ₆	$X_{i,\infty}$ [-]	1.00E-06 Normal Distribution, Analyzer Prec. [$2\sigma = 1e-9$] +0.1 $X_{i,\infty}$
		CO ₂	$X_{i,\infty}$ [-]	4.00E-04 Normal Distribution, Analyzer Prec. [$2\sigma = 3.5e-7$] +0.1 $X_{i,\infty}$
		CO	$X_{i,\infty}$ [-]	1.00E-07 Normal Distribution, Analyzer Prec. [$2\sigma = 1e-9$] +0.1 $X_{i,\infty}$
		N ₂ O	$X_{i,\infty}$ [-]	3.00E-07 Normal Distribution, Analyzer Prec. [$2\sigma = 1e-9$] +0.1 $X_{i,\infty}$
	Instantaneous Measurement of Concentration	CH ₄ C ₂ H ₆	$X_{i,cv}$ [-]	Range Range

		CO ₂		Range	Normal Distribution, Analyzer Precision [$2\sigma = 3.5e-7$]
		CO		Range	Normal Distribution, Analyzer Precision [$2\sigma = 1e-9$]
		N ₂ O		Range	Normal Distribution, Analyzer Precision [$2\sigma = 1e-9$]
	Calibration Span Error on Concentration Dataset	CH ₄	$X_{i,cv} [-]$	Range	Uniform Distribution, -2% to 2%
		C ₂ H ₆		Range	Uniform Distribution, -2% to 2%
		CO ₂		Range	Uniform Distribution, -2% to 2%
		CO		Range	Uniform Distribution, -2% to 2%
		N ₂ O		Range	Uniform Distribution, -2% to 2%
	Analyzer Linearity	CH ₄	$X_{i,cv} [-]$	Range	Maximum 2% Deviation from Linear
		C ₂ H ₆		Range	Maximum 2% Deviation from Linear
		CO ₂		Range	Maximum 2% Deviation from Linear
		CO		Range	Maximum 2% Deviation from Linear
		N ₂ O		Range	Maximum 2% Deviation from Linear
Flare Gas Properties	Gas Cylinder Purities	CH ₄	$X [-]$	1	0.01
		C ₂ H ₆		1	0.01
		C ₃ H ₈		1	0.01
		C ₄ H ₁₀		1	0.01
		CO ₂		1	0.005
		N ₂		1	0.005
		N ₂ O		1	0.005
	MFC Flow Rates	$\dot{V}_{f,\infty}$ [SLPM]	0-1000	0.5% Relative + 0.1% Full Scale	
Molecular Weight	CV	M_{cv} [kg/kmol]	28.97	0.246 ^b	
	Ambient	M_{∞} [kg/kmol]	28.97	0.246 ^b	
Temperature	CV	T_{cv} [K]	293.15	0.46 ^c	
	Ambient	T_{∞} [K]	293.15	0.46 ^c	
Combustion Properties	Volume of Combustion Air Consumed	$\dot{V}_{air,comb,\infty}$ [m ³ /s]	Stoichiometric	0.37 × Stoichiometric ^d	
	UMHC	$i = UMHC$ [%]	Eq. (4.14)	0-Eq. (4.14) ^d	

^a Test time uncertainties were not applicable for the synthetic data uncertainty analysis.

^b Maximum variance in relative humidity of air at 273.15K

^c Maximum expected deviation of reading from resistance temperature device (RTD) read through the data acquisition system (DAQ)

^d Based on assuming a uniform distribution of values using the maximum deviation in moles of air consumed for a flare burning H6 at stoichiometric conditions and at an efficiency of 70%

^e Based on analysis in Section A.4.1.1 assuming a uniform distribution of values between the limits of the fuel stripping assumption and the “heavy-burns first” assumption in which only methane is emitted as a hydrocarbon.

Figure A5 shows sample results of 10 000 Monte Carlo draws for a 3-inch flare burning the M6 flare gas mixture at an exit velocity of 1 m/s while subjected to a crosswind of 2 m/s. The 2.5th and 97.5th percentiles of these distributions were used to define the measurement uncertainties (95% confidence interval) as plotted in Figure A6.

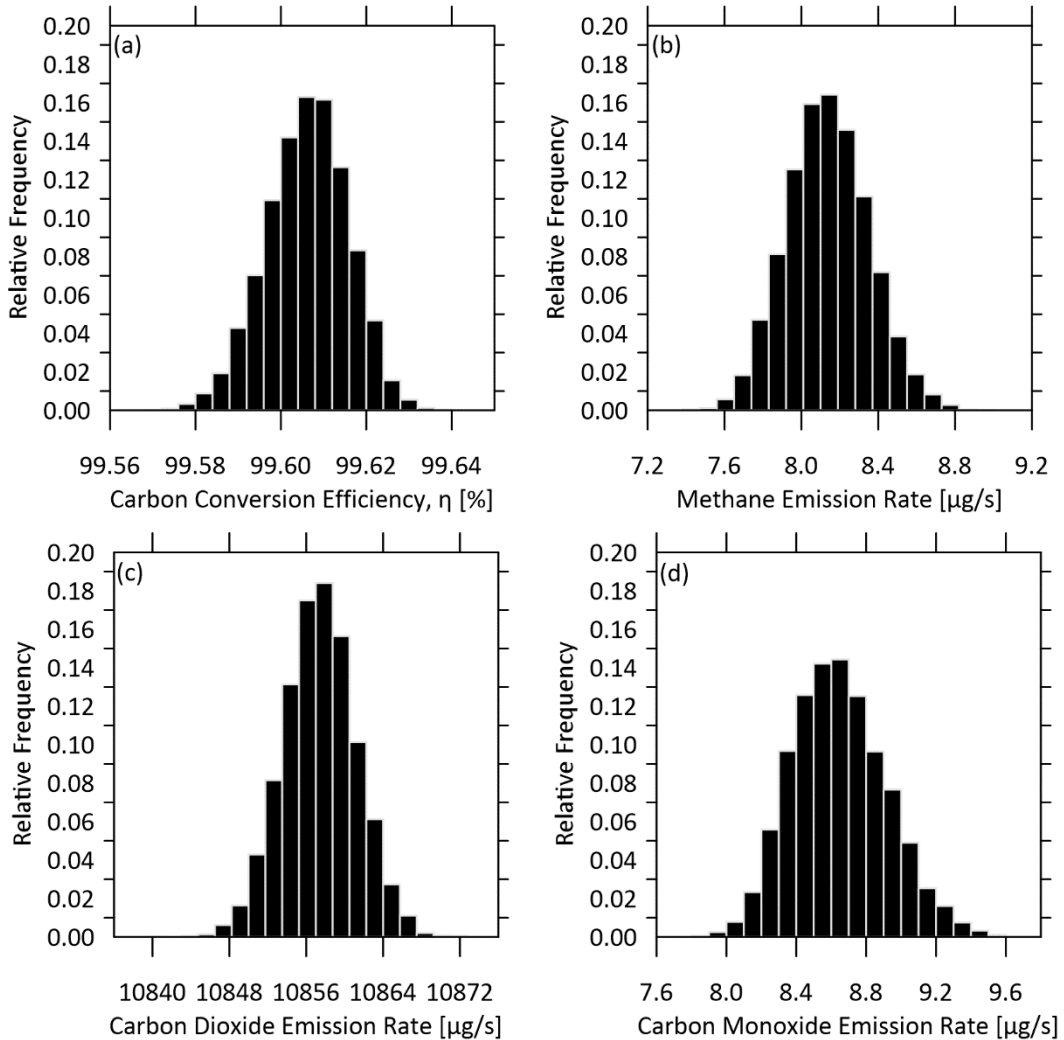


Figure A5: Example uncertainty distributions from the Monte Carlo simulation of a 3-inch (77.9-mm) flare burning the M6 flare gas mixture at a flow rate of 286 SLPM ($V_f=1\text{m/s}$) while subjected to a crosswind of 2 m/s. (a) Carbon conversion efficiency, (b) methane emissions, (c) carbon dioxide emissions, and (d) carbon monoxide emissions.

Figure A6 plots Monte Carlo calculated uncertainties in carbon conversion efficiency for a range of cases using the carbon balance and tracer methods. The carbon balance approach achieves absolute uncertainties of $\leq 0.55\%$ in all cases and is notably more accurate than the tracer method which has uncertainties of $< 3.5\%$. The uncertainty using the carbon balance approach is most

sensitive to the magnitude of the efficiency and is more accurate as the efficiency increases. The uncertainties are effectively independent of flare gas flow rates and are negligibly affected by the differences in flare gas composition.

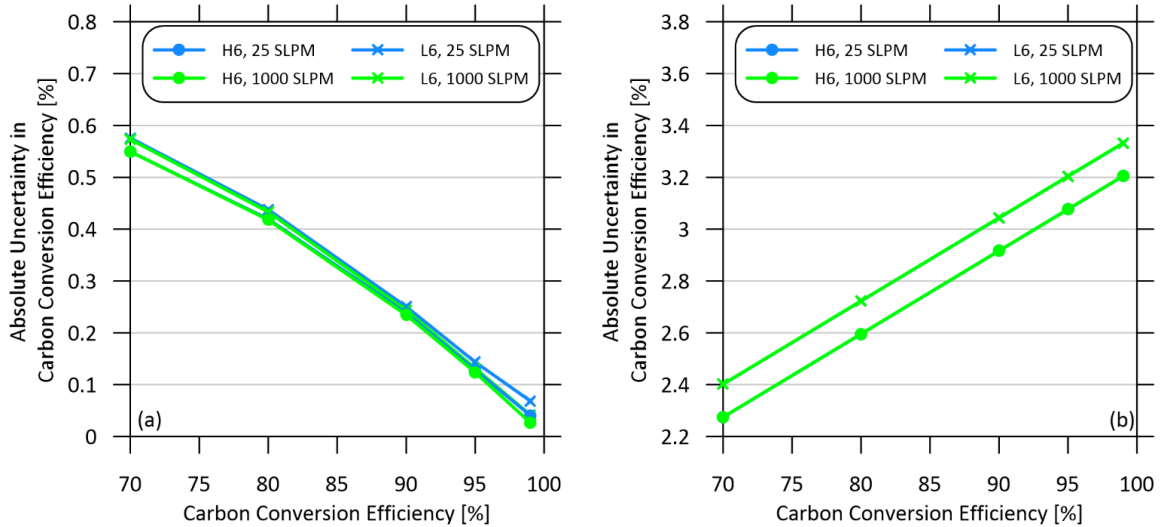


Figure A6: Comparison of absolute Monte Carlo estimated uncertainties in carbon conversion efficiency using either the a) carbon balance or b) tracer methods to determine V_{cv} for a flare burning the L6 or H6 flare gas mixtures.

Figure A7 plots Monte Carlo estimated species emission rate uncertainties using the carbon balance method for the same conditions as in Figure A6. In all scenarios, CO_2 emission rate uncertainties are $<1\%$ and CH_4 and CO uncertainties $<3.5\%$. These simulations assume a maximum linearity error of 2% (at 95% confidence) for all gas phase analyzers, which is based on preliminary experimental results introduced in Section 0. Emission rate uncertainties improve as the amount of the species of interest in the wind tunnel increases. Thus, as the combustion efficiency decreases, the CH_4 and CO emission rate uncertainties decrease, whereas the CO_2 uncertainty increases. For these test cases using the carbon balance method, Figure A7 shows that the choice of fuel has a negligible effect on the uncertainties.

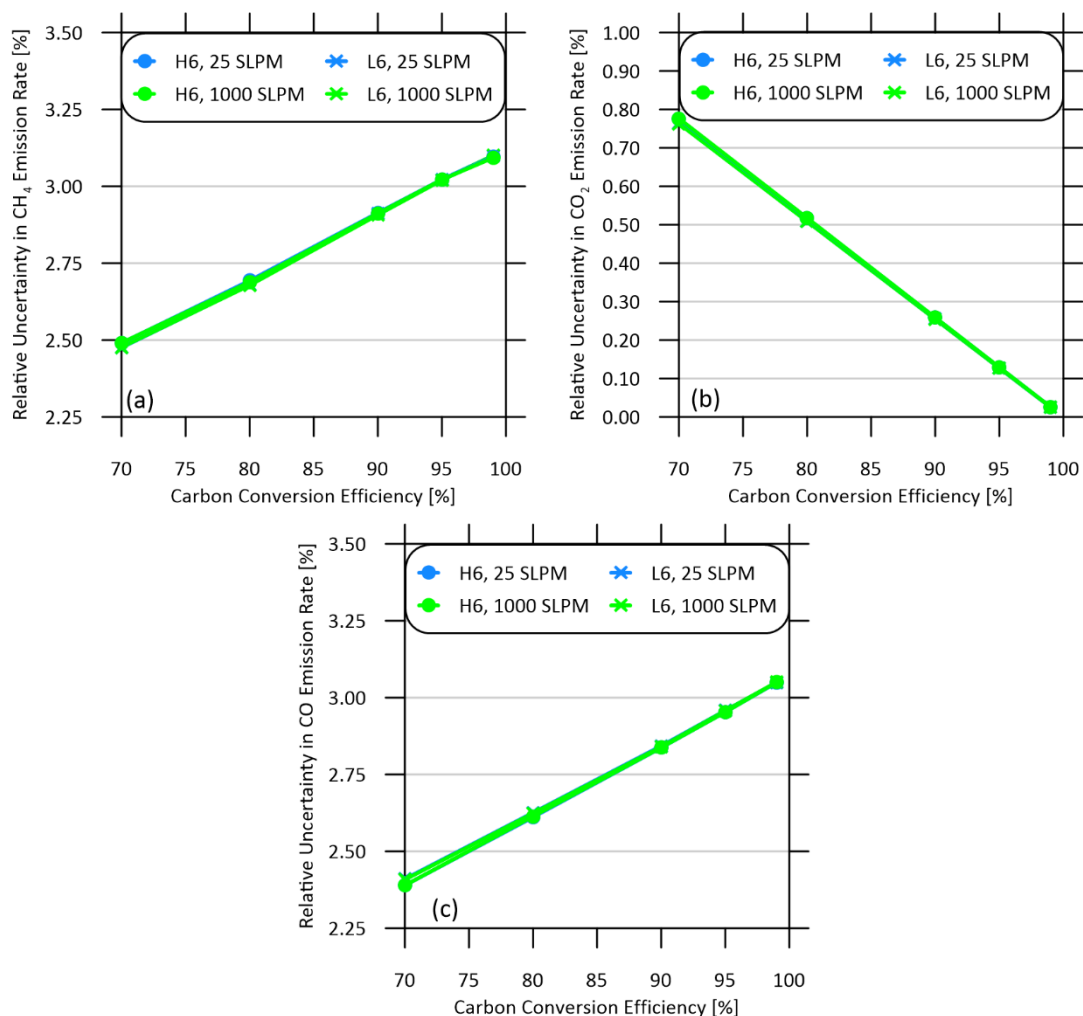


Figure A7: Monte Carlo estimated uncertainties in emission rates of a) CH₄, b) CO₂, and c) CO calculated using the carbon balance method.

The preceding results considered linearity uncertainties of 2% in the gas analyzers which gave results consistent with the present experimental system. However, in conjunction with the sensitivity analysis presented in Section A.6.2, it is recognized that higher accuracy analyzers could significantly reduce measurement uncertainties. Figure A8 considers a case where analyzer linearities were at the manufacturer specified values of 1%, which suggests that CO₂, CO, and CH₄ emission rate uncertainties of $\lesssim 1.5\%$ should be achievable with the present methodology.

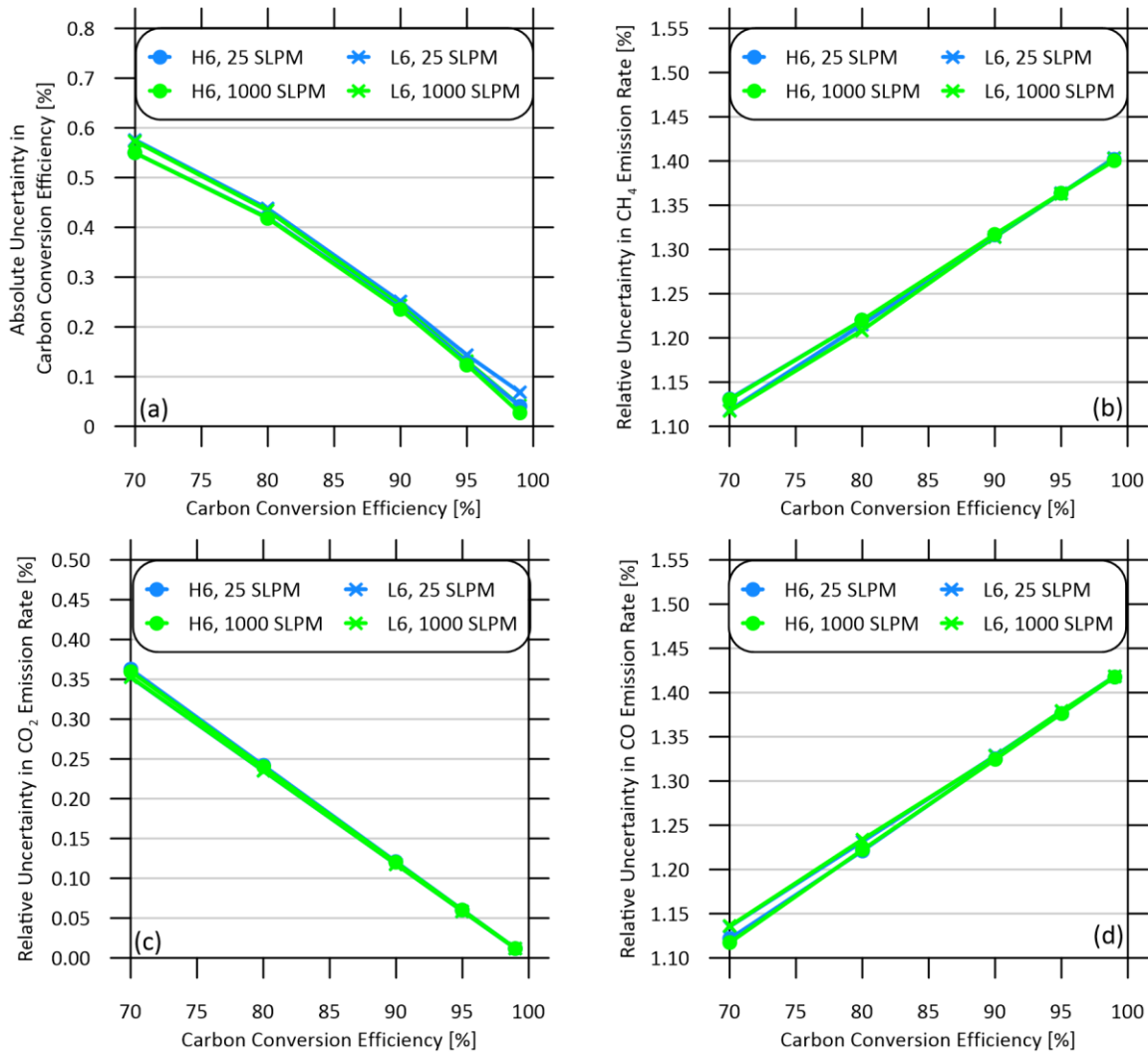


Figure A8: Monte Carlo Simulation for a) carbon conversion efficiency, b) CH₄ emissions, c) CO₂ emissions, and d) CO emissions assuming a 1% linearity error of gas-phase analyzers.

A.6.2 Sensitivity Analysis

A separate sensitivity analysis was performed to elucidate the main drivers of overall uncertainties. The sensitivity analysis considered a flare gas burning 250 SLPM of H6 fuel at 90% efficiency. Figure A9 plots the percentage change in calculated methane emission rate (sensitivity) to individually varied parameters (with all other parameters held constant in each graph). Figure A10 shows the net sensitivity of methane emission rate to each of these same parameters while all other parameters are simultaneously varied. Results in both Figure A9 and Figure A10 suggest that the uncertainty in the measured CO₂ and CH₄ concentrations have by far the largest influence on CH₄ emission rate uncertainty. All other parameters have negligible influence by comparison. Although not plotted here, similar analysis shows that the CO emission

rate uncertainty is dominated by uncertainty in measured CO and CO₂, and CO₂ emission rate uncertainty is dominated by the uncertainty of measured CO₂ alone. These results show that the accuracy of the CO₂ measurement the primary factor in determining the uncertainty of all measured species emission rates.

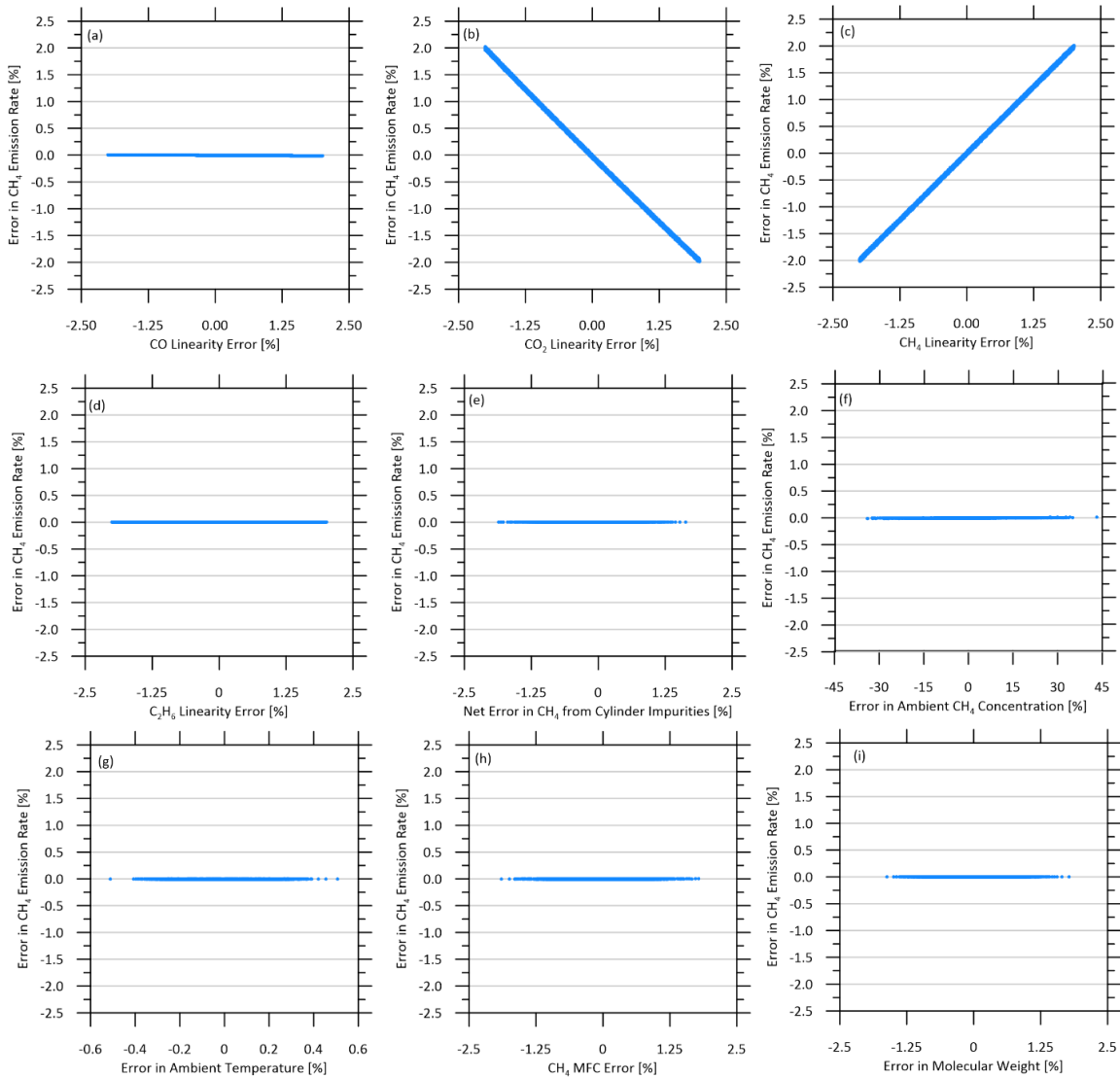


Figure A9: Sensitivity of uncertainty in methane emission rate to individual input variables, while other variables remain fixed. Analysis considers a flare burning 250 SLPM of H6 with 90% carbon conversion efficiency. †CO₂/CO/CH₄ measurement error includes both calibration error and analyzer non-linearity.

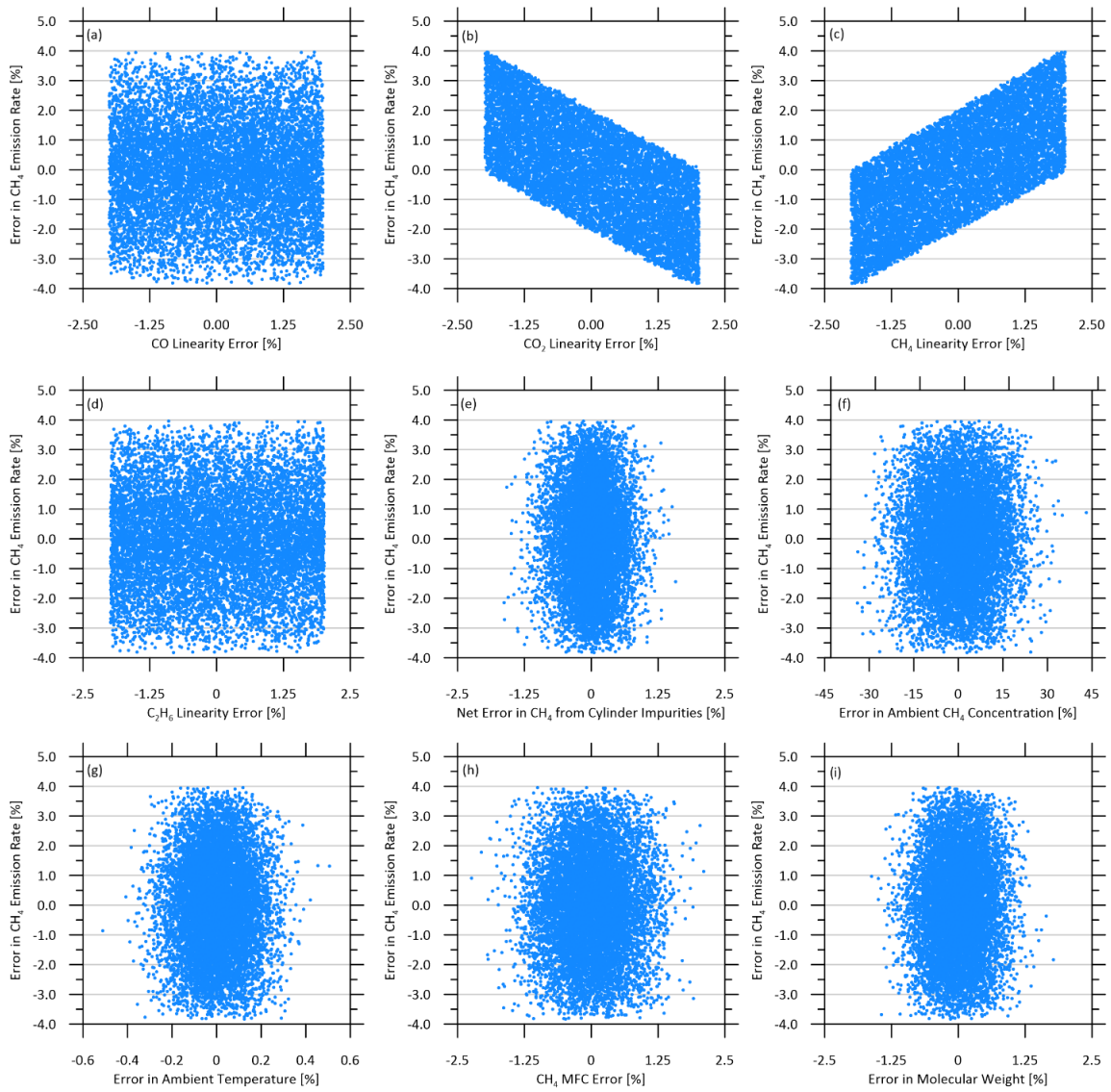


Figure A10: Sensitivity of uncertainty in methane emission rate to individual input variables with all other variables simultaneously varying. Analysis considers a flare burning 250 SLPM of H6 with 90% carbon conversion efficiency. \dagger CO₂/CO/CH₄ measurement error includes both calibration error and analyzer non-linearity.

A.6.3 Potential Influence of Analyzer Non-Linearity

The potential influence of non-linear response from the gas analyzers was included in the Monte Carlo uncertainty analysis by multiplying the measured concentrations by randomly generated parabolic functions with a specified maximum deviation from linearity. The parabolas of the following form were generated across the domain [0,1] with a range of $\pm y_{max}$, where y_{max} was the desired maximum percentage deviation from linearity:

$$y = ax^2 + bx + c \quad \text{B.44}$$

To ensure the maximum deviation occurred within the range [0,1], the location of the maximum, x_{max} , was first selected from a uniform distribution on the domain [0,1]. The parameters a and b were then selected such that:

$$\frac{dy}{dx} = 2ax_{max} + b = 0 \quad \text{B.45}$$

$$y_{max} = ax_{max}^2 + bx_{max} + c \quad \text{B.46}$$

To ensure that the value of the parabola at $x = 0$ was within the domain $[-y_{max}, y_{max}]$, the value of the coefficient b was selected subject to the condition:

$$-y_{max} \leq c \leq y_{max}$$

which can be simplified as follows using B.45 and B.46:

$$-y_{max} \leq y_{max} - ax_{max}^2 - bx_{max} \leq y_{max}$$

$$-2y_{max} \leq -\left(\frac{-b}{2x_{max}}\right)x_{max}^2 - bx_{max} \leq 0$$

$$-2y_{max} \leq -\frac{b}{2}x_{max} \leq 0$$

$$0 \leq b \leq \frac{4y_{max}}{x_{max}} \quad \text{B.47}$$

To ensure that the value of the parabola at $x = 1$ was within the domain $[-y_{max}, y_{max}]$, the value of the parameter b was selected subject to the additional condition:

$$-y_{max} \leq a + b + c \leq y_{max}$$

which can be simplified as follows using B.45 and B.46:

$$-y_{max} \leq \left(-\frac{b}{2x_{max}}\right) + b + \left(y_{max} - \left(\frac{-b}{2x_{max}}\right)x_{max}^2 - bx_{max}\right) \leq y_{max}$$

$$-2y_{max} \leq b\left(1 - \frac{1}{2x_{max}} - \frac{x_{max}}{2}\right) \leq 0$$

The term $\left(1 - \frac{1}{2x_{max}} - \frac{x_{max}}{2}\right)$ is always ≤ 0 for values of x_{max} on the domain [0,1], causing the direction of the inequalities to change when the expression is divided by this term. This results in the second pair of conditions on the selection of b :

$$-\frac{2y_{max}}{\left(1 - \frac{1}{2x_{max}} - \frac{x_{max}}{2}\right)} \geq b \geq 0 \quad \text{B.48}$$

Thus given (i) the desired maximum deviation value $\pm y_{max}$, (ii) a randomly selected value on [0,1] for the location of the maximum deviation x_{max} , and (iii) a randomly generated value of the coefficient b subject to the conditions specified in B.47 and B.48, it is possible to solve for the values of the coefficients a and c in B.45 and B.46 and generate curves such as shown in Figure A11(a).

The generic parabolas were then used to generate non-linear calibration curves for a desired instrument span. The span value was chosen to be 1.25x the maximum measured value for any given experiment, simulating a calibration wherein the measured value is located at 80% of the analyzer span. Thus for an example experiment measuring mole fraction X_i and having a maximum measurement $X_{i,final}$, the measurements with non-linearity error added to them are calculated as:

$$X_{i,with\ non-linearity}(X_i) = X_i \left[1 + \left(a \left(\frac{X_i}{1.25X_{i,final}} \right)^2 + b \left(\frac{X_i}{1.25X_{i,final}} \right) + c \right) \right] \quad \text{B.49}$$

Example non-linear calibration curves of this form are shown in Figure A11(b) for five randomly generated sets of values a, b, c with a span value of 600 ppm and a maximum deviation of 5%.

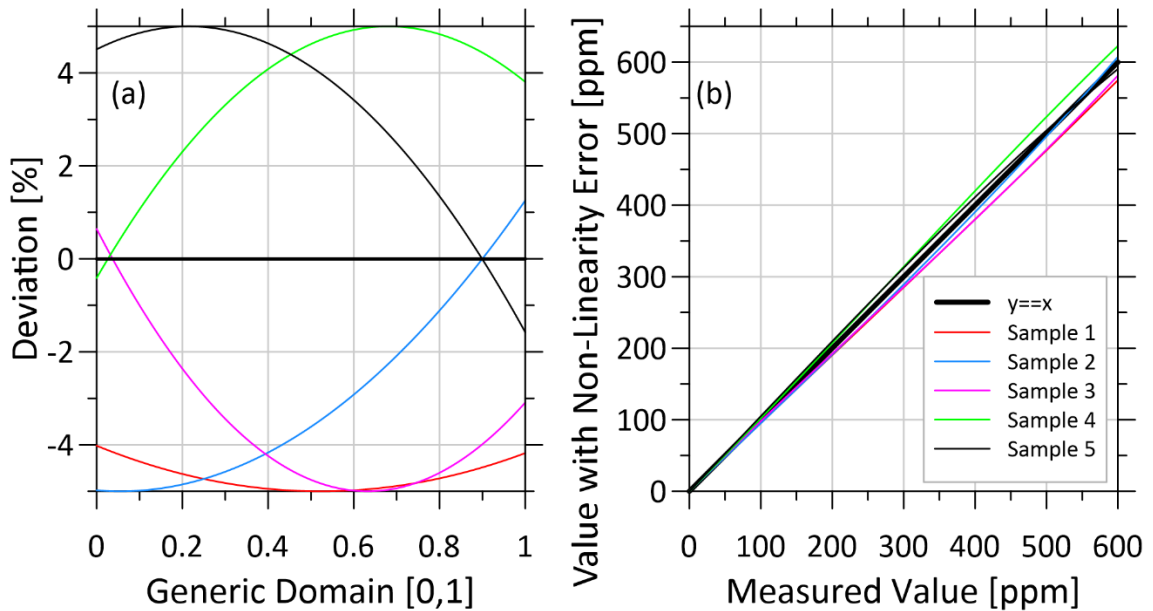


Figure A11: (a) Generic parabolas used to simulate non-linearity in gas analyzer response with a maximum deviation of 5%; (b) example non-linear calibration curves generated using the generic parabolas with an example span of 600 ppm.

A.7 Experimental Validation of Methodology

A.7.1 Convergence Tests

Due to the longitudinal variation of concentrations within the wind tunnel, especially near the start of an experiment, species accumulation rates, and therefore production rates and carbon conversion efficiency can take time to reach a stable value. Figure A12 shows the efficiencies and

emission rates calculated as the test time progresses. Parameters stabilize after 200–300 s, with negligible changes occurring past this point. Assuming a nominal test duration of between 300 and 360 s, an upper bound on the convergence error may be estimated by comparing the emission rate and carbon conversion efficiency data at tests ended between 350 and 700 s in in Figure A12. As summarized in Table A5, these upper bound convergence errors of carbon conversion efficiency, methane emission rate, and CO₂ emission rate fall well within overall uncertainties estimated from the Monte Carlo analysis. In practice, it would be possible to calculate these results in real-time during and experiment and check for convergence prior to ending each experiment.

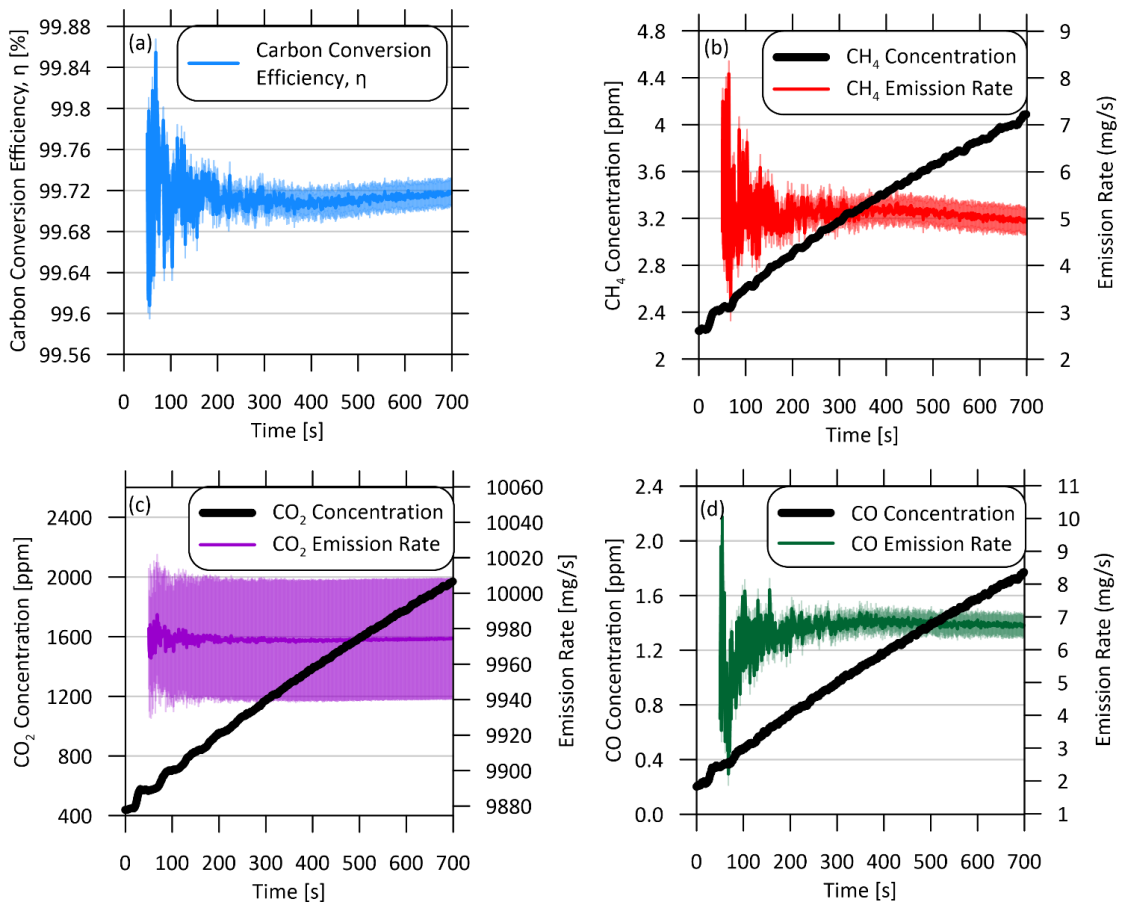


Figure A12: Convergence of (a) carbon conversion efficiency, (b) CH₄ emission rate, (c) CO₂ emission rate, and (d) CO emission rate at varying experiment durations for a 4-inch (102.3-mm) diameter flare burning M6 at a flow rate of 246 SLPM.

Table A5: Comparison of upper bound convergence errors from Figure A12 to total bias uncertainties estimate from the Monte Carlo Analysis for tests concluded after 350–700 s.

Parameter	Measured Magnitude	Max Convergence Error†	Monte Carlo Calculated Bias Uncertainty
Efficiency [%]	99.72	0.0006 (0.06%)	0.0013 (0.13%)
CH ₄ [mg/s]	5.07	0.14 (2.84%)	0.27 (5.53%)
CO ₂ [mg/s]	9973.7	5.8 (0.01%)	33.9 (0.34%)
CO [mg/s]	6.71	0.034 (0.51%)	0.34 (5.06%)

A.7.2 Cold-flow (Non-Reacting) Validation Experiments

Cold-flow experiments were performed in which CH₄, CO, and CO₂ were injected via the unlit flare stack into the wind tunnel. The relative flow rates of the species were adjusted to match the anticipated combustion products of flares burning at carbon conversion efficiencies between 80–99% with total flow rates between 50–125 SLPM. Figure A13 plots the percent difference between the prescribed and measured values of the carbon conversion inefficiency and CO₂, CH₄, and CO emission rates. The plotted error bars show the total experimental uncertainties combining the calculated bias error from the Monte Carlo analysis which used the inputs presented in Table A4 with the precision uncertainty from repeated measurements as detailed in Table A6. Across the range of tests, the measured carbon conversion inefficiency falls within –7.4% to +5.5% of the prescribed value and these differences are generally well within the estimated uncertainties. Similarly, the measured CO₂, CH₄, and CO emission rates are within –1.5% to +2.0%, –6.5% to +6.5%, and –9.5% to +1.4% of the prescribed values and are similarly consistent with estimated uncertainties. These results are especially encouraging since it is likely that the current cold-flow validation tests are near the limits of current experimental capabilities, given the relatively small flare gas flow rates (50–125 LPM) and correspondingly small volumes of measurable methane (0.25–5 SLPM) relative to the wind tunnel volume (~2,000,000 L). Ultimately, this reiterates the importance of accurate species concentration measurement in the CV when calculating emission rates. Future experiments could consider enhanced analyzer calibrations or alternative measurement technology to further reduce uncertainties if warranted. However, in the context of improving knowledge and understanding of emissions from global gas flaring as noted in the introduction to the paper, the apparent uncertainties in Figure A8 are more

than sufficient to enable quantitative experiments to elucidate the effects of turbulent crosswinds on flare performance.

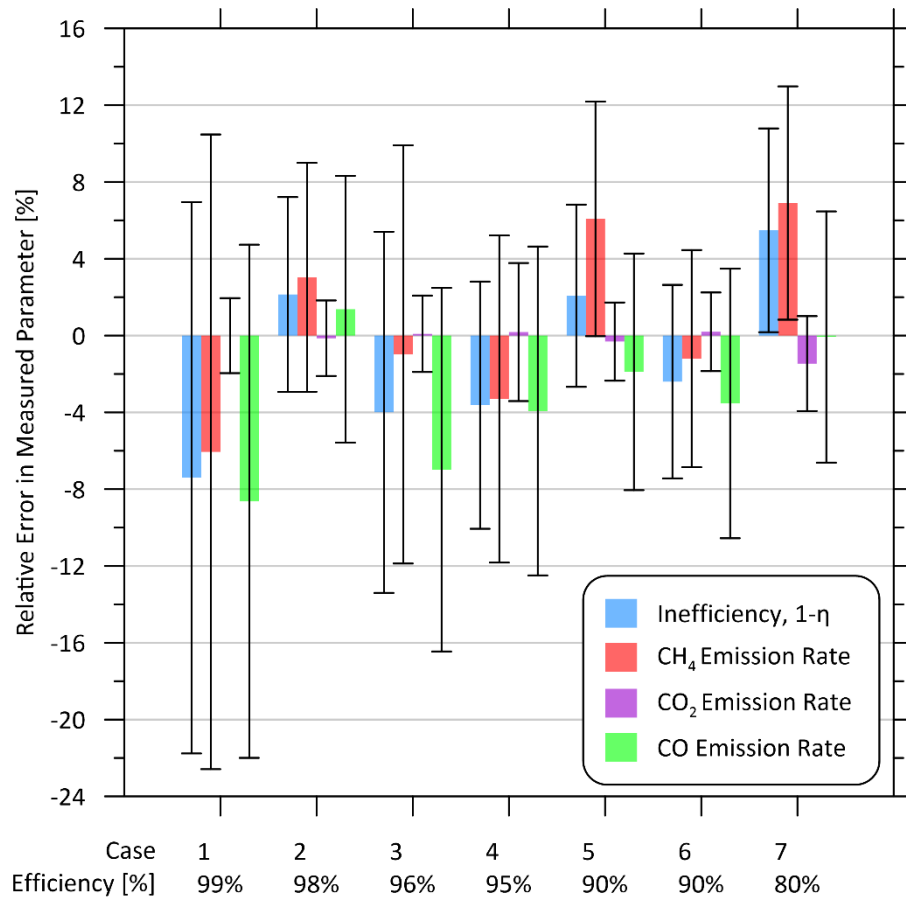


Figure A13: Cold flow experiment results conducted at the BLWTL simulating a flare burning CH₄ at efficiencies of 80–99% and flow rates of 50–125 SLPM subject to crosswind speeds of 2–9m/s. The error bars represent the total experimental uncertainty, combining bias errors from the Monte Carlo analysis with precision errors from repeated experiments as detailed in Table A6.

Table A6: Cold flow experimental results conducted at the BLWTL simulating a flare burning CH₄. Uncertainties in the table were calculated considering an analyzer calibration (span) uncertainty of 2% in the Monte Carlo analysis.

Case	Injected flow rates [SLPM]				# of Tests	Cross-wind speed [m/s]	Carbon Conversion Inefficiency, 1- η [%]					
	Total	CO ₂	CH ₄	CO			Target	Measured Value				
								Avg.	Exp. Bias Uncertainty from MC Analysis	Experimental Precision Uncertainty	Total Experimental Uncertainty	Bias Error from Target
1	50	50	0.25	0.25	3	2-9	1	0.93	0.0245 (4.87%)	0.125 (13.5%)	0.133 (14.4%)	-0.074 (-7.40%)
2	50	49	0.5	0.5	10	2-9	2	2.0	0.0993 (4.86%)	0.0297 (1.45%)	0.104 (5.07%)	0.043 (2.14%)
3	50	48	1	1	3	2-9	4	3.8	0.190 (4.95%)	0.207 (8.00%)	0.361 (9.41%)	-0.160 (-4.00%)
4	100	95	2.5	2.5	3	2-9	5	4.8	0.246 (5.11%)	0.189 (3.92%)	0.310 (6.44%)	-0.181 (3.63%)
5	50	45	2.5	2.5	14	2-9	10	9.8	0.434 (4.45%)	0.231 (2.37%)	0.492 (5.04%)	-0.240 (-2.40%)
6	50	45	2.5	2.5	3	2-9	10	10.2	0.467 (2.58%)	0.128 (1.25%)	0.485 (4.75%)	0.208 (2.08%)
7	125	100	20	5	4	2-9	20	21.1	0.852 (4.04%)	0.726 (3.44%)	1.12 (5.31%)	1.10 (5.48%)

Case	Injected flow rates [SLPM]				# of Tests	Cross-wind speed [m/s]	CO ₂ Emission Rate [mg/s]					
	Total	CO ₂	CH ₄	CO			Target	Measured Value				
								Avg.	Exp. Bias Uncertainty from MC Analysis	Experimental Precision Uncertainty	Total Experimental Uncertainty	Bias Error from Target
1	50	50	0.25	0.25	3	2-9	1536	1535	29.9 (1.95%)	1.71 (0.111%)	20.0 (1.95%)	0.051 (1.95%)
2	50	49	0.5	0.5	10	2-9	1521	1518	29.9 (1.97%)	0.278 (0.018%)	29.9 (1.97%)	-2.04 (-0.135%)
3	50	48	1	1	3	2-9	1489	1490	29.2 (1.96%)	5.02 (0.337%)	29.6 (1.99%)	1.36 (0.091%)
4	100	95	2.5	2.5	3	2-9	2949	2950	105.8 (3.59%)	7.04 (0.239%)	106 (3.60%)	1.56 (0.053%)
6	50	45	2.5	2.5	14	2-9	1396	1391	28.3 (2.03%)	1.97 (0.141%)	28.4 (2.04%)	-4.40 (-0.316%)
5	50	45	2.5	2.5	3	2-9	1396	1399	28.2 (2.02%)	4.43 (0.317%)	28.6 (2.05%)	2.70 (0.193%)
7	125	100	20	5	4	2-9	3103	3057	69.7 (2.28%)	29.1 (0.952%)	75.5 (2.47%)	-45.2 (-1.479%)

Case	Injected flow rates [SLPM]				# of Tests	Cross-wind speed [m/s]	CH ₄ Emission Rate [mg/s]					
	Total	CO ₂	CH ₄	CO			Target	Measured Value				
								Avg.	Exp. Bias Uncertainty from MC Analysis	Experimental Precision Uncertainty	Total Experimental Uncertainty	Bias Error from Target
1	50	50	0.25	0.25	3	2–9	2.83	2.66	0.152 (5.72%)	0.412 (15.5%)	0.439 (16.5%)	-0.171 (-6.45%)
2	50	49	0.5	0.5	10	2–9	5.65	5.8	0.340 (5.84%)	0.070 (1.21%)	0.346 (5.96%)	0.172 (2.95%)
3	50	48	1	1	3	2–9	11.3	11.2	0.651 (5.81%)	1.03 (9.21%)	1.219 (10.9%)	-0.111 (-0.99%)
4	100	95	2.5	2.5	3	2–9	28.3	27.3	1.93 (7.07%)	1.30 (4.75%)	2.329 (8.52%)	-0.935 (-3.42%)
6	50	45	2.5	2.5	14	2–9	28.3	30.0	1.77 (5.91%)	0.466 (1.56%)	1.83 (6.11%)	1.718 (5.73%)
5	50	45	2.5	2.5	3	2–9	28.3	27.9	1.56 (5.57%)	0.277 (0.991%)	1.58 (5.66%)	-0.339 (-1.22%)
7	125	100	20	5	4	2–9	226	241.8	12.1 (5.01%)	8.31 (3.44%)	14.6 (6.08%)	15.6 (6.46%)

Case	Injected flow rates [SLPM]				# of Tests	Cross-wind speed [m/s]	CO Emission Rate [mg/s]					
	Total	CO ₂	CH ₄	CO			Target	Measured Value				
								Avg.	Exp. Bias Uncertainty from MC Analysis	Experimental Precision Uncertainty	Total Experimental Uncertainty	Bias Error from Target
1	50	50	0.25	0.25	3	2–9	4.93	4.51	0.295 (6.55%)	0.525 (11.7%)	0.602 (13.4%)	-0.427 (-9.47%)
2	50	49	0.5	0.5	10	2–9	9.87	10.0	0.621 (6.21%)	0.313 (3.12%)	0.695 (6.95%)	0.135 (1.35%)
3	50	48	1	1	3	2–9	19.7	18.4	1.23 (6.71%)	1.23 (6.69%)	1.74 (9.47%)	-1.38 (-7.49%)
4	100	95	2.5	2.5	3	2–9	49.4	47.4	3.68 (7.77%)	1.71 (3.60%)	1.74 (9.47%)	-1.93 (-4.07%)
6	50	45	2.5	2.5	14	2–9	49.4	48.4	2.89 (5.97%)	0.741 (1.53%)	4.06 (8.56%)	-0.932 (-1.92%)
5	50	45	2.5	2.5	3	2–9	49.4	47.6	2.85 (5.99%)	1.74 (3.66%)	2.99 (6.17%)	-1.74 (-3.66%)
7	125	100	20	5	4	2–9	98.7	98.6	5.40 (5.47%)	3.54 (3.59%)	6.45 (6.54%)	-0.075 (-0.08%)

A.8 Comparing to Bourguignon et al. (1999)

As noted in the main text, the present work corrects an error in the methodology published by (Bourguignon et al. 1999). Derivations follow a similar method as outlined in Eq. B.1 – B.9, at

which point the methodologies diverge. To account for the exfiltration of gases from the CV, (Bourguignon et al. 1999) incorrectly substituted the following expression into Eq. (4.3)

$$\dot{V}_{ex} = (\dot{V}_{in} + \gamma' \dot{V} + \dot{V}_{inert}) \frac{T_{cv}}{T_{\infty}} \quad \text{B.50}$$

where γ' is a coefficient to account for the number of moles of combustion products introduced into the tunnel relative to the number of moles of fuel. However, Eq. B.50 fails to consider the time rate of change of T_{cv} during an experiment and the associated effect on \dot{V}_{ex} as well as the change in mass within the CV with temperature. Fortunately, the variations in temperature during published experiments (Johnson and Kostiuk 2000, 2002b; Johnson et al. 2001; Kostiuk et al. 2000) using the methodology of (Bourguignon et al. 1999) were small, such that the influence of this error is shown here to be negligible. Selected raw data collected in these previous studies was re-evaluated using the methodology developed in the present paper. Four natural gas tests that represent limiting cases of measured efficiency in the U of A tests were considered. Because these experiments measured total hydrocarbons (THCs) via a flame ionization detector (FID) which reported total hydrocarbons as CH₄, Eq. (4.17) was modified to:

$$\eta = \frac{\left(\begin{array}{l} \left[\begin{array}{l} \#_{C,f} \dot{V}_{f,\infty} - \sum_{i \neq HC} \#_{C,i} X_{i,\infty} \frac{M_f}{M_{\infty}} \dot{V}_{f,\infty} \\ - \#_{C,f} X_{CH_4,\infty} \frac{M_f}{M_{\infty}} \dot{V}_{f,\infty} \\ - \#_{C,f} \{X_{CH_4,\infty} \dot{V}_{air,comb,\infty}\}_{i=HC} \end{array} \right] \frac{dX_{CO_2,cv}}{dt} \Big|_{t \rightarrow t_0} + X_{CO_2,\infty} \frac{M_f}{M_{\infty}} \dot{V}_{f,\infty} - \dot{V}_{f,\infty} X_{CO_2,f} \\ \left[\begin{array}{l} \sum_{i \neq HC} \#_{C,i} \frac{dX_{i,cv}}{dt} \Big|_{t \rightarrow t_0} + \\ \#_{C,f} \frac{dX_{CH_4,cv}}{dt} \Big|_{t \rightarrow t_0} \end{array} \right] \end{array} \right)}{\#_{C,f} \dot{V}_{f,\infty}} \quad \text{B.51}$$

Figure A14 shows the efficiency results calculated by using the method of Bourguignon et al. compared to those re-evaluated using B.51. Results vary by less than the 0.5 percent uncertainty quoted in their developed methodology and therefore have negligible impact on the validity of previously published results based on this methodology. However, temperature changes at the much larger scale tests performed at the present BLTWL have the potential to be significantly larger than in previous experiments, which was a key motivation for correcting the error in Bourguignon et al. (1999) as part of creating the more robust methodology outlined in this paper.

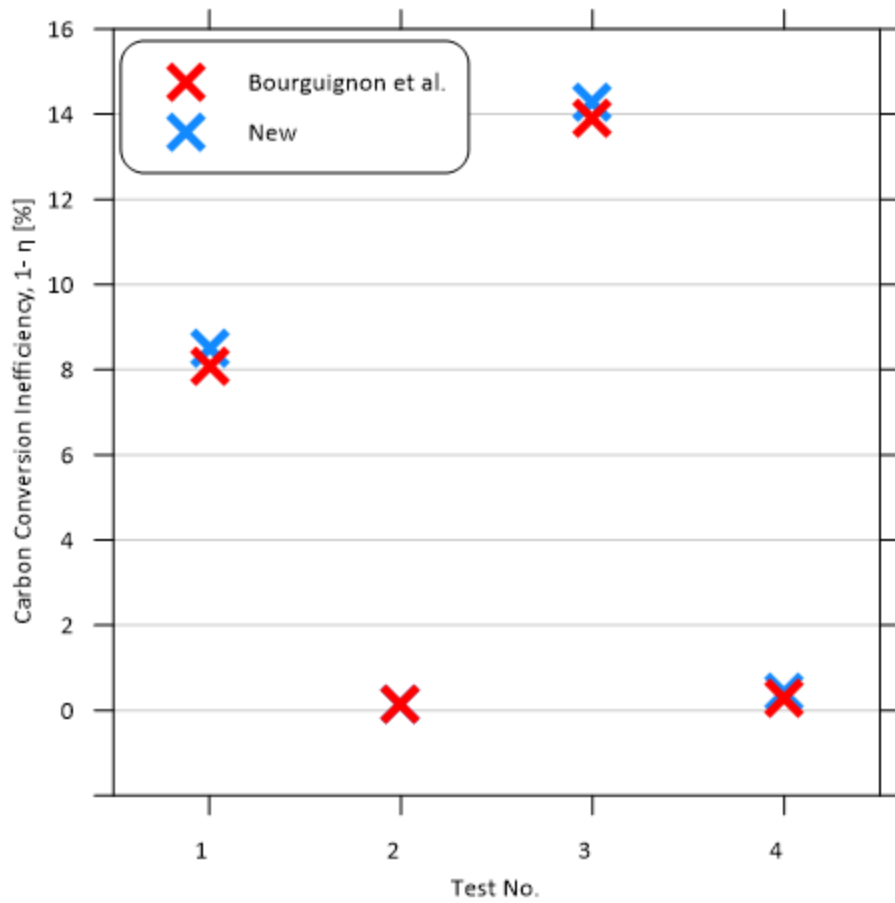


Figure A14: Reanalysis of selected flare efficiency experimental data from (Johnson and Kostiuk 2000, 2002b) comparing results using the presently derived calculation methodology to the original method of (Bourguignon et al. 1999) which included an error in the tunnel volume-temperature term as noted. Results show the impact of this error was negligible, consistent with the small temperature changes within the CV during their experiments.

Appendix B Inefficiency Curves

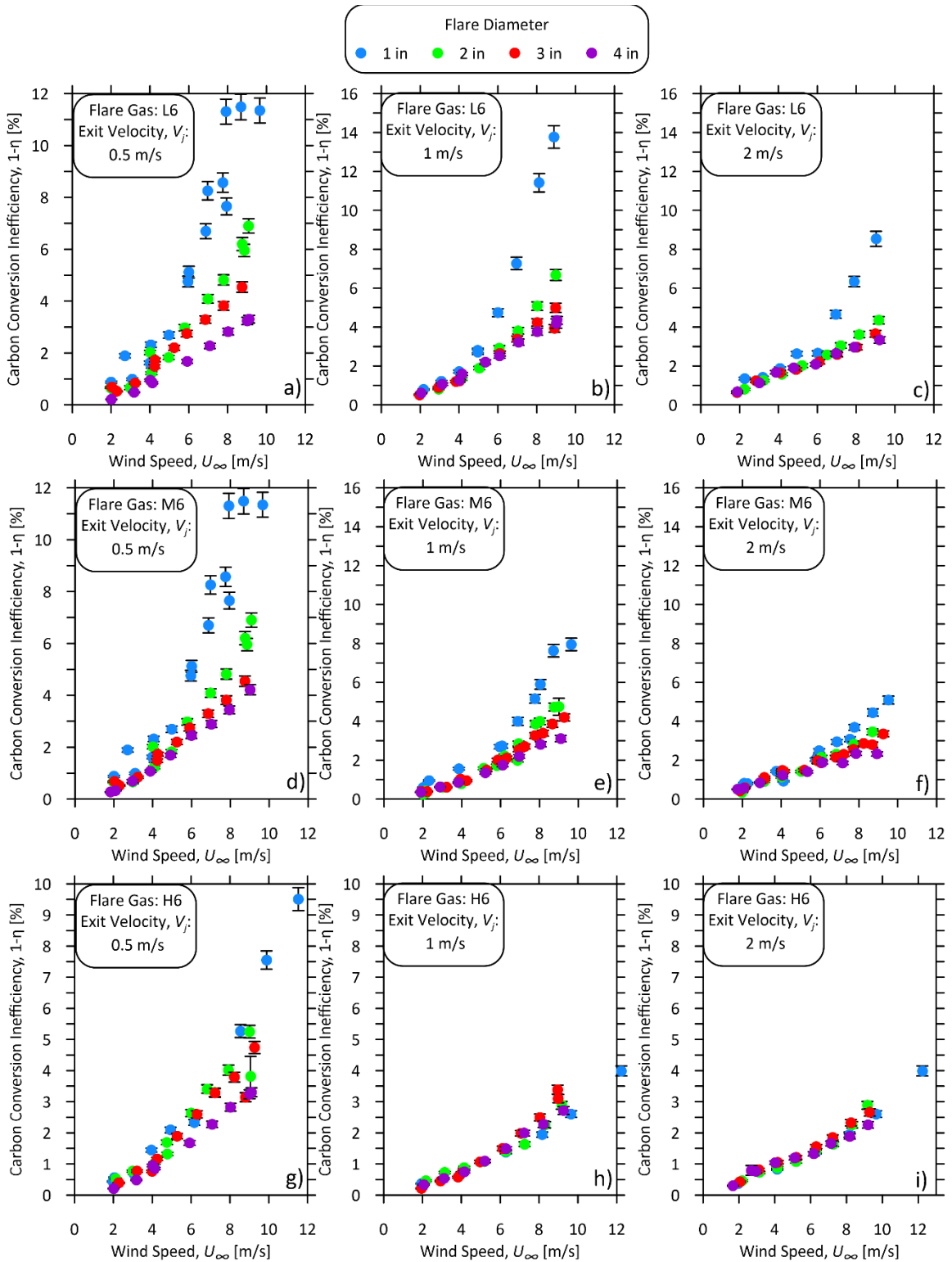


Figure B1: Inefficiency curves for a-c) L6, d-f) M6 and g-i) H6, plotted as a function of crosswind speed.

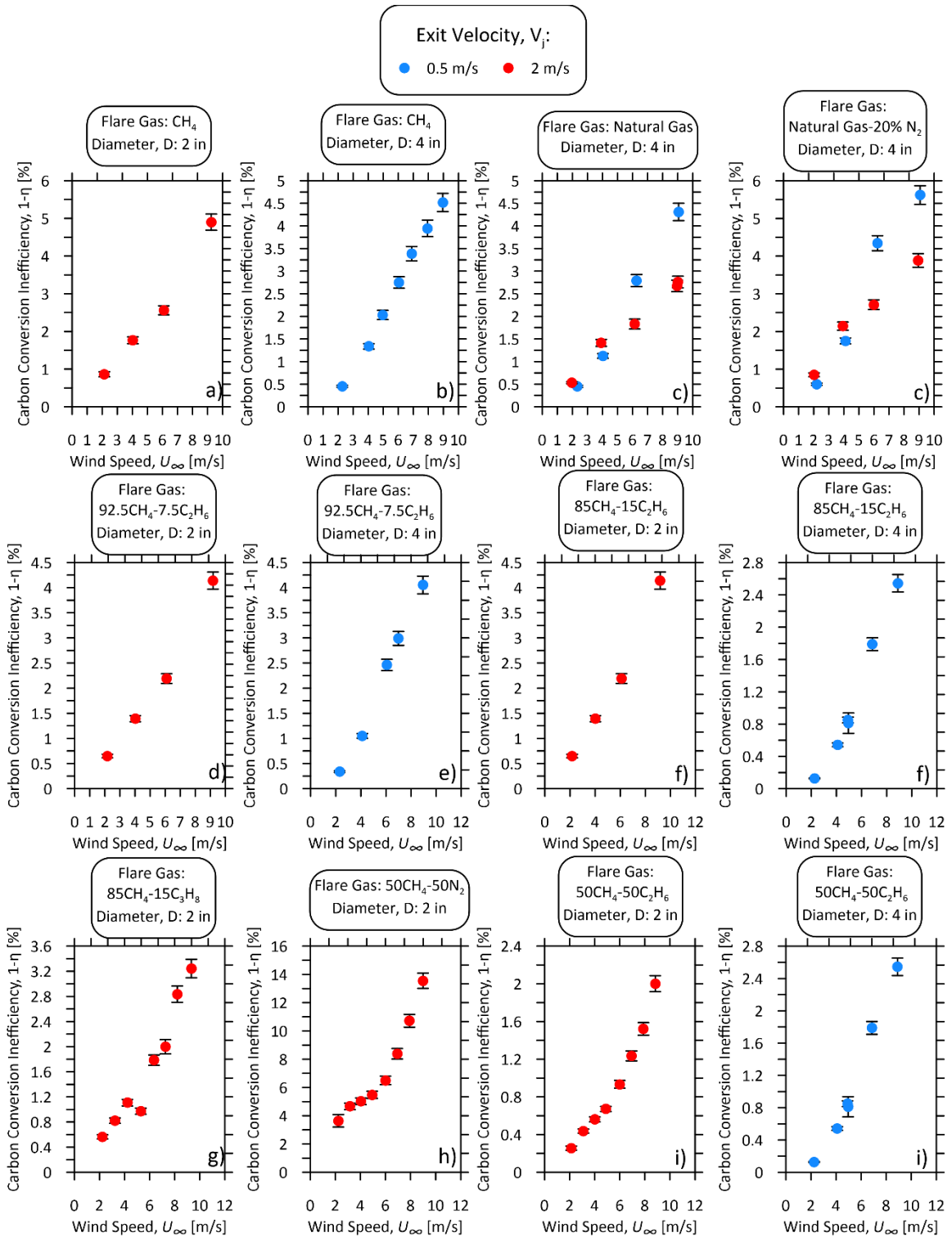


Figure B.2 Inefficiency curves of various simple fuel mixtures, plotted as a function of crosswind speed.

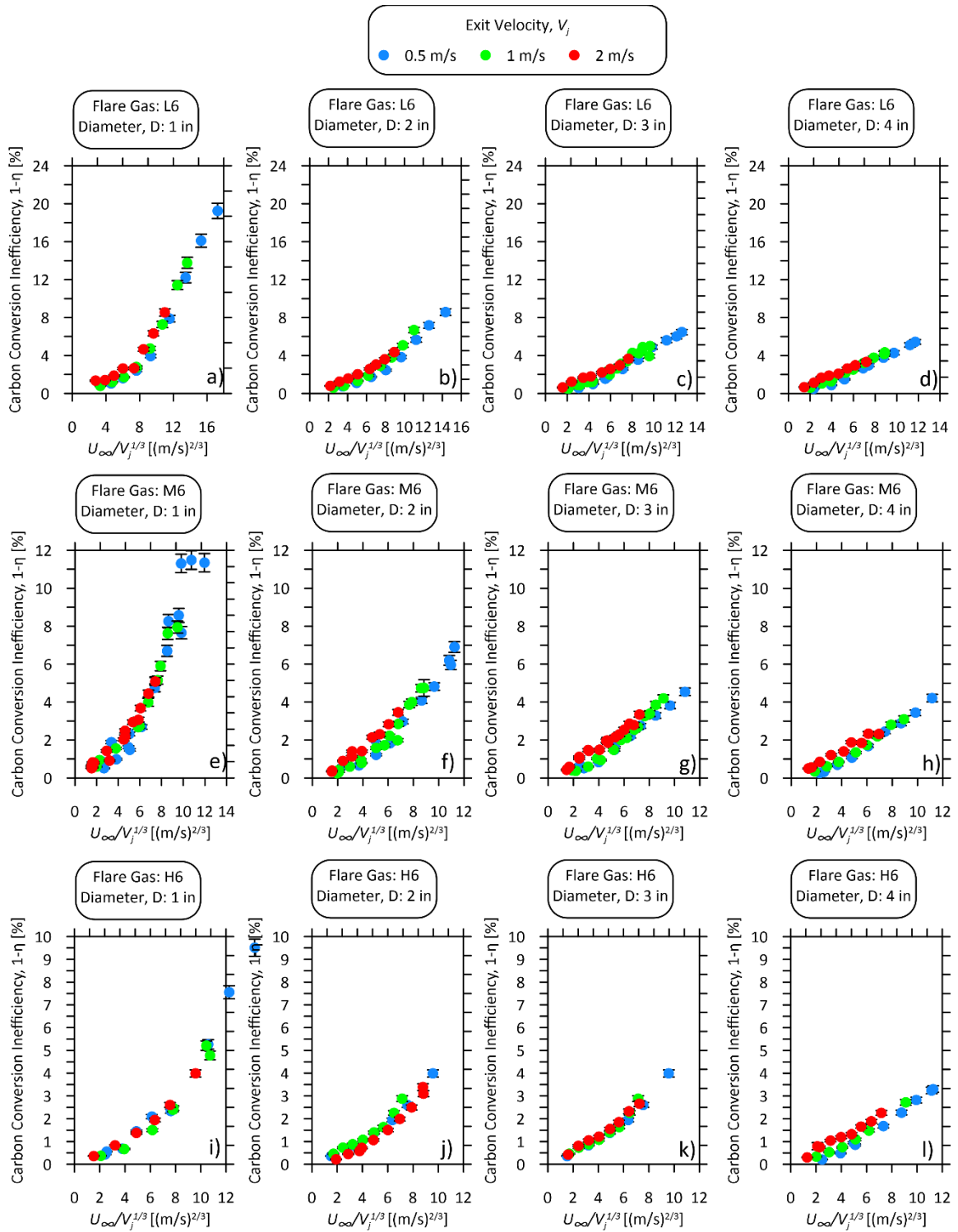


Figure B.3 Inefficiency curves for a-c) L6, d-f) M6 and g-i) H6, plotted as a function of Eq. 5.2.

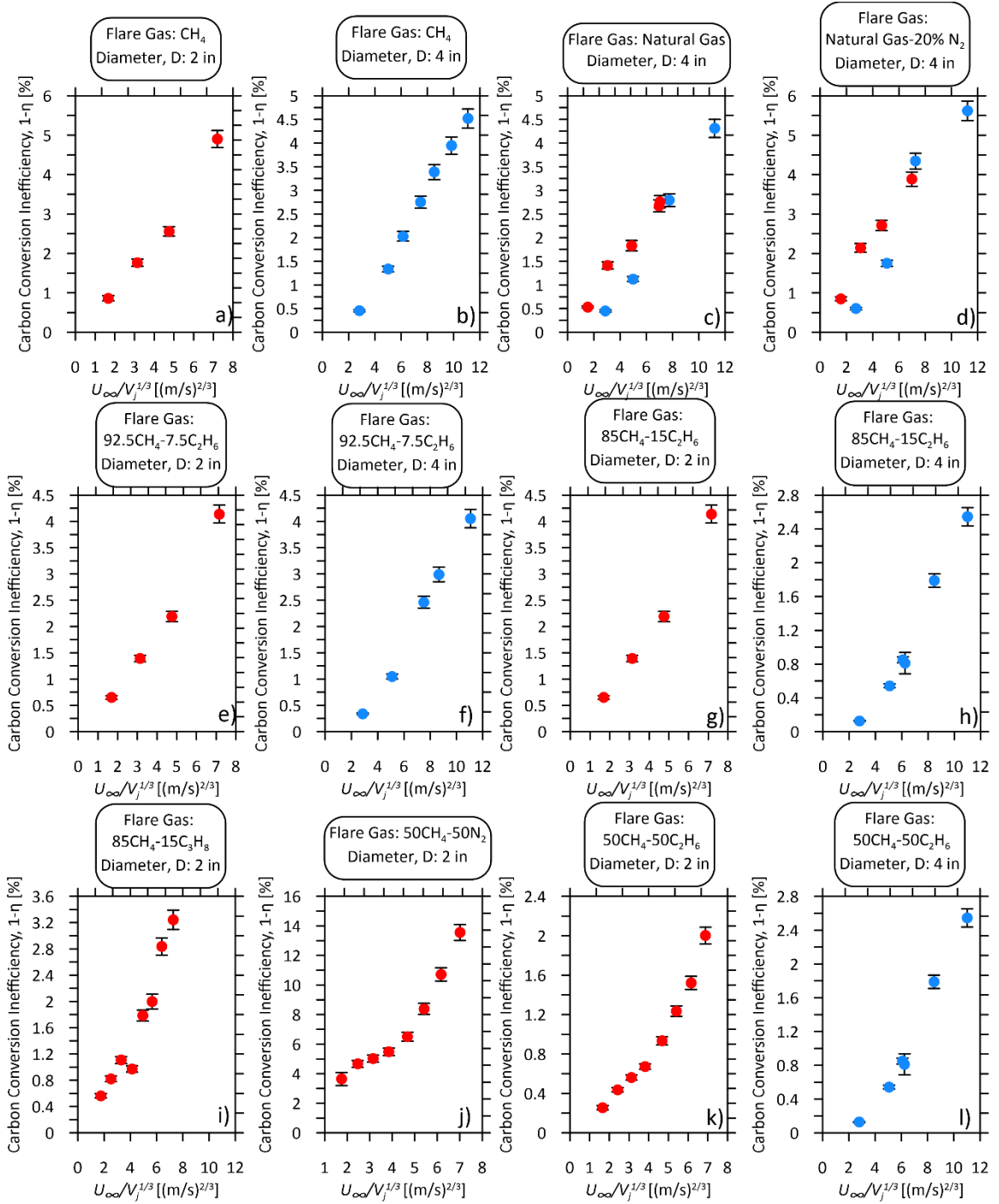


Figure B.4 Inefficiency curves of various simple fuel plotted as a function of Eq. 5.2.

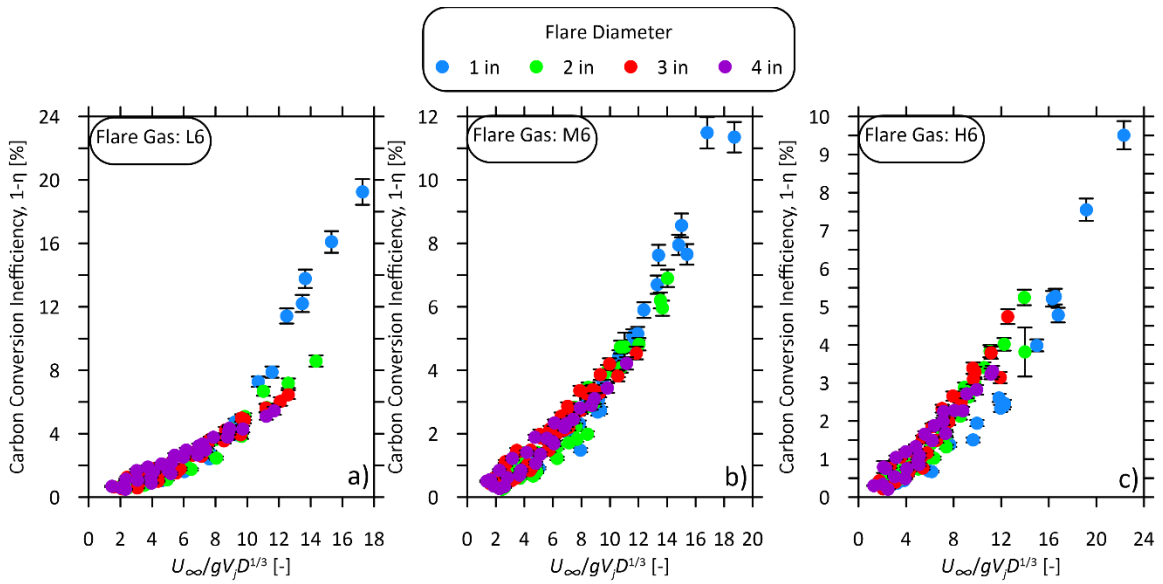


Figure B.5 Inefficiency curves for a-c) L6, d-f) M6 and g-i) H6, plotted as a function of Eq.5.3, where $n = 1/3$.

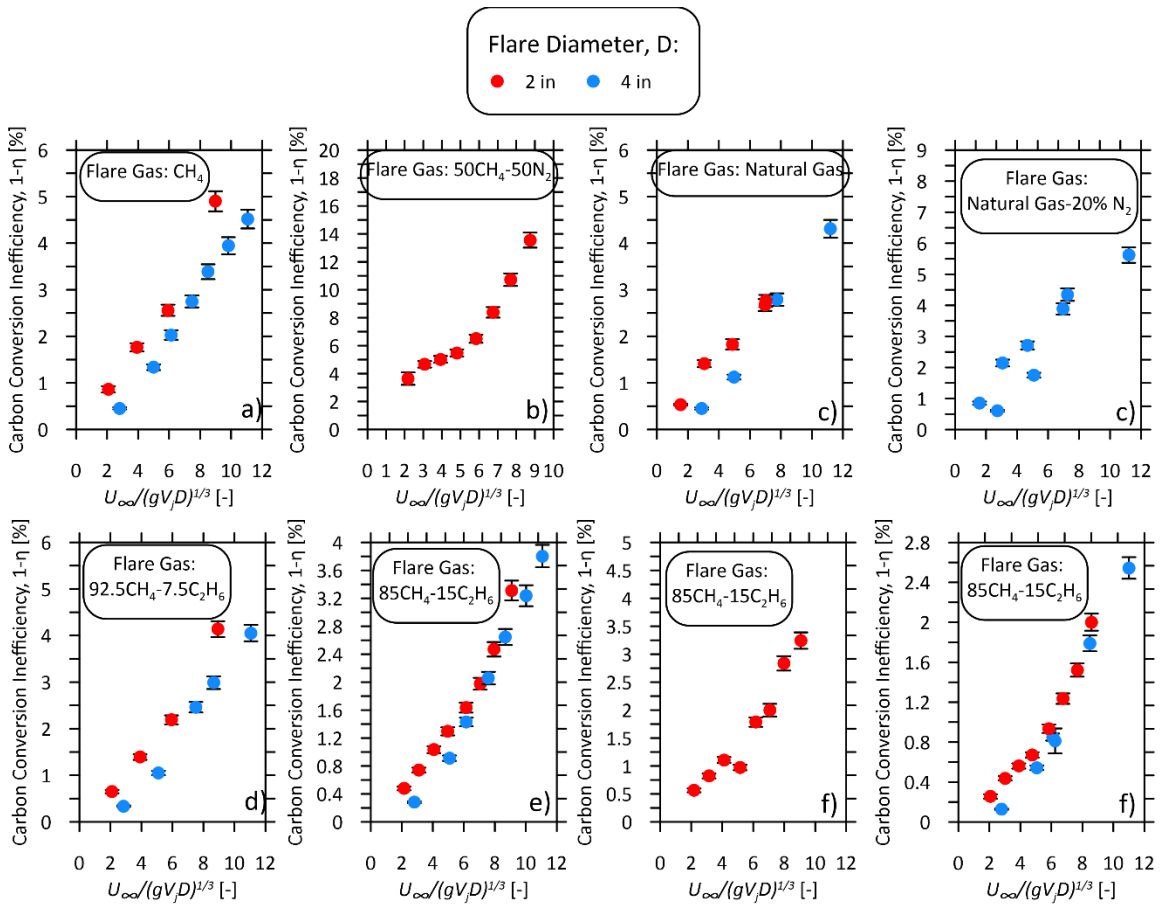


Figure B.6 Inefficiency curves for various simple fuel plotted as a function of Eq.5.3, where $n = 1/3$.

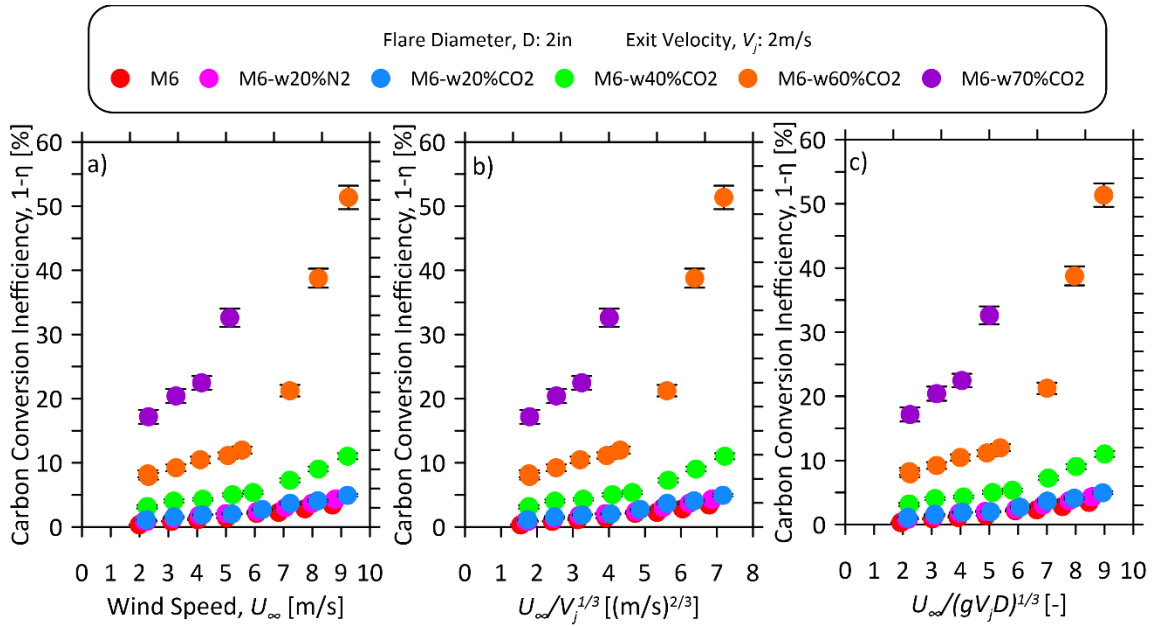


Figure B.7 Inefficiency curves for a-M6 diluted with inert species as a function of a) wind speed, b) 5.2 and c) Eq.5.3, where $n = 1/3$.

Appendix C Candidate Empirical Models for Predicting Flare Carbon Conversion Inefficiencies

As discussed in Section 6.2, several candidate empirical models were considered to predict carbon conversion inefficiencies of flares in a turbulent crosswind burning a range of flare gas compositions, for which either $AF_{vol,stoic}$, $AF_{mass,stoic}$, T_{ad} , LHV , $C_{\#}$, or S_L were used as a correlating parameter. In each case, power law fits in the form of $f(x) = ax^b + c$ were applied to the correlated data and fit coefficients of the model parameters were optimized to minimize the absolute errors in the predicted inefficiencies. Figure C to Figure C5 show candidate models and corresponding histograms of the absolute error when predicting the experimentally measured flare carbon conversion inefficiencies of 2–4 inch diameter pipe flare burning C1–C4 alkane mixtures with <20% inert fraction in turbulent crossflow. Figure C6 to Figure C10 show similar candidate models but considering fuel mixtures with up to 70% inert fraction. The table below each figure shows its corresponding fit equation and associated statistics.

C.1 Candidate inefficiency models for flares burning C1–C4 alkane flare gas mixtures with less than 20% inert fraction

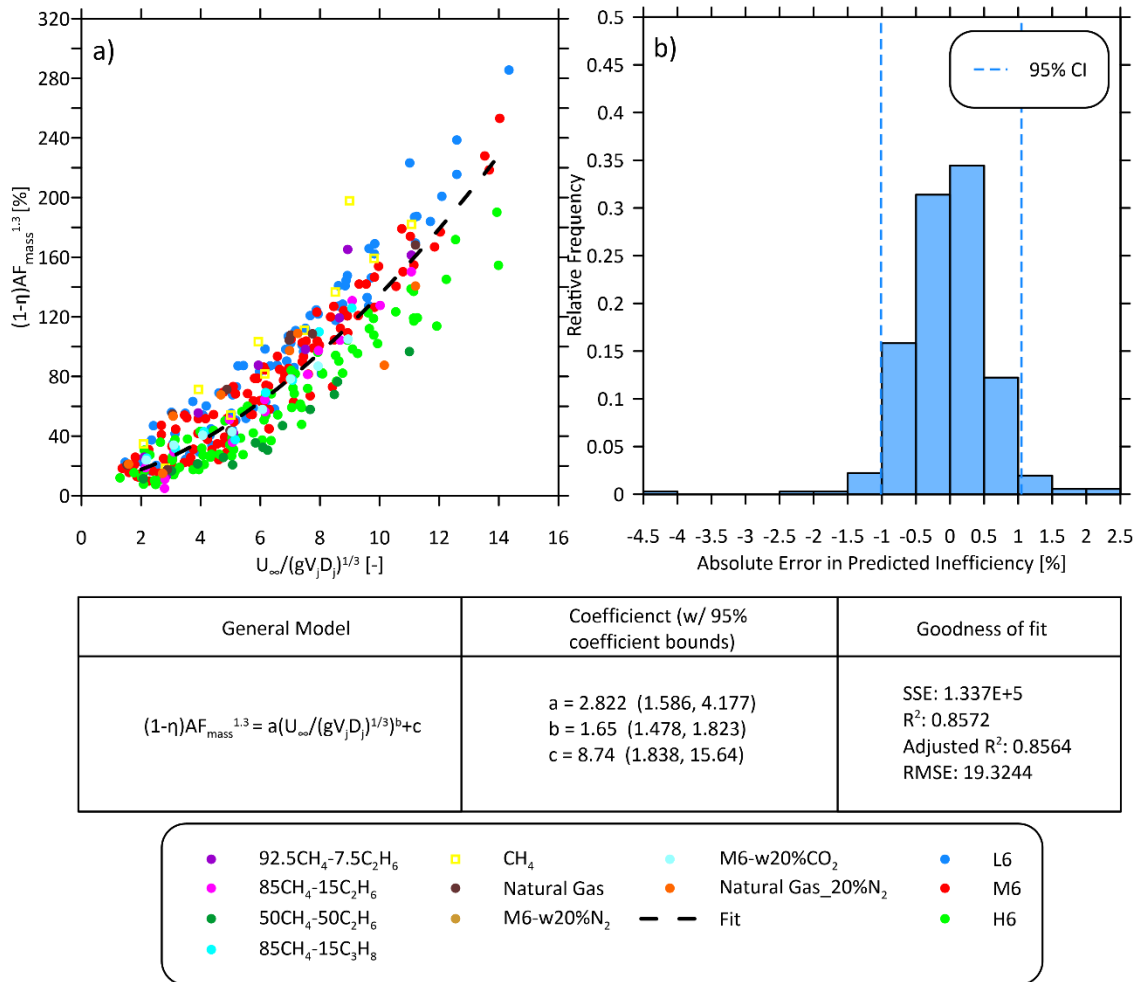


Figure C1: a) Empirical model using $AF_{mass,stoic}^{1.3}$ as a correlating parameter to predict carbon conversion inefficiency of 2–4 inch diameter pipe flares burning C1–C4 alkane-based flare gas mixtures with less than 20% inert fraction (CO₂ and N₂) and b) corresponding histograms of the errors in the predicted inefficiency.

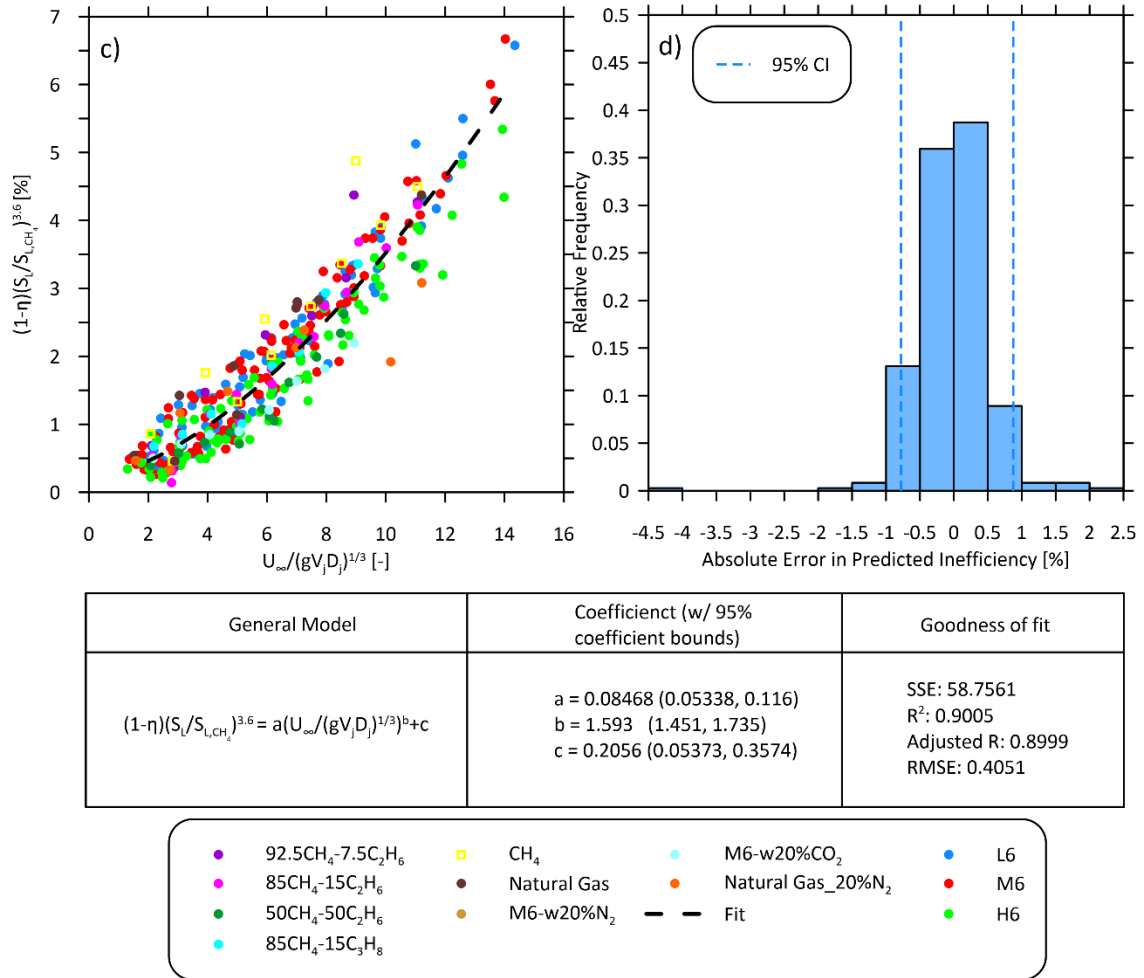
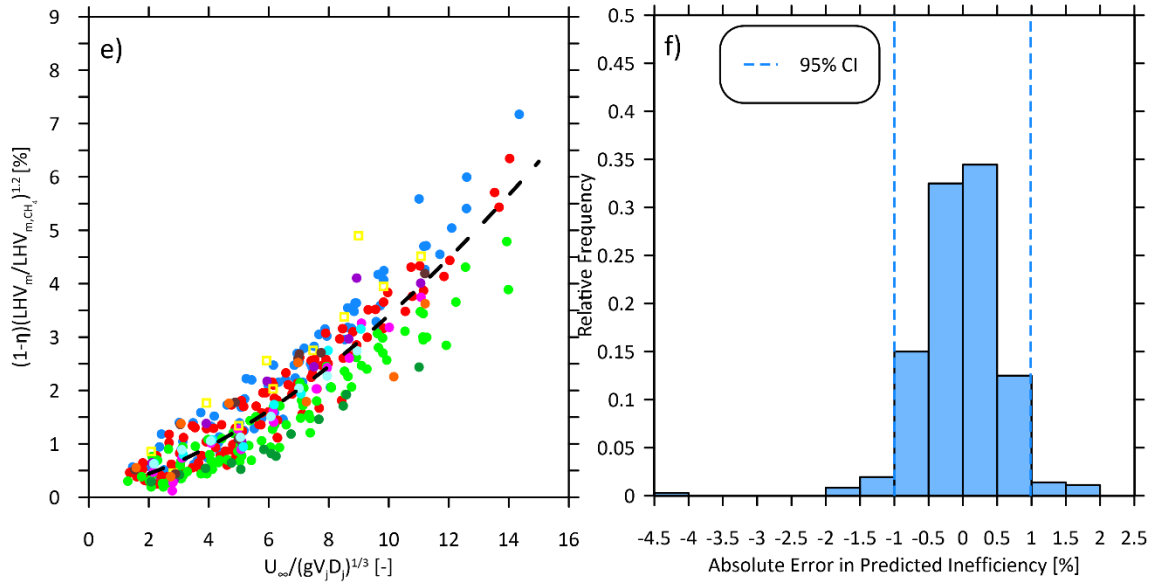


Figure C2: c) Empirical model using S_L as a correlating parameter to predict carbon conversion inefficiency of 2–4 inch diameter pipe flares burning C1–C4 alkane-based flare gas mixtures with less than 20% inert fraction (CO₂ and N₂) and d) corresponding histograms of the errors in the predicted inefficiency.



General Model	Coefficient (w/ 95% coefficient bounds)	Goodness of fit
$(1-\eta)(LHV_m/LHV_{m,CH_4})^{1.2} = a(U_\infty/(gV_j D)^{1/3})^b + c$	$a = 0.08548$ (0.047, 0.124) $b = 1.576$ (1.404, 1.748) $c = 0.1867$ (0.005179, 0.3683)	SSE: 81.5334 R^2 : 0.8602 Adjusted R^2 : 0.8594 RMSE: 0.4772

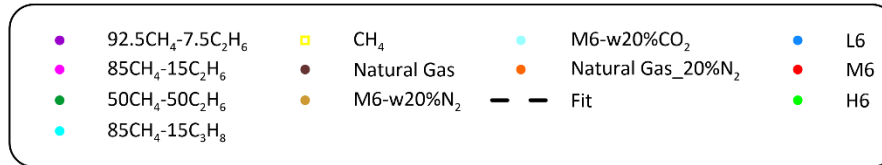
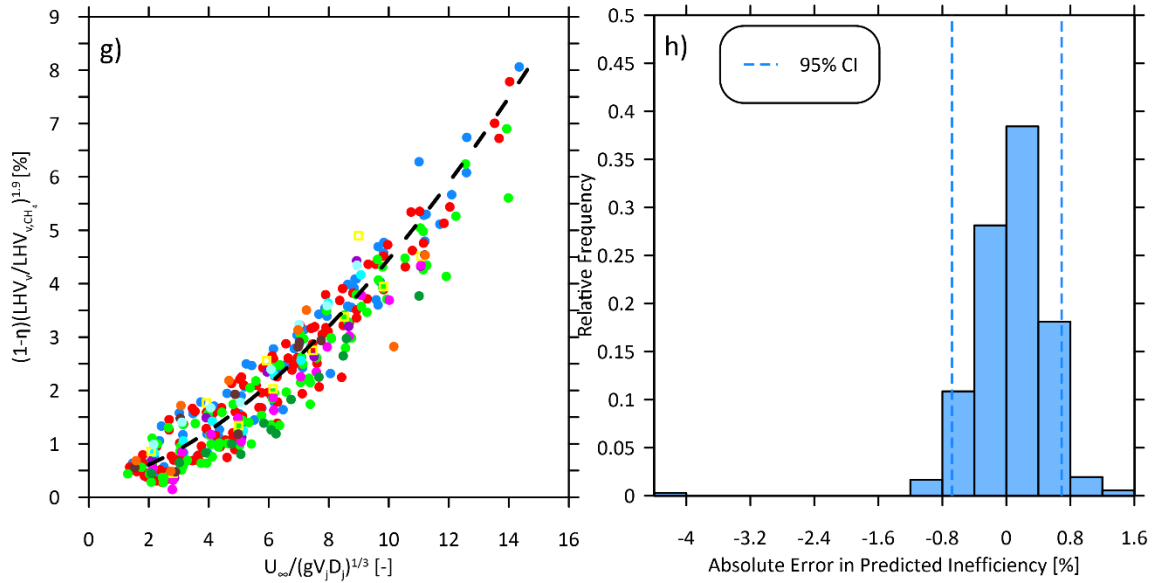


Figure C3: e) Empirical model using LHV_{mass} as a correlating parameter to predict carbon conversion inefficiency of 2–4 inch diameter pipe flares burning C1–C4 alkane-based flare gas mixtures with less than 20% inert fraction (CO₂ and N₂) and f) corresponding histograms of the errors in the predicted inefficiency.



General Model	Coefficient (w/ 95% coefficient bounds)	Goodness of fit
$(1-\eta)(LHV_m / LHV_{m,CH_4})^{1.9} = a(U_\infty / (gV_j D)^{1/3})^b + c$	$a = 0.09855$ (0.06771, 0.1294) $b = 1.625$ (1.505, 1.745) $c = 0.3071$ (0.1495, 0.4647)	SSE: 66.8497 R^2 : 0.9294 Adjusted R^2 : 0.9290 RMSE: 0.4321

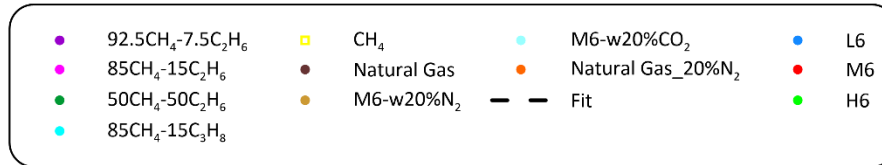


Figure C4: g) Empirical model using LHV_{vol} as a correlating parameter to predict carbon conversion inefficiency of 2–4 inch diameter pipe flares burning C1–C4 alkane-based flare gas mixtures with less than 20% inert fraction (CO₂ and N₂) and h) corresponding histograms of the errors in the predicted inefficiency.

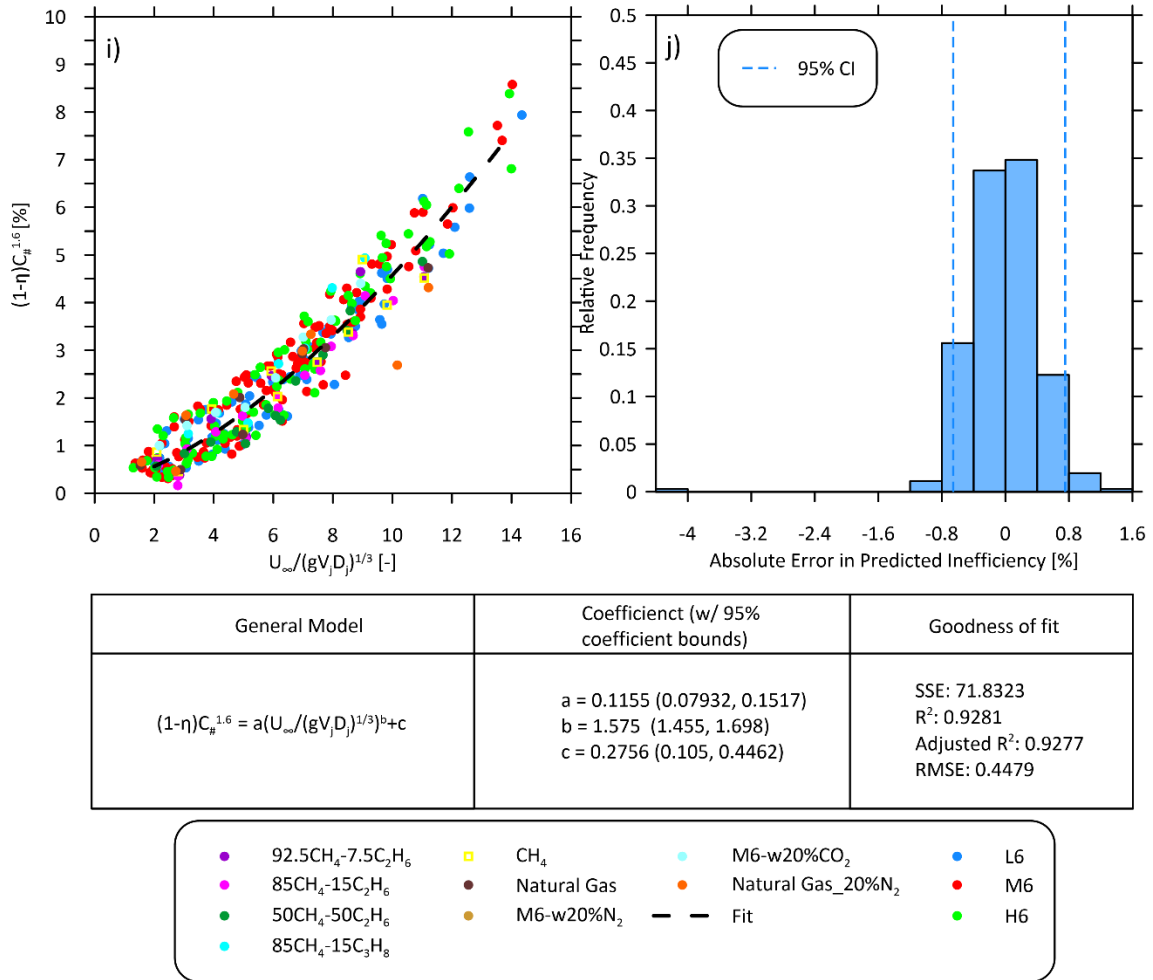


Figure C5: i) Empirical model using mean carbon number ($C_{\#}$) as a correlating parameter to predict carbon conversion inefficiency of 2–4 inch diameter pipe flares burning C1–C4 alkane-based flare gas mixtures with less than 20% inert fraction (CO_2 and N_2) and j) corresponding histograms of the errors in the predicted inefficiency.

C.2 Candidate inefficiency models for flares burning C1–C4 alkane flare gas mixtures with up to 70% inert fraction

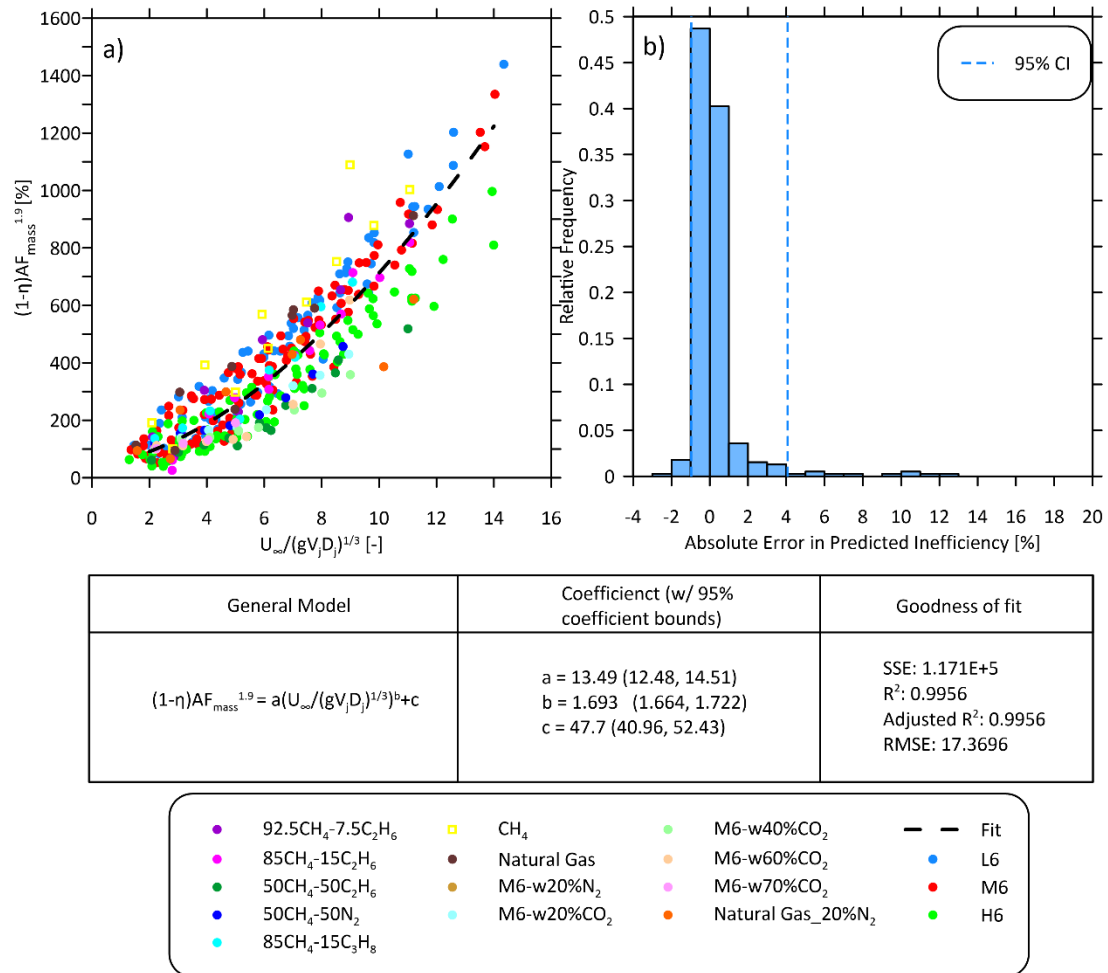
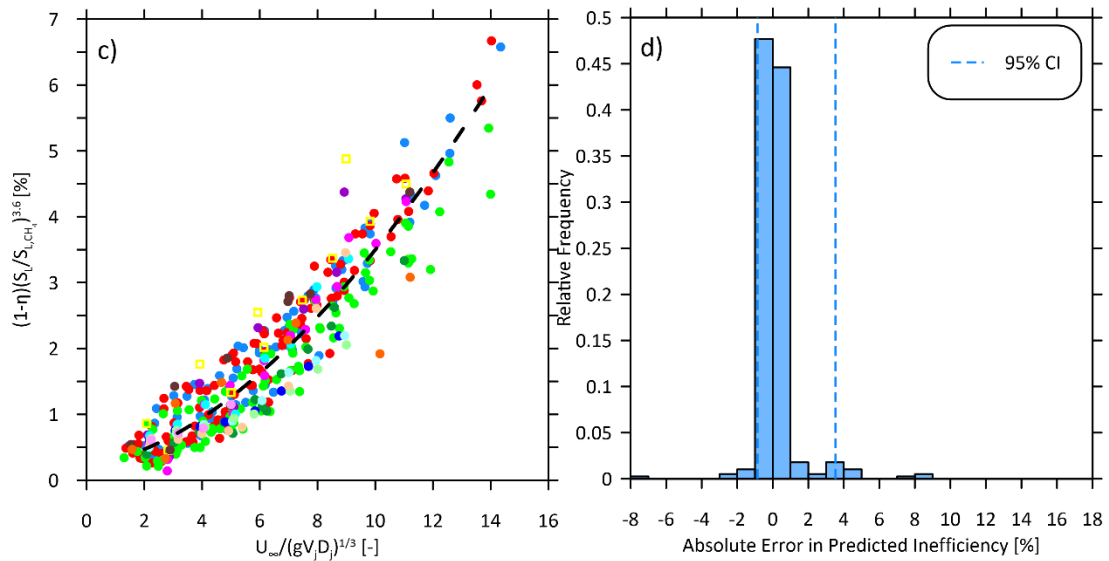


Figure C6: a) Empirical model using $AF_{mass,stoic}$ as a correlating parameter to predict carbon conversion inefficiency of 2–4 inch diameter pipe flares burning C1–C4 alkane-based flare gas mixtures with up to 70% inert fraction (CO₂ and N₂) and b) corresponding histograms of the errors in the predicted inefficiency.



General Model	Coefficient (w/ 95% coefficient bounds)	Goodness of fit
$(1-\eta)(S_L/S_{L,CH_4})^{3.6} = a(U_{\infty}/(gV_j D_j)^{1/3})^b + c$	a = 0.06603 (0.06218, 0.06989) b = 1.691 (1.668, 1.713) c = 0.2574 (0.2357, 0.2791)	SSE: 1.6693 R ² : 0.9973 Adjusted R ² : 0.9973 RMSE: 0.0656

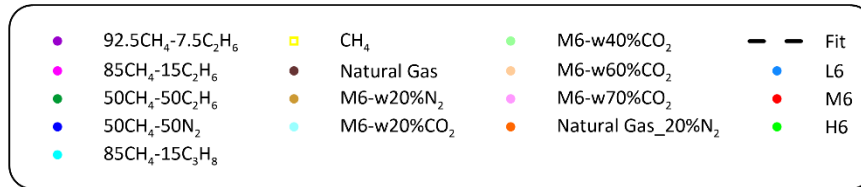
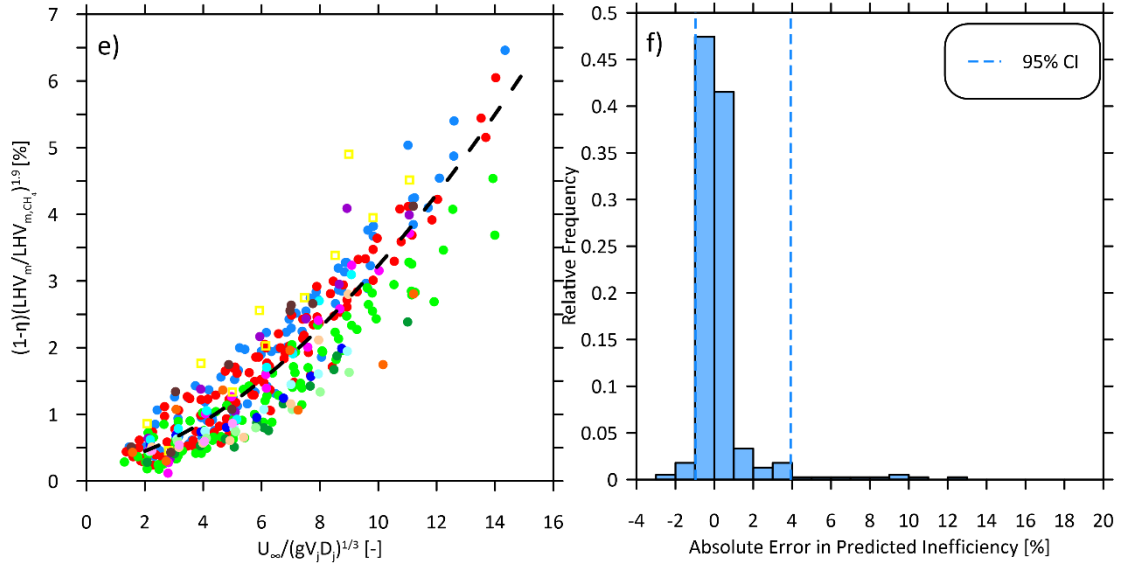


Figure C7: c) Empirical model using S_L as a correlating parameter to predict carbon conversion inefficiency of 2–4 inch diameter pipe flares burning C1–C4 alkane-based flare gas mixtures with up to 70% inert fraction (CO_2 and N_2) and d) corresponding histograms of the errors in the predicted inefficiency.



General Model	Coefficient (w/ 95% coefficient bounds)	Goodness of fit
$(1-\eta)(LHV_m/LHV_{m,CH_4})^{1.9} = a(U_\infty/(gV_j D_j)^{1/3})^b + c$	$a = 0.05429$ (0.05023, 0.05834) $b = 1.734$ (1.705, 1.763) $c = 0.2354$ (0.2109, 0.26)	SSE: 2.2823 R^2 : 0.9958 Adjusted R^2 : 0.9957 RMSE: 0.0767

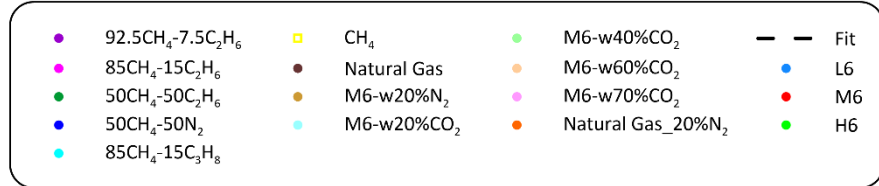
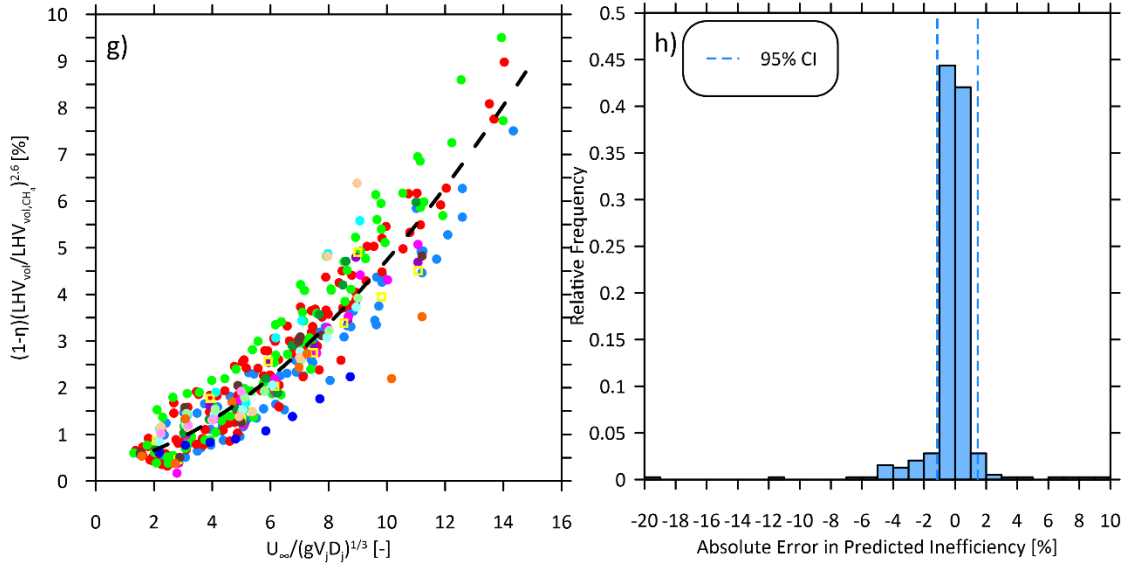


Figure C8: e) Empirical model using LHV_{mass} as a correlating parameter to predict carbon conversion inefficiency of 2–4 inch diameter pipe flares burning C1–C4 alkane-based flare gas mixtures with up to 70% inert fraction (CO₂ and N₂) and f) corresponding histograms of the errors in the predicted inefficiency.



General Model	Coefficient (w/ 95% coefficient bounds)	Goodness of fit
$(1-\eta)(LHV_{vol}/LHV_{vol,CH_4})^{2.6} = a(U_{\infty}/(gV_j D)^{1/3})^b + c$	a = 0.09189 (0.05666, 0.1271) b = 1.677 (1.529, 1.825) c = 0.3677 (0.1739, 0.5616)	SSE: 130.2902 R ² : 0.8908 Adjusted R ² : 0.8903 RMSE: 0.5795

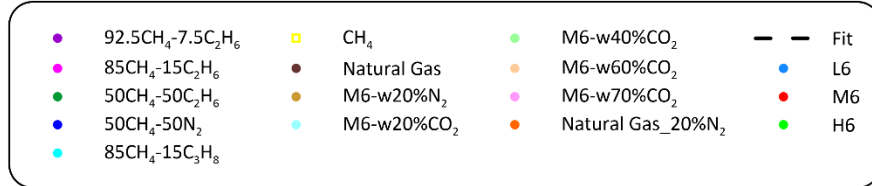


Figure C9: g) Empirical model using LHV_{vol} as a correlating parameter to predict carbon conversion inefficiency of 2–4 inch diameter pipe flares burning C1–C4 alkane-based flare gas mixtures with up to 70% inert fraction (CO₂ and N₂) and h) corresponding histograms of the errors in the predicted inefficiency.

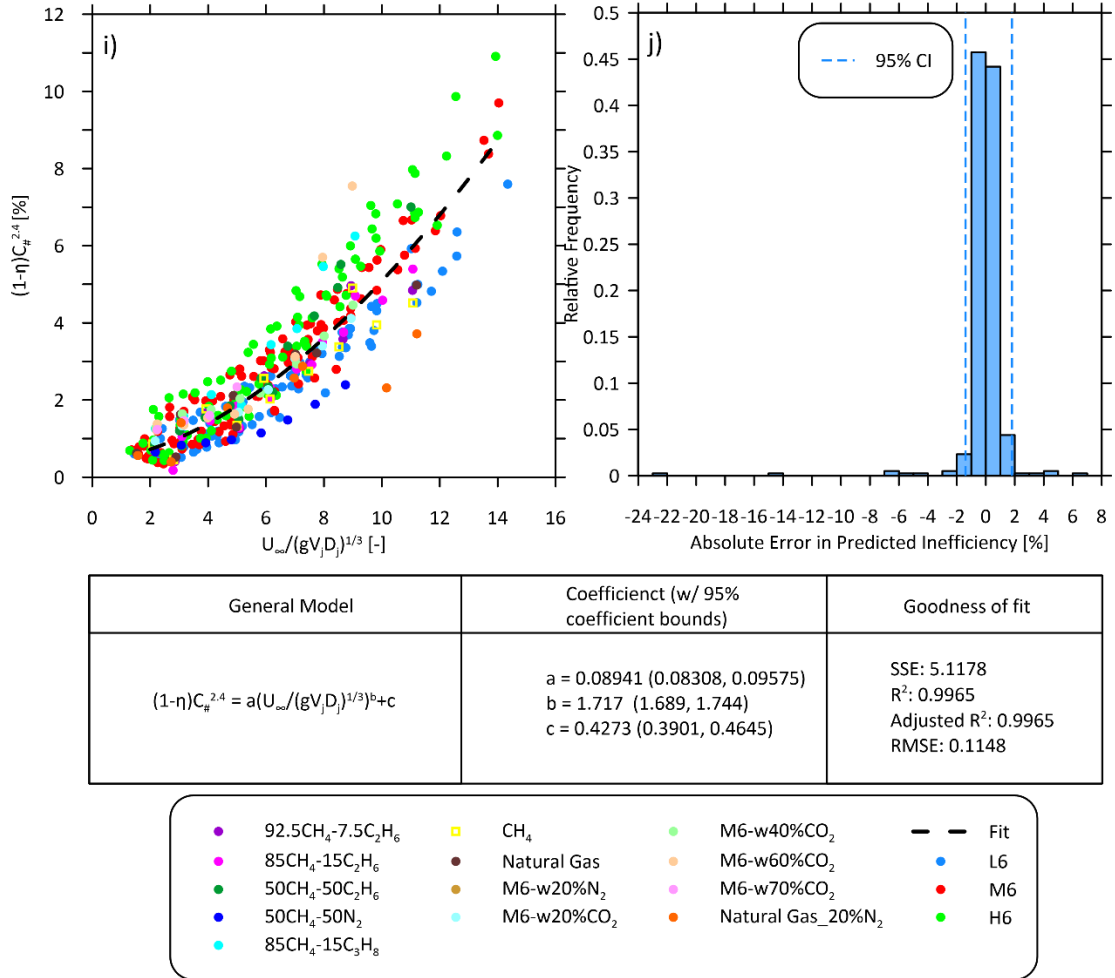


Figure C10: i) Empirical model using mean carbon number ($C_{\#}$) as a correlating parameter to predict carbon conversion inefficiency of 2–4 inch diameter pipe flares burning C1–C4 alkane-based flare gas mixtures with up to 70% inert fraction (CO₂ and N₂) and j) corresponding histograms of the errors in the predicted inefficiency.

Appendix D Candidate Empirical Models for Predicting Flare Methane Yields

As discussed in Section 6.3, several candidate empirical models were considered to predict methane yields of flares in a turbulent crosswind burning a range of flare gas compositions, for which either $AF_{vol,stoic}$, $AF_{mass,stoic}$, T_{ad} , LHV , $C_{\#}$, or S_L were used as a correlating parameter. In each case, power law fits in the form of $f(x) = ax^b + c$ were applied to the correlated data and fit coefficients of the model parameters were optimized to minimize the absolute errors in the predicted inefficiencies. Figure C to Figure C5 show candidate models and corresponding histograms of the relative error when predicting the experimentally measured methane yields of 2–4 inch diameter pipe flare burning C1–C4 alkane mixtures with <20% inert fraction in turbulent crossflow. Figure C6 to Figure C10 show similar candidate models but considering fuel mixtures with up to 70% inert fraction. The table below each figure shows its corresponding fit equation and associated statistics.

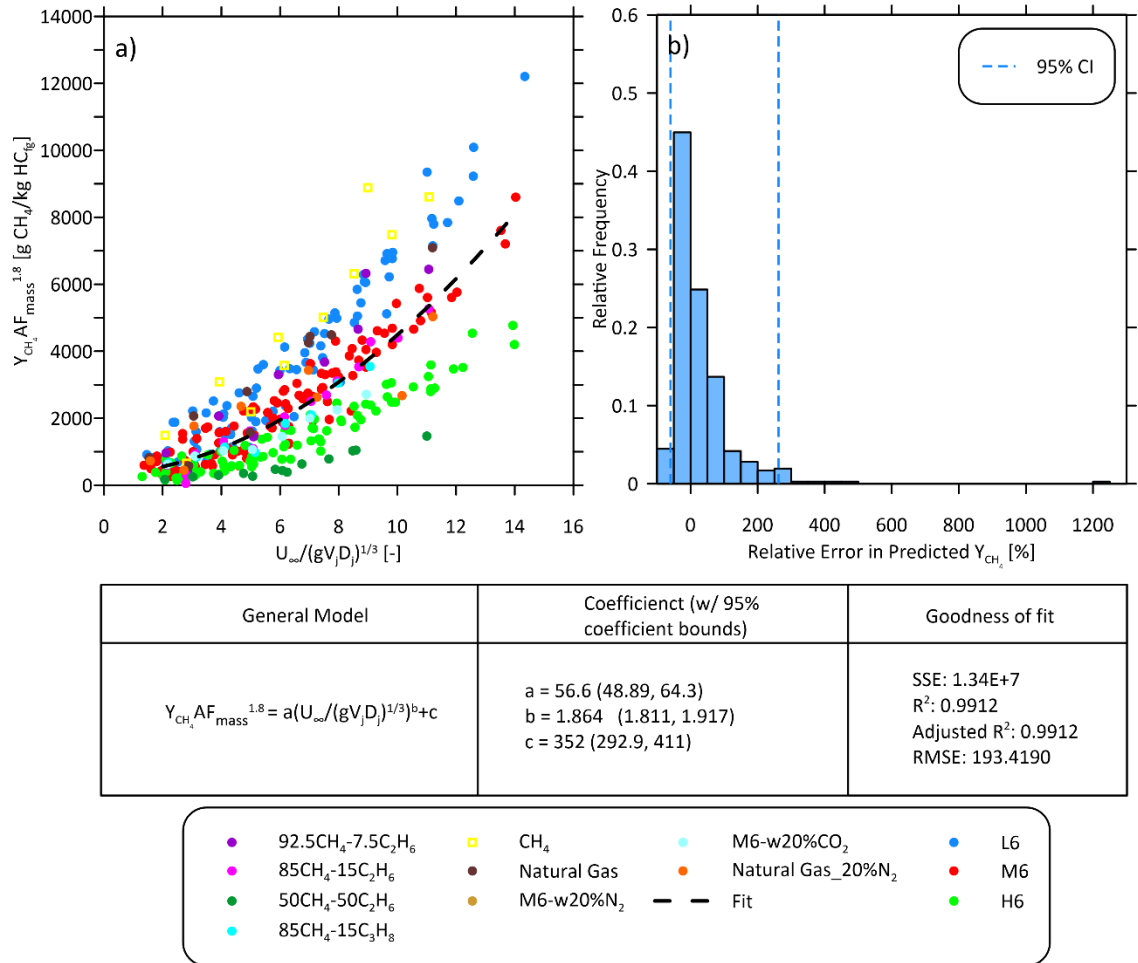
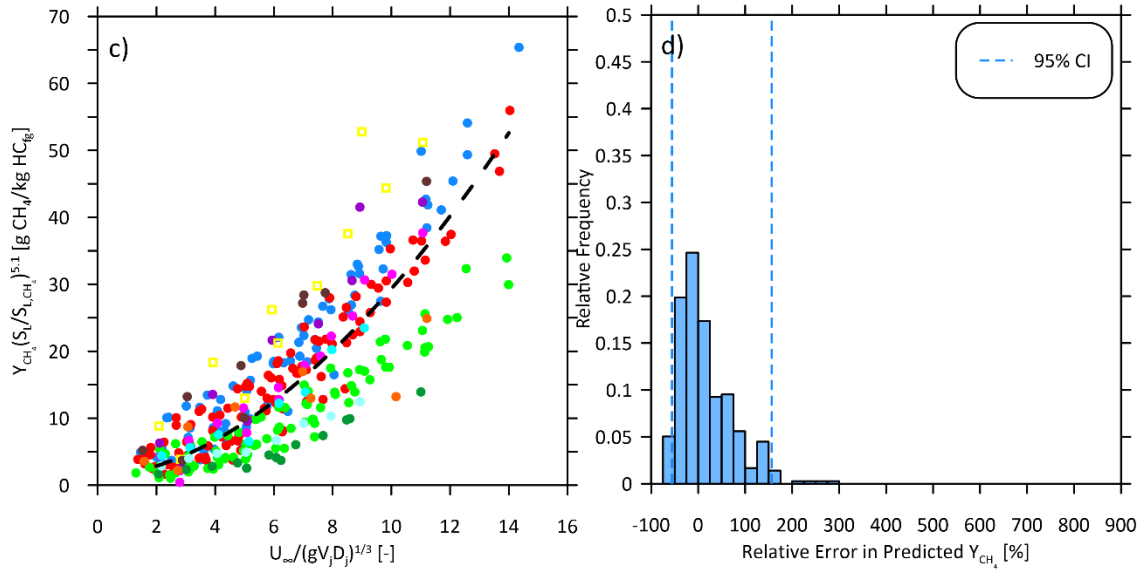


Figure D1: a) Empirical model using $AF_{mass,stoic}$ as a correlating parameter to predict carbon conversion inefficiency of 2–4 inch diameter pipe flares burning C1–C4 alkane-based flare gas mixtures with less than 20% inert fraction (CO₂ and N₂) and b) corresponding histograms of the errors in the predicted inefficiency.



General Model	Coefficient (w/ 95% coefficient bounds)	Goodness of fit
$Y_{CH_4}(S_L/S_{L,CH_4})^{5.1} = a(U_{\infty}/(gV_j D))^{1/3} + b + c$	a = 0.4483 (0.4016, 0.4949) b = 1.796 (1.755, 1.836) c = 1.306 (0.9882, 1.624)	SSE: 353.3401 R ² : 0.9931 Adjusted R ² : 0.9931 RMSE: 0.9935

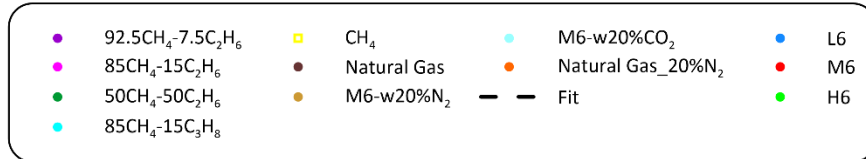
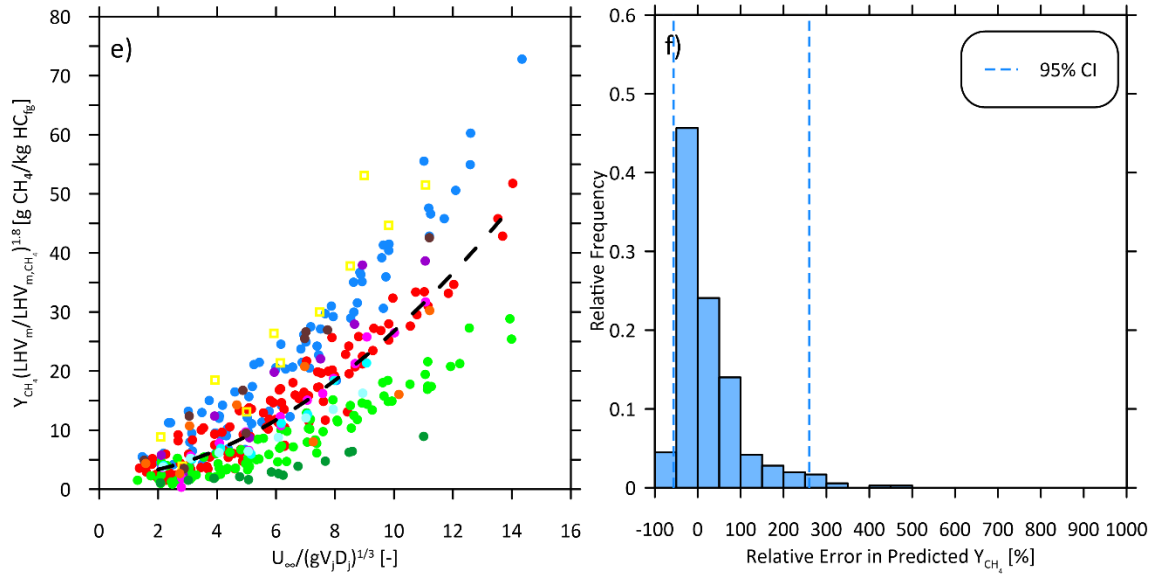


Figure D2: c) Empirical model using S_L as a correlating parameter to predict carbon conversion inefficiency of 2–4 inch diameter pipe flares burning C1–C4 alkane-based flare gas mixtures with less than 20% inert fraction (CO₂ and N₂) and d) corresponding histograms of the errors in the predicted inefficiency.



General Model	Coefficient (w/ 95% coefficient bounds)	Goodness of fit
$Y_{CH_4} (LHV_m/LHV_{m,CH_4})^{1.8} = a(U_{\infty}/(gVD)^{1/3})^b + c$	a = 0.3577 (0.2997, 0.4157) b = 1.839 (1.776, 1.902) c = 2.063 (1.638, 2.489)	SSE: 670,9785 R ² : 0.9876 Adjusted R ² : 0.9875 RMSE: 1.3690

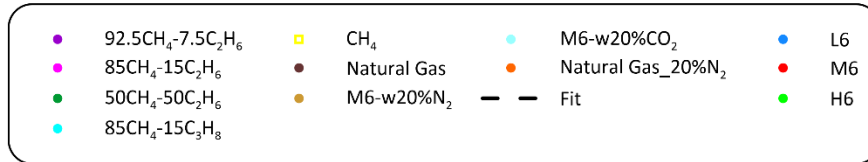
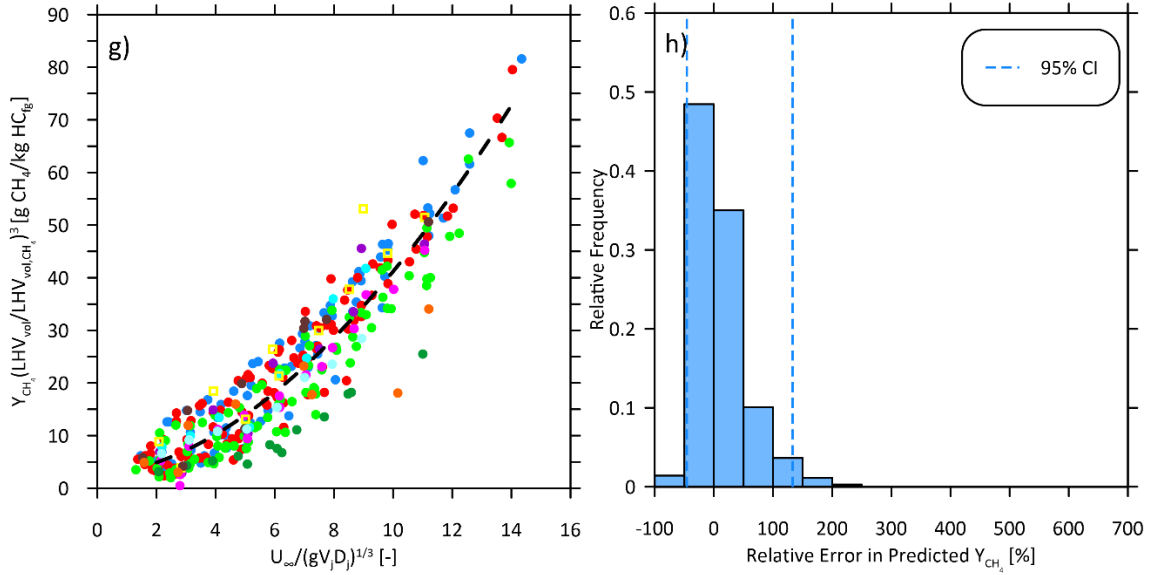


Figure D3: e) Empirical model using LHV_{mass} as a correlating parameter to predict carbon conversion inefficiency of 2–4 inch diameter pipe flares burning C1–C4 alkane-based flare gas mixtures with less than 20% inert fraction (CO₂ and N₂) and f) corresponding histograms of the errors in the predicted inefficiency.



General Model	Coefficient (w/ 95% coefficient bounds)	Goodness of fit
$Y_{CH_4} (LHV_{vol}/LHV_{vol,CH_4})^3 = a(U_{\infty}/(gV_1D_1)^{1/3})^b + c$	a = 0.6403 (0.384, 0.8966) b = 1.779 (1.624, 1.934) c = 2.698 (1.002, 4.394)	SSE: 9822 R ² : 0.8874 Adjusted R ² : 0.8868 RMSE: 5.2381

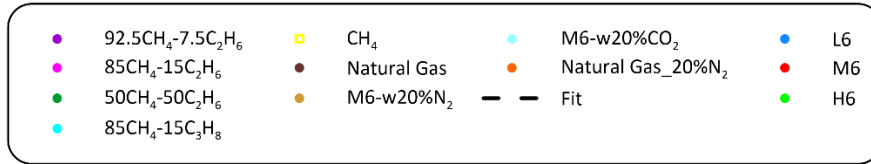


Figure D4: g) Empirical model using LHV_{vol} as a correlating parameter to predict carbon conversion inefficiency of 2–4 inch diameter pipe flares burning C1–C4 alkane-based flare gas mixtures with less than 20% inert fraction (CO₂ and N₂) and h) corresponding histograms of the errors in the predicted inefficiency.

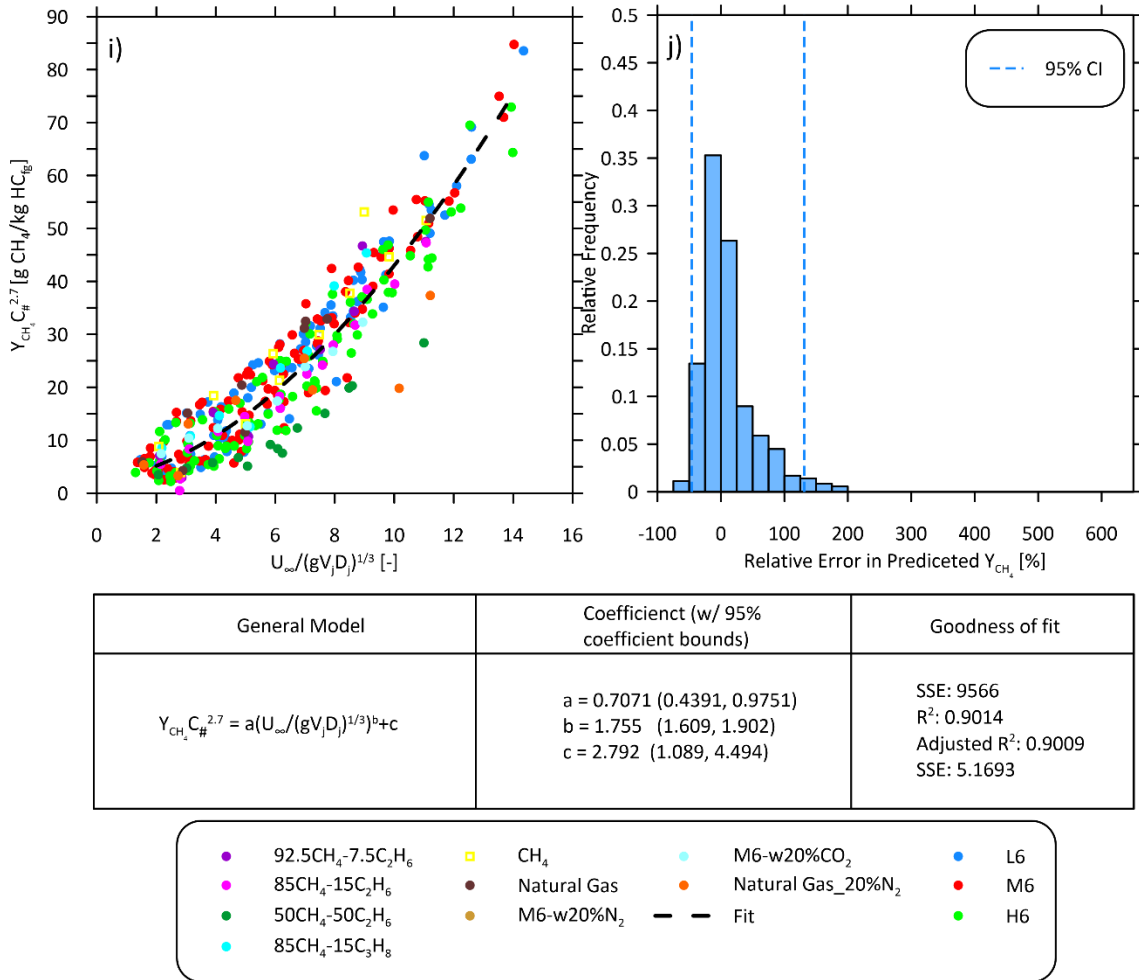


Figure D5: i) Empirical model using mean carbon number ($C_{\#}$) as a correlating parameter to predict carbon conversion inefficiency of 2–4 inch diameter pipe flares burning C1–C4 alkane-based flare gas mixtures with less than 20% inert fraction (CO₂ and N₂) and j) corresponding histograms of the errors in the predicted inefficiency.

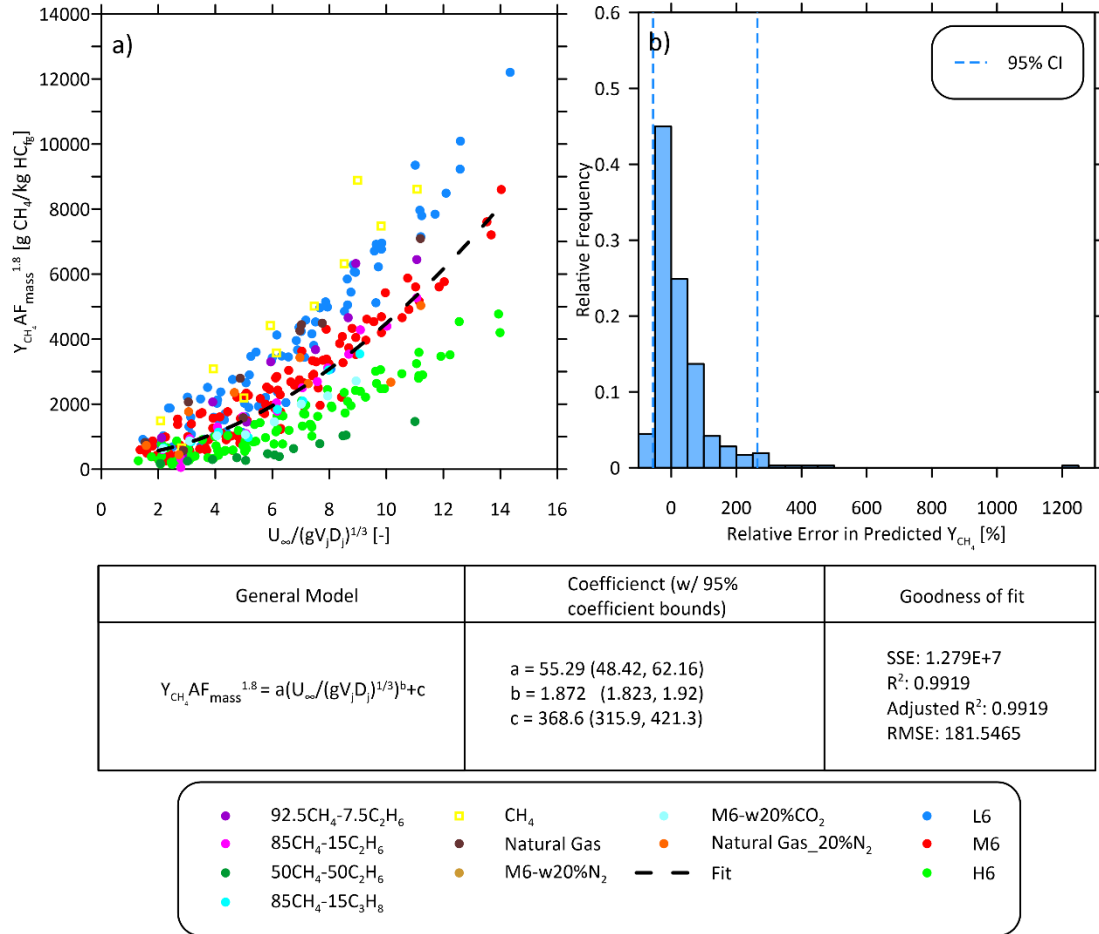
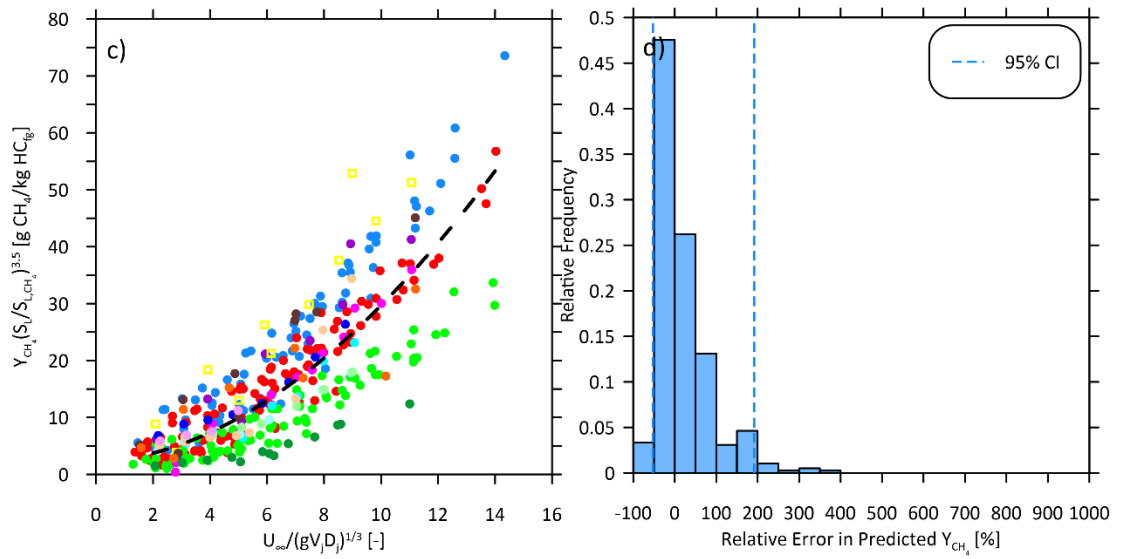


Figure D6: a) Empirical model using $AF_{mass,stoic}$ as a correlating parameter to predict methane yields of 2–4 inch diameter pipe flares burning C1–C4 alkane-based flare gas mixtures with up to 70% inert fraction (CO₂ and N₂) and b) corresponding histograms of the errors in the predicted methane yield.



General Model	Coefficient (w/ 95% coefficient bounds)	Goodness of fit
$Y_{CH_4} (S_L/S_{L,CH_4})^{3.5} = a(U_{\infty}/(gVD)^{1/3})^b + c$	a = 0.3874 (0.3474, 0.4274) b = 1.849 (1.809, 1.89) c = 2.333 (2.039, 2.628)	SSE: 389.1081 R ² : 0.9935 Adjusted R ² : 0.9934 RMSE: 1.0014

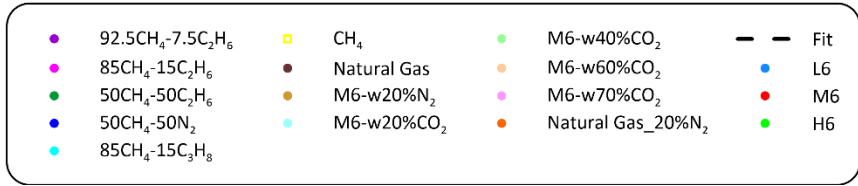


Figure D7: c) Empirical model using S_L as a correlating parameter to predict methane yields of 2–4 inch diameter pipe flares burning C1–C4 alkane-based flare gas mixtures with up to 70% inert fraction (CO₂ and N₂) and d) corresponding histograms of the errors in the predicted methane yield.

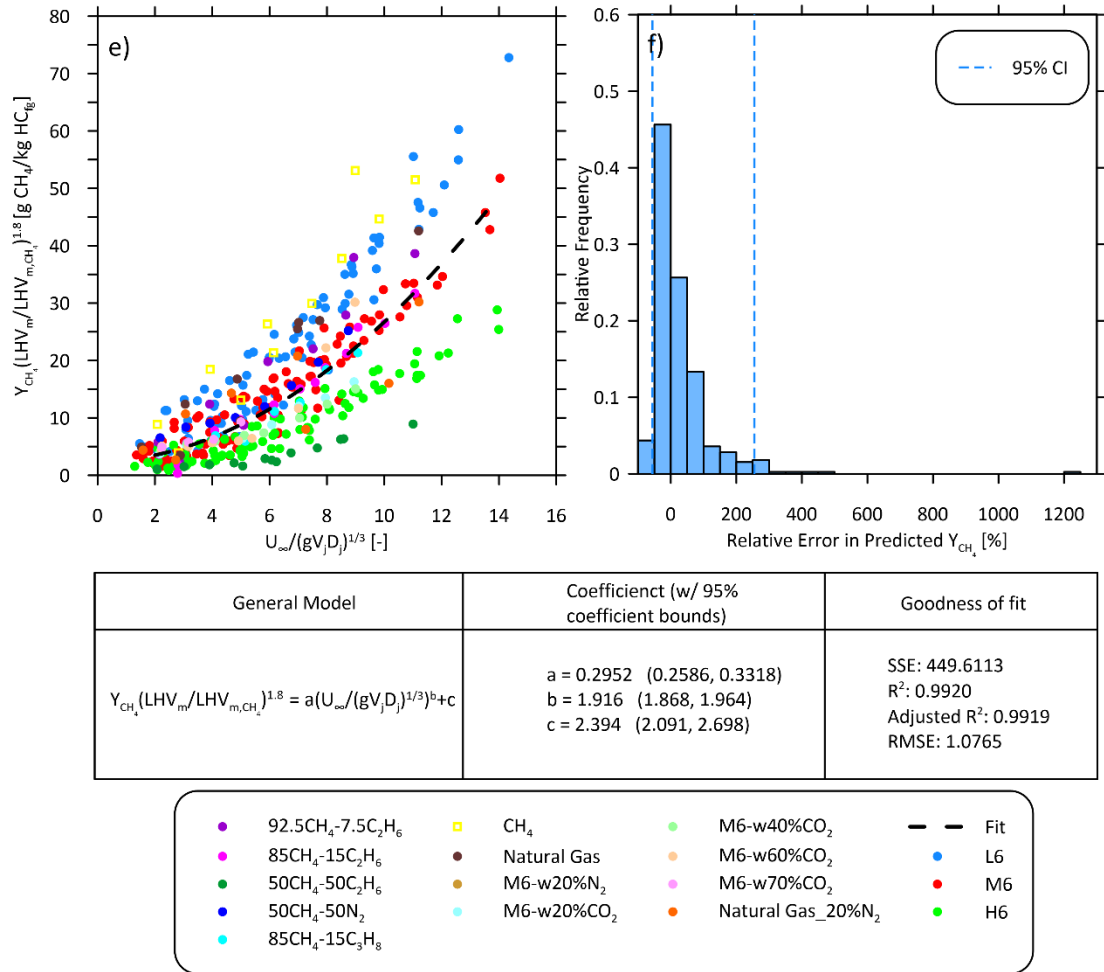
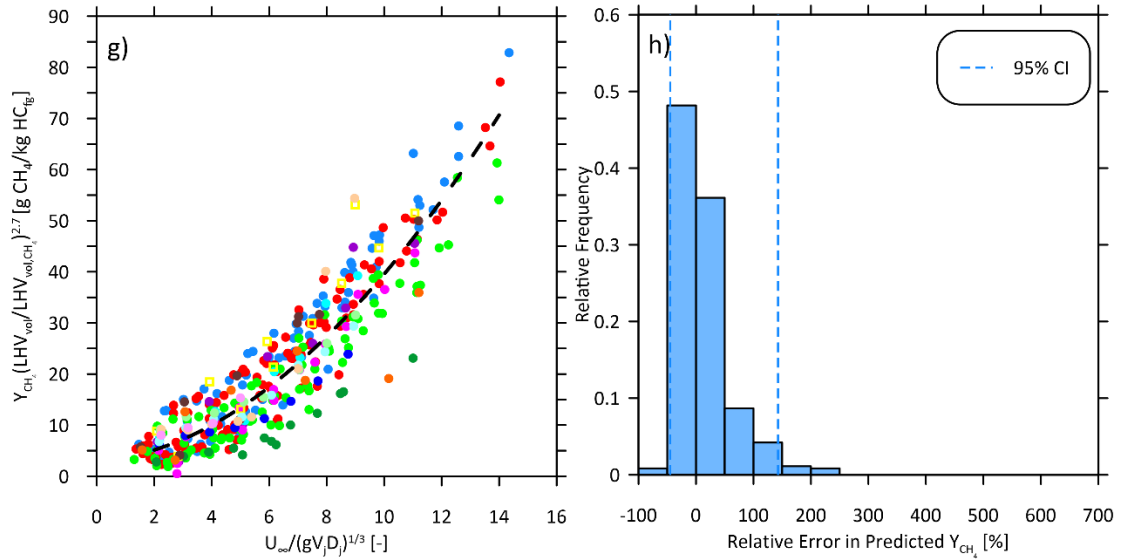


Figure D8: e) Empirical model using LHV_{mass} as a correlating parameter to predict methane yields of 2–4 inch diameter pipe flares burning C1–C4 alkane-based flare gas mixtures with up to 70% inert fraction (CO₂ and N₂) and f) corresponding histograms of the errors in the predicted methane yield.



General Model	Coefficient (w/ 95% coefficient bounds)	Goodness of fit
$Y_{CH_4}(\text{LHV}_{vol}/\text{LHV}_{vol,CH_4})^{2.7} = a(U_{\infty}/(gVD)^{1/3})^b + c$	a = 0.5259 (0.3024, 0.7493) b = 1.839 (1.674, 2.005) c = 3.265 (1.645, 4.885)	SSE: 1.1574E+4 R ² : 0.8689 Adjusted R ² : 0.8682 RMSE: 5.4617

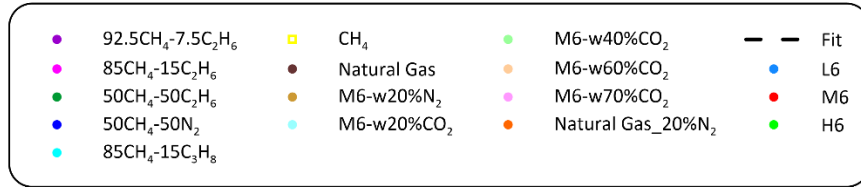
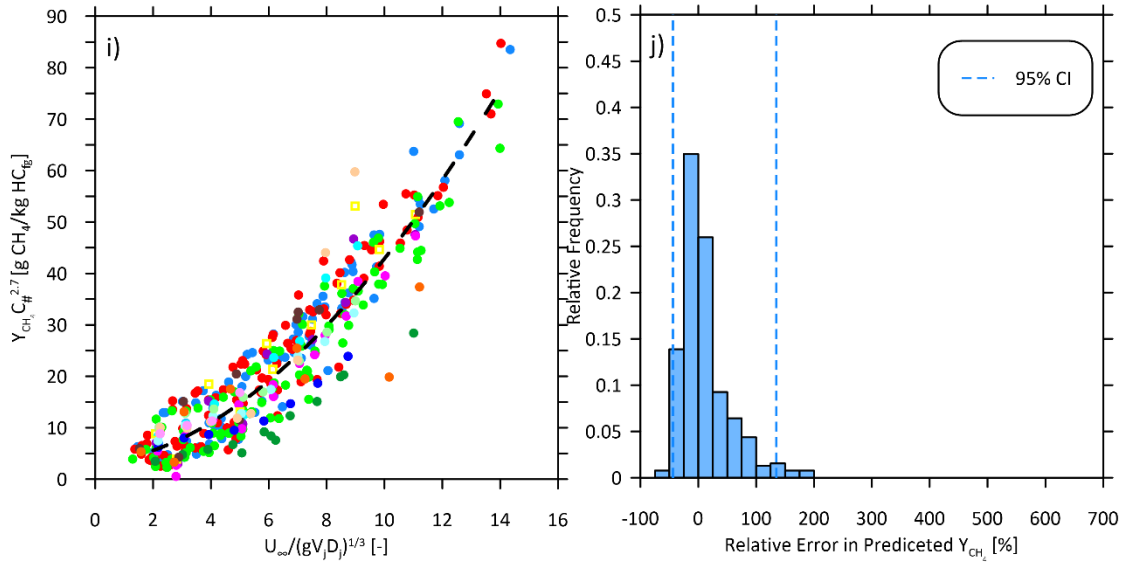


Figure D9: g) Empirical model using LHV_{vol} as a correlating parameter to predict methane yields of 2–4 inch diameter pipe flares burning C1–C4 alkane-based flare gas mixtures with up to 70% inert fraction (CO₂ and N₂) and h) corresponding histograms of the errors in the predicted methane yield.



General Model	Coefficient (w/ 95% coefficient bounds)	Goodness of fit
$Y_{CH_4, C_{\#}}^{2.7} = a(U_{\infty}/(gV_i D_i)^{1/3})^b + c$	a = 0.6271 (0.3886, 0.8656) b = 1.799 (1.651, 1.947) c = 3.404 (1.792, 5.015)	SSE: 1.08E+4 R ² : 0.8939 Adjusted R ² : 0.8934 SSE: 5.2816

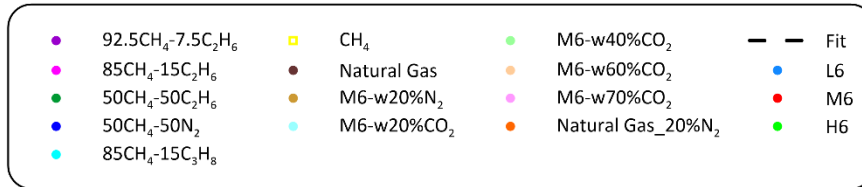


Figure D10: i) Empirical model using mean carbon number ($C_{\#}$) as a correlating parameter to predict methane yields of 2–4 inch diameter pipe flares burning C1–C4 alkane-based flare gas mixtures with up to 70% inert fraction (CO₂ and N₂) and j) corresponding histograms of the errors in the predicted methane yield.

Appendix E Flare Carbon Conversion Inefficiencies and Methane Yields for Different Fuel Mixtures as a Function of Flare Gas Properties

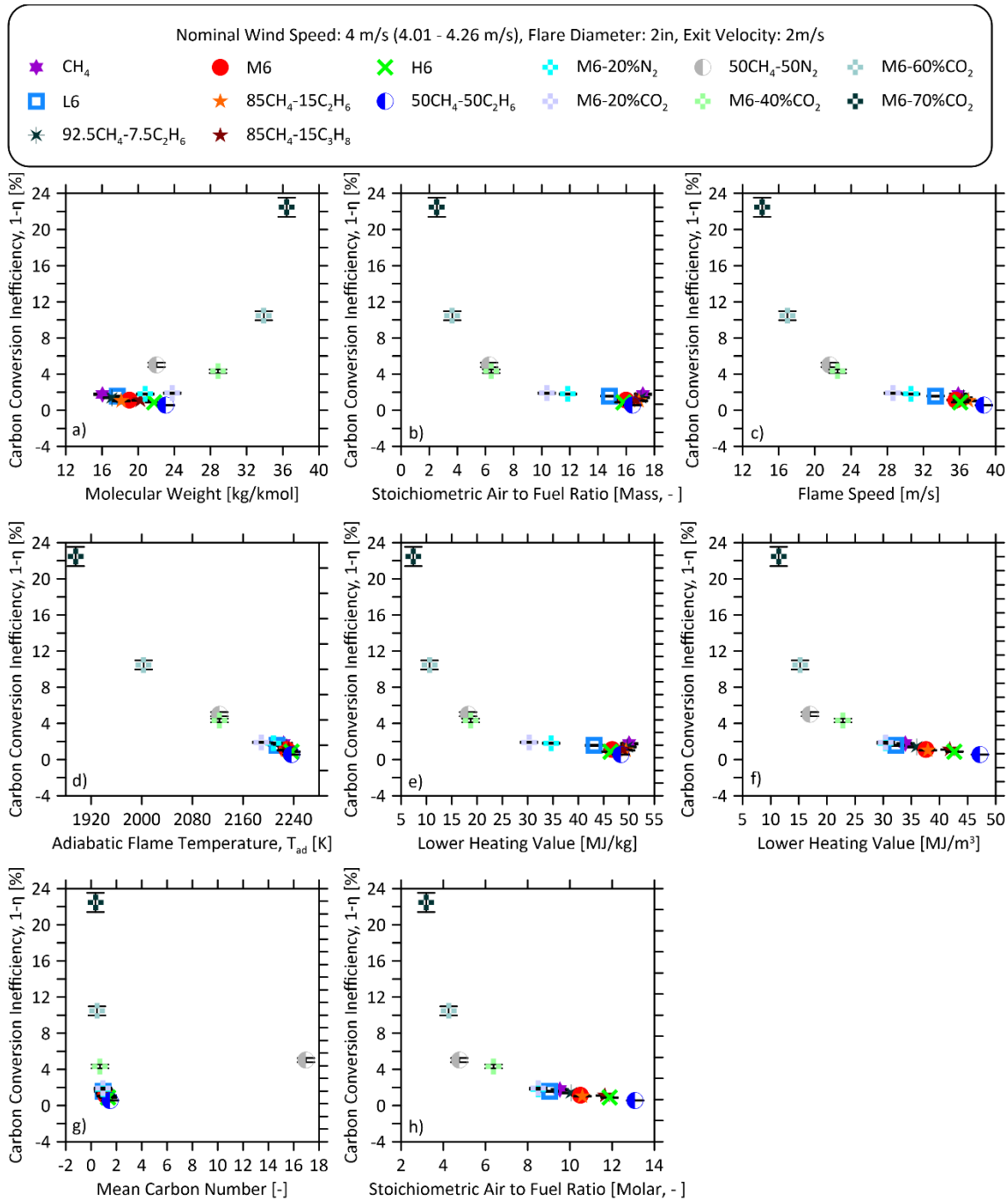


Figure E1: Carbon conversion inefficiency of 2-inch diameter flares burning a range of flare gas mixtures flare at an exit velocity of 2 m/s at a nominal crosswind speed of 4 m/s plotted as a function of several different potential correlating parameters.

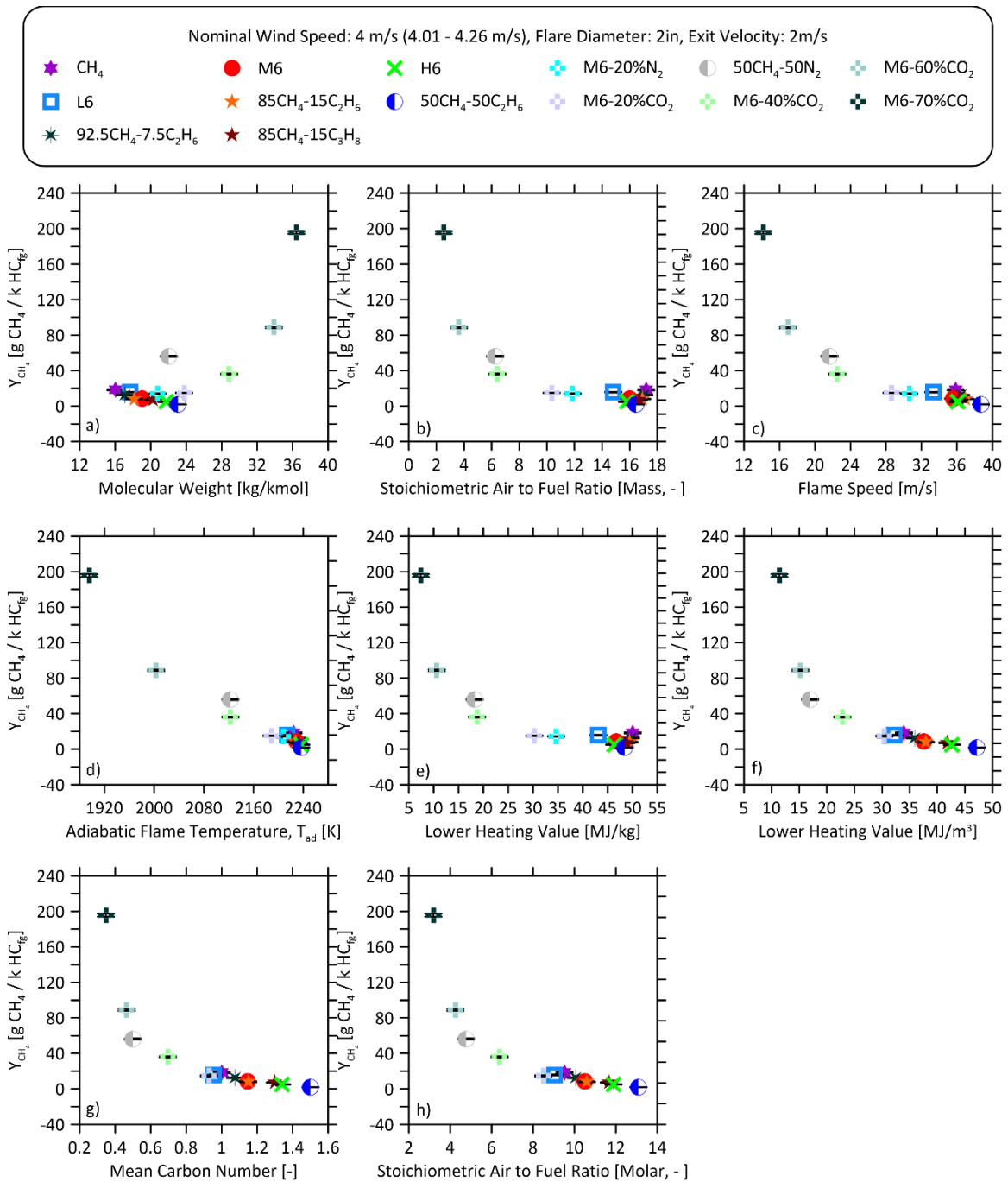


Figure E2: Methane yields of 2-inch diameter flares burning a range of flare gas mixtures flare at an exit velocity of 2 m/s at a nominal crosswind speed of 4 m/s plotted as a function of several different potential correlating parameters.

Appendix F Reference Laminar Flame Speed Calculations

Reference stoichiometric laminar flame speeds, S_L , for the flare gas compositions used in experiments were calculated via 1D premixed flame simulations using Cantera 2.5.1. Simulations used the San Diego mechanism, a kinetic mechanism tailored for combustion processes involving C1–C4 hydrocarbons that includes 57 species and 268 reactions (UCSD 2016). To validate the Cantera results, simulated S_L values for CH₄, C₂H₆, C₃H₈, and C₄H₁₀ were compared to experimental measurements reported by Davis and Law (1998) and Vagelopoulos and Egolfopoulos (1998). Relative to experimental results, simulated results vary by up to 16% CH₄, 4.47% for C₂H₆, 8.91% for C₃H₈, and overestimate C₄H₁₀ by 8.62%.

Table F1: Experimentally measured Laminar flame speeds of C1–C4 alkanes and relative differences to flame speeds calculated in Cantera using the San Diego mechanism (UCSD 2016). S_L values were calculated at 298.15K and 1 atm[†].

Species	Laminar Flame Speed [m/s]		
	Experimental Measurements		Cantera Simulated value using the San Diego Mechanism (UCSD 2016) (% error relative to (Davis and Law 1998) / % error relative to (Vagelopoulos and Egolfopoulos 1998))
	(Davis and Law 1998)	(Vagelopoulos and Egolfopoulos 1998)	
Methane	0.400	0.374	0.3359 (-16.03%/-10.12%)
Ethane	0.430	0.405	0.4231 (-1.6%/4.47%)
Propane	0.440	0.384	0.4008 (-8.91%/4.38%)
Butane	0.362	0.362	0.3932 (8.62%/8.62%)

[†]Experimental results were referenced at atmospheric conditions, without providing precise temperature and pressure. Therefore, conditions have been interpreted as a temperature of 298.15K (which was referenced by (Turns 2000)) and a pressure of 1 atm.

Flame speed was calculated for all compositions in this thesis and are presented in Figure F1 and Table F2. Laminar flame speeds were evaluated at a temperature of 288.15K and pressure of 1 atmosphere (101325 Pa) at stoichiometric conditions. To the author’s knowledge, these are the best available data and provide a good first approximation of the reference laminar flame speed of the multicomponent gas-mixtures used in this thesis.

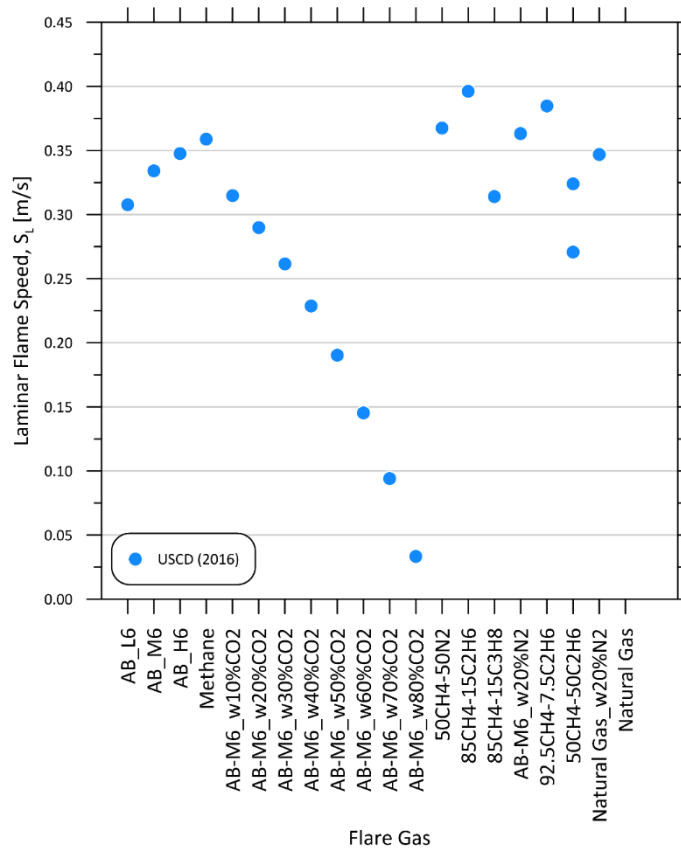


Figure F1: Reference laminar flame speeds for different flare gas mixtures calculated via Cantera 5.2.1 using the San Diego mechanism (UCSD 2016) at 288.15K and 1 atm.

Table F2: Reference laminar flame speeds for different flare gas mixtures calculated via Cantera 5.2.1 using the San Diego mechanism (UCSD 2016) at 288.15K and 1 atm.

Flare Gas	Laminar Flame Speed, S_L [m/s] (15°C and 1 atm)
Methane	0.359
AB_L6	0.308
AB_M6	0.334
AB_H6	0.348
AB-M6_w20%N2	0.314
AB-M6_w20%CO2	0.290
AB-M6_w40%CO2	0.229
AB-M6_w60%CO2	0.145
AB-M6_w70%CO2	0.094
92.5CH4-7.5C2H6	0.363
85CH4-15C2H6	0.367
85CH4-15C3H8	0.396
50CH4-50C2H6	0.385
50CH4-50N2	0.271
NATURAL GAS	0.347
NATURAL GAS_w20%N2	0.324